Degradation of Environmental Protection Coatings for Gas Turbine Materials

Laura Nalin

MPhil Thesis

Supervisors
Dr. Nigel Simms
Prof. John Nicholls

December 2008

School of Applied Sciences
Energy Technology Centre, Sustainable Systems Department
Cranfield University, Cranfield, Bedfordshire MK43 0AL, UK

Abstract

Nowadays, problems of component materials reliability in gas and oil-fired gas turbines focus on assessing the potential behaviour of commonly employed coatings, in order to avoid expensive and unpredictable failure in service and producing new materials whose performance meets life time and manufacturing/ repairing requirements.

This MPhil project has investigated the oxidative and corrosive degradation mechanisms for some of the alloy/coatings systems (CMSX-4, CMSX-4/ RT22, CMSX-4/ CN91 and CMSX-4/ "LCO22"), which are currently used for turbines blades and vanes, in order to achieve a better knowledge of materials behaviour and to improve models for the prediction of turbine components' lives. To achieve this target the study has made use of realistic simulations of turbine exposure conditions in combined with pre- and post-exposure metrology of bar shape materials samples, while optical microscopy has been applied to describe the microstructural evolution during the exposure and the products of the degradation for the hot corrosion.

For high temperature oxidation, over extended periods of time (up to 10,000 hours), the research has allowed to describe the morphological changes in respect of the exposure time and temperature and to determine the oxidation kinetics experienced by the alloy and coatings. A model has been presented for predicting θ- α-Al_2O_3 growth. Moreover, using NASA COSP spalling model, with rate constants values coming from this study, a comparison between experimental mass change data and prediction has been shown.

The hot corrosion study has provided new quantitative metal loss data and observations that extend/validate an existing model for materials life prediction, based on defining the severity of the corrosion conditions through measures of gas composition and contaminant deposition flux.

Contents list

Tables list

Figures list

Introduction

World energy consumption is expected to increase by 57 percent from 2004 to 2030 (Fig.1), in order to satisfy the demand by industrial, transportation, domestic and commercial service (hospital, shopping centres, office, etc.) sectors [31]. Thus, the consumption of fuels employed to provide energy, i.e. coal, oil, gas, nuclear and renewable, is projected to increase as well, but by different degrees for the various fuels types (Fig. 2).

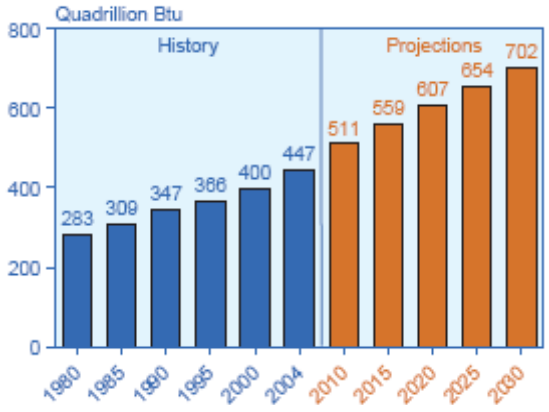

Fig.1 World marketed energy consumption, time vs quadrillion Btu [1].

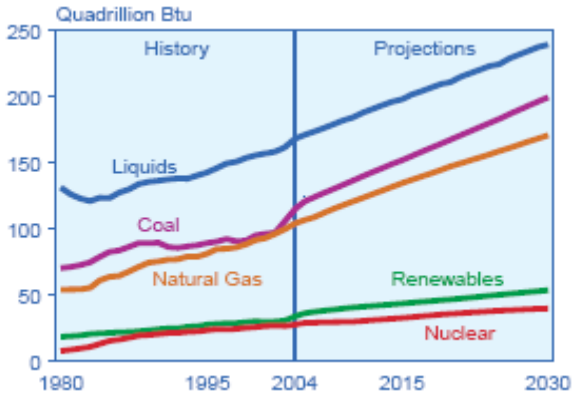

Fig.2 World marketed energy use by fuel type, time vs quadrillion Btu [1]

Due to the gradual depletion of fuels for electricity generation and global warming due to CO_2 emissions, providing energy cleanly, safely and in a sustainable way has become a serious and worrying issue [86].

Combined cycle power generation is one approach to the challenge of generating electricity from coal much more efficiently and cleanly than conventional power plants (e.g. pulverized power generation) [92]. Moreover, to meet both environmental pressures and market demands some changes in operating conditions and procedures are being introduced, such as using co-firing with biomass, increasing of plant shut-downs and raising operating temperature for higher energy production efficiency [73, 96].

The gas turbine is a component within different natural gas-fired combined cycle power systems and in systems designed to use coal-derived fuel gases.
The changes to the operating conditions that are life limiting for turbine blades and vanes are a result of increased thermal and mechanical stresses and the corrosive environment [20]. For

example sulphur oxides (SO_x), hydrogen chlorine (HCl) and alkalis, coming from dirtier fuels, may enhanced materials corrosion [92]; oxidation rate increases with higher temperature; frequent outages may lead to rupturing in the protective oxide layer, placing fresh metal in contact with the aggressive environment and thus markedly increasing the corrosion rate [23].

Problems of component materials reliability in gas and oil-fired gas turbine have been investigated since about 1970 [61]. Nowadays, material issues focus on

- assessing the potential behaviour of commonly employed coatings, in order to avoid expensive and unpredictable failure in service;
- producing new materials whose performance meets life time and manufacturing/ repairing/ refurbishing requirements [73].

The Engineering and Physical Sciences Research Council (**EPSRC**) supports the **SUPERGEN** Consortium on **"Conventional Power Plant Lifetime Extension"** that is investigating increased efficiency and extending components' lives in conventional fossil fuel fired power plants as they use new fuels and operating conditions. Within the consortium Cranfield University's role is to address issues related to oxidation and corrosion.

This MPhil project, carried out over the last two years, has investigated the oxidative and corrosive degradation mechanisms for some of the alloy/coatings systems that are currently used for turbines blades and vanes in order to achieve a better knowledge of materials damage. In particular the experimental data have been generated for extend/validate existing models for the prediction of turbine components' lives.

In order to define the materials behaviour, and in particular to quantify the materials damage (e.g. damage depth, weight loss/gain), the study has made use of realistic simulations of turbine exposure conditions in furnaces (i.e. temperature, time of exposure, gas composition and deposit flux) combined with pre- and post-exposure metrology of bar shape materials samples. Moreover, optical microscopy has allowed of the observation of the main characteristics of oxidation and Type I/ Type II hot corrosion degradation experienced by the uncoated superalloy CMSX-4 and by its three coated systems: CMSX-4/ RT22, CMSX-4/ CN91 and CMSX-4/ "LCO22" .

MPhil objectives

This MPhil project has aimed to investigate the different oxidation/hot corrosion behaviour that alloy/coatings systems exhibit during their employment as materials making up turbines blades and vanes.

To achieve this objective two main conditions of exposure have been selected for the study: isothermal oxidation and hot corrosion, both with interrupted shut downs to allow materials inspection. For each of them the aim has been that to quantify the material loss and to describe the microstructural evolution during the exposure.

In addition, for high temperature oxidation, the research has been targeted at determining, over extended periods of time, the oxidation kinetics experienced by the alloy and coatings, in order to promote understanding and hence develop a new model for predicting materials consumption in respect of the extended exposure time and temperature.

Concerning the hot corrosion, the study has aimed to provide new quantitative metal loss data and observations for extending/validating an existing model for materials life prediction, based on defining the severity of the corrosion conditions through measures of gas composition and contaminant deposition flux.

1. Literature review

1.1 Gas turbine operation

The gas turbine is a critical component within various combined cycle power plants whose working system can be described and illustrated (Fig. 3) as follows:

- Compressed air (up to 30bar [13]) enters a combustion chamber where fuel is injected. The combustion takes place and combustion products exit the chamber at temperature between 800° and 1380°C, depending on the power systems [69, 70, 95]
- Combustion products expand through the multiple turbine blade rows, cause them to spin. The spinning turbine shaft drives an electricity generator and also the air compressor, which feeds the combustion chamber.
- Hot gas leaves the gas turbine via the exhaust at temperatures around 600°C [13, 95] and 1 bar of pressure.

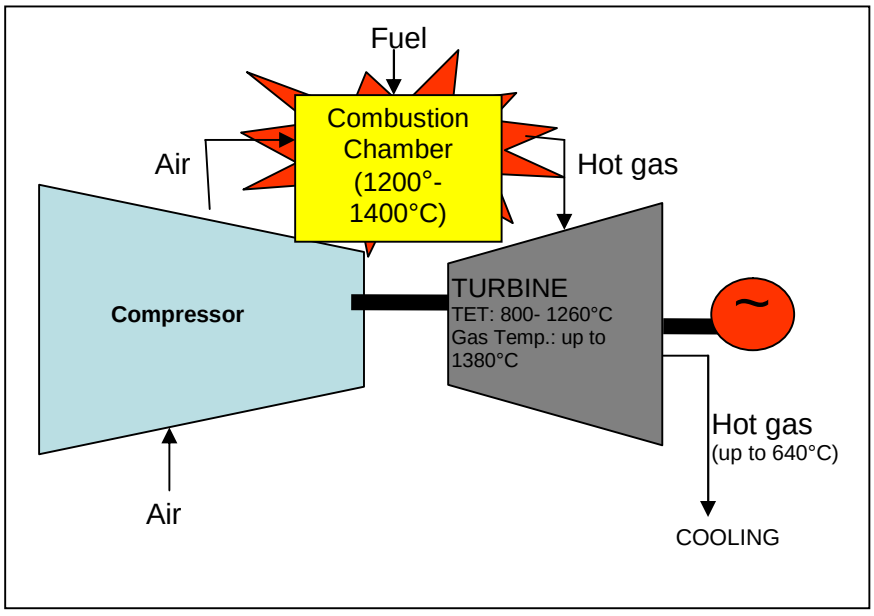

Fig. 3 Main components of a conventional gas turbine engine.

.

Ideally, thermodynamically gas turbines operate according to the Brayton cycle (whose detailed description may be found elsewhere, for example [25]).

When a power producing engine or plant employs more than one thermodynamic cycle it is named a combined cycle. In a combined cycle power plant (CCPP), or combined cycle gas turbine (CCGT) plant, a gas turbine generates electricity and the waste heat from that is used

to make steam to generate additional electricity via a steam turbine**;** this last step enhances the efficiency of electricity generation.

Many new power plants are built using various types of combine cycle and these have become widespread in use by the late 1980s [74]. A combine cycle system can convert more than 50-60% of the chemical energy in the gas to electrical energy [24, 44, 74], overtaking the efficiency of a simple Brayton cycle which achieves a value of 39% [52].

Moreover, the efficiency of power generation is determined by the difference in temperature at which heat is input to and rejected from the engine, according to the Carnot efficiency equation:

$$Efficiency = \frac{T_1 - T_2}{T_1}$$

where T_1 and T_2 are inlet and exit temperatures respectively.

As any temperature (and pressure) rise in the inlet gas can directly be translated in power generation efficiency improvement [67, 106], continuing efforts are being made to increase operating temperature [72] (upwards to 1500°C [74]).

Different approaches are being currently taken into consideration to achieve this purpose, such as [103]:

- Improvement of high temperature strength of the alloy
- Development of methods of cooling the blades and vanes
- Use of protecting coatings and improvement of their technology
- Application of thermal barrier coatings

Fig. 4 Turbine rotor before it is placed inside the turbine housing.

1.2 Nickel-base superalloys for turbine blades

Gas turbine should satisfy a lifetime up to 25,000 hours [23, 106] and, as they must withstand different types of degradation (such as creep, thermo-mechanical fatigue, oxidation and corrosion), occurring during the service exposure to aggressive environment, high-performance alloys, or superalloys, are employed as material to make them up.
Three main groups of superalloys exist: nickel-, iron-nickel- and cobalt base.
Blades of gas turbine for land base power plants are mainly constituted of Ni-base superalloys, because nickel is able to retain more high strengths at high temperature than the others [Smith 102].

The research carried out in order to study turbines blade degradation by oxidation and corrosion has pertained to the nickel-base superalloys CMSX-4 (plus three coated systems on the same cast superalloy, § 2.2.1).
CMSX-4 is a single crystal alloy (SX) of second generation (about 3wt% Re), available from the second half of the 1980 (Fig.5) and endowed with ultra high strength [27]. CMSX-4 has not been applied in industrial gas turbines until late 1990.

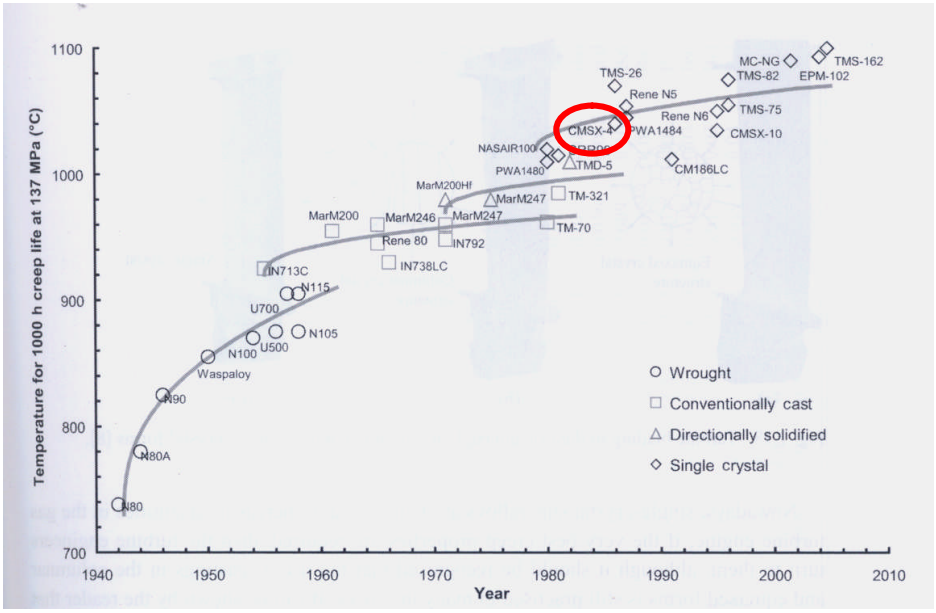

Fig. 5 Evolution of the high-temperature capability of superalloys over a 60 years period since they emerged in the 1940 s. (the creep performance is considered a suitable measure for the progres made) [84]

1.2.1 Phases in Ni base superalloys

The properties of a superalloy depend on its chemical composition and microstructure, which in turn are functions of processing and heat treatment.

The alloying elements of Ni-base superalloys partition to the following structures:

Gamma matrix (γ) (Fig. 6a): It consists of austenitic face-centered cubic (fcc) matrix also known as geometrically closed-packed (gcp) phase. Other than nickel and aluminum, it contains solid solution elements such as Co and Cr and refractory alloying elements (Ta, Re, W, Mo). The gamma lattice structure is not observed; Ni , Cr, Co or Al atoms can occupy any atom sites.

Gamma prime (γ') (Fig.6b): It represents the main strengthening phase [20, 106, 123] formed from aluminum and titanium in combination with Ni in stoichiometric ratio 3Ni to 1Al. It has a primitive cubic lattice, which is derived from the γ, fcc, by ordering Al atoms on cube corners and Ni atoms at the face centres. An example of chemical formula of the precipitate is Ni_3X; where X, the electropositive element, comes from groups III, IV and V (Al, Ti, Hf, Ta…). Thus for a nickel base alloy Ni_3Al or $Ni_3(Al,Ti)$, $(Ni, Co)_3(Al,Ti)$. It appears with either spherical, cubic or plate like shape.

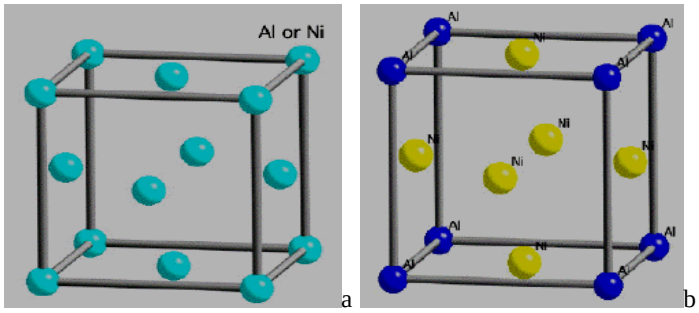

a b

Fig. 6 Crystal structures of γ (a) and γ´(b). The former hasn't a strictly fixed structure (Ni atoms can occupy Al sites and vice-versa); the latter presents Ni atoms at the face centres, Al and Ti atoms at the cube corner [12].

The presence of γ′ at the oxide/coating interface may have a detrimental effect on the oxide quality since this phase has a greater solubility of refractory metal elements [3].

Gamma prime may also present as a film along the grain boundaries, formed after heat treatment and service exposure. It improves creep-rupture properties [27, 106]. Finally, γ′ occurs in raft structures (elongated γ′ in the grains produced after long exposure to tensile stresses) [11, 75].

*Carbides***:** carbon addition of 0.6 % in cast alloy gives reactions between carbon and refractory elements such as Cr, Mo, W, Ti, Ta, Hf and Nb to form MC carbides. They precipitate at the grain boundaries, reducing the tendency for grain boundaries sliding, and in the matrix. During

heat treatment and service carbides begin to decompose and generate lower carbides ($M_{23}C_6$, M_6C). Improved heat treatments have eliminated the cellular carbide problems (shortening rupture life). Since carbides are harder and more brittle than the alloy matrix, their distribution along the grain boundaries will affect the high temperature strength, ductility and creep properties of the nickel base heat resistant alloys. Thus there's an optimum amount and distribution of carbides along grain boundaries. If there are no carbides along grain boundaries, voids will coalesce along them and excess grain boundaries sliding will take place. On the other hand if continuous chains of carbides extend along the grain boundaries continuous fracture paths will be formed [102].

Topologically close packed (TCP) phases: they consist of thin plate-like or needle-like phases such as σ, μ and laves. Often they nucleate on the grain boundary carbides and are detrimental because of the lowered rupture strength and ductility [18, 19, 27, 102], since they deplete the matrix of valuable elements (Co, Mo, W, Re, Cr, etc). Changing the alloy chemistry has led to the elimination of the σ phase in newly developed nickel-base superalloys [102].

1.2.2 Properties of elements in alloys and coatings

Ni-based superalloys are constituted, beside the base metal, of various alloying elements, as illustrated in figure 7. A trade-off must be made when designing alloys for turbine applications, to achieve an optimal combination of resistances to oxidation, corrosion and creep [102].

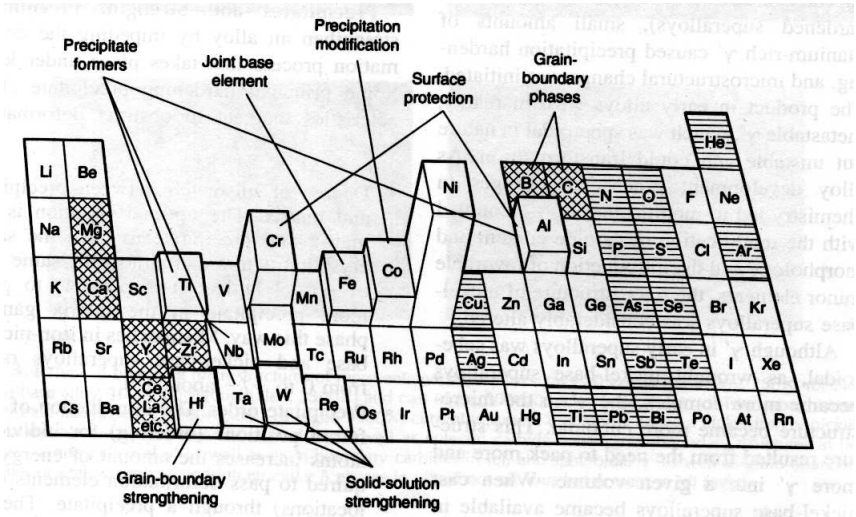

Fig. 7 Alloy elements present in Ni-based superalloys.

Beneficial minor elements are marked with cross-hatch, while detrimental tramp elements are marked with horizontal line hatch [27]

Chromium, Aluminum and Cobalt:

Alloys with high Cr content are found to resist degradation by hot corrosion and sulphidation, while the highest temperature oxidation resistance requires an alumina oxide formation and thus high Al content in addition to sufficient Cr[102].

According to Mevrel R. [66] the role of Cr is essentially to buffer the salt basicity in a range where alumina solubility is at a minimum. Leyens, C. et al. [60] demonstrated increased corrosion resistance (at 950°C) of NiAl-Cr alloy, resembling a commercial aluminide coatings, with increasing Cr contents from 2 to 5 at% (less from 5 to 10%); however NiCoCrAlY (17% Cr) alloy resulted in the best performances in this study. As Cr additions raise corrosion resistance they may decrease oxidation resistance. Cr is believed to accelerate oxide scale formation rate. Moreover, high Cr level may promote TCP [102] (§ 1.2.1), and α-Cr formation at the scale-metal interface, which may keep growing during exposure ultimately causing the onset of spallation [60]. However, best oxidation resistance may be associated with 20-22% Cr and 8% Al.

Cobalt may constitute either the base alloy component or an alloying element along side Nickel. The foremost property motivating its use in the past has been creep resistance [22]; nowadays this property has been called into question [60]. The oxidation resistance of cobalt-base alloys at high temperatures is largely a function of their chromium content: those containing chromium in the amount of 20% (and above) have good oxidation resistance at temperature as high as 1100°C [21]. The corrosion resistance of Co-based alloy is a function of chromium concentration as well [22].

Considering coatings, in particular overlay coating (§ 1.6.2), cobalt, for given level of aluminium and chromium, provides better Type I corrosion resistance due to the inherent resistance of cobalt-base alloys to the sulphidation propagation model (§ 1.5.3) [22].

Rhenium, Titanium and Tantalum in the nickel superalloy:

Rhenium is a very expensive addition and leads to an improvement in the creep strength and fatigue resistance [113, 123]. Prior to Re addition, Ta and W were included to obtain the same creep strengthening [113].

Initially added as strengtheners, titanium and tantalum have been reduced in nickel superalloys as these additions have adverse effects on the oxide scale. Cracking and acceleration of coating oxidation are ascribed [20, 62, 113].

Yttrium and Hafnium in superalloys and coatings:

The reactive elements, such as yttrium and rare earth elements, are added to alloys and coatings for improving oxide layers adherence and improved resistance to thermal shock [49, 76], as far as if segregated at the grain boundaries within the oxide layer, such elements cause a reduction in Al and O transport rates through the scale and thus improve the oxidation kinetics [117].

The properties of yttrium's addition in overlay coating and TBC (thermal barrier coating) have been widely investigated [35, 51, 76, 118] and here following it is summarised:

- Below a Y concentration the element increases adherence between TGO and the coating [20, 58, 67, 72, 76, 123]; Y added into alloy leads to oxide intrusion (peg) formation which mechanically keys the scale to the substrate [49]. Y, moreover, dissolved either in the alloy or in the coating prevents sulphur segregation to the aluminia scale/ coating interface. This helps because sulphur reduces the chemical bonding. Exhaustion of the Y reservoir, in fact, is found to promote TGO spallation.
- The incorporation of yttria or yttrium aluminate at the grain boundaries modify the transport processes in oxide scale [75],
- High Y concentration leads to high TGO growth rates, which are detrimental to scale adherence; Y/ Al-oxide precipitates in the TGO act as crack initiation sites [118]
- Y increases Al selective oxidation [20]

Reactive elements combine with sulphur and phosphorus impurities in the metallic materials and coatings limiting their effect, as a result that these impurities can't selectively diffuse to the surface and contaminate the scale/metallic interface [75].

Hafnium improves scale adherence [20, 58] and oxidation resistance [35] and reduces the growth kinetics of α-Al_2O_3 [116], but has negative effects on hot corrosion resistance, due to the ready reaction of this element with the corrosive salts at elevated temperature [35].
Quaternary additions of Re, Cr, Ti and Ta were found to be detrimental to Hf-doped-NiAl [121].

Pt in coatings

The use of platinum as modification of diffusion coatings composition is widely recognised and was due to the conviction that it increases their oxidation performance, as showed by Meier and Pettit [65], although the mechanisms are not completely clear [1, 60],

Some principal Pt effects are:

- Pt promotes selective Al oxidation [3, 5, 53, 111, 123]. It may act as a "catalyst" promoting the reaction between O and Al to form α-Al_2O_3, possibly by increasing the dissociation rate of O_2 , thus decreasing the time for a continuous α-Al_2O_3 scale to form [6]
- Pt improves adhesion between coating and substrate [3, 53], by suppressing voids formation at the coating-alumina scale interface [76]
- Pt addition aids the retention of Al within the interdiffusion zone [33]
- Pt suppresses deleterious spinels formation, preventing both nucleation of oxides and the reaction between them to form spinels and the nucleation of spinel itself [6].
- Pt delays the β-γ phase transformation (§ 1.2.1 and 1.6.4)[1]
- Pt delays the transient-alpha (γ, δ, θ –α Al_2O_3) phase transformation (§ 1.4.3)[119]
- Pt lowers the scale growth rate [1, 64]. But, according to Vialas et al. [119] Pt effect on cycling oxidation is the decrease in oxide spallation rather than lowering the oxidation kinetics.
- Pt remains most concentrated at the coating-gas interface, thereby retarding diffusion of certain refractory elements to the coating–alumina scale interface, improving isothermal (and cyclic) oxidation. Pt addition improves oxidation resistance, compared with conventional aluminide coatings, due to increased scale adherence and cracking resistance [60].

1.3 Oxidation and Corrosion of turbines

Industrial gas turbine components should satisfy a lifetime from 25,000 to 100,000 hours [23, 106] but their materials, mainly Ni-base superalloy, experience severe conditions including mechanical creep/fatigue, thermal and chemical loadings (oxidation and corrosion), as consequence of gas stream particulate, high temperature, working cycles, gas composition (SO_x, HCl) and molten salt deposition (e.g. alkali sulphate) [20]. Stresses are often interrelated among them [50].
As the bare alloys are unable to resist such aggressive exposure conditions the blades are coated with materials to perform better in oxidative/corrosive environments.

Due to the blade shape (Fig. 8) and its position in turbine sub-system, the aerofoil temperature may vary from a maximum of 1100°C at leading and trailing edges of the first stage blade to about 600°C in the centre of the aerofoil roots (for aero engine applications). This gives rise to a variation in the degradation from oxidation through Type I hot corrosion to Type II hot corrosion [64,75].

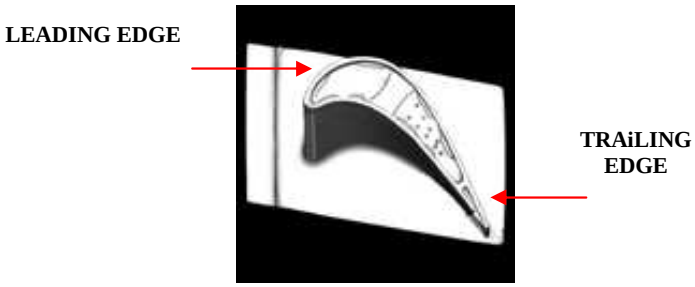

Fig. 8 Top of a turbine's blade

At high temperature, ≥ 1000°C, gases are mainly oxidizing and promote the formation of oxides at the material surface. At intermediate temperature, ≤ 950°C, deposition can occur, either at the leading edges or on the concave side of the blade according to particles dimension, and makes corrosion processes dominant [69]. The oxidation rate below 900-1000°C metal temperature is sufficiently slow to not be life limiting, but hot corrosion can occur much more rapidly and has become a potentially life limiting factor [27, 73].

Oxidation and corrosion cause chemical and structural changes to both alloys and coatings, resulting in materials consumption and weakening. Consequently, materials for turbine blades with longer lives are demanding to reduce costs of components refurbishment and replacement [43].

1.4 Oxidation of metals and alloys

As described by many authors**,** and documented in the book of Birks et al. [53], and Kofstad [50], a truly clean metal surface exposed to oxygen is subjected to the following reaction (eq.1):

$$xM + \left(\frac{1}{2}\right)yO_2 = M_xO_y \quad (1)$$

where M represents the metal, O the oxygen and x-y the stoichiometric factors.

There are three main types of oxidation: general or uniform (taking place at the exposed surface), intergranular (occurring along grain boundaries) and internal (taking place below the external surface but not just at grain boundaries) [27].

The oxidation of an alloy is more complex than that of a pure metal since the alloy components have different affinities for oxygen and different diffusion rates for atoms and ions through alloy and oxide respectively. Moreover, the oxidation mechanisms change during the exposure, according to the establishment of different metal activity gradients and gas pressures.

The oxidation of a Ni-Cr-Al alloy can be summarized in a series of schematics (Fig.9), which resemble oxidation processes of some coatings (overlay coatings, § 1.6.2) as well. During the initial stage (or transient stage) of oxidation, kinetics and thermodynamics (§1.4.1; 1.4.2) can support the formation of several oxides, those of the basis metals (Ni) or of alloying elements (Cr and Al), figure 9a and 9b, and the formation of spinel phases (i.e. $NiAl_2O_4$, $NiCr_2O_4$). The relative proportion of these phases is determined by the initial composition of the alloy. Moreover, the length of the transient period over which the selective oxidation process is taking place can vary significantly from alloy to alloy, according to their composition and environment characteristics [20].

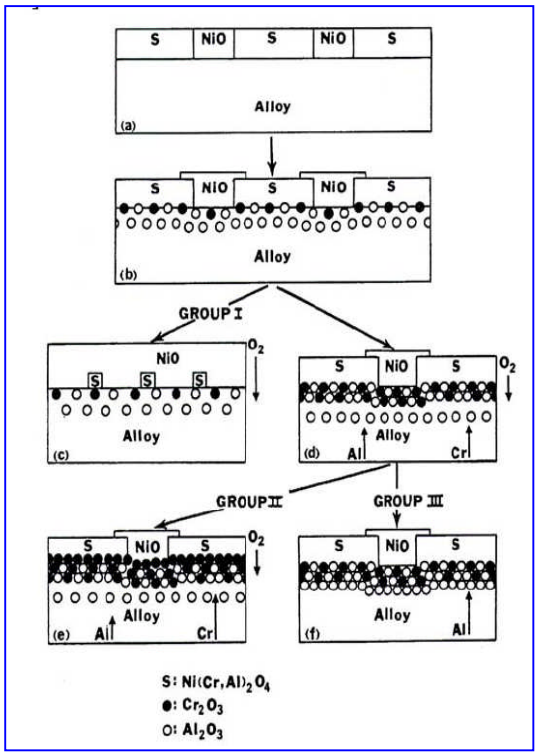

Fig. 9 Illustration of oxide scale development on a Ni-Cr-Al alloy [20].

As oxidation continues, diffusion of atoms takes place: inward diffusion of oxygen and outward diffusion of the alloying elements. When the first one is slower than the second, the lateral growth of oxides becomes possible leading to oxide spreading over the surface.

During the exposure, changes in the scale development occur, until the thermodynamic conditions make one oxide (the most stable) dominant over the other [20], and in relation to Al and Cr content the following situations can be set:

- Low Cr-and Al-levels: a continuous layer of NiO is formed with internal oxidation of Cr and Al (Fig. 9c)
- High Cr- and Al-levels: a continuous layer of Al_2O_3 is formed and Al internal oxidation persists (Fig. 9d). Furthermore,
  - for higher Cr content, chromia-former alloys, a continuous layer of Cr_2O_3 forms with internal oxidation of Al (Fig. 9e). Other oxides may be dissolved in the chromia and other oxides may exist above or below the chromia scale (e.g. “tentacles/fingers” of alumina).
  - for larger Al concentration, alumina-former alloys, the Al_2O_3 subscale becomes continuous and no internal oxidation takes place.

1.4.1 Thermodynamics of oxidation

The scale formation over a metal/alloy surface during oxidation is controlled by thermodynamic and kinetics factors, notably gas composition and temperature [122].

With reference to the equation 1, ΔG° is the standard free energy of oxide formation at a certain temperature and the more negative is ΔG° the more stable is the product of the oxidation/corrosion process (M_xO_y). ΔG° has been introduced in order to judge the possibilities and tendency of oxidation reactions [122].

The dissociation pressure of the same product oxide is defined by the equation (eq.2)

$$p_{O_2} = \frac{a_{M_xO_y}}{a_M} = \exp(\Delta G^\circ / RT) \quad (2)$$

Where:

p_{O2}= Oxygen partial pressare

a_M= metal activity

a_{MxOy}= oxide activity

ΔG°= Change in Gibbs Free Energy in standard condition

R= Gas constant

T= Temperature

Below the p_{O2} value expressed by this equation, no oxide is formed and the metal is still stable. Above this value the oxide is stable and a protective scale may form [29]. The most stable oxides are those where the equilibrium partial pressures take the lowest values, such as alumina (α- Al_2O_3), chromia (Cr_2O_3) and silica (SiO_2) and this motivates the employment of materials forming these oxides for alloy protection [53].

For the case of alloys, a_M must be considered for each component metal and the activities of all oxides must fall into a_{MO}. In the presence of a complex environment, where not only oxygen exists but gas mixtures, the stability of the oxide depends on the partial pressures, or activities, of the individual component reaction products.

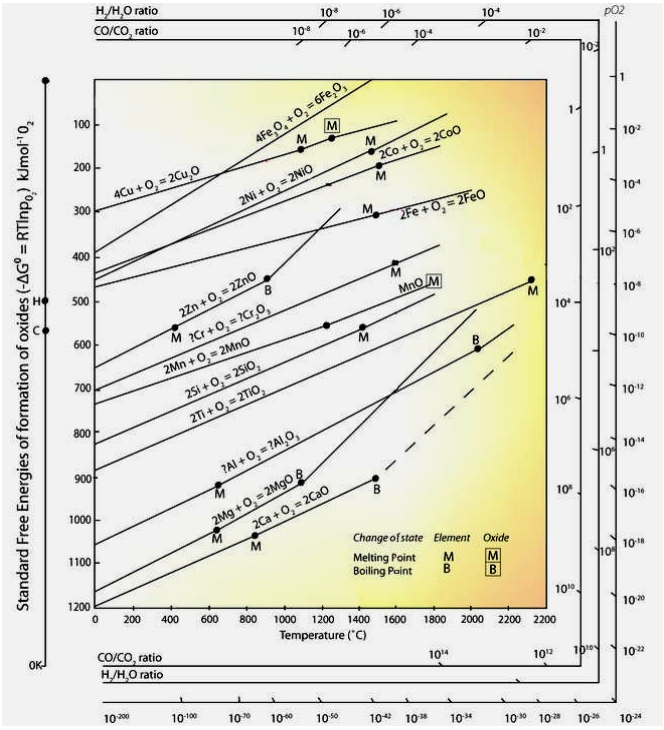

Fig. 10 Richardson-Ellingham diagram for some reactions [53].

Published tables and graphs provide the standard free energy values for several reactions, for example in figure 10, which presents the free energy of formation as a function of the dissociation pressure and temperature. Corresponding diagrams exist for carbides, sulphides, halides, etc, for instance those reported by Yedong He [122], are useful to define metal and reaction products stability at specific exposure conditions.

In recent years Richardson-Ellingham diagrams have been revisited since there are not fully consistent with some experimental results obtained studying the effect of reactive elements on the oxidation behaviour of the alloy [122].

1.4.2 Kinetics of oxidation

At high temperatures the oxidation and corrosion of many metals are found to follow parabolic time dependence and this behaviour is described by Wagner's Theory (whose detailed description can be found in literature, for example [50, 53, 122]). According to this theory, when a dense and protective scale is formed above a metal/alloy surface, the oxidation rate is given by the equation (eq. 3)

$$\frac{d(\Delta m / A)}{dt} = \frac{k_p}{\Delta m / A} \qquad (3)$$

where m is a measure of weight change per unit surface area of the metal, A, or oxide thickness; t is the time and k_p the parabolic rate constant.

High temperature parabolic oxidation signifies that diffusion of metal and/or oxygen ions through the oxide lattice is rate determining [52, 80].

If the oxide scale is non-protective, it doesn't act as a barrier to inhibit oxidation and the oxidation rate doesn't decrease with time. Thus, such kinetics are described by the following linear equation (eq. 4), where k_c is a constant:

$$\frac{d(\Delta m / A)}{dt} = k_c \quad (4)$$

If the relationship (4) is linear, a surface or phase boundary process or reaction may be rate determining [50].

Sometimes the oxidation process follows other rate laws or a combination of parabolic and linear [50, 50]. For instance, a reaction may be interface controlled (linear) during initial stages and diffusion limited (parabolic) after extended oxidation.

The oxidation kinetics are a function of several factors among which temperature and grain size play a role, but also gases partial pressure, activities of the constituents, porosity, etc [50]. Since kinetics define the growth rate of protective scales, they provide a measure of the rate of alloy destruction by chemical reactions and exfoliation as well, the rate of depletion of protective scale forming elements and the rate at which the surface of a component gets damaged. Thus the kinetics of the corrosion reactions determine the useful life of a component, if this is not controlled by other limiting mechanisms like for instance creep, fatigue and wear [43].

1.4.3 The alumina scale

Many materials, such as the coatings studied in this thesis, rely on an alumina scale for oxidation and corrosion protection. The scale formation is affected by factors such as temperature, coating composition (Al activity, Y addition, various impurities) and coating structure [117].

Aluminium oxide has several different crystal structures, including γ, δ, θ (needle structure) and α- Al_2O_3 (corundum, equiaxed or elongated grains), providing the highest stability.

The metastable structures (γ, δ, θ), have faster growth rates and form at low temperature. Theta-alumina also forms during the transient oxidation period at higher temperature (>900°C), see Fig. 11, before the formation of a slow-growing α- Al_2O_3 film [5, 39, 117].

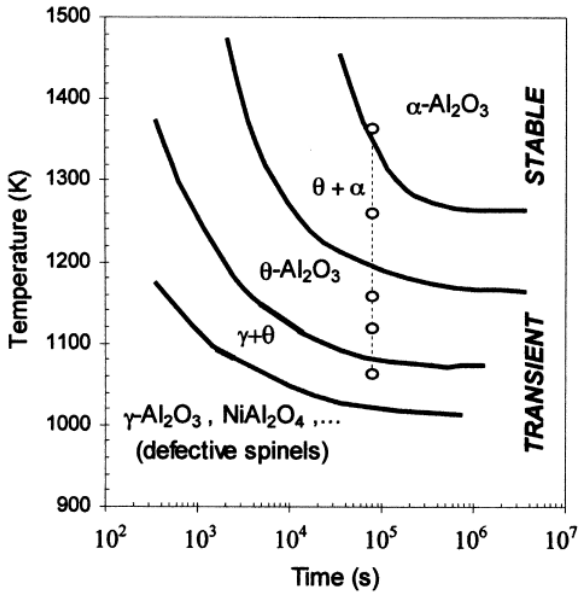

Fig. 11 Schematic temperature-time transformation diagram for the high temperature oxidation of β -NiAl [40].

On heating the non-reversible transformation from metastable phases to the stable α- Al_2O_3 takes place through the succession γ-δ-θ-α [18, 50, 117], starting from the metal/oxide interface [60]. The transformation is accelerated at higher temperatures and takes much longer at lower temperature (Fig. 11) [104, 114]. During cyclic oxidation transient phases re-form on the bare metal surface left by oxide-scale spalling at the metal/oxide interface [121]. The occurrence of different phases of alumina moves the oxidation kinetics away from the parabolic law [40].

Rates of transport are slower through α-Al_2O_3 and thus it provides better oxidation resistance [50].

The growing scale usually exhibits wrinkles and convolutions [5, 50, 115], which are more prominent for coating with slower oxide growth [115], and smooth ridges [117]. Moreover, the rumpled surface roughness provides places for alpha nucleation and thus a continuous alpha layer grows faster above a rough surface [114].

1.4.4 Spallation

Mainly ascribed to failure as a result of thermally induced stresses, which arise from the large thermal expansion mismatch between substrate and scale [20, 78] spallation represents the detachment of either the oxide layer, or TBC subsequent to their cracking (Fig. 12).

The onset of spallation increases with the cyclic nature of the operating engine [20, 27, 104].

Causes, other than thermal stress, are:

- transformation from metastable to stable alumina (due to volume reduction) [117]
- formation of large voids at the oxide/metal interface [20, 39]
- transformation of β-NiAl to less Al-rich intermetallics (with volume reduction as result) [4, 116]
- surface roughening (or rumpling) that gives compressive and tensile stresses to the oxide films grown on initially flat surfaces [73, 116].

The cycle of scale formation and spallation of a coating continues at the expense of the sacrificial metallic coating layer, which can be refurbished or repaired. However, when an aluminide or an overlay coating is used as a bond coat of a TBC system, local scale spallation can initiate coating failure [58].

The growth and failure of the protective oxide scale have been being studied for about 30 years and, as explained in section 4.1.4, a number of studies have been devoted to modelling the growth and the spalling of the oxide scale [e.g. 62, 77, 98, 99, 100, 101].

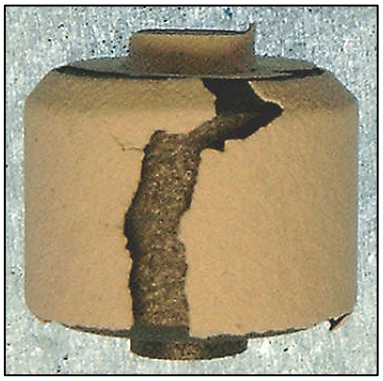

Fig. 12 Spalled samples of LCO22+ TBC coated INL738LC exposed 1000 hours at 1050°C.

1.5 Hot corrosion

Hot corrosion represents an accelerated form of attack, leading to the protective oxide barrier being damaged or destroyed and results from the presence of molten salt on top of the alloy surface. For gas turbines these salts are mainly given by sodium sulphate (Na_2SO_4) [116] along with potassium sulphate (K_2SO_4) and some chlorides (e.g. KCl, NaCl) [28, 83].
Sodium sulphate is an ionic conductor, so that the corrosion is a result of electrochemical processes [35, 83]. Moreover, the hot gas stream may contain, other than Na, K and S, vapour phase contaminants of vanadium and lead, or other metals, present as contaminants in the fuel, that are all possible reactants within the salt deposit.

Salt deposition affects the high temperature corrosion processes taking place between the alloy and gas environment. The main important consequence is mix sulphate formation ($NiSO_4$, $CoSO_4$, Na_2SO_4-$CoSO_4$, Na_2SO_4-$NiSO_4$) which in turn lowers the Na_2SO_4 melting point from 884°C to 671°C (for Na_2SO_4-$CoSO_4$ system) [83]. The presence of molten salt causes higher reaction rates between the salt and the scale. Potassium sulphate behaves similarly to sodium sulphate in regard to high temperature hot corrosion [57], with the eutectic of Na_2SO_4 and K_2SO_4 lowering the temperature of the attack.
It has been observed that the higher the salt deposition the higher the oxidation/corrosion rate [20, 28, 45, 97]. In exception at very high deposit flux the salt deposit may lead to the formation of an alkali sulphate “protective” layer; this, since it separates the environmental gases from the metal delays SO_2-SO_3 diffusion [95, 97] can lead to a reduction in the corrosion rate.

With general agreement, two types of hot corrosion are distinguished:
Type I (high-temperature hot corrosion, HTHC), known since 1950 [57]within the range ~800°-950°C, and
Type II (low-temperature hot corrosion, LTHC), recognised in the mid-1970 [57] observed within the range ~600°-750°C.
Various parameters may affect the development of these two forms of damage, including alloy composition and thermo-mechanical conditions, deposit compositions and its flux rates, temperature and cycling, gas composition and velocity, and erosion processes [28, 37].

Corrosion, similar to that already seen for oxidation and described in figure 13, proceeds through two different stages:

- **Incubation or the initiation stage**, with a low level of metal damage, which corresponds to the formation of a protective oxide layer, the same formed on an alloy in the absence of deposit [57], and its dissolution due to fluxing reaction.
- **Propagation stage,** characterized by oxide scale breakdown and high resultant corrosion rates.

The transition time between the two stages may vary from material to material and for the same material with relation to different environmental parameters; sometimes two clear separate steps may be seen, but not always [45]. The best means to avoid or minimize hot corrosion attack of any alloy is to extend the initiation stage as long as possible [73].

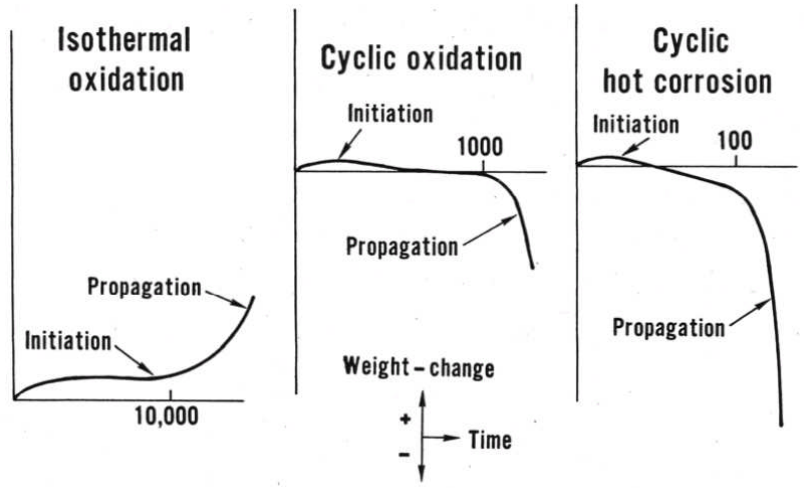

Fig. 13 Weight change versus time curves in relation to the different degradation stage (initiation and propagation) in three different situations: isothermal oxidation, cyclic oxidation and hot corrosion [79].

The second stage of a hot corrosion process is often attributed to failure of the protective oxide layer, which allows the molten salt to access directly the substrate metal. Initiation of failure may result from erosion, thermal stresses, erosion-corrosion, chemical reactions, etc. [28, 50, 53, 73].

The mechanisms proposed for the hot corrosion propagation stage are the salt **fluxing** mechanisms originally proposed by Goebel, J.A. and Pettit, F.S. [37, 38], and the **sulphidation-oxidation** mechanism, as described in detail, for instance, by Kofstad [50] and Birks [53].

According to Goebel and Pettit the protection efficiency of the surface oxide layer might be lost as a result of reactions (fluxing) of this layer with the molten salt. The fluxing can be

caused either by combination of oxides with O^{2-} to form anions, specifically termed **'basic fluxing'**, to which Ni-base superalloys are susceptible [20], or by decomposition of oxides into the corresponding cations and O^{2-} (i.e. **'acidic fluxing'**), which, if is induced by alloy cations, can be self propagating.

Sulphidation concerns those processes related to sulphur accumulation on alloy surface, due to salt deposition, and further oxidation of sulphides, which allow sulphur release and further sulphur penetration. New sulphides are thus formed and the cycle keeps repairing consuming the metal [69].

However, it has been suggested that hot corrosion attacks may proceed through other mechanisms, and with specific differences for HTHC and LTHC, as described by Luthra et al. [63], Coutsouradis et al. [23].

Moreover, more processes can occur during alloy exposure to corrosive environment since the chemical conditions evolve through out the corrosion attack.

The following sections present these hot corrosion processes in more detail.

1.5.1 Basic fluxing

The basic fluxing, whose steps are presented in figure 14, is described considering the degradation of nickel in pure oxygen. At the beginning of the oxidation reaction some NiO is formed on the nickel surface. Some of the oxygen of this reaction is removed from Na_2SO_4 deposit, adjacent to the nickel, which causes the sulphur potential in the Na_2SO_4 to increase. Sulphur from Na_2SO_4 reduction penetrates the nickel oxide to form nickel sulphide (NiS) beneath the NiO scale.

The effect of the oxygen and sulphur removal from Na_2SO_4 deposited on nickel oxide, in air, is to increase both the oxide-ion and Na_2O activity (as understandable from the following equations, 5-7). The raised oxide-ion activity permits a reaction between oxygen ions and NiO to form nickelate ions, namely NiO_2^- .

$$SO_4^{2-} = O^{2-}\left(inNa_2SO_4\right) + \frac{3}{2}O_2\left(UsedToFormNiO\right) + \frac{1}{2}S_2\left(UsedtoFormNiS\right) \quad (5)$$

$$Na_2SO_4 = Na_2O\left(inNa_2SO_4\right) + \frac{3}{2}O_2\left(UsedToFormNiO\right) + \frac{1}{2}S_2\left(UsedtoFormNiS\right) \quad (6)$$

$$2NiO + Na_2O + \frac{1}{2}O_2 = 2Na^+ + 2NiO_2^- \quad (7)$$

The increased oxygen ion activity is restricted to the Na_2SO_4, adjacent to the nickel and therefore, as the NiO_2^{-2} ions diffuse away from the nickel they decompose into NiO particles

and O^{-2} ions. The NiO particles are not protective and consequently the initially protective NiO is destroyed. The production of oxide ions will cause the sulphur potential to decrease and a condition can be reached where sulphur can no longer react with nickel. Under this condition, as oxidation continues, a protective scale will form and the corrosion ceases.

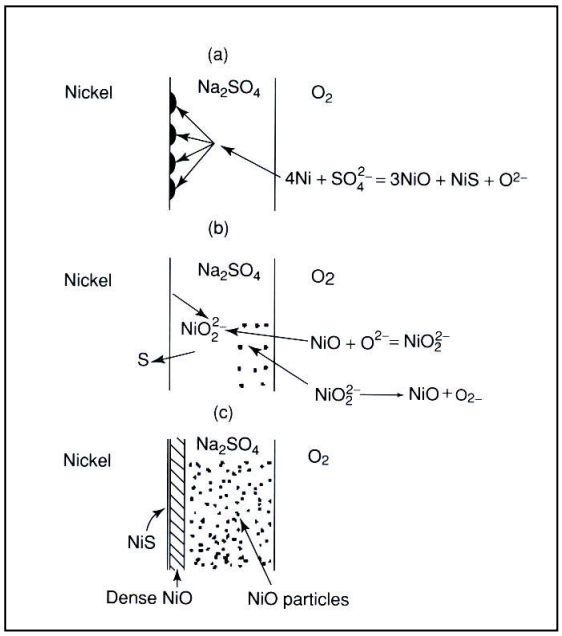

Fig.14 Na_2SO_4-induced accelerated oxidation of nickel in pure oxygen [53].

The processes described are those prevailing when SO_3 is either absent or present with a pressure below 10^{-3} atmosphere.

Moreover, basic fluxing occurs during the initiation stage of attack of some Ni-Cr-Al alloys [53, 27, 84], which subsequently may suffer propagation attack by oxidation of sulphides in the alloy zone beneath the oxide scale (sulphidation § 1.5.3) and in the case of some Ni-Cr-Al alloys where Cr_2O_3 and Al_2O_3 are present along with NiO.

Hot corrosion by basic fluxing is usually not self-sustaining, since sulphur removal from Na_2SO_4 eventually ceases unless deposition of the salt occurs again. Moreover, chromium is effective in retarding accelerated oxidation because Cr_2O_3 establishes an oxide ion activity in Na_2SO_4 which is not sufficient to cause basic fluxing but is still not low enough to cause acidic fluxing [37].

1.5.2 Acidic fluxing

Acidic fluxing may be separated in two different types: alloy-induced acidic fluxing and gas-induced acidic fluxing; the former characterizing Type I hot corrosion and the latter Type II hot corrosion.

Alloy-induced acidic fluxing

Alloy-induced acidic fluxing results from the accumulation of oxides, such as MoO_3, WO_3, V_2O_5, in the salt deposit. Indeed, the solutions of oxides of these elements with Na_2SO_4 decrease the oxygen ion activity of the molten salts, producing melts that are acidic fluxes for the oxide scale. This form of hot corrosion attack may be reduced by decreasing the Mo, W, V concentration in the alloy. Tantalum does not have the same effect as the other refractory metals, and therefore, appears to be a good replacement for Mo, W and V in the alloy.

The hot corrosion of the nickel base superalloy B1900 (Bal.-Ni, 8% Cr, 10% Co, 6% Mo, 1% Ti, 6% Al, 4.3% Ta, 0.1% C) is illustrated to allow the understanding of alloy-induced acidic fluxing.

During the initiation stage, Cr_2O_3, Al_2O_3 and MoO_3 are formed in addition to base metal oxides NiO and CoO. Cr_2O_3 and MoO_3 react with the Na_2SO_4 to form Na_2CrO_4 and Na_2MoO_4 according to a basic fluxing. Sulphur trioxide is evolved but decomposes to sulphur dioxide and oxygen, and sulphur may also react with the base alloy to form nickel sulphide, whereby the oxidation activity is increased and the Al_2O_3 is dissolved forming $NaAlO_2$, as shown by the equations 8-10.

$$Na_2SO_4 = Na_2O\ (in\ Na_2SO_4) + \frac{3}{2}O_2(UsedToFormNiO) + \frac{1}{2}S_2(UsedToFormNiS) \quad (8)$$

$$Cr_2O_3 + 2\ O^{2-} + \frac{3}{2}O_2 = 2\ CrO_4^{2-} \quad (9)$$

$$Al_2O_3 + O^{2-} = 2AlO_2^- \quad (10)$$

This basic fluxing of Al_2O_3 causes accelerated oxidation and it is responsible for the initial increase of the oxidation rate and the oxidation of nickel sulphide, which produces the evolution of SO_2. This accelerated oxidation, moreover, causes MoO_3 enrichment in the deposit and this, now low in SO_4^{2-} concentration, becomes acidic; whereby the oxides of aluminium, chromium and nickel are dissolved in region near the alloy via acidic fluxing reactions, further stated (11-15), and reprecipitate near the gas interface where the MoO_3 activity is lower due to the vaporization of MoO_3.

$$Mo + \frac{3}{2}O_2 = MoO_3 \quad (11)$$

$$MoO_3 + Na_2SO_4 = Na_2MoO_4 + SO_3 \quad (12)$$

$$Al_2O_3 + 3MoO_3(in\ Na_2SO_4) = 2Al^{3+} + 3MoO_4^{2-} \quad (13)$$

$$Cr_2O_3 + 3MoO_3(in\ Na_2SO_4) = 2Cr^{3+} + 3MoO_4^{2-} \quad (14)$$

$$3Ni\ O + 3MoO_3(in\ Na_2SO_4) = 3Ni^{2+} + 3MoO_4^{2-} \quad (15)$$

Moreover, such acidic fluxing is self sustaining and catastrophic. It represents the most severe attack for these refractory metal containing alloys [37].

Gas-phase induced acidic fluxing

A widely accepted model for the occurrence of LTHC was proposed by Luthra et al [61]. According to this model, LTHC follows two stages: (1) formation of liquid sodium-cobalt sulphate on the surface (Na_2SO_4-$CoSO_4$); and (2) propagation of attack via migration of $S0_3$ and cobalt outward (Co^{2+}) and inward (Co^{3+}), respectively, through the liquid salt.

The authors describe a rapid mode of attack at intermediate temperature 650°-750°C caused by sulphating of the transient surface nickel or cobalt oxides and the dissolution of these transition metal sulphates into $NaSO_4$ to yield a liquid phase ($NiSO_4$, $CoSO_4$, Na_2SO_4-$CoSO_4$, Na_2SO_4-$NiSO_4$) with lower melting point.

This degradation is also self-sustaining. Metal ions go into solution at the alloy-salt interface and precipitate as a non-protective solid in the salt, but the metal that dissolves and reprecipitates is the more noble metal rather than the elements that would form the protective scale in absence of hot corrosion.

Unlike the alloy-induced acidic fluxing, this second type of corrosion occurs with high SO_3 pressure in the salt deposit and gas phase. The acidic component is supplied to the deposit from the gas via reactions, such as those listed below (eq. 16 and 17):

$$SO_3 + O^{2-} = SO_4^{2-} \quad (16)$$

$$SO_3 + SO_4^{2-} = S_2O_7^{2-} \quad (17)$$

The attack appears to decrease as the pressure of SO_3 is decreased [53], while at the same SO_3 pressure, the corrosion process is more severe at intermediate temperature, about 700°C, than at 1000°C [53, 61].

In fact, the SO_3 partial pressure decreases with increasing temperature, and sulphates such as $CoSO_4$ and $NiSO_4$ are not produced anymore, or the eutectics that drop the salt melting point (as shown in Fig.15). For this reason gas-phased induced acidic fluxing is referred also as Type II hot corrosion, or low temperature hot corrosion.

Nevertheless, several alternative mechanisms have been proposed for low temperature hot corrosion but there is no universal agreement on these mechanisms [64]. In addition to

Luthra's model Shih et al. [89] suggested sulphidation (§1.5.3) as a contributing mechanism of LTHC in nickel-based alloys.

1.5.3 Sulphidation

Sulphidation, like the basic fluxing, is mainly associated with Type I hot corrosion and the two processes are often interrelated. As reported by Coutsouradis et al. [23] sulphidation is correlated to both "heavy" and "light" corrosion.

Sulphidation kinetics are faster than oxidation, because sulphides are more defective and have lower melting temperatures and less stability than oxides [29].

Sulphur-induced corrosion takes place at low oxygen pressure at the alloy/ Na_2SO_4 or oxide/ Na_2SO_4 interface. In that situation the sulphur pressure may be high enough to form aluminium and/or chromium sulphides. In some cases Co, Ni, Fe sulphides, unless the SO_3 pressure is very low, can form as well.

In an alloy exposed to SO_2-O_2, sulphides result from the sulphur in the gas rather than from Na_2SO_4.

The sulphides accumulation in the alloy negatively affects the protective oxide formation: when sulphur diffuses into the surface of the alloy, it usually reacts with the same elements that are diffusing to the surface that should react with oxygen to form a protective scale. The sulphides production results in the flux to the surface of these elements, being selectively oxidised, to decrease and thus the formation of a less protective oxide scale, which brings about a substantial degradation during subsequent oxidation. The corrosion rate increases rapidly in the oxidation/sulphidizing regime with increasingly sulphidation conditions and increases more slowly on entering the sulphidation regime [96].

Reaction mechanisms for nickel sulphides formation that occurs in presence of O_2, SO_2 and SO_3, are illustrated in the following figure (Fig.15). It describes the formation in the inner zone of NiO along with NiS_3 for Type II hot corrosion, while a Ni-S liquid is formed for Type I. In both cases the outer zone is a mixture of NiO and liquid Na_2SO_4- $NiSO_4$.

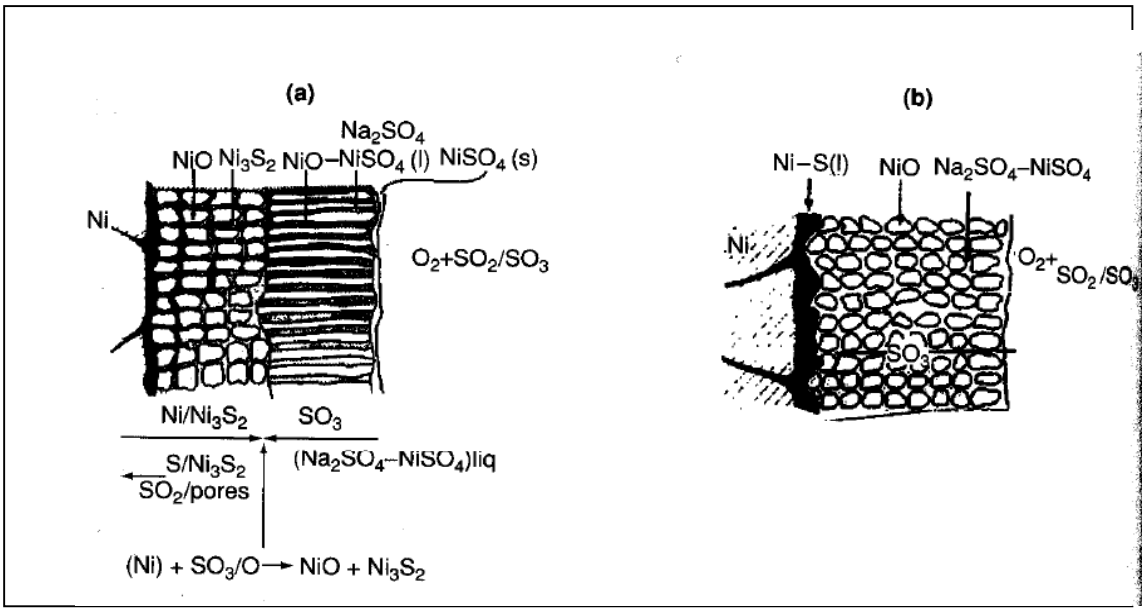

Fig. 15 Reaction mechanisms of hot corrosion of Ni at 700°C (a) and 900°C (b) in gases containing O_2, SO_2 and SO_3 [53].

The susceptibility of nickel-base superalloys to sulphur-induced corrosion is generally observed when aluminium is present in the alloy at levels between 1-6% wt [40].
CMSX-4 has an Al concentration falling into this range, while the overlay coated and the Pt-aluminide diffusion coatings studied have respectively 8% wt and 50 % of aluminium.

1.5.4 Morphology of Type I and Type II hot corrosion

As explained previously hot corrosion processes fall either in Type I or Type II hot corrosion in relation to the temperature they occur (respectively above and under the sodium sulphate melting point). These two types of degradation differ, moreover, from the morphology of the corrosion products.
For example, the macroscopic appearance of high temperature hot corrosion is characterized in many cases by severe peeling of metal and by significant colour changes. Microscopically, the morphology of Type I is characterised by the presence of subscale sulphide particles and depletion region beneath the porous, non-protective scale [16, 57]. The reaction products frequently exhibit oxide precipitates dispersed in the salt film. Also, Type I hot corrosion usually exhibits grain boundary diffusion [57]. These characteristics are shown in figure 16.
Differently, low temperature hot corrosion may produce both localised pitting and a broader front of corrosion with a layered type of corrosion scale [57, 63, 97]. The localized nature of the attack is related to localized failure of the scale as a result of thermal cycling, erosion and chemical reactions. In this corrosion type, as shown in figure 16, neither an advancing front

of discrete sulphides nor denuded zone nor little intergranular attack are generally observed [16, 57, 91], although a peak in sulphur is observed at the scale/alloy interface.

Sometimes, however, the morphology doesn't permit to identify the exact corrosion process; the damage may have features that have characteristics of both types of corrosion, hence the name transition hot corrosion (THC) [57].

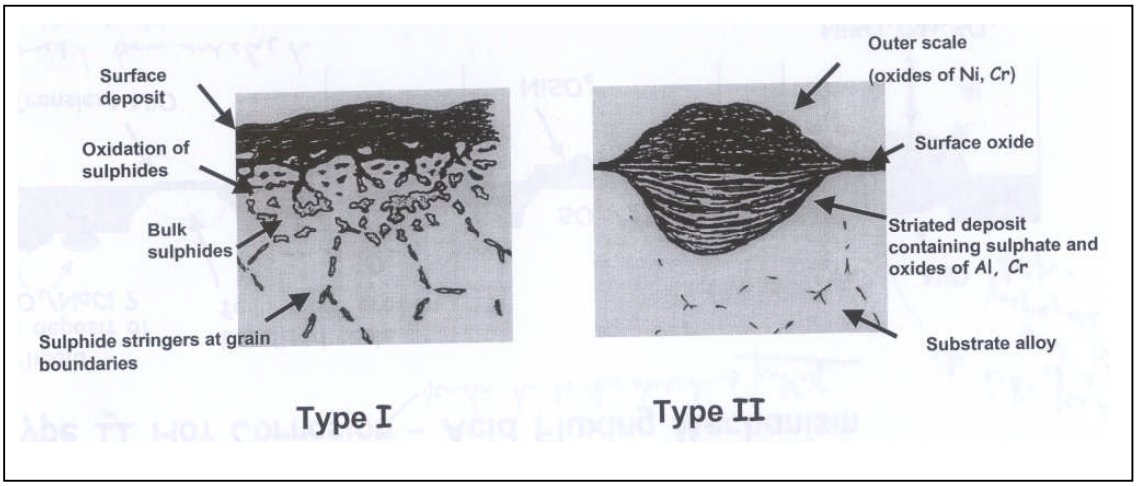

Fig. 16 Type I and Type II hot corrosion morphology [53].

1.6 Coatings

Overlay coatings (MCrAlY type) and Diffusion coatings (e.g. PtAl- diffusion coatings type) are commonly employed to delay oxidation/corrosion effects on turbines blades alloys: they provide a metal surface composition which reacts with the environment to produce the most protective scale, usually α-Al_2O_3.The formation of a protective oxide scale depends on several chemical and structural factors of the coating and substrate (e.g. coating thickness and composition, atoms interdiffusion between alloy and coating, etc.) [27, 64, 117].
The cause of chromia and silica inadequacy, even if considered stable oxides, in some condition of high temperature degradation protection can be found elsewhere, for instance in Mévrel [66].

Metallic coatings can be used either individually or as a bond/key coat layer beneath a ceramic thermal barrier coating (TBC), employed to reduce the temperature of the substrate material.

During service coatings are degraded by oxidation and corrosion as well as mechanical factors. The protective oxide barrier eventually becomes damaged, due to thermal stress, cracks and spalls (§1.4.4) [20, 67]. The development of a new oxide layer follows, leading to the depletion of the element being selectively oxidised.

Even when operating at high temperature where oxidation rather than corrosion is a major problem, degradation of components by contaminants in a gas turbine environment cannot be excluded. Cr seems the only element which improves the hot corrosion resistance, but at the expense of higher temperature oxidation. At the time, it appears that combined hot corrosion resistance and exceptional scale spallation resistance is an unattainable goal for nickel aluminide coating performance [60].

1.6.1 Diffusion coatings

This type of coating enriches the alloy surface with a high temperature corrosion resistant element and the substrate takes part in coating formation through atom diffusion [6, 53, 64, 123], as part of the base metal is consumed in its formation [27]. Coating-substrate interaction

is absolutely necessary to ensure an adherent coating and an interdiffusion zone develops beneath the coating (Fig. 21) [27].

Examples of diffusion coatings are nickel and cobalt aluminide and platinum modified aluminide coatings, which can be separated into “outward-growing” and “inward-growing” versions. The direction of formation of these coatings depends on the coating method and coating parameters [3] and the resulting different structures, after deposition, are illustrated in figure 17.

In the first case when Al activity is lower than Ni activity (low activity process), an outward growing coating forms, which means Ni diffuses outward through Al deficient β-NiAl [27]. Thus the Al/Ni ratio in the beta phase is lower than one for outward grown coatings.

When Al activity, during aluminizing process, is higher than the Ni activity (high activity process), Ni_2Al_3 forms on the surface and Al diffuses inward faster than Ni through this nickel-aluminium intermetallic, which initially forms at the surface [27]. β-NiAl forms under this surface layer of Ni_2Al_3, which is subsequently converted to β-NiAl in the alloy recovery heat treatment after the aluminising process. For a high activity process the Al/Ni ratio is equal to or greater than one.

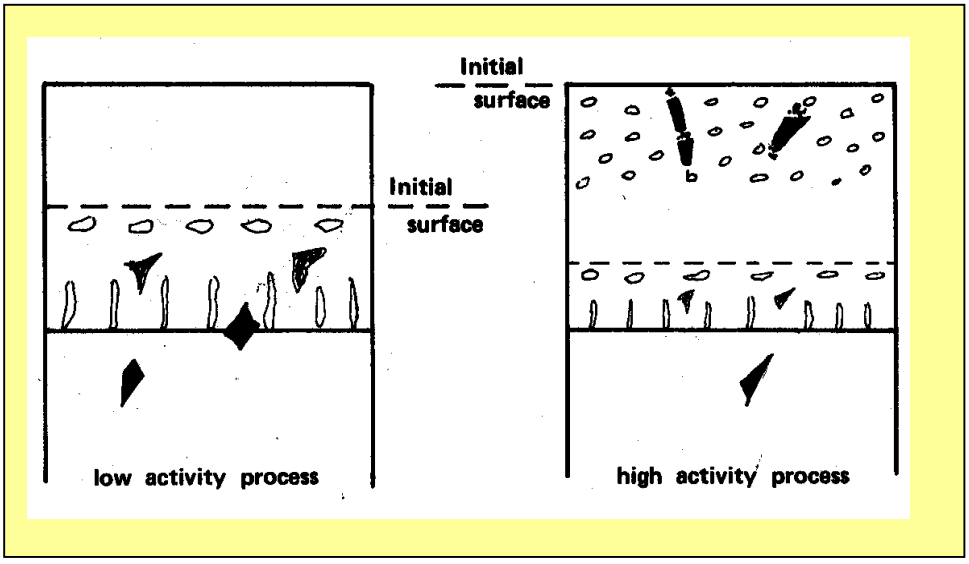

Fig. 17 Comparison between outward and inward grown coating structure [27].

Platinum-aluminide coatings are produced by electroplating a layer of Pt or Pt-Ni, with a mean thickness of 7 μm and then annealed it to diffuse the platinum prior to aluminizing.

Aluminizing is carried out by Pack Cementation or Chemical Vapour Deposition (CVD) [27, 27, 64]. After aluminization the component is heat treated, between 1040-1120°C to strengthen the base alloy [27].

After deposition, as described by Vialas, N. et al. [120], Angenete, J. et al. [5], Zhang et al. [123], two main zones form: the outer zone (OZ) and the interdiffusion zone (IZ) (Fig. 18).

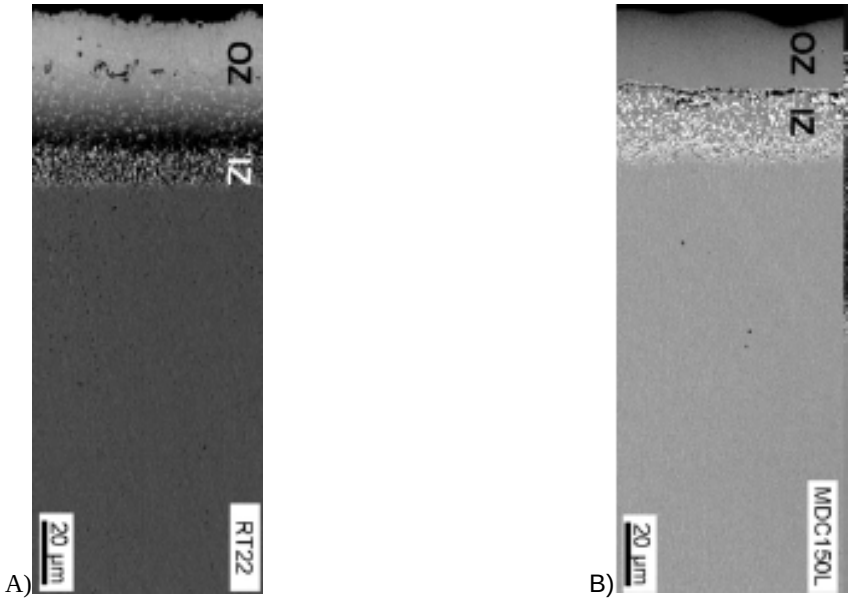

Fig. 18 Outer and Interdiffusion zone of two Pt-aluminide coatings (A=Inward; B=Outward) on CMSX-4 substrate [5].

In the outer zone $PtAl_2$ is the predominant phase, above a thicker layer characterized by equiaxed microstructure with β-NiAl and $PtAl_2$ equally distributed. It's also possible to find fine tungsten precipitates, mainly α-W, and rarely σ or μ phases (Fig.19). An outward growing coating (e.g. MDC150L), appears differently from inward one (e.g. RT22) as it forms a precipitate-free outer zone due to the lower amount of alloying elements from the substrate incorporated into the coating [5]. Moving inward from the outer zone, a dominant β-NiAl phase with more elongated α-W and σ-phase precipitates are formed.

In all the coatings the interdiffusion zone grows inward during heat treatment as the result of outward Ni diffusion, which is the main diffusion flow, to the outer zone from the substrate [5].

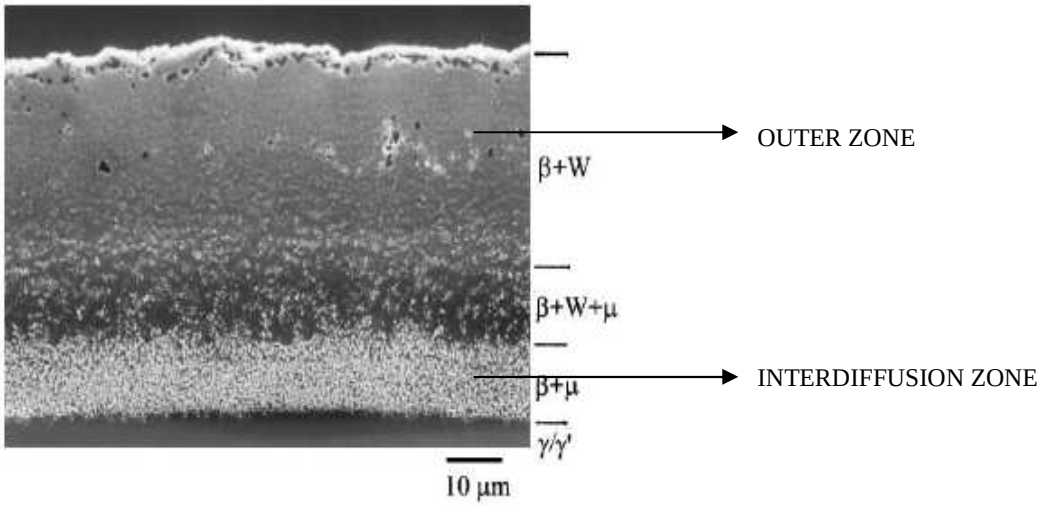

Fig. 19 Representative microstructure of a as-coated Pt-aluminide coating and the CMSX-4 substrate [123].

The composition of the outer zone of an inward grown diffusion coating is much more dependent on the alloy composition as compared to the outward diffusion coatings. This situation is generally not favoured for good corrosion behaviour of the layer [20].

Usually Pt aluminide coatings have a thickness approximately of 60-70μm, are relatively brittle and have good adherence. They perform exceptionally well under high temperature oxidation and Type I hot corrosion environments (800°-950°C) but performed less well under Type II hot corrosion conditions [72].

Platinum modified aluminide coatings were applied to the specimens employed in this study. They are identified as CN91 (single-phase coating, Fig. 20a) and RT22 (two-phase coating, Fig. 20b) and were produced commercially by electroplating platinum followed by the CVD aluminising technique.

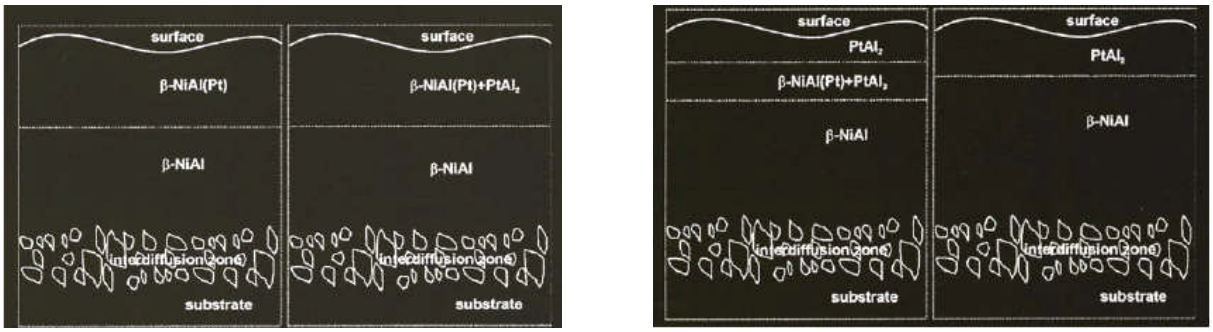

Fig. 20 a) Two profiles of a single-phase Pt-modified aluminide coating. b) Two profiles of a two-phases Pt-modified aluminide coating [30].

1.6.2 Overlay coatings

Overlay coatings are referred to as M-Cr-Al-X, where M is the main metal element(s), like Ni, Co, Fe…, and X an oxygen active element other than yttrium, thus for example Hf, Si, Zr, Yb, etc (mostly <1 wt%). The amount of Ni and Co depends upon the coating ductility required (>Ni) and Type I hot corrosion resistance (>Co) [27, 75]. As described by Nicholls et al. [72], the Cr and Al contents must be modified in relation to the type of degradation expected (Type II /Type I hot corrosion or oxidation). Generally Ni-Cr-Al-Y are the most oxidation resistant overlay coating, while Co-Cr-Al-Y have good Type I hot corrosion resistance (Fig.21).

About 25%-40% Cr is required for type II hot corrosion whereas 15%-20% Cr is usually recommended for type I [66]; in fact according to Nicholls [72] overlay coating with 18-22%Cr and 8-12%Al are designed to withstand corrosion at above 900°C.
It is to be noted that too high Cr content may have deleterious effects on the diffusional stability of the systems [66].
CoCrAlY coatings, with 17-22% Cr and 10-12% Al, have the best resistance to attack at high temperature, but not with the most severe salt environments. For lower-temperature corrosion protection, CoCrAlY coatings with very high Cr level (25 to 35%) are required for maximum protection [27]. Cobalt sulphates lower the sulphate deposit melting point under type II hot corrosion conditions, thus increasing the corrosion rate when compared to nickel.

The application temperature of M-Cr-Al-Y coatings is limited to 1100°C, because of the relatively thick oxide scales that are which is formed, followed by enhanced local spallation, particularly when thermal cycling is encountered [17, 105].

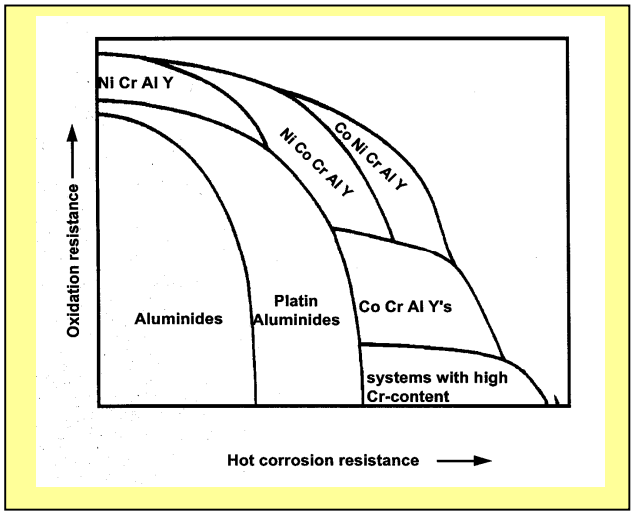

Fig. 21 Relative oxidation and corrosion resistance of high temperature coating systems [43].

Overlay coatings do not, or barely, interact with the substrate [27, 75] during their application, permitting much greater coating composition flexibility than diffusion coatings (Fig. 22) [74], but do interdiffuse during subsequent service.

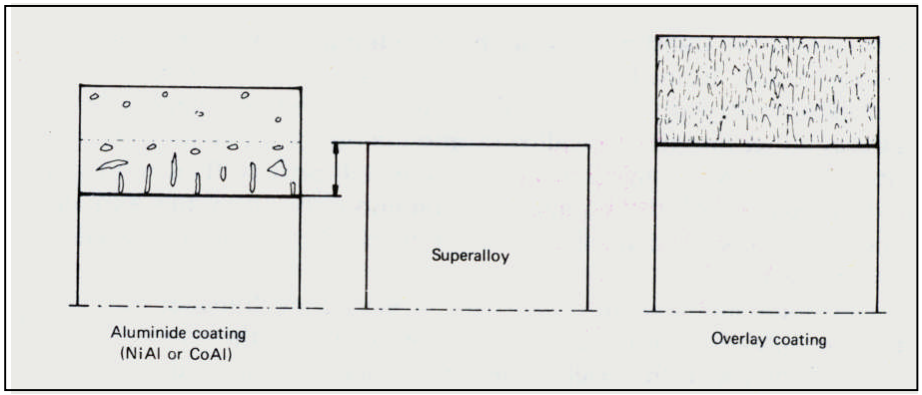

Fig. 22 Schematic illustration of the interaction with the substrate (superalloy) of Aluminade and Overlay coating: bare interaction for the latter, interdiffusion between coat and alloy for the former [27].

Overlay coatings are applied often by various types of thermal spray process, for example air plasma spray (APS) or high-velocity oxy-fuel (HVOF). The latter is illustrated in figure 23. The process is cost effective and produces good product quality, since it achieves coating properties similar to those produced by vacuum plasma spray: strength, ductility, low porosity (which prevents gaseous reactants diffusing across the coating layer) and low contents of oxides [48, 68].

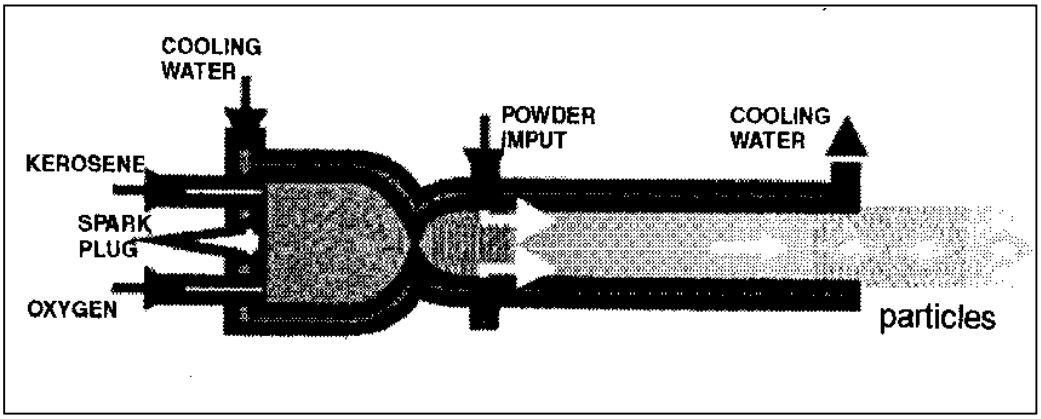

Fig. 23 HVOF: oxygen and a fuel gas (hydrogen, propane or propylene) are burnt in the spray gun where powder is added. Successively the products are sprayed by the gun on the substrate (about 5-10 μm) [48].

The degradation behaviour of overlay coating can be described in a similar way to that of Pt-aluminide: the Al-rich β-phase begins to dissolve at the coating-scale interface because of scale replenishment and also at the coating-substrate interface because of interdiffusion with

the substrate. With longer exposure these depletion zones move toward the centre of the coating until the β-phase is completely consumed [48].

1.6.3 Microstructural evolution during oxidation and corrosion

During service coatings are degraded because of interactions with both the surrounding environmental (e.g. oxygen, sulphur oxide, salt deposit) and the alloy beneath [10]. These interactions lead to chemical and micro-structural changes, described for example by Mevrel et al. and Vialas et al. [66, 120], which can be correlated to exposure time, temperature and other environmental variables (such as concentration of contaminants). The coating-alloy interdiffusion rate decreases within overlay coatings in the following order NiCrAlY>CoCrAlY>NiCoAlY>CoNiAlY [75]. Moreover, by increasing the temperature the chemical-structural changes are more evident over the same exposure time [120].

The continued development of a new oxide layer leads to depletion of the element being selectively oxidised. When the metal being selectively oxidised can no longer form a continuous protective oxide layer anymore, other less stable oxides form, starting at a localised area, increasing in size as the exposure continues. Chemical failure consists of the impossibility of the oxide film re-healing damages due to cracks and spallation or in the preferential oxidation of chromium rather than aluminium (for M-Cr-Al system). In both cases oxidation rate will increase and lead to the eventual formation of non-protective nickel-cobalt-rich oxides [33].

The degradation behaviour of overlay coating is similar to that of Pt-aluminide ones.
As described by several authors, reference Tolpygo et al. [116], Angenete et al. [5], Grabke et al. [39], for alumina forming coatings exposed to oxidation and corrosion the main atoms fluxes, visualized in figure 24, are:

1. Outward diffusion of Al for alumina formation
2. Inward Al diffusion, due to composition gradient between the coating and the substrate.
3. Outward diffusion of nickel from the superalloy.

Moreover, inward Ni diffusion from the surface is possible: according to Grabke et al. [39], who studied alumina forming on NiAl, Ni diffuses inward due the concentration gradients correlated to Al depletion. In presence of Pt-aluminide coatings, Pt inward diffusion is expected during service as well [75].

Finally, as shown in figure 24, inward vacancy diffusion is expected during oxidation/corrosion.

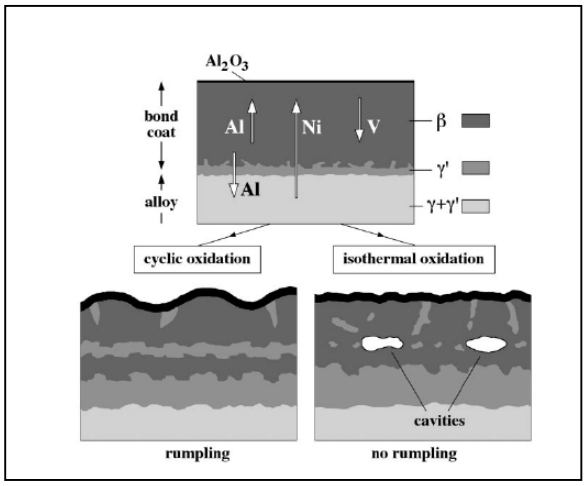

Fig. 24 Schematic illustration of the major fluxes, Ni, Al and Vacancy (V) during bond coat oxidation and microstructure evolution leading to rumpling or cavity formation [116]

Besides the dominant diffusion of Al and Ni, alloying elements, such as Co, Cr, Ti, Ta, Mo, W and Re diffuse to enrich the coating [121]. These elements may result in the formation of TCP (§1.2.1) phases which can cause embrittlement in the coating/alloy interface region and lead to loss of the coating under high mechanical loading [121]. Moreover, also the Pt migration into the substrate has been shown to result in TCP formation [75].

Figure 24, a schematic representation of the effect of cycling oxidation on (Ni, Pt)Al bond coat protecting a Ni base superalloy, shows that cavities may form during coating degradation. Their origin is not completely clarified [50], but two processes are supposed to be the main causes: vacancy diffusion, which leads to the so call Kirkendall porosity [50] and phase transformation, occurring according to equation 18, that bring about a volume reduction [116].

$$3NiAl+3/2O_2=Ni_3Al+Al_2O_3 \quad (18)$$

Figure 24 shows, moreover, one micostructural evolution correlated to the wear of alumina forming coatings, such as β- γ phase transformation.

The oxide barrier, initially formed over the coating surface, eventually becomes damaged, due to thermal stress, cracks and spalls [50]. Afterwards, as mentioned, Al diffuses outward to replenish the oxide layer and inward due to interdiffusion with the substrate. That causes Al-rich β-phase dissolution respectively at the coating-scale interface and at the coating-substrate interface [10, 53, 81]. With longer exposure these depletion zones move toward the centre of the coating until the β-phase is completely consumed [53]. As described by example Hayashi

et al. [47] in relation to Ni-Al-Pt system oxidised at 1150°C, β-phase decomposes into the less Al rich phase γ' and then γ (§ 1.2.1).

Also during corrosion, as illustrated in figure 25, (for the corrosion behaviour of CoNiCrAlY coated IN738LC), the exposure leads to the beta phase transformation, due to the loss in aluminium to replenish the alumina scale. The complete depletion of β means that Al reservoir has been consumed and thus the protective scale can no longer form.

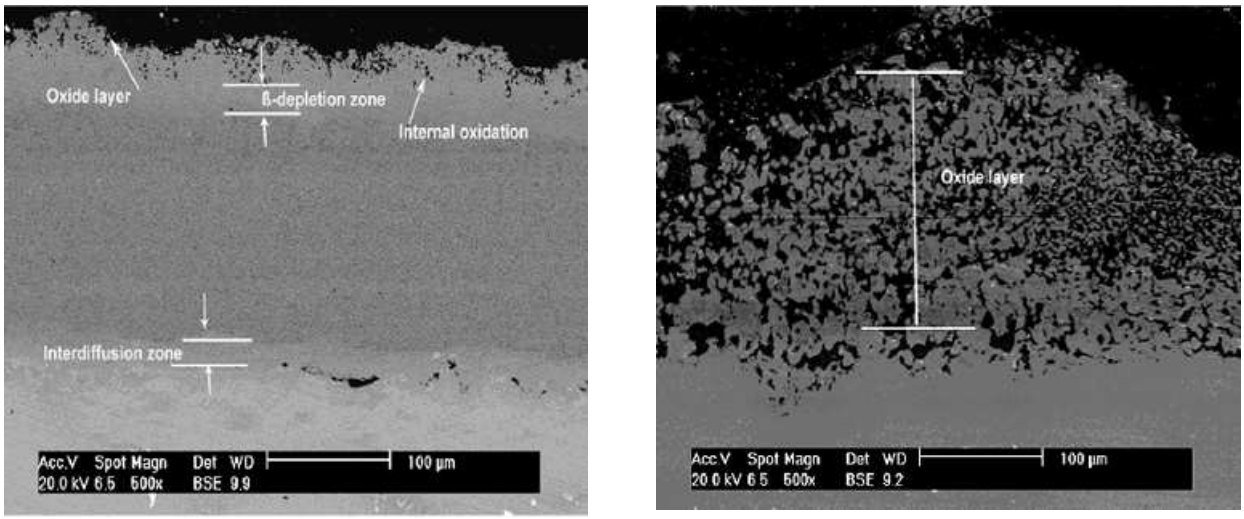

Fig. 25 CoNiCrAlY coating degradation (on IN738LC alloy) after 120 and 168 hours of exposure at 850°C coated with 2.5mg/cm^2 of salt (Na_2SO_4-10%NaCl) [67].

2. Research project

The increasing aggressiveness of the power plants operating environment, due to a rise of temperature, number of outages and employment of coal/biomass derived fuel gases in place of more tradition fuel (natural gas), has resulted in the need of a better understanding of materials behaviour and reliability under a range of oxidation and corrosion conditions.
With regard to the existing problem, this MPhil research project takes into consideration gas turbine blades and deals with the study of the performance of one superalloy and three coatings. The research concerns the study of materials degradation processes under the following two different exposure conditions:

- Isothermal oxidation and
- Hot corrosion

2.1 Experimental approach and procedure

The MPhil research has been carried out through two main stages:

- laboratory experiments for materials ageing/testing and data gathering
- data analysis

Laboratory experiments consist of exposing the samples of each material system (bare superalloy and superalloy+coating system) in furnace assemblies for various temperatures, times of exposure, gas compositions and deposit fluxes that closely define the oxidative and corrosive conditions within an operating gas turbine.

Before and after exposure metrology is applied to both oxidation and corrosion samples, as proposed by Simms et al. [94]. This consists of an accurate measurement of samples dimensions before and after exposure that guarantees to quantify material degradation in terms of both mass loss and depth of attack [94, 96].
According to the **metrology method** the most useful data for accurate and reliable material life time predictions are identified as thickness loss/depth of attack; this information may be collected only through a destructive method of analysis.

Once the samples have been tested, they are mounted in resin, along with reference samples (which are samples passing through every stage of the measurement and cross-section preparation process without being previously exposed) and their cross-sections prepared.
Cross-sections of oxidised samples are analysed by **Optical Microscope** (§2.2.3) and **Environmental Scanning Electron Microscopy** (ESEM) (§2.2.4) respectively for oxide chemical analysis and thickness measurement. Moreover, oxidised specimens undergo **Energy Dispersive X-ray** (EDX) Spot Analysis in order to define the element concentration profiles before and after the oxidation tests.
Cross-sections of corroded samples are initially **Image analysed** to investigate the material loss; afterwards they are observed by ESEM and undergo EDX for morphological and chemical analysis of the corrosion processes.

Data of **weight change** are gathered as well for oxidised and corroded samples.
These produce average measures of the attack because a single measurement is obtained from a sample, whereas in reality damage is not uniform over the specimen's surface (for example, due to pitting and internal corrosion) [20, 27], and oxide scale/TGO thickening isn't properly characterized once oxide starts to flake off [19]. However weight change data do allow a general overview of materials behaviour and oxidation kinetics measurement. This last point can be used for obtaining a rough estimate of the life time of the coating (under some circumstances) [67].

The use of **reference samples** of all materials enables the evaluation and elimination of the error, both systematic, which is correlated to the use of different measurement methods during pre- and post-exposure measurements, and random.
Moreover, reference samples permit the checking of repeatability and reproducibility and thus give more accuracy to the final result [93].

2.2 Experimental design

2.2.1 Materials

The specimens employed in the tests consist of bar samples. They are made up of either nickel-based superalloys CMSX-4, whose composition, is recorded in several literatures [23, 27, 67, 69, 112] with low variability, and is presented in table 1, or a superalloy CMSX-4 coated with one of the following coating: RT22, CN91 and "LCO22" (Table 2).
The morphology of the reference materials is shown in figure 26.
The existing difference between inward and outward Pt-alumined coatings' structures is described in paragraph 1.6.1; while the overlay coatings structure is described in paragraph 1.6.2.

The samples have been provided as long bar of each material systems; afterward these were machined, in order to create individual cylindrical samples.
The coated systems were supplied by the following SUPERGEN PLE sponsors:
RT22 and CN91 by Chromalloy UK Ltd,
"LCO22" by Sermatech International UK Ltd.
The long bars supplied, even if of the same materials system, belong to different batches. Consequently, samples, having the same protecting coating, can present structural differences and so they can behave differently under the same exposure condition.
The samples' structure, wrongly, has not been checked before introducing the samples into the furnaces. Later, in presenting results and discussion of the oxidation tests**,** differences in samples behaviours of the same materials systems will be led back to differences in the microstructure, but this conclusion can't be supported by previous analysis.
This issue came out, primarily, through the analysis of the oxidation results, thanks the employment of an greater number of samples than that tested in the corrosive environment.
The presence of different batches hardly allows the repeatability and reproducibility of the results.

Table 1 Composition of under examination alloy (wt%)

	Ni	**Cr**	**Co**	**Al**	**W**	**Mo**	**Ta**	**Ti**	**C**	**Hf**	**Re**
CMSX-4	61.8	6.5	9	5.6	6	0.6	6.5	1	-	0.1	3

Table 2 Materials systems under examination

Base alloy	*Metallic coating*
CMSX-4	-
CMSX-4	**RT22** Pt modified-aluminide coating (inward grown coating).
CMSX-4	**CN91** Pt modified-aluminide coating (outward grown coating).
CMSX-4	**"LCO22"** *Overlay coating (Co-32Ni-21Cr-8Al-0.5Y), HVOF

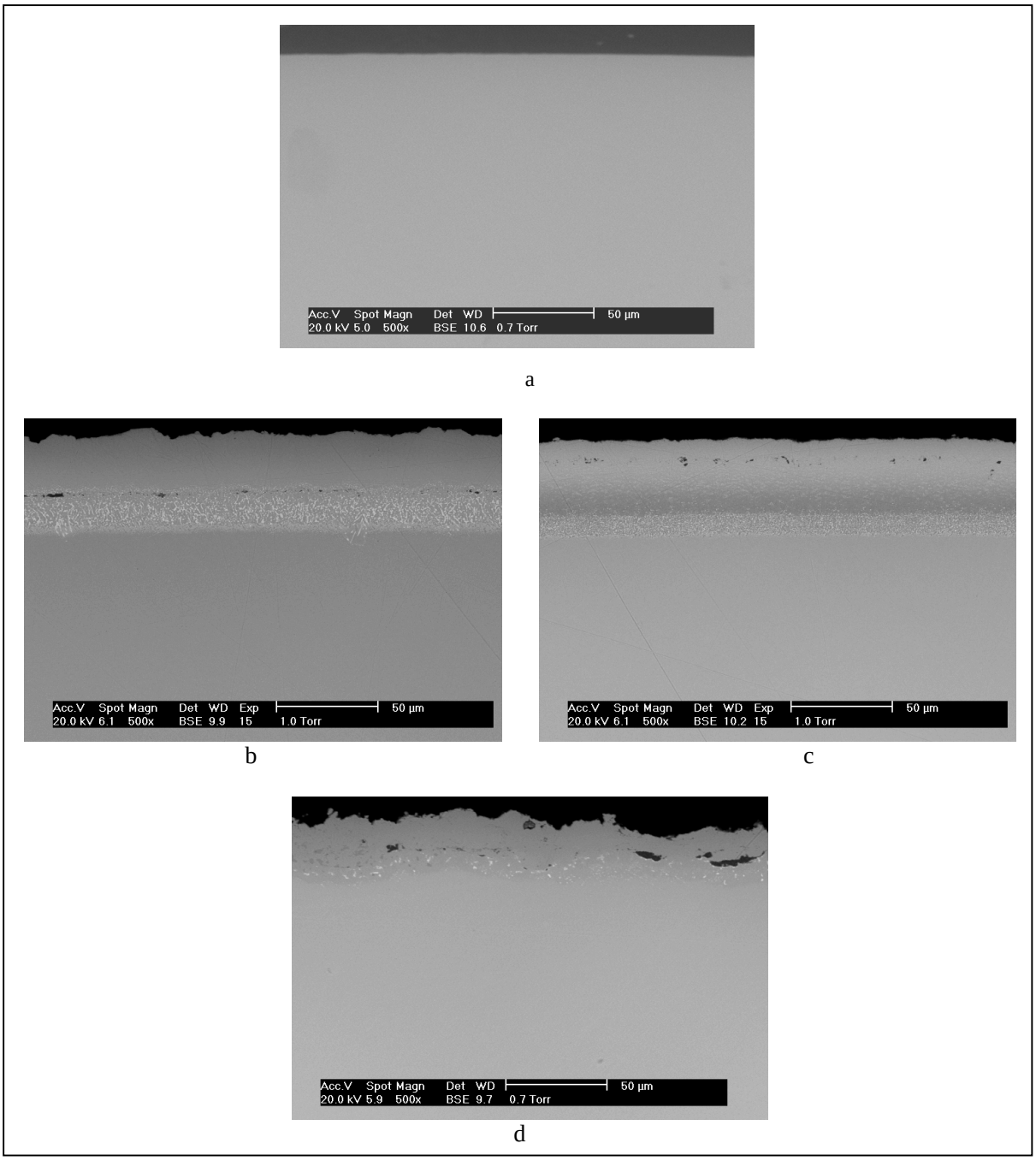

Fig. 26 ESEM picture of a, uncoated CMSX-4 and of the three coated systems b, CMSX-4/CN91, c, CMSX-4/RT22 and d,CMSX-4/"LCO22".

2.2.2 Tests conditions

Oxidation:

Table 3 illustrates temperatures and exposure time for isothermal oxidation tests.

Table 3 Temperature and exposure time.

Temperature (ºC)	**Length of time (hours)**
850	1000, 2000, 3000, 4000, 5000, 6000, 7000, 8000, 9000 and 10000
900	1000, 2000, 3000, 4000, 5000, 6000, 7000, 8000, 9000 and 10000
950	1000, 2000, 3000, 4000, 5000, 6000, 7000, 8000, 9000 and 10000
1000	1000, 2000, 3000, 4000
1050	1000, 2000, 3000, 4000

Corrosion:

Table 4 illustrates temperatures, exposures times and gas compositions for corrosion tests; table 5 reports salt deposit composition and flux.

Table 4 Temperatures, exposure time and gas compositions for corrosion tests.

Temperature (ºC)	**Length of time (hours)**	**Gas composition**
700/900	500	Air + 300vpm SO_2
700/900	500	Air + 300vpm SO_2 +100vpm HCl +H_2O

The deposits are renewed on each cycle by spraying solutions containing the required deposit ("deposit replenishment"); different fluxes are obtained by spraying different weights of deposits onto the surface.

Table 5 Sprayed deposit composition and fluxes

Deposit Composition (Weight %)		**Flux** (µg/cm^2 h)
Na_2SO_4	K_2SO_4	0.5/ 1.5/ 5
76.5	23.5	

The gases concentrations in the exposure environment of the corrosion tests, have been selected in order to fill in the gap of experimental data came out at the conclusion of the previous project [30].

In fact, Ecinas-Oropesa [30] tested a SO_2 concentration of 50 and 500 vpm, and from that the choice of testing the effect of an intermediate level (300 vpm). The basic idea was that thee new experimental data could validate the model developed during that previous study.

Moreover, Ecinas-Oropesa [30] investigated the effect of the gas composition: 50vpm SO_2+500vpmHCl. Since that was the first and unique selected mix composition to be tested, the HCl concentration was chosen high in order to obtain a condition where the effect of this gas was as much clear as possible. The concentration of HCl has been reduced in this study for approaching the real exposure condition.

The gas concentration tested is higher than that characterising the gas turbines exposure environment, for compensating for the higher pressure present in the second case.

The exposure environment of the real turbines is characterised by higher pressure.

The experimental component of this study has recreated the hot corrosion processes occurring in the real turbines, but what has been observed isn't the real damage. Shape/size of the samples, gas composition/pressure and time have been adjusted in order to obtain data that can be correlated to the real material loss experienced by the gas turbines. Procedures similar to that applied with this study allow to gather more data and quickly than using real power plants.

The salt composition and the ratio K/Na has been chosen in order to test the effect correlated to the worst case. In fact, the ratio 1:4, K_2SO_4:Na_2SO_4, represents the alkali sulphate composition with lowest melting point [].

As already mention, this study falls in a big project, called Conventional Power Plant Lifetime Extension (Introduction) and the investigation of the gas turbines degradation is proceding through several short researches. Concerning the value deposit flux, it is being lower gradually from the first study.

Furnaces

The oxidation and corrosion tests employ respectively horizontal and vertical tube furnaces, whose schematic design is visualised in figures 27 and 28. Inside the furnace the samples are

located within a zone where the temperature is ±5ºC of the target test temperature. Bottles containing gases are connected to the bottom (for oxidation) or to the top (for corrosion) of the furnaces to allow gas fluxing throughout the exposure environment.

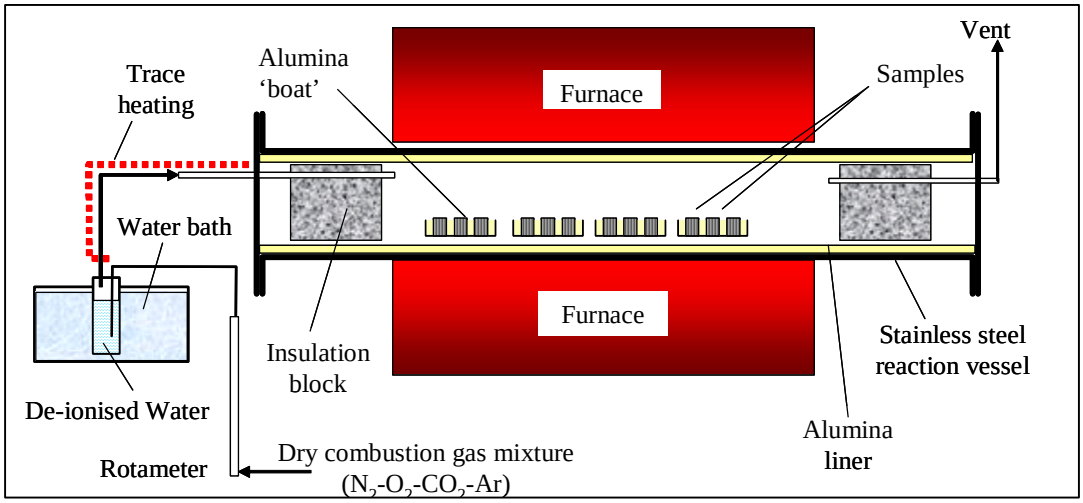

Fig. 27 Controlled atmosphere furnace for specimens exposure to oxidative environment.

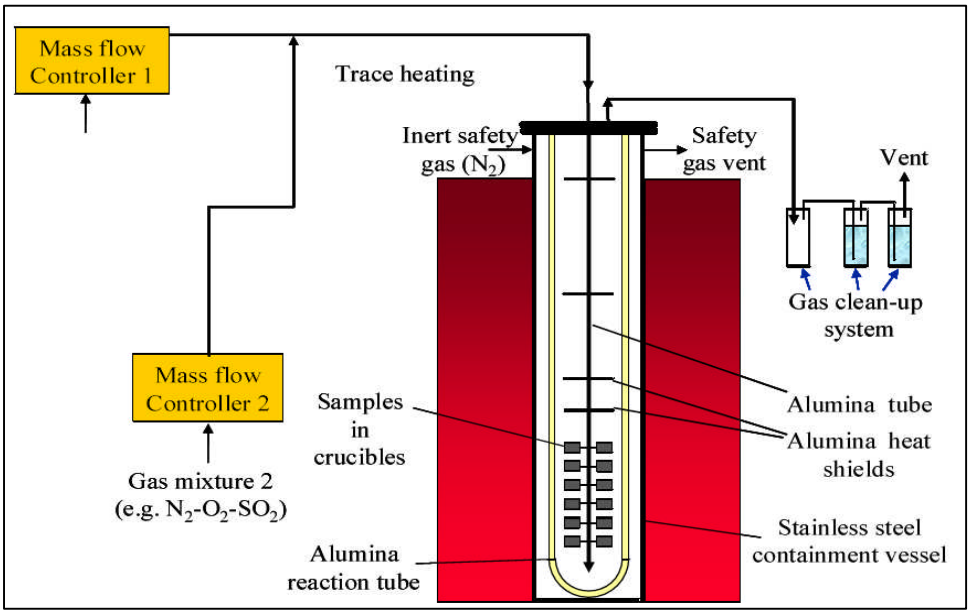

Fig. 28 Controlled atmosphere furnace for specimens exposure to corrosive environment.

2.2.3 Optical Metallography

IMAGE ANALYSIS

The principles and functioning of the image analysis is well described in Simms et al. [94]. Briefly, the cross section is measured using a reflected light microscope with calibrated x-y-stage. The Image Analyser system follows and measures the position of the edge of the metal relative to the origin of the system of coordinates. The analysis may define also the depth of the internal damage.

The comparison between the measurements gathered with the image analyzer and those taken, before samples exposure in furnace by the means of a micrometer, are used to calculate the metal loss. This step required the application of a complex spreadsheet, which also considers and corrects the systematic and random errors introduced using the micrometer, through the comparison of the results obtained from measuring a reference specimen (that is not exposed) with Image Analyzer and micrometer.

OPTICAL MICROSCOPE

The Optical Microscope is employed for the observation of the oxidised samples. It permits, through the use of a colour scale, to differentiate the oxides formed during the exposure and thus it's a useful tool for understanding the material consuming processes which occurred and the effect of time and temperature.

2.2.4 ESEM Analysis

The characterization of damage in the oxidation tests employs an ESEM and consists in taking 8 picture of cross-sections for each sample, typified by the figure below (Fig. 29), these are taken using a magnification of 500x/1000x.

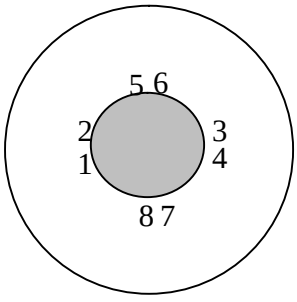

Fig. 29 Schematic of sample showing typical image locations.

Once taken, the photos are analysed using *ImageJ* software to collect measurements of thickness of oxide scale/TGO measured 90° to surface (as depicted by yellow arrows in figure 30)

For each photo 3 measurements are taken, therefore 24 data, according to the metrology method [94], result from the analysis of one specimen.

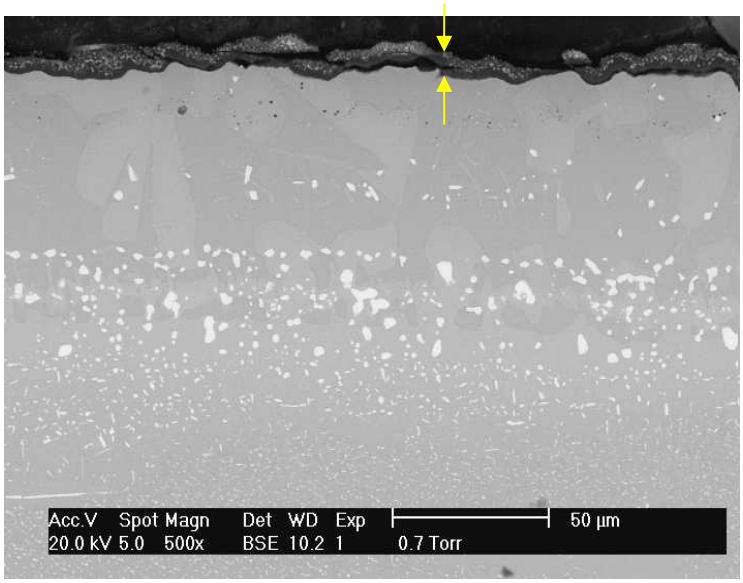

Fig. 30 Examples of pictures: a) CMSX4/RT22 system after 2000hr of exposure at 950°C.

For each corroded sample 4 pictures are taken. The magnification used changes in order to have a compromise between the best picture describing the results of the corrosive processes and the possibility to compare performance between alloy/coating systems under environmental conditions tested.

2.2.5 EDX Analysis

A quantitative analysis (*Spot Analysis*) by EDX of the oxidation specimens' cross-section has allowed to obtain the concentration profile of the metals present in the alloy/coating systems. As described in the figure below the concentration of these two elements has been detected in several sites lining on a line normal to the surface and crossing each layer (TGO, if present, coating, interdiffusion zone and substrate). In such a way the atoms diffusion's result after each exposure time and temperature has been compared and the rate at which it occurs calculated.

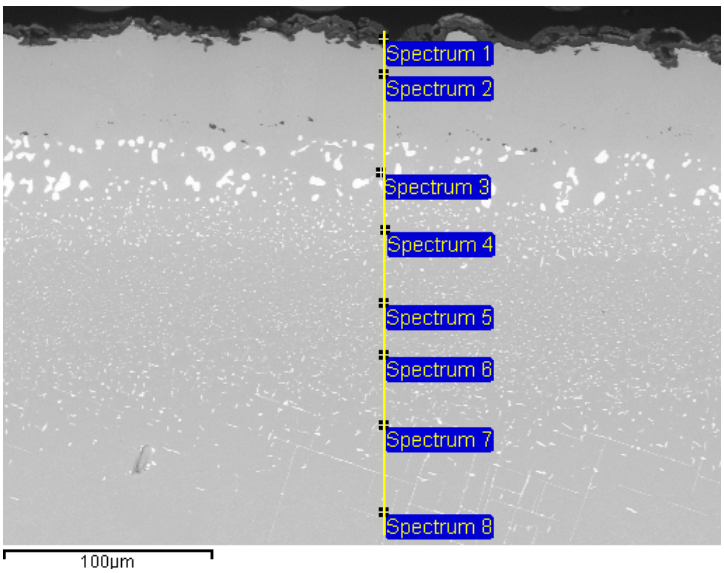

Fig. 31 Example of EDX analysis on CMSX-4/CN91 (exposed for 10,000hr at 950°C)

EDX analysis performed over corroded samples provides a qualitative description of corrosion product composition, location and coating depletion.

3. Results

3.1 Oxidation

The oxidation tests have been carried out on the three different coated systems (CMSX-4/RT22, CMSX-4/CN91 and CMSX-4/ “LCO22”) at the exposure condition exposed in table 3 (§2.2.2).
The results of the isothermal oxidation of both Pt-aluminide and overlay coated specimens are visualised as mass change plots, ESEM pictures, EDX maps and probability plots.

3.1.1 Kinetics of oxidation

The first results of the oxidation test are presented in form of mass change plots, which represent one tool for studying the kinetics of the oxidation reaction (§ 1.4.2). They in fact provide a general overview about the oxidation behaviour of the coating, the evolution in alumina phase formation and the occurrence of coating failure.

In the following figures we see as the mass change trends may be parabolic (at the lowest temperature) or a combination of parabolic and linear curves. The global shape of the curves results from the competition between mass gain caused by oxidation and mass loss due to scale spallation. Especially at the highest temperature (≥ 950°C), where oxidation rate should be higher and the scale spalling more intense, the mass change plots present complex curves.

Effect of temperature

CMSX-4 / RT22

The oxidation behaviour of RT22**,** as visualised in figures 32-36, changes as a function of the temperature. In fact the mass change curve trend looks to be parabolic at the lowest temperature (850°C), at 900°C the curve is composed clearly by a first part (0-1000 hours) with higher slope and a second one less steep, whilst at the highest temperatures, especially at 950-1050°C, the mass change curves assume complex shapes. The trend visualised by the mass change plot, as it will be analysed and described in chapter 4, is the result of different

oxidation kinetics of the coating/alloying metals at different temperatures, the growth of two alumina phases (θ-Al_2O_3 and α- Al_2O_3) and the occurrence of spalling.

In the following plots each line represents the mass change experienced by one samples. A variable number of samples (two, four or seven) have been tested for each exposure time.

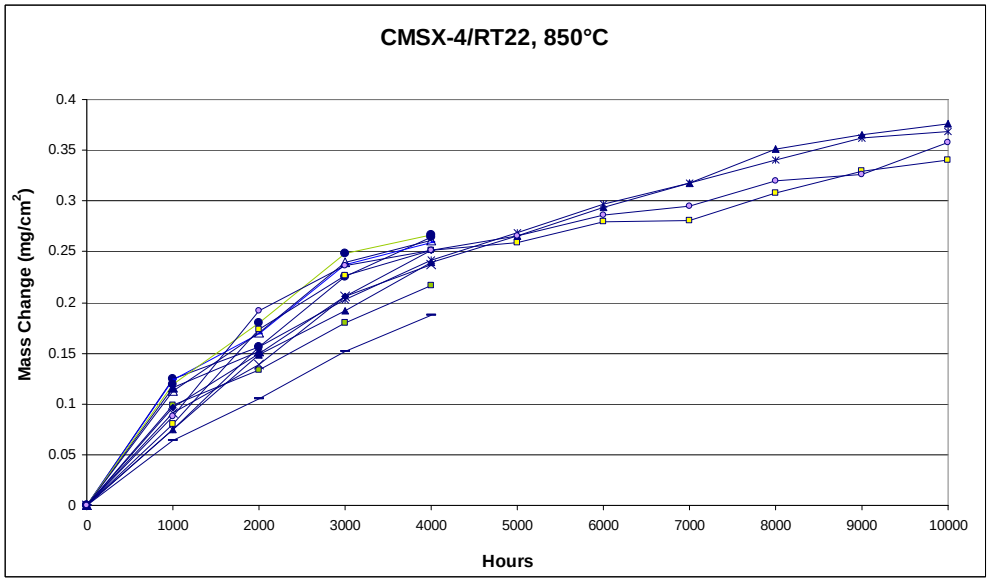

Fig. 32 Mass change plot for the system CMSX-4 / RT22 subjected to isothermal oxidation at 850°C.

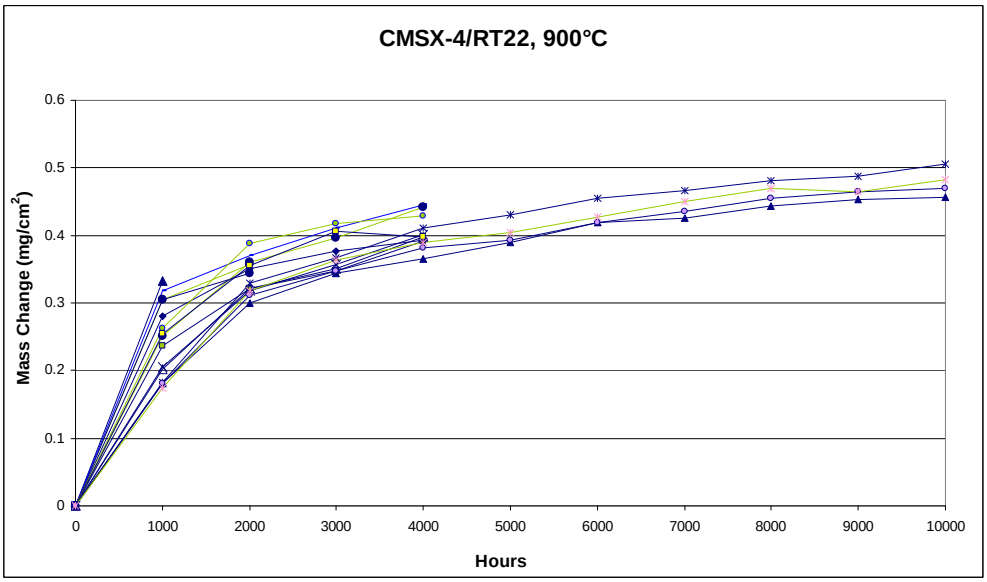

Fig. 33 Mass change plot for the system CMSX-4 / RT22 subjected to isothermal oxidation at 900°C.

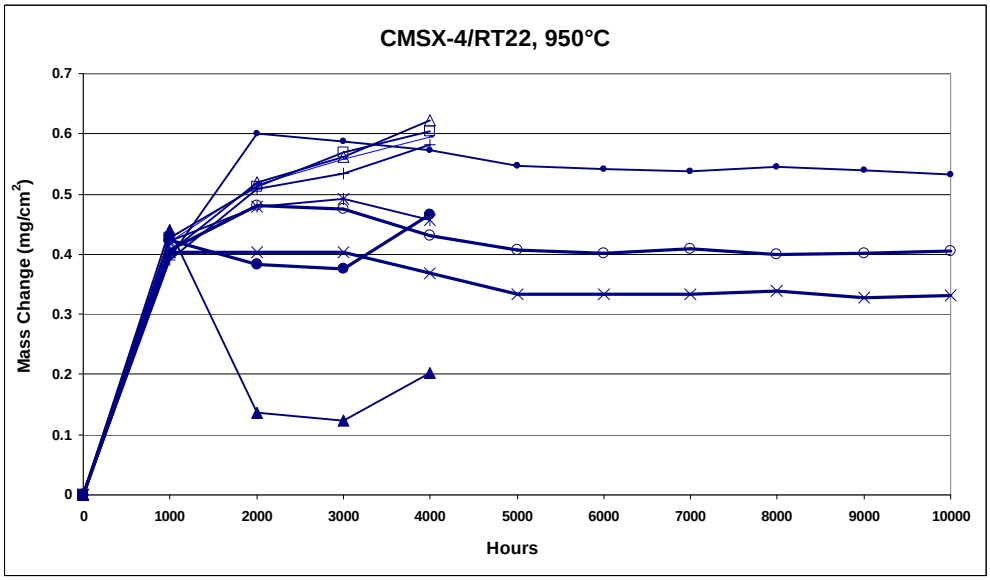

Fig. 34 Mass change plot for the system CMSX-4 / RT22 subjected to isothermal oxidation at 950°C.

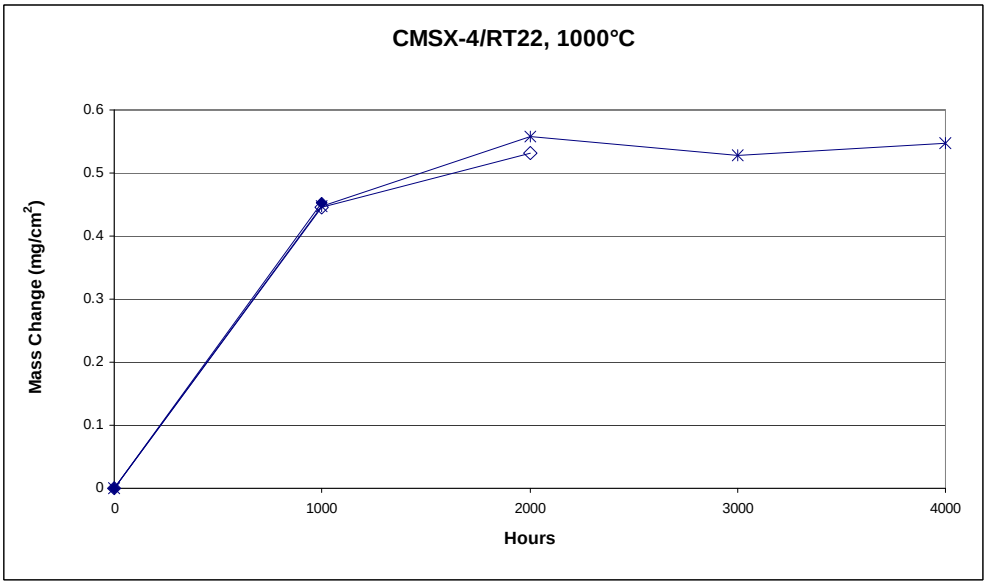

Fig. 35 Mass change plot for the system CMSX-4 / RT22 subjected to isothermal oxidation at 1000°C.

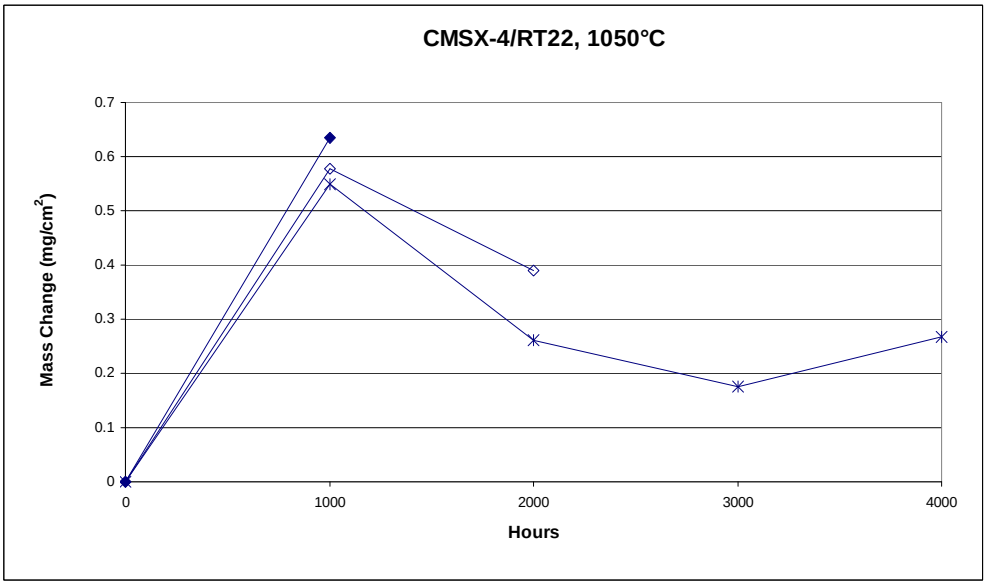

Fig. 36 Mass change plot for the system CMSX-4 / RT22 subjected to isothermal oxidation at 1050°C.

CMSX-4 / CN91

The mass change plots of figures 37-41 illustrate the temperature effect on the oxidation of CMSX-4/CN91 specimens. As already observed for RT22 coated superalloy at 850°C, the oxidation trend looks quite parabolic and the plots show clusters of samples following similar trends. At 900°C (Fig.38) there's a visible difference in the curve slope correlated to the first 1000 hours of exposure and that of the following period, which, as explained in chapter 4, are due to the growth of different phases of alumina. The oxidation behaviour shown by CN91 at 950°C and illustrated in the mass plot of figure 39 manifests itself in three ways. Two of them are represented by parabolic trends, but the kinetics are different, and the third case exhibits early spallation after a few hours and in one case very heavy. With the exception of one case (sample tested for 2000 hours at 1000°C) at 1000 and 1050°C (Fig. 40 and 41) the mass gain dominates over the spalling.

To be noticed is the wide range of mass change produced by different samples during the exposure at 850-900-950°C; the causes, which will be considered in the discussion chapter (chapter 4), lead to a non-reproducible behaviour of the coated system.

In the following plots each line represents the mass change experienced by one samples. A variable number of samples (two, four or seven) have been tested for each exposure time.

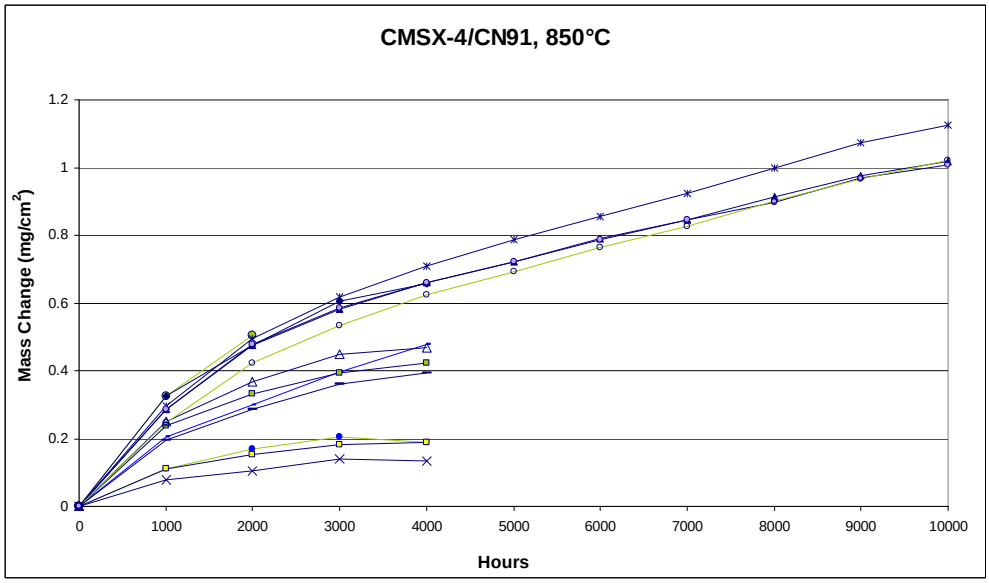

Fig. 37 Mass change plot for the system CMSX-4 / CN91 subjected to isothermal oxidation at 850°C.

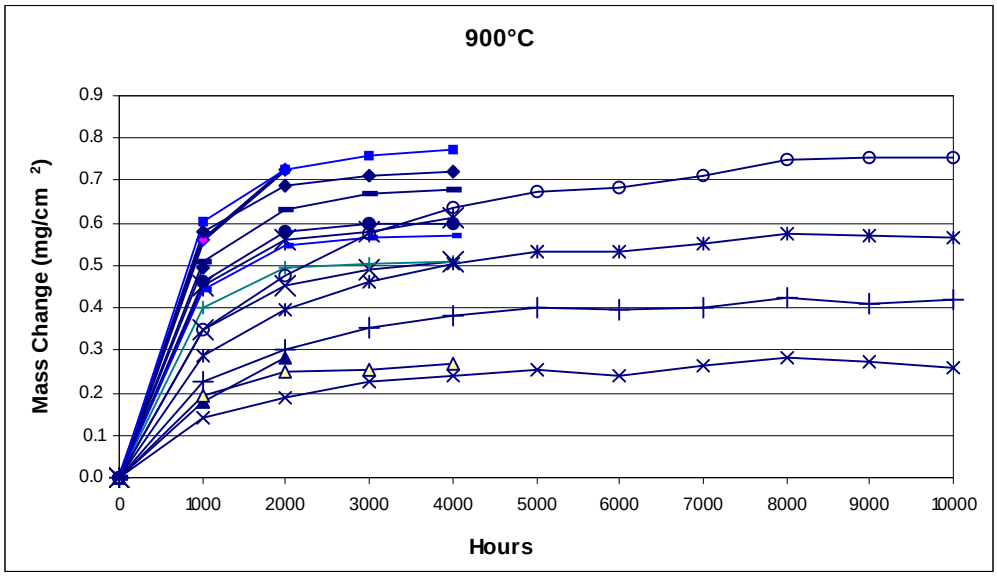

Fig. 38 Mass change plot for the system CMSX-4 / CN91 subjected to isothermal oxidation at 900°C.

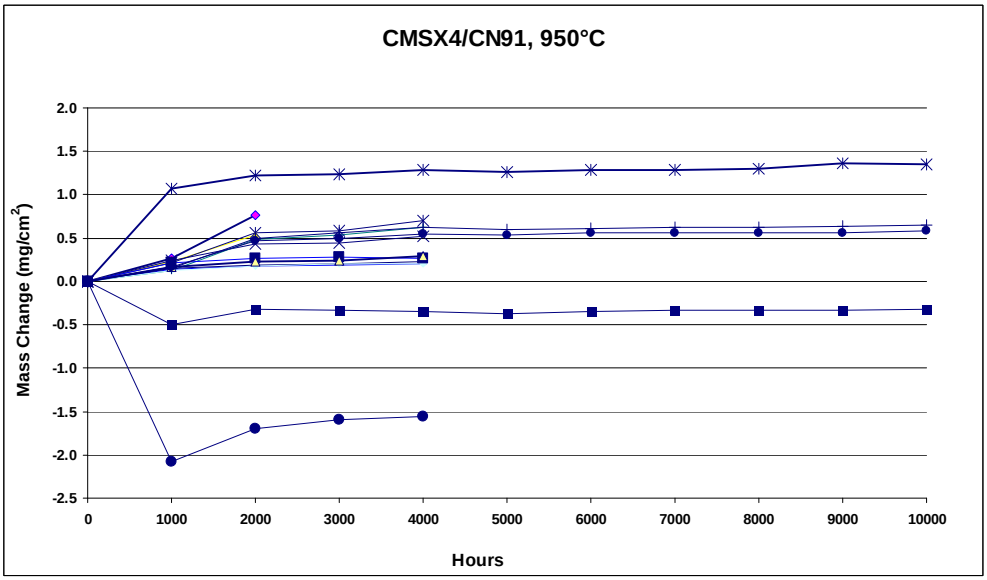

Fig. 39 Mass change plot for the system CMSX-4 / CN91 subjected to isothermal oxidation at 950°C**.**

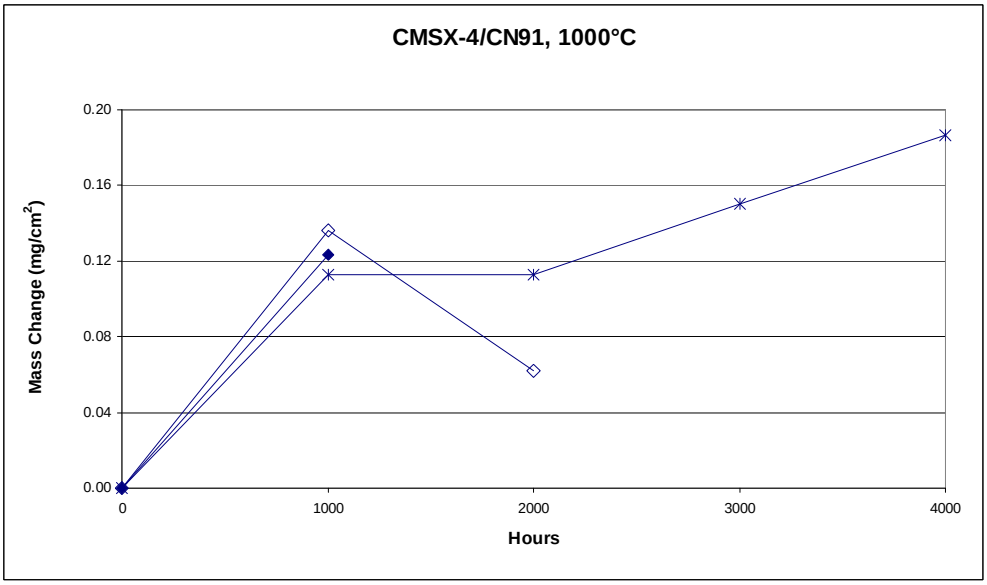

Fig. 40 Mass change plot for the system CMSX-4 / CN91 subjected to isothermal oxidation at 1000°C.

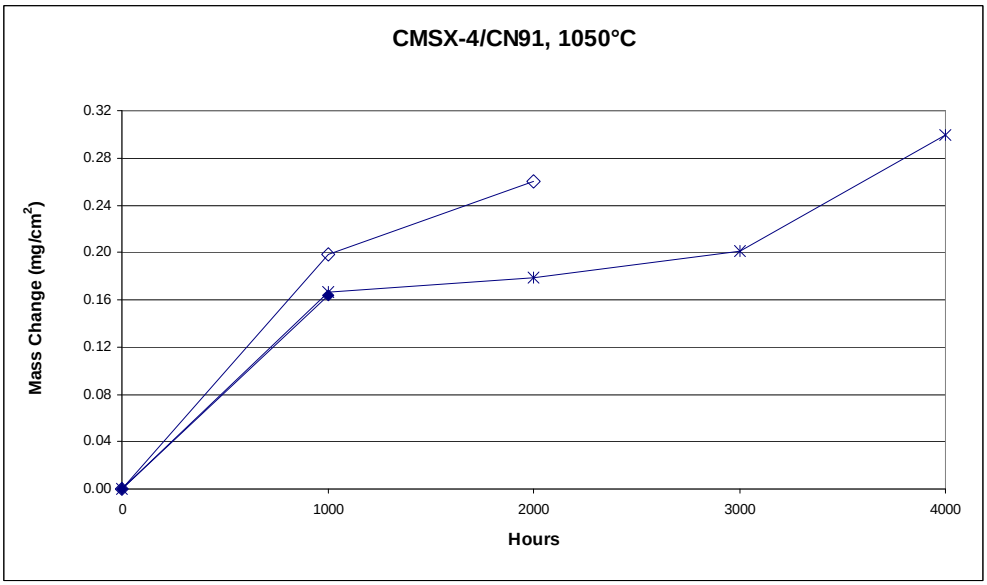

Fig. 41. Mass change plot for the system CMSX-4 / CN91 subjected to isothermal oxidation at 1050°C.

CMSX-4 / “LCO22”

The mass change plots related to CMSX-4/”LCO22” tested at 850-900-950°C (Fig.42-44) show a dominant mass gain during the exposure and nearly parabolic trend, with a steeper slope of the curve corresponding to the first 1000 hours; this slope, moreover, increases with increasing temperature. The causes of this behaviour, probably correlated to the growth of two different phases of alumina, will be discussed in chapter 4. Moreover, the causes of the variability in the mass change during the exposure at 900°C will be considered, so that the samples can be separated into 3 main groups.

Due to one furnace failure three samples have been tested for 7000 hours instead of 10000 at 950°C.

At 1000°C (Fig. 45) the mass gain dominates up to 3000 hours of exposure, afterwards spallation has occurred prominently. Two different behaviours have been detected for LCO22 coated samples at 1050°C (Fig.46). After 1000 hours of exposure, during which the specimens performed equally, the plot follows a reduced mass change for the sample exposed for 2000 hours, whilst a heavy spallation occurs for the other sample especially within 2000 and 3000 hours.

In the following plots each lines represents the mass change experienced by one samples. A variable number of samples (two, four or seven) have been tested for each exposure time.

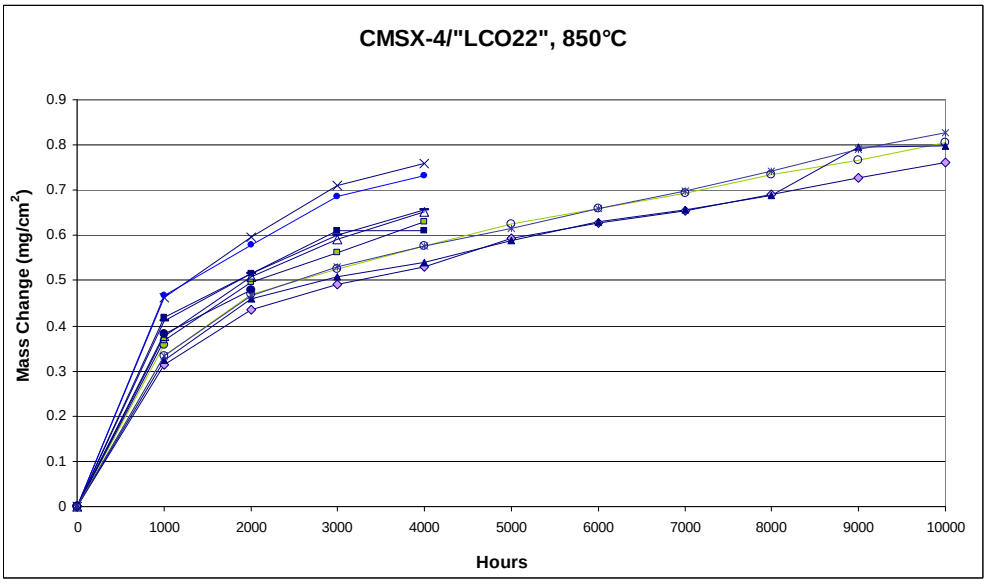

Fig. 42. Mass change plot for the system CMSX-4 / “LCO22” subjected to isothermal oxidation at 850°C.

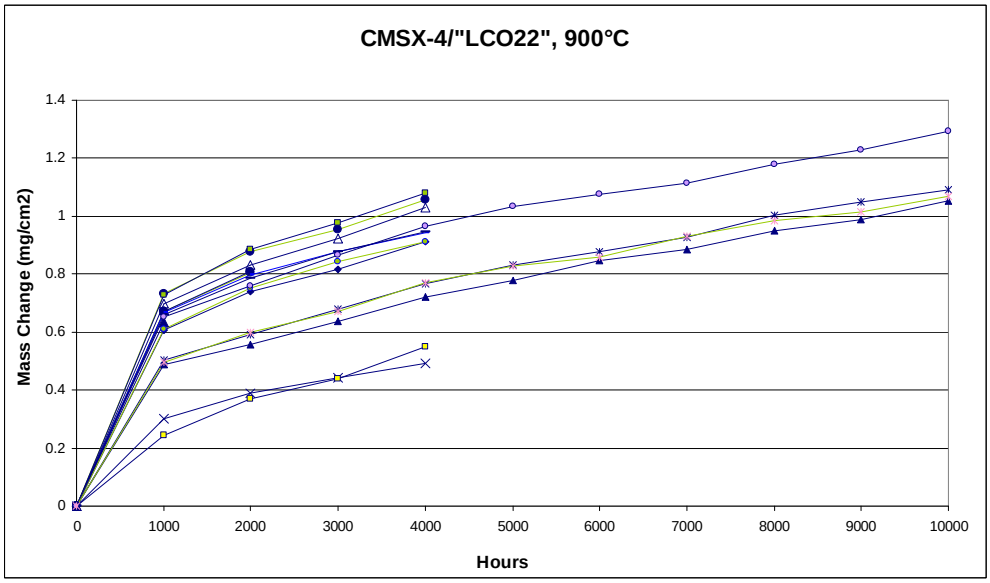

Fig. 43 Mass change plot for the system CMSX-4 / “LCO22” subjected to isothermal oxidation at 900°C.

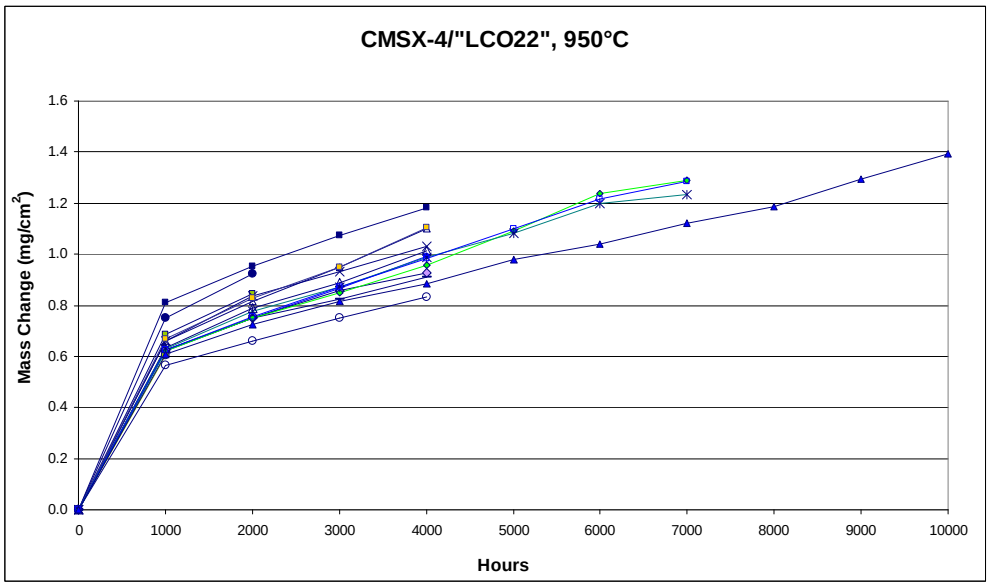

Fig. 44. Mass change plot for the system CMSX-4 / “LCO22” subjected to isothermal oxidation at 950°C.

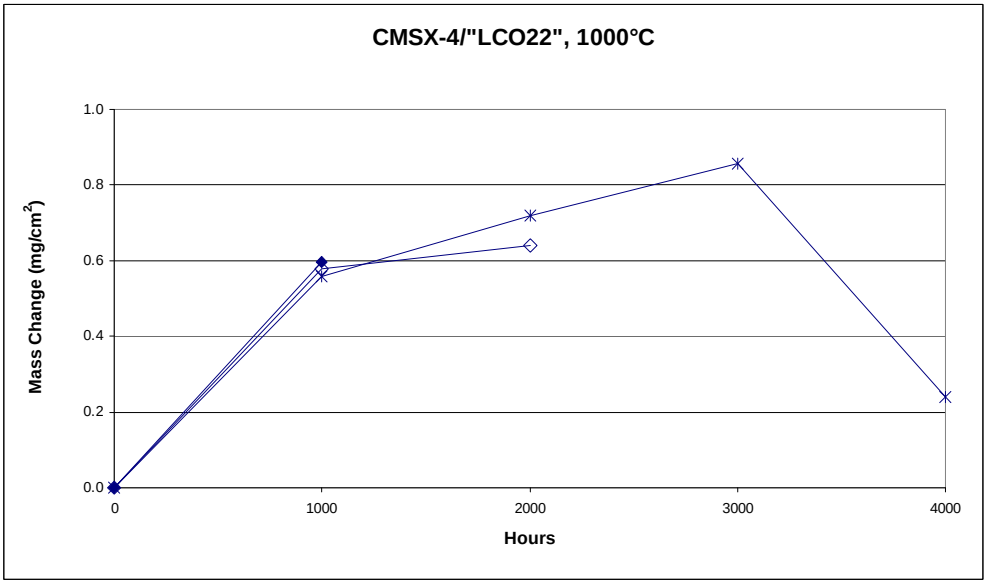

Fig. 45. Mass change plot for the system CMSX-4 / “LCO22” subjected to isothermal oxidation at 1000°C.

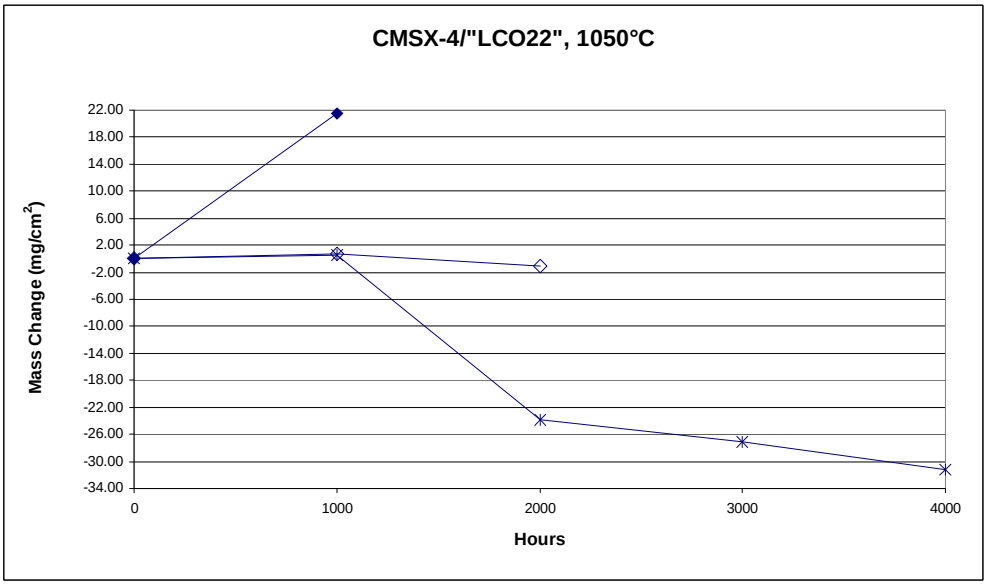

Fig. 46 Mass change plot for the system CMSX-4 / "LCO22" subjected to isothermal oxidation at 1050°C.

Effect of materials' composition

The following section provides by mass change plots a comparison among materials behaviours, which have been observed at each of the testing temperatures (850, 900, 950, 1000 and 1050°C) for the mid and long period of exposure (4000 and 10000 hours).

At 850, 900 and 950°C, plots of figures 47-49, the best protection of the underneath superalloy, described as the lowest mass change, has been provided by the Pt-aluminide RT22. The samples coated with the other Pt-alumined coating, CN91, resulted generally in the higher mass changes and so did not provide the same degree of substrate protection (as already mentioned in paragraph 3.1.1). This last observation leads to say that the overlay coating "LCO22" performed better than CN91.

At 1000°C (Fig. 50), lowest mass change has been observed for the coating CN91, while at the highest temperatures the two Pt-aluminide coatings behaved similarly. The overlay coating provided worse protection to the substrate as well as the other coatings; markedly it completely failed after 1000 hours of exposure at 1050°C (Fig. 51).

In the following plots each line represents the mass change experienced by one samples.

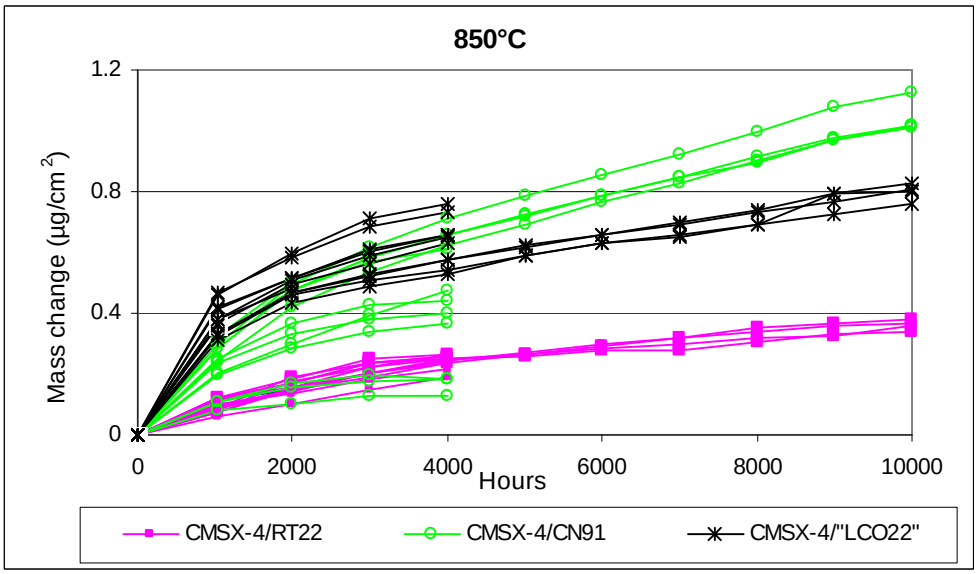

Fig. 47 Mass change plot comparing materials' behaviour at 850°C.

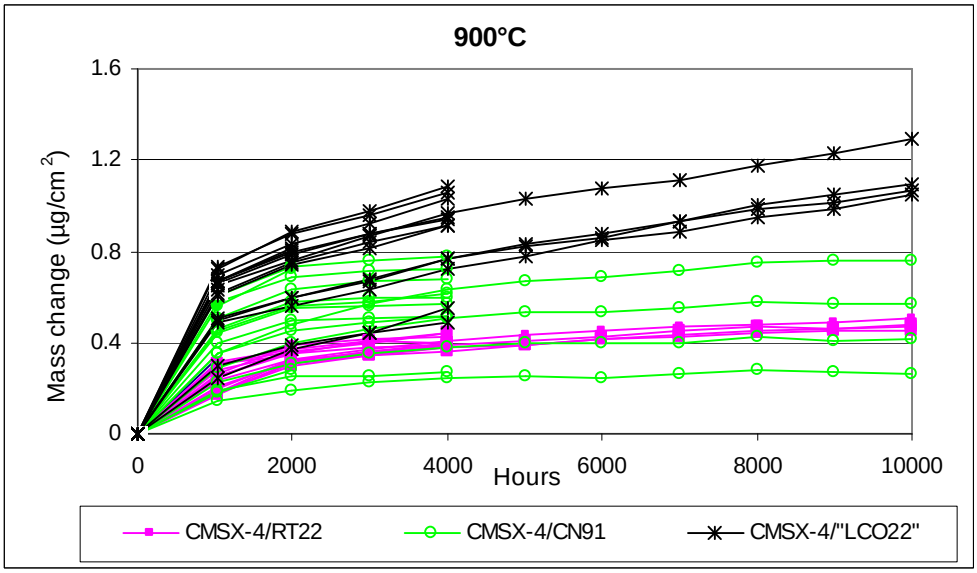

Fig. 48 Mass change plot comparing materials' behaviour at 900°C.

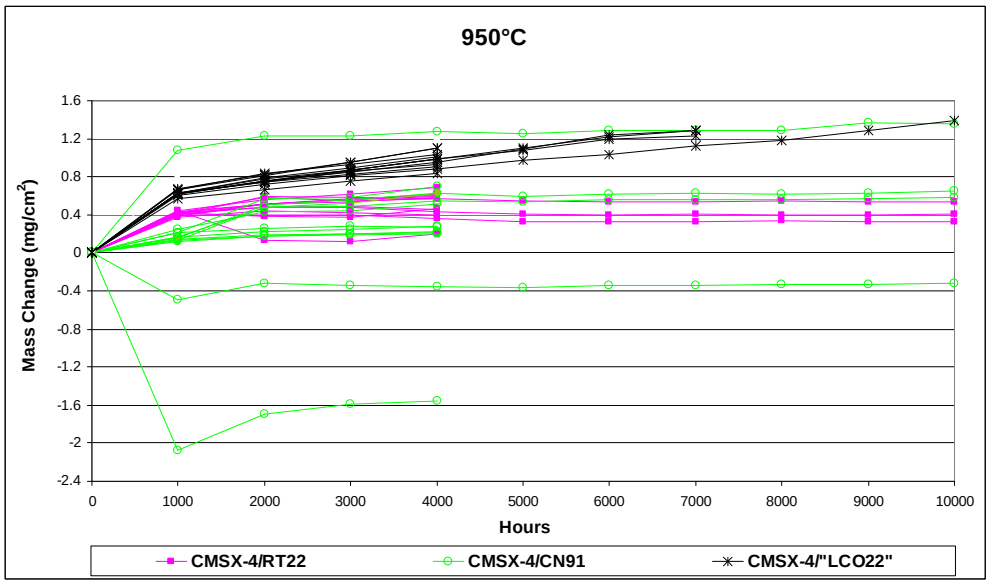

Fig. 49 Mass change plot comparing materials' behaviour at 950°C.

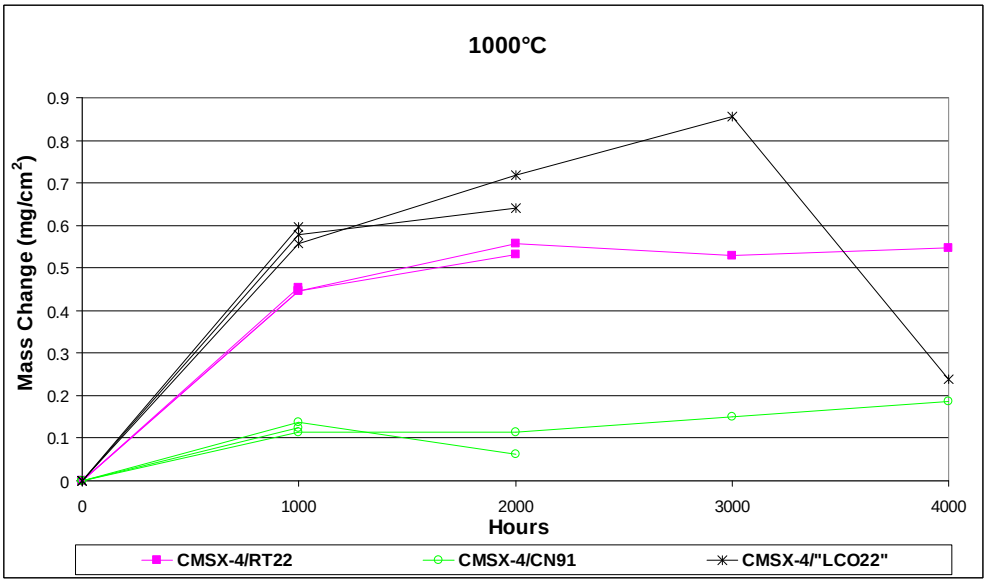

Fig. 50 Mass change plot comparing materials' behaviour at 100°C.

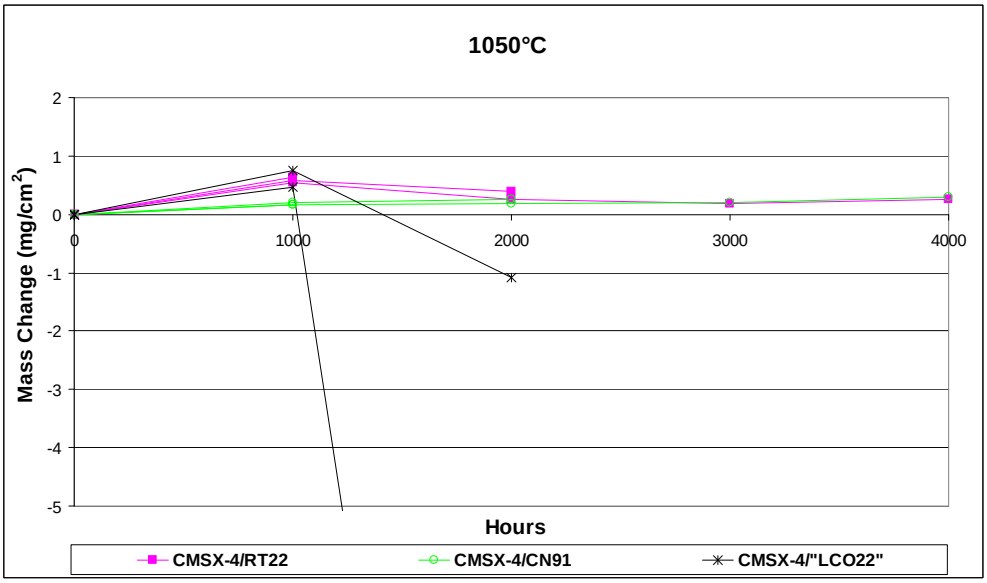

Fig. 51 Mass change plot comparing materials' behaviour at 1050°C.

3.1.2 Morphology and chemistry of oxidation

In this section three series of ESEM pictures, one for each coated system tested, are presented (Fig.52-54), along with an example of the EDX analysis carried out. These pictures and metals distribution maps represent the tool for studying the oxidation morphology and chemistry.

The elements emerging from the pictures, which are described in the following section, demonstrate chemical and microstructural changes more and deeper after increased time and temperature of the exposure conditions.

Pt-aluminide coatings

Pictures of figure 52, 53 and 26a and 26b (as-coated system CMSX-4/CN91 and CMSX-4/RT22) highlight the materials system evolution during longer exposure time (along the rows) and higher temperature (down the columns).

For both the Pt-auminide coatings from 850 to 900°C the pictures illustrate the formation of a thicker TGO at the higher temperature, even if with exceptions (Fig. 53, pictures 6 and 8) due to oxide spallation from CN91. At higher temperatures the scales, if present, don't look to be thicker; however that may be better appreciated looking at the probability plots (section 3.1.3). The TGO can also appear detached from the surface; that is visible for CMSX-4/CN91 even at 850°C (pictures 4, 5, 10, 11, 15, 18) and for CMSX-4/RT22 at 950 and 1050°C (pictures 28, 29, 30, 34, 35). The presence of a non-contiguous and detached scale can be a clue of a less protective behaviour of CN91 than RT22, at least, at the lower temperatures.

Second important evolution of the coating surface is given by its increasing undulation with the aging and temperature, which is mainly visible in pictures 18 and 36 (respectively of Fig. 52 and 53). In some cases, that are at 950°C, from 2000 to 10000 hours of exposure, moreover, voids formed in the outer part of the two Pt-aluminide coatings (pictures 10, 11, 12 of Fig.52 and 28, 29, 30 of Fig.53).

A third visible effect of the increasing time/temperature is the increased thickness of the IZ. However after long heat treatment it didn't increase further. Finally, the aging has clearly led to precipitate formation both throughout the outer zone and beneath the IZ (for the RT22 coated systems) and just below the IZ for the CN91 coated specimens. These denote that the materials degradation products have a different shape, mainly round and needle, and at the highest temperatures (1000 and 1050°C) they developed to be much bigger within the substrate.

Comparing figures 52 to 53 it emerged that Pt-aluminide coatings CN91 and RT22 have been subjected to a different degree of substrate degradation after identical exposure. After 1000 hour of exposure at 1000°C, the RT22 coated system shows the formation of needle shape TCP, while the same shape precipitates are clearly present in CN91 coated system just after 2000 hours of exposure at 1050°C. In the remaining conditions of time exposure of CN91 at 1000 and 1050°C the precipitates are smaller. The easily observed microstructural changes at 1000 and 1050°C illustrate that interdiffusion is a more significant process at higher temperature.

Overlay coating

The main feature that must be emphasized looking at the pictures of figure 26d (§ 2.2.1) is the small thickness of the coating deposited on the superalloy's surface. Consequently, some of the pictures of figure 54, illustrating the effect of increasing oxidation exposure temperature and time, down the columns and across the rows respectively, show that the coating has been completely depleted. That, obviously, occurred at the highest temperature and for longer exposure times (e.g. pictures 47, 48, 50, 51, 52, 53, 54).

Other points to be underlined, occurring both at high and lower temperature, are: the undulation of the coating surface, more evident at low temperatures than for Pt-aluminide coatings, the presence of internal oxidation (pictures 39, 47, 50, 51) the absence, even at 850°C, of a continuous scale. Those features, if compared within the figures 52 and 53, suggest that the overlay coating had less protection.

Fig. 52 ESEM pictures of CMSX-4/CN91 systems
Fig. 53 ESEM pictures of CMSX-4/RT22 systems.
Fig. 54 ESEM pictures of CMSX-4/”LCO22” systems.

EDX analysis performed on RT22

Figure 55 represents an example of the results of the EDX analysis performed on RT22 coated CMSX-4 tested for 2000 hours at 950°C.

The following scale features have been observed:

- outer oxide layer: composed of mixed oxide such as TiO_2 and Ta_2O_5 (the brightest grains), Al_2O_3, Cr_2O_3 likely along with spinels (e.g. $NiAl_2O_4$, $CoAl_2O_4$, $CoCr_2O_4$);
- inner oxide layer: composed of Al_2O_3.

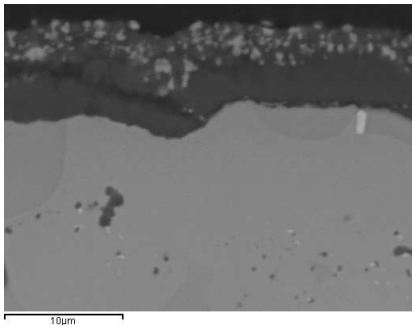

10 µm

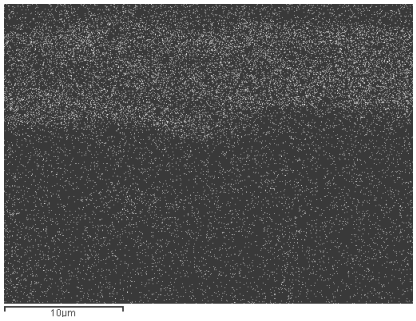

Oxygen

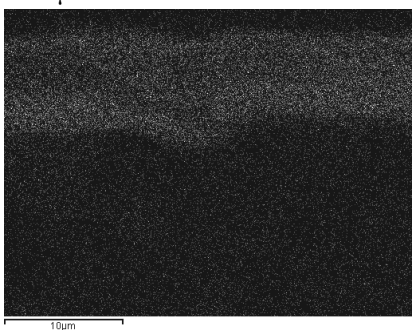

Aluminium

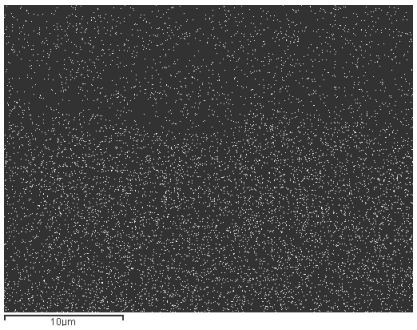

Cobolt

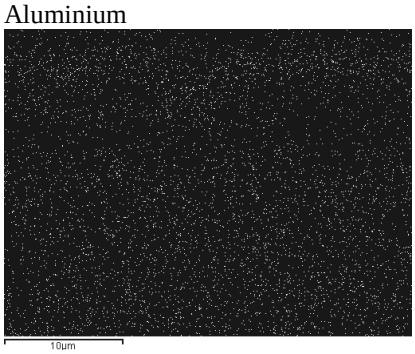

Titanium

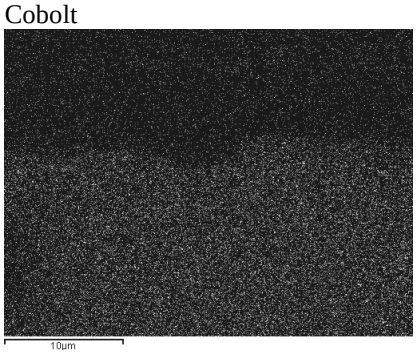

Nickel

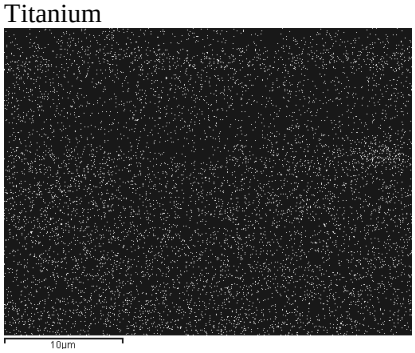

Chromium

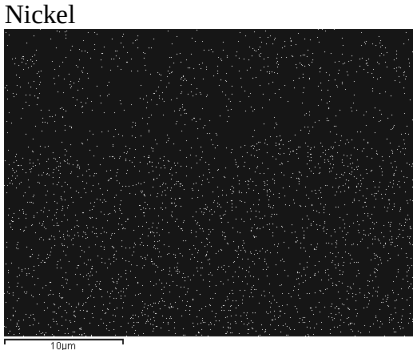

Platinum

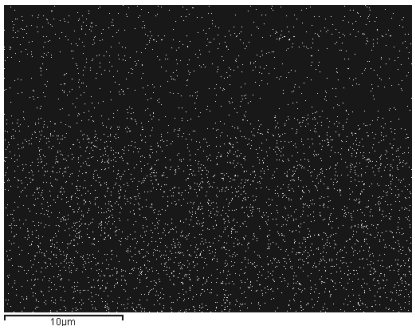

Tungsten

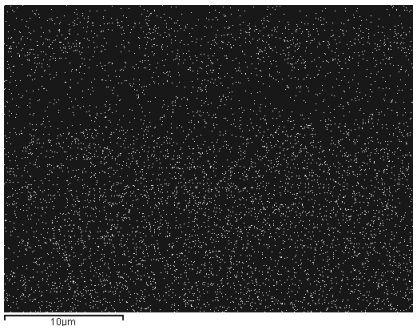

Tantalum

Fig. 55 EDX analysis on CMSX-4/RT22 tested 2000 hours at 950°C.

3.1.3 Scale thickness measurements

In this section three series of probability plots (Fig.56-70), one for each material system, are given. These show the trend of TGO thickness as a function of its probability of not being exceeded. Once the oxide thickness has been measured, as described in section 2.2.4, the 24 data points, according the method of data analysis proposed by Nicholls et al. [71], are ordered and the cumulative distribution function created considering:

$$P(x_i) = \frac{No.\ of\ \ Obseravtions < x_i}{n+1} \tag{19}$$

The probability plots provide useful information about the scale, for example: maximum thickness of the oxide, probability of having a substrate not protected anymore after a period of time, distribution of the damage, when a non linear transformation of the probability plot is carried out [71].

The results obtained by the statistical analysis are considered in chapter 4.

CMSX-4/CN91

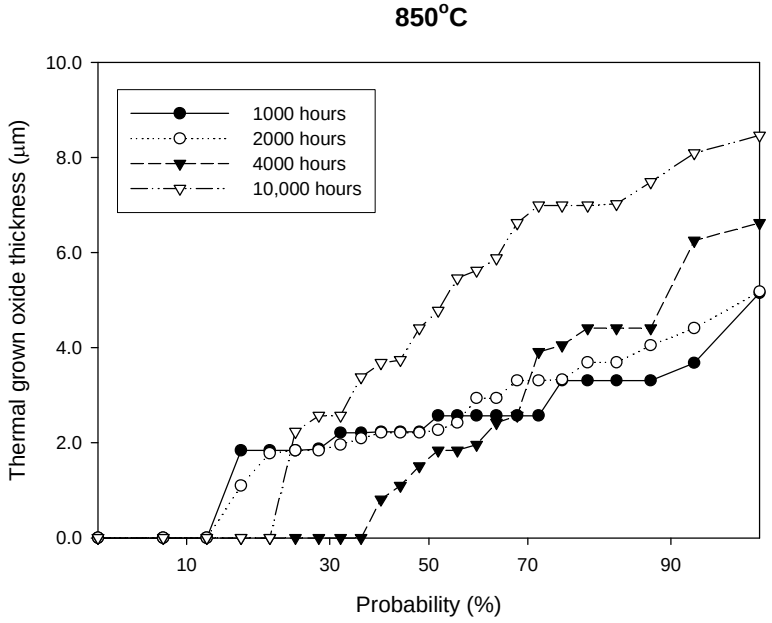

Fig. 56 CMSX-4/CN91 system : TGO thickness vs probability plot, 850°C.

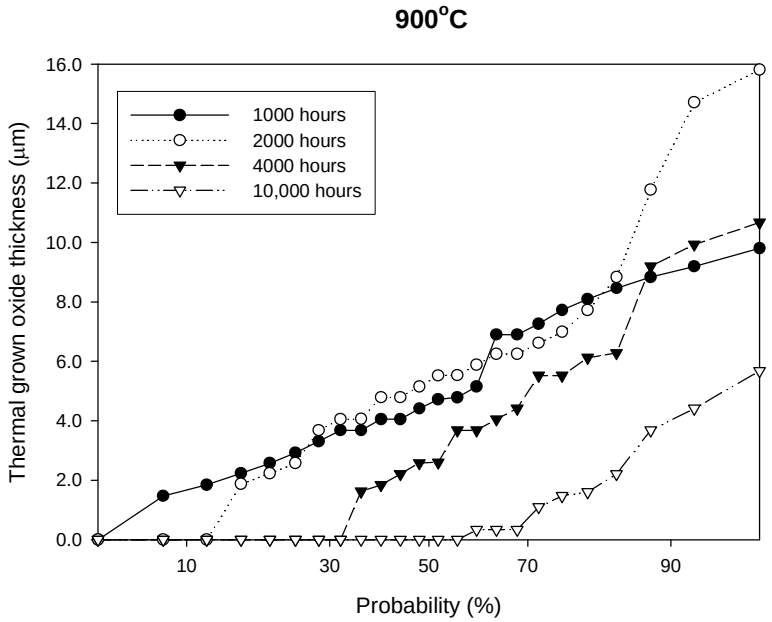

Fig. 57 CMSX-4/CN91 system : TGO thickness vs probability plot, 900°C.

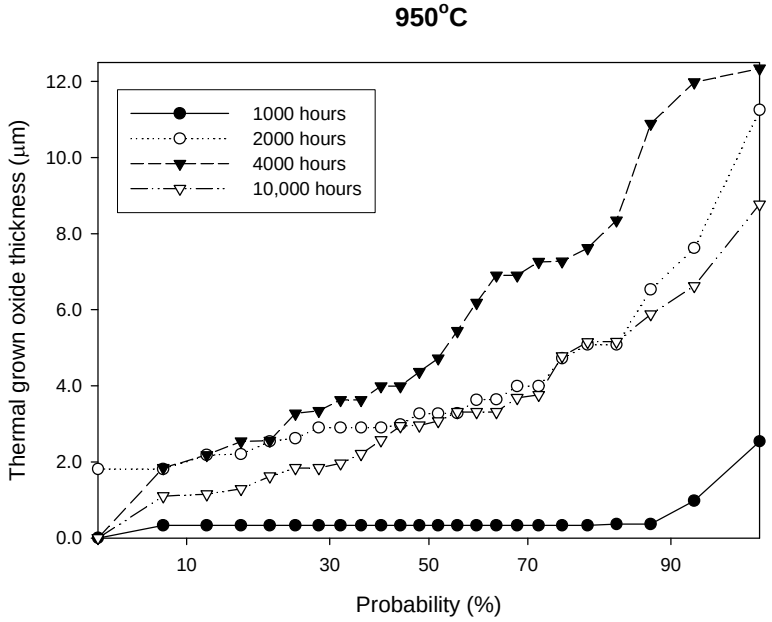

Fig. 58 CMSX-4/CN91 system : TGO thickness vs probability plot, 950°C.

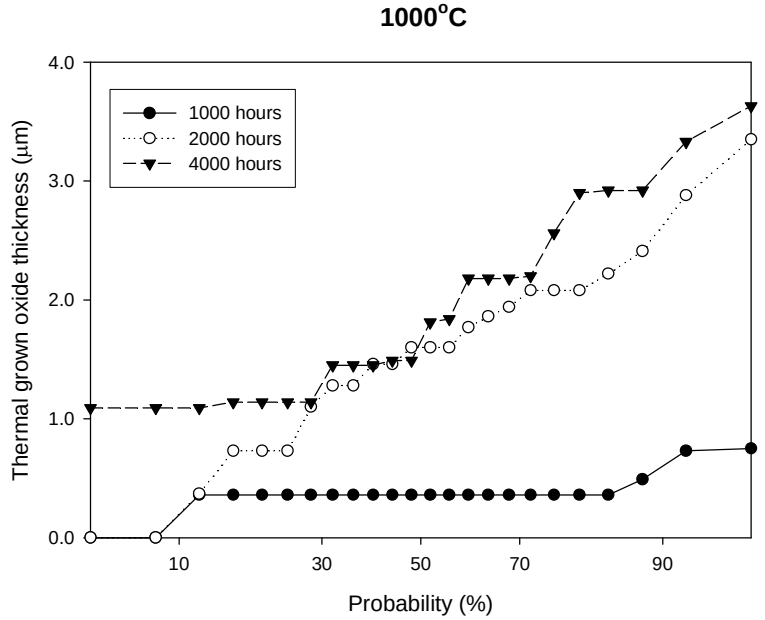

Fig. 59 CMSX-4/CN91 system : TGO thickness vs probability plot, 1000°C.

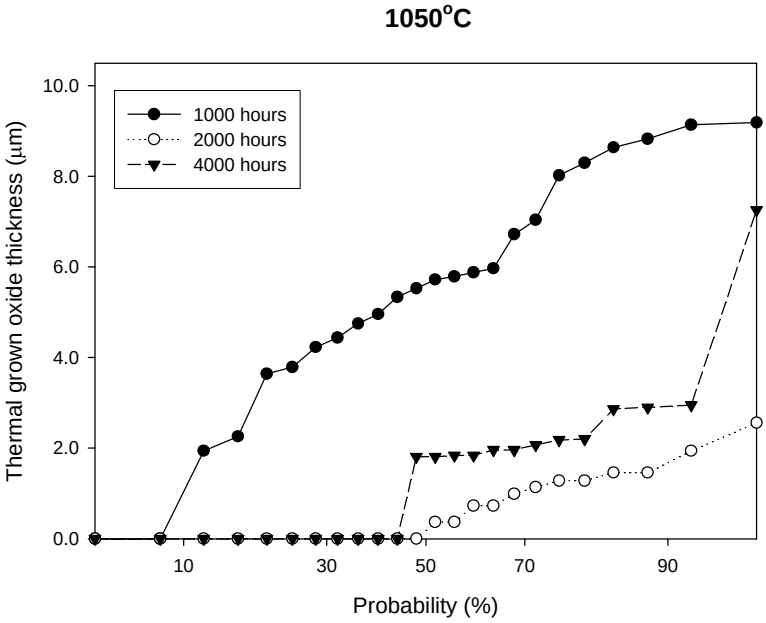

Fig. 60 CMSX-4/CN91 system : TGO thickness vs probability plot, 1050°C.

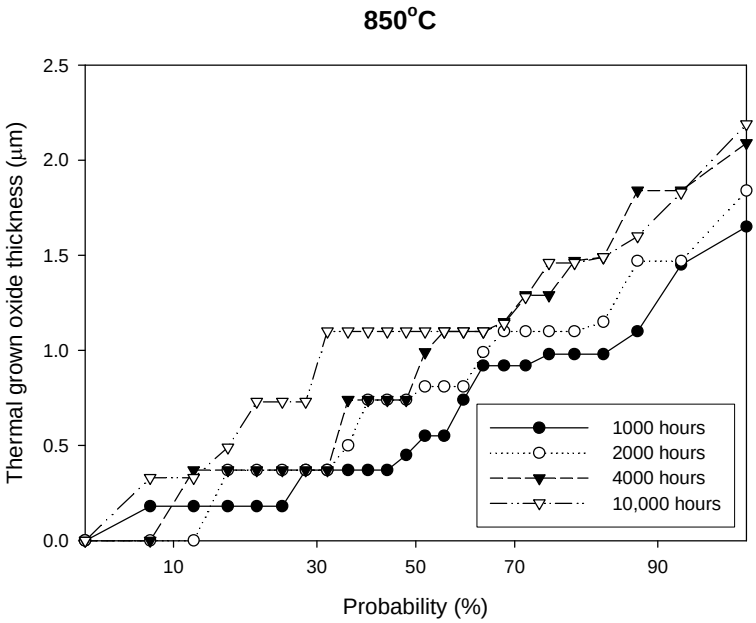

Fig. 61 CMSX-4/RT22 system: TGO thickness vs probability plot, 850°C.

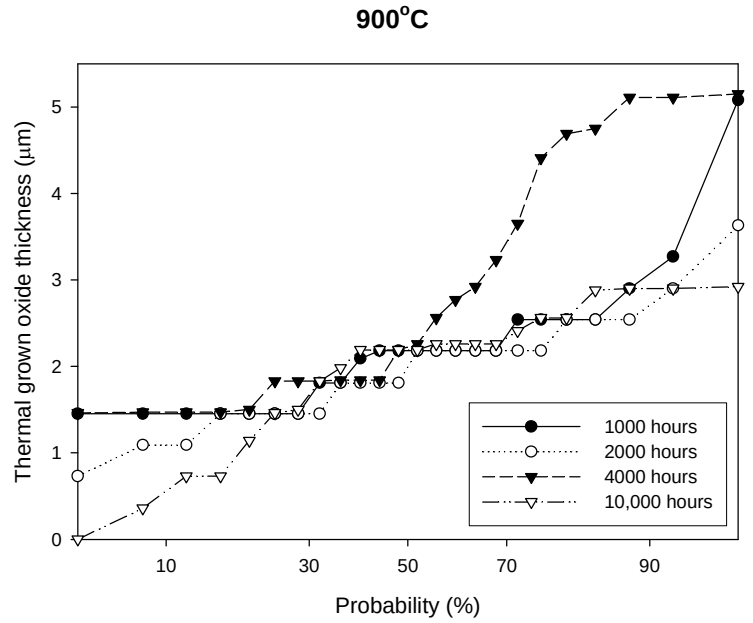

Fig. 62 CMSX-4/RT22 system: TGO thickness vs probability plot, 900°C.

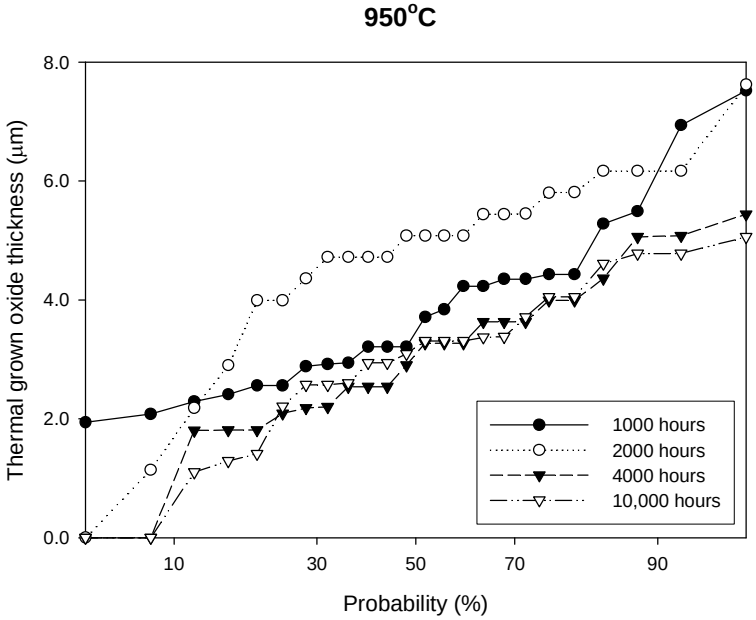

Fig. 63 CMSX-4/RT22 system : TGO thickness vs probability plot, 950°C.

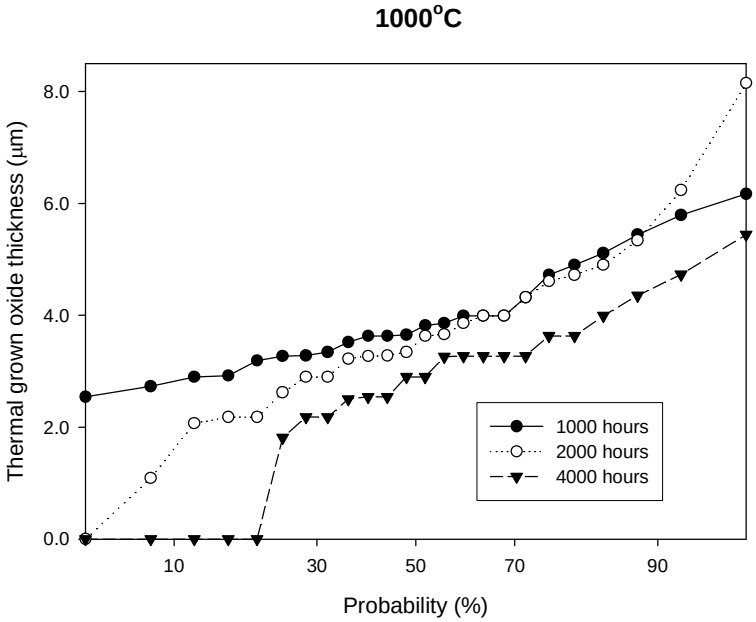

Fig. 64 CMSX-4/RT22 system : TGO thickness vs probability plot, 1000°C.

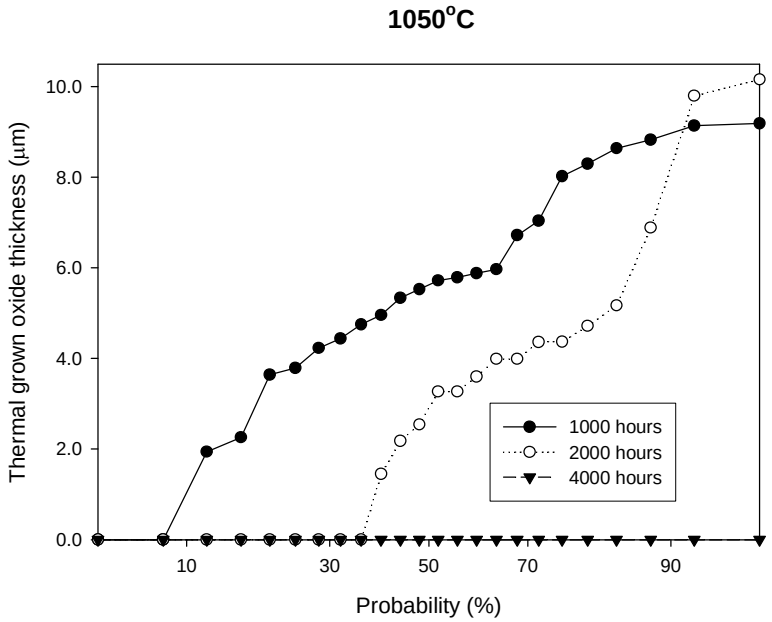

Fig. 65 CMSX-4/RT22 system: TGO thickness vs probability plot, 1050°C.

CMSX-4/”LCO22” system

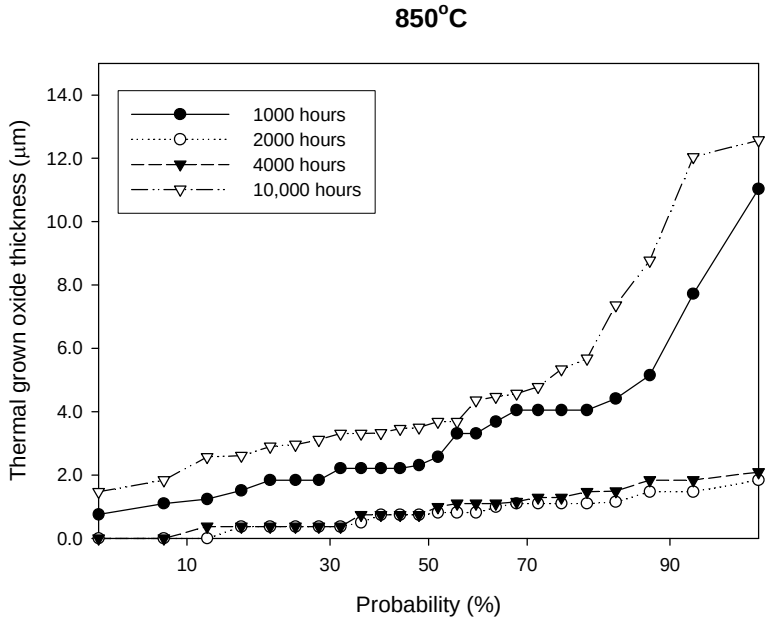

Fig. 66 CMSX-4/”LCO22” system: TGO thickness vs probability plot, 850°C.

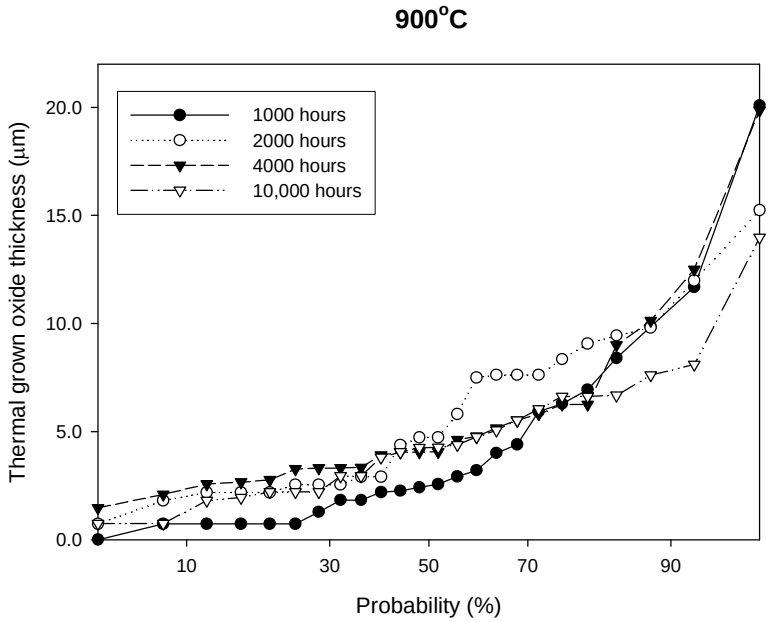

Fig. 67 CMSX-4/"LCO22" system: TGO thickness vs probability plot, 900°C.

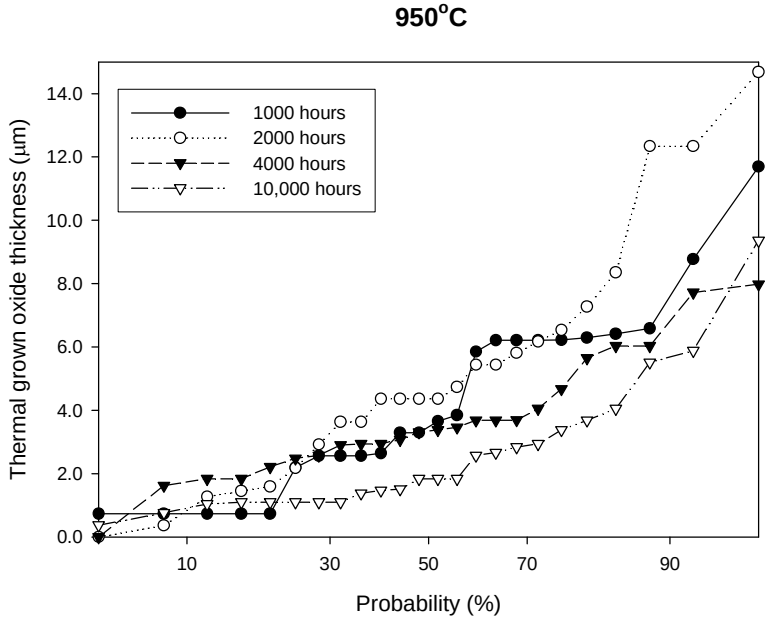

Fig. 68 CMSX-4/"LCO22" system: TGO thickness vs probability plot, 950°C.

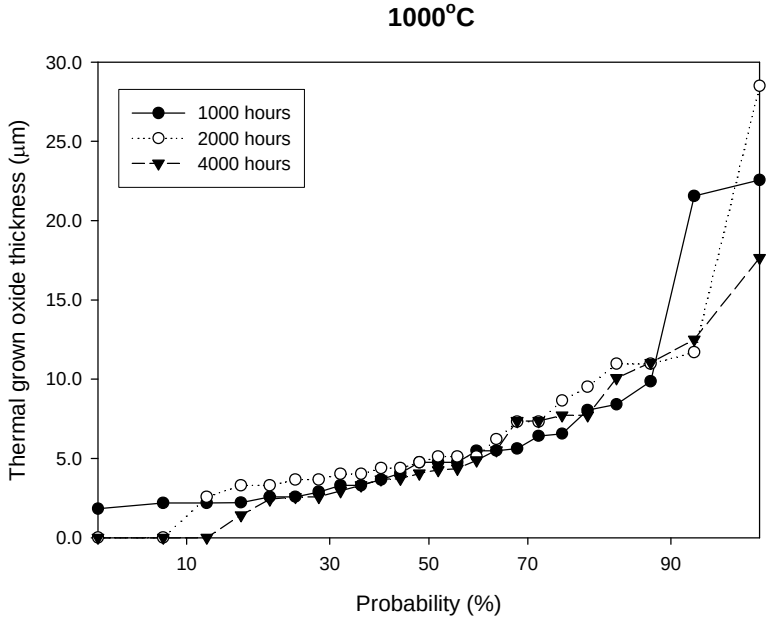

Fig. 69 CMSX-4/"LCO22" system: TGO thickness vs probability plot, 1000°C.

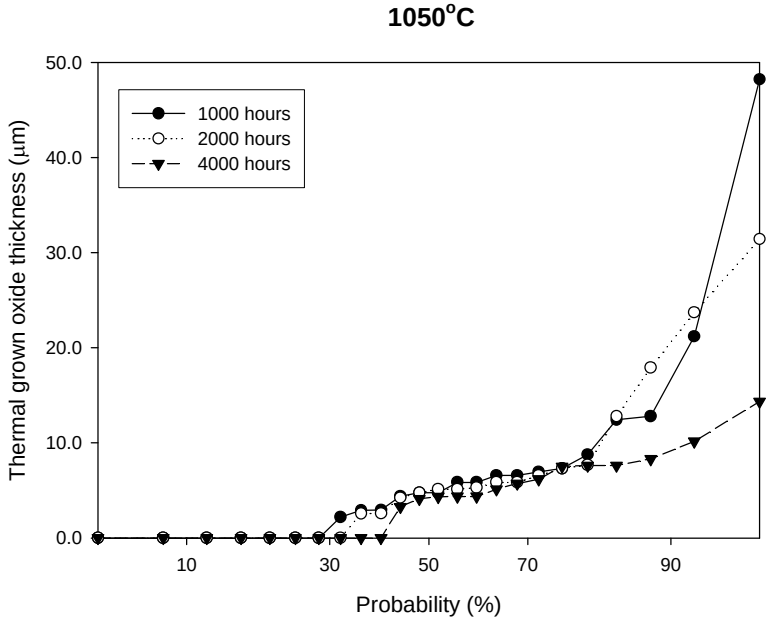

Fig. 70 CMSX-4/"LCO22" system: TGO thickness vs probability plot, 1050°C.

3.1.4 Modelling

It has been mentioned that some of the experimental data have been produced for modelling purpose. This stage of the study has dealt with the use of mass change data in order to:

- compare observations to simulations, these last obtained by using a model developed by Nigel S., not published yet and describing alumina scale growth at high temperature ;
- calculate rate constant vales for improving the model.

Since modelling has required to consider and compare data to information, not produced directly with this study, this activity has been described in the following chapter (§ 4.1.4).

3.2 Corrosion

3.2.1 Kinetics of corrosion

The second part of this work has dealt with the study of the protection performed by the three different coatings, CN91, RT22 and “LCO22”, deposited on the superalloy CMSX-4, in different conditions of corrosive environment (described in section 2.2.2).

MASS CHANGE PLOTS

This section presents the results of the corrosion tests by mass change plots.

As already mentioned in section 1.4.2 and 3.1.1 these plots provide basic data about the rate of material consumption and in addition to the results obtained by the means of optical and electronic microscopy they are used for estimating the materials useful life in service conditions.

The following mass change plots analyse the effect of different deposit fluxes, temperatures and materials on the kinetics of degradation. These effects of hot corrosion are larger than those of oxidation alone.

Deposit flux effect at 700°C

The main feature coming from the mass change plots is increasing damage with increasing deposit flux.

The uncoated CMSX-4 specimen has exhibited spallation with the lowest deposit flux. As a result of this phenomenon these samples have a little increase in weight for 1.5 µg/(cm^{2}h), while it became extremely important for 5 µg/(cm^{2}h) (Fig.71).

On RT22 coated samples the corrosion has determined a moderate increase of mass gain from 0.5 µg/(cm^{2}h) to 1.5 µg/(cm^{2}h), while much more mass gain has been observed for the highest deposit flux (Fig.72). The other Pt-aluminide, CN91 (Fig.73) coating behaved similarly for the lowest and highest value of deposit, whilst higher mass gain has resulted from an intermediate flux.

The system CMSX-4/”LCO22” (Fig. 74) shows an increase in mass gain for 0.5 µg/(cm^{2}h), while the spallation occurred for the other two deposit fluxes with the largest effect from 5 µg/(cm^{2}h).

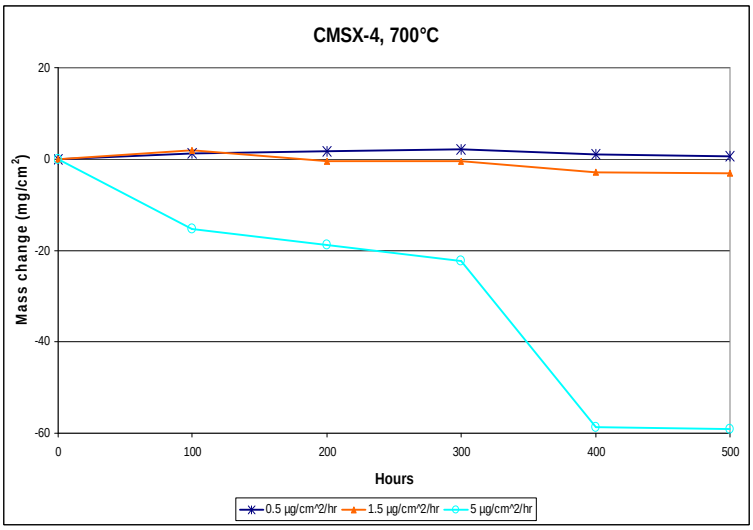

Fig. 71 Comparison of deposit fluxes, in 300 vpm SO_2, at 700°C on uncoated CMSX-4.

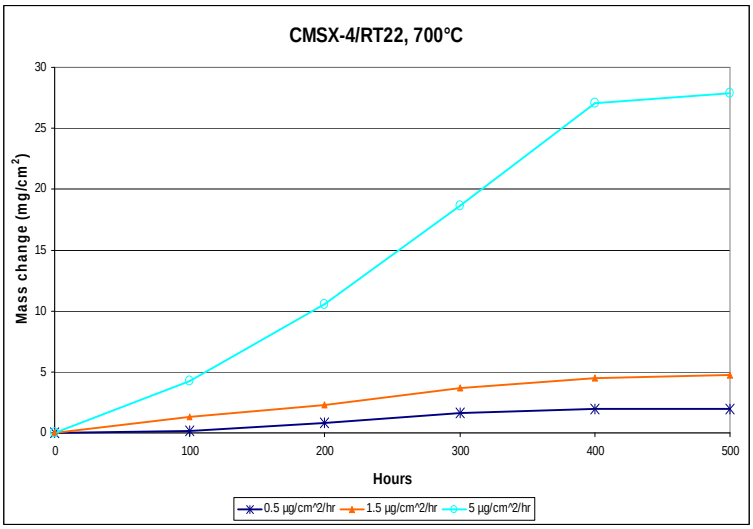

Fig. 72 Comparison of deposit fluxes, in 300 vpm SO_2, at 700°C on CMSX-4/RT22.

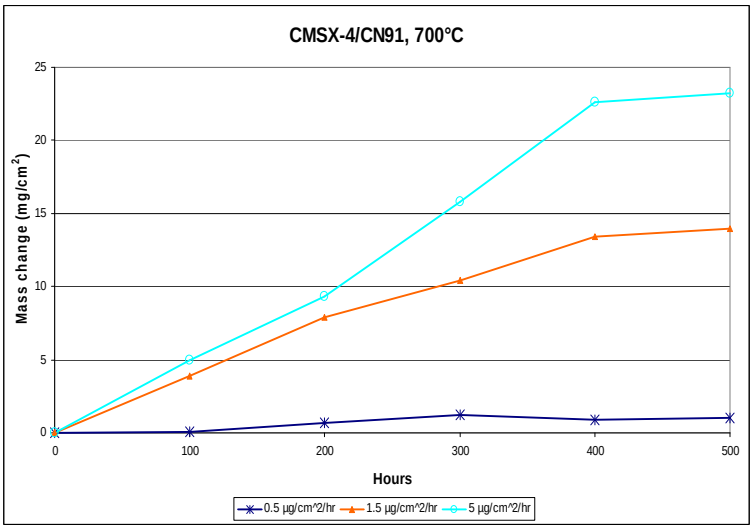

Fig. 73 Comparison of deposit fluxes, in 300 vpm SO_2, at 700°C on CMSX-4/CN91.

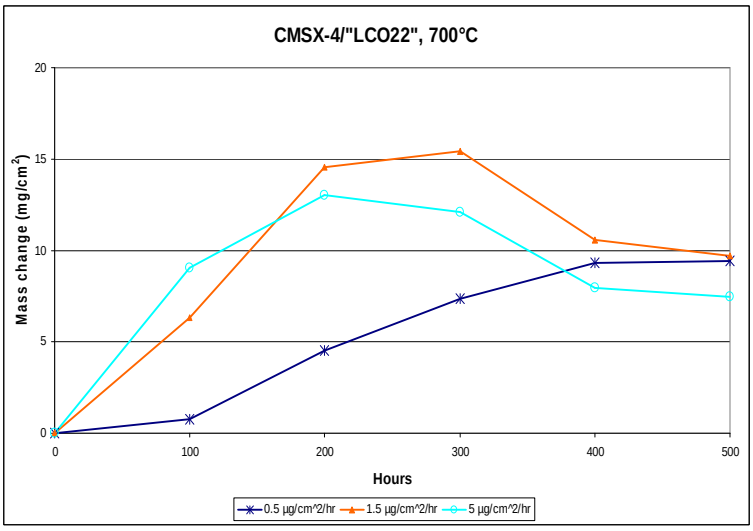

Fig. 74 Comparison of deposit fluxes, in 300 vpm SO_2, at 700°C on CMSX-4/"LCO22".

Deposit flux effect at 900°C

As equally noted for the previous temperature (700°C), at 900°C the corrosion damage, measured as mass change, markedly increases when raising the deposit flux from 0.5 to 5 µg/(cm^2h) (Fig.75-78). Generally, it has been observed that while the degree of damage caused by the lowest and intermediate flux doesn't differ much, the highest deposit flux has caused much greater degradation (except for the overlay coated system).

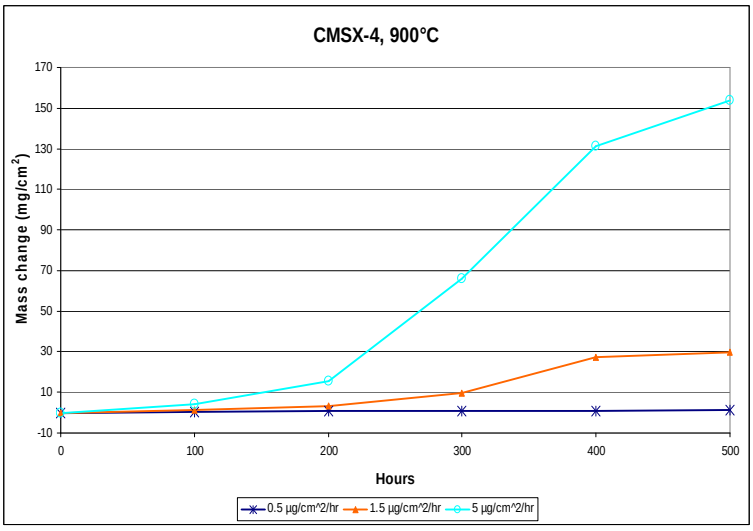

Fig. 75 Comparison of deposit fluxes, in 300 vpm SO_2, at 900°C on CMSX-4.

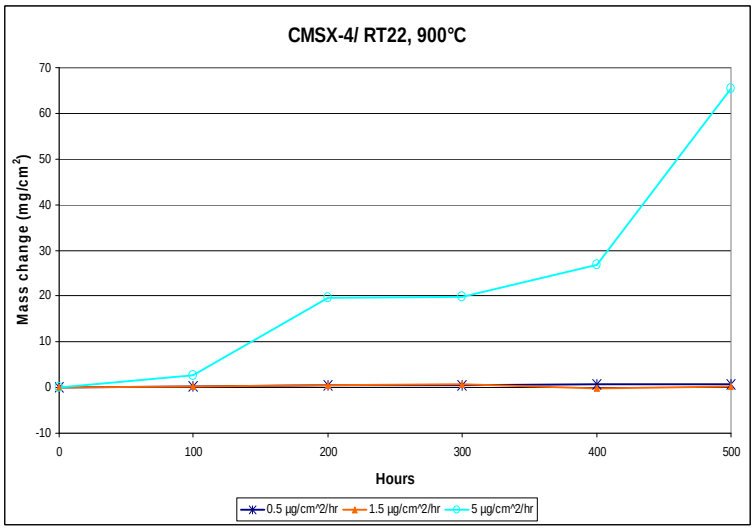

Fig. 76 Comparison of deposit fluxes, in 300 vpm SO_2, at 900°C on CMSX-4/RT22.

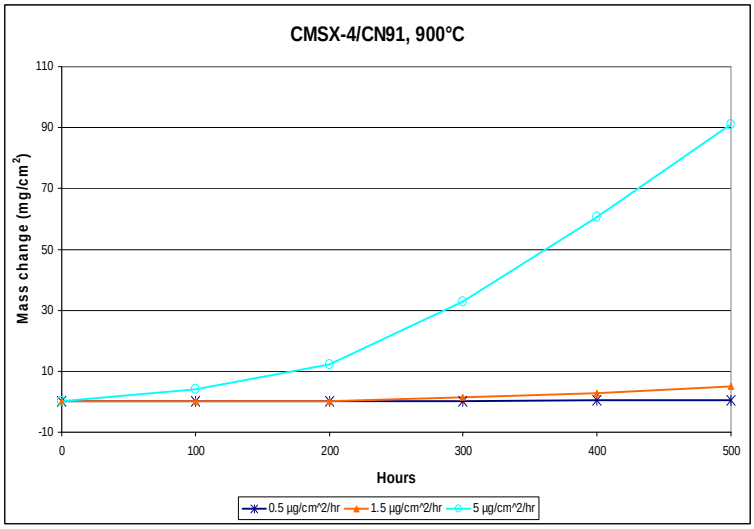

Fig. 77 Comparison of deposit fluxes, in 300 vpm SO_2, at 900°C on CMSX-4/CN91.

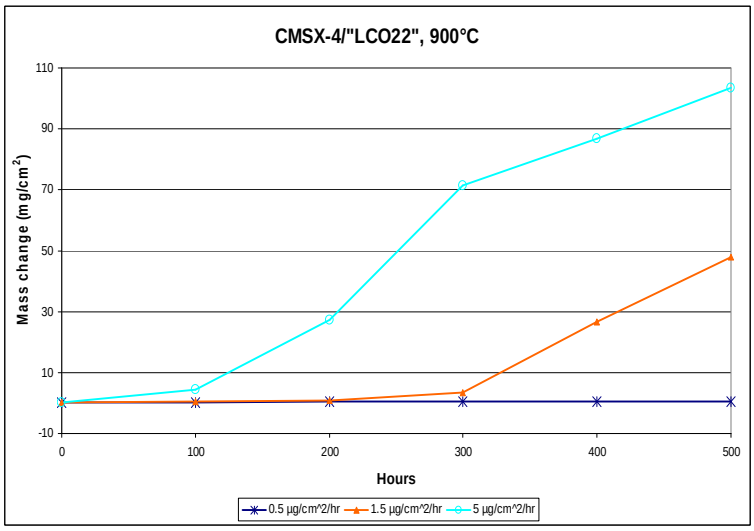

Fig. 78 Comparison of deposit fluxes, in 300 vpm SO_2, at 900°C on CMSX-4/"LCO22".

Temperature effect

On uncoated CMSX-4 the corrosion with mid and highest deposit flux has mainly caused mass gain at 900°C, whilst scale/deposit detachment has prevailed at 700°C. In case of 0.5 µg/(cm^{2}h) of deposit flux, the plot shows the same resistance at both the temperatures (Fig.79) .

Pt-aluminides have been observed having less mass change at 900°C for intermediate deposit flux, less mass change at 700°C with the highest deposit flux and almost equal mass change with the lowest deposit flux (Fig.80-81) .

"LCO22" coated CMSX-4 has been shown to have had much less mass change at 700°C with 1.5 µg/(cm^{2}h) and 5 µg/(cm^{2}h) and little higher mass change with 0.5 µg/(cm^{2}h) (Fig.82).

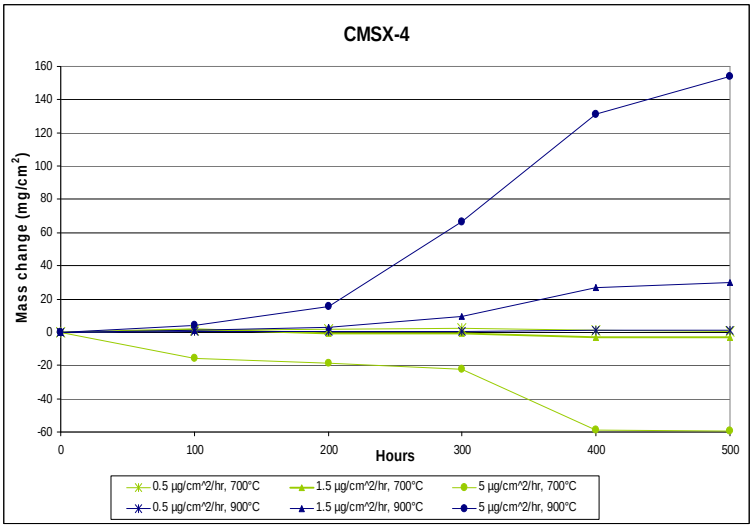

Fig. 79 Comparison of temperatures, in 300 vpm SO_2, on CMSX-4.

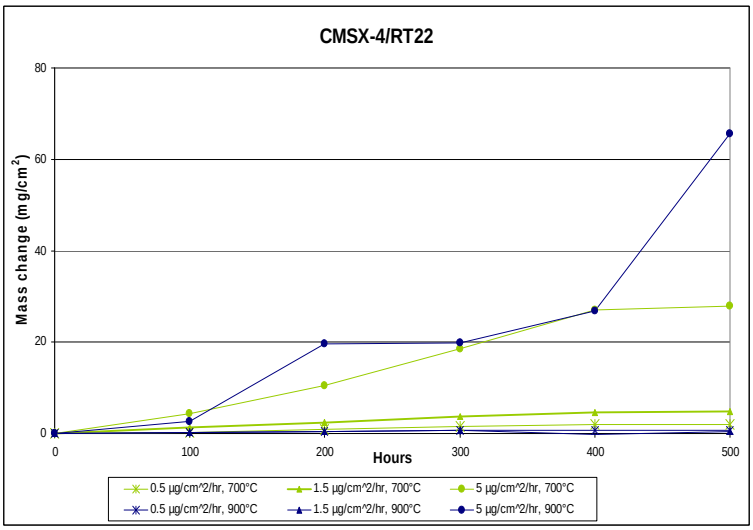

Fig. 80 Comparison of temperatures, in 300 vpm SO_2, on CMSX-4/RT22.

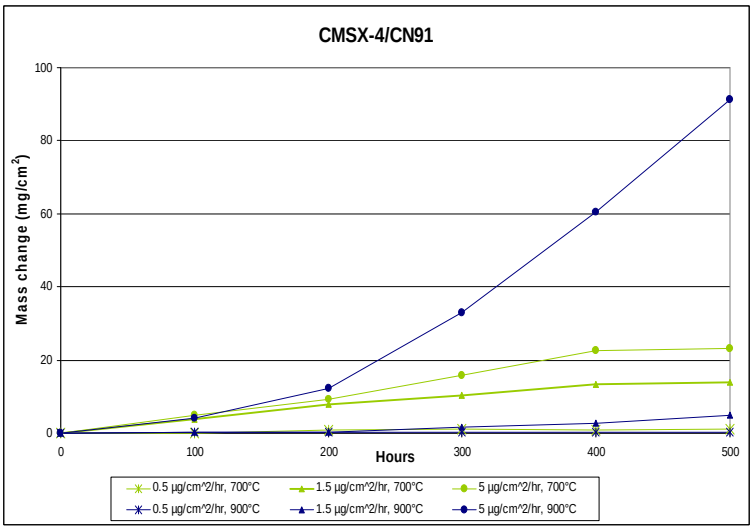

Fig. 81 Comparison of temperatures, in 300 vpm SO_2, on CMSX-4/CN91.

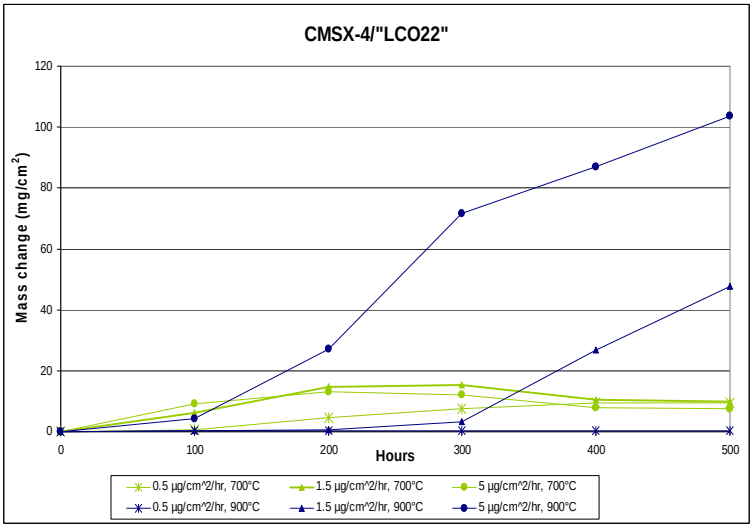

Fig. 82 Comparison of temperatures, in 300 vpm SO_2, on CMSX-4/"LCO22".

Gas composition effect at 700°C

The following plots (Fig. 83-86) illustrate the effect of adding 100 vpm of HCl to 300 vpm of SO_2, at 700°C.

Generally, it has been observed that HCl has a neutral effect at the lowest deposit flux. At intermediate flux the HCl gave rise to less mass change on the bare alloy and RT22 coated specimens. For the highest deposit flux, the plots show that the presence of HCl might promote more mass gain than spallation.

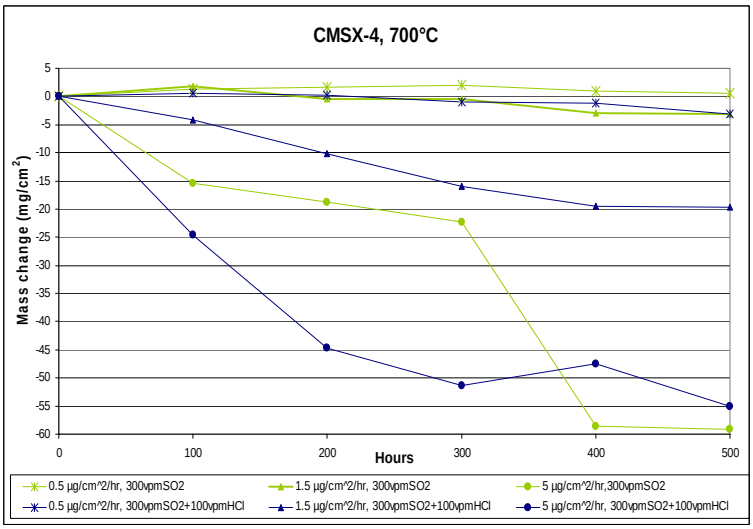

Fig. 83 Comparison of atmosphere compositions, at 700°C on CMSX-4.

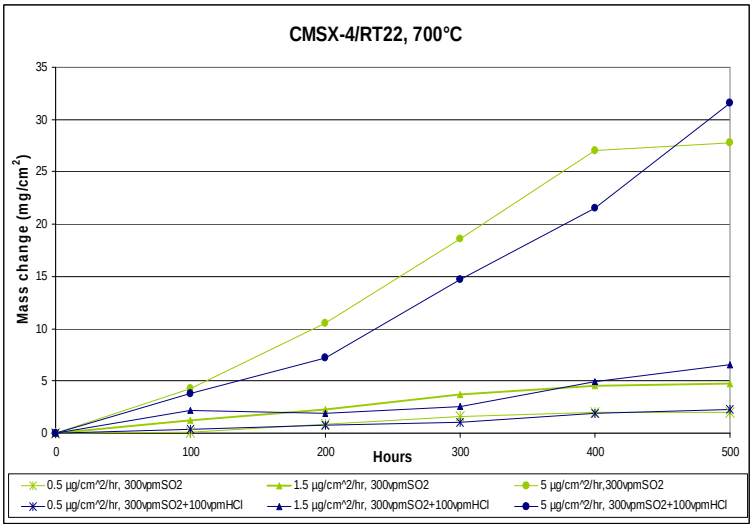

Fig. 84 Comparison of atmosphere compositions, at 700°C on CMSX-4/RT22.

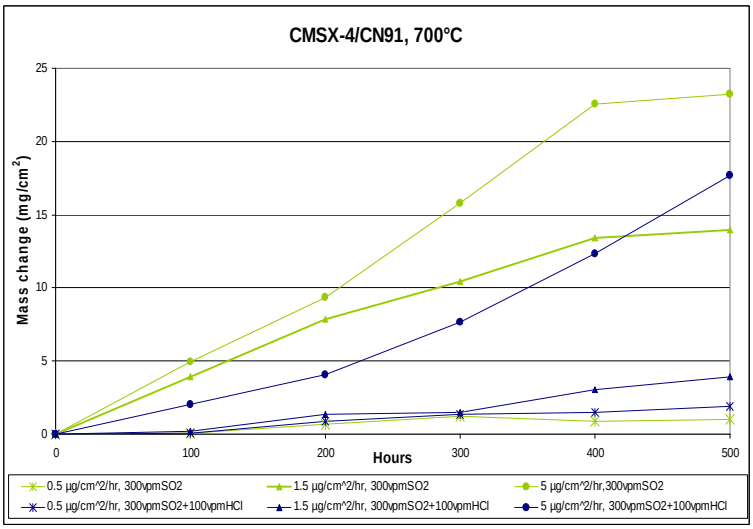

Fig. 85 Comparison of atmosphere compositions, at 700°C on CMSX-4/CN91.

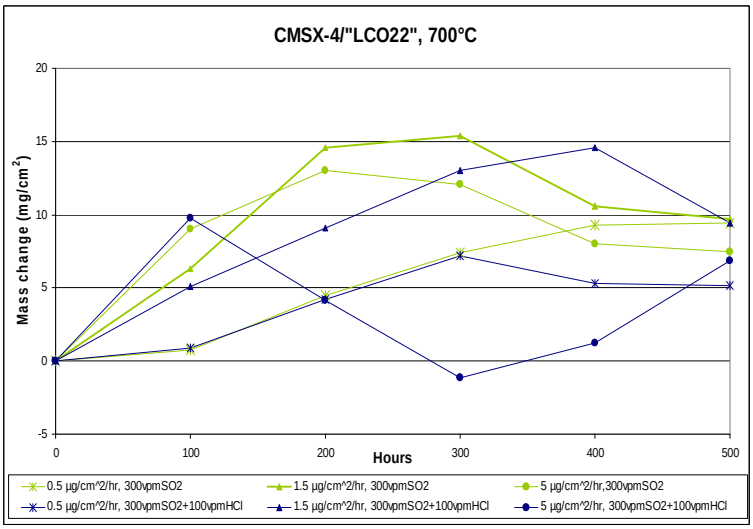

Fig. 86 Comparison of atmosphere compositions, at 700°C on CMSX-4/"LCO22".

Gas composition effect at 900°C

The following plots (Fig. 87-90) illustrate the effect of adding 100 vpm of HCl to 300 vpm of SO_2, at 900°C.

Firstly, figure 87 illustrates the effect on the uncoated CMSX-4 of adding 100 vpm HCl to the atmosphere, for various salt deposition levels. At deposition flux of 5 µg/(cm^{2}h) in an air-300vpm SO_2 environment, the incubation ends at approximately 200 hours and afterward the propagation phase begins. Adding 100 vpm HCl to this environment the incubation time has been extended and it reduced the rate of propagation attack.

At 1.5 µg/(cm^{2}h) in an air-300vpm SO_2, the rate of attack is reduced to values similar to 5 µg/(cm^{2}h) when exposed in SO_2+HCl rich atmosphere. As the salt fluxes are further reduced the rates of attack proportionally decrease for both the environment compositions tested.

For the Pt-aluminide samples, figures 88 and 89, the worst attack is for the 5 µg/(cm^{2}h) salt flux and air-300vpm SO_2. In an air-300vpm SO_2+100vpm HCl environment the level of attack is significantly reduced. Reducing the salt flux increases the incubation time to 300-500 hours, so that a very low level of attack was observed at 0.5 µg/(cm^{2}h).

"LCO22" coated CMSX-4, figure 90, followed similar trends to CMSX-4. The incubation time is reduced to about 100 hours for a salt flux of 5 µg/(cm^{2}h) in air-300vpm SO_2, and the mass gain at 500 hours is also reduced.

One has to question the results derived from 5 µg/(cm^{2}h) in air-300vpm SO_2+100vpm HCl. The sudden change over the first 100 hours is contrary to all other salt flux data seen in this phase of the study.

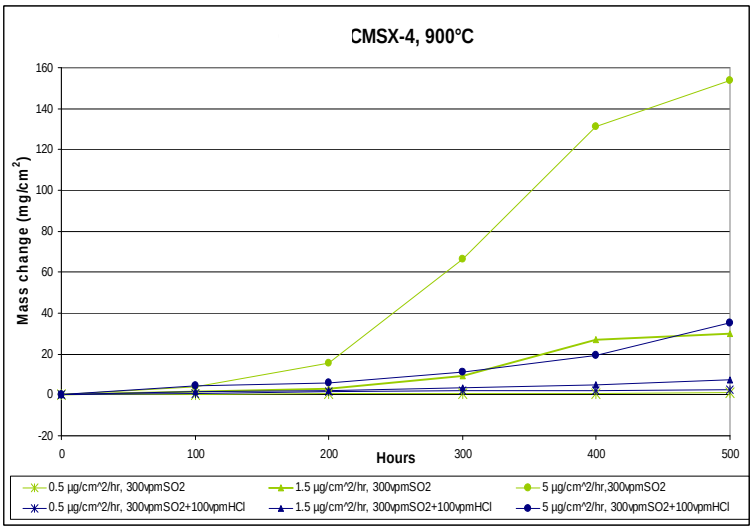

Fig. 87 Comparison of atmosphere compositions, at 900°C on CMSX-4.

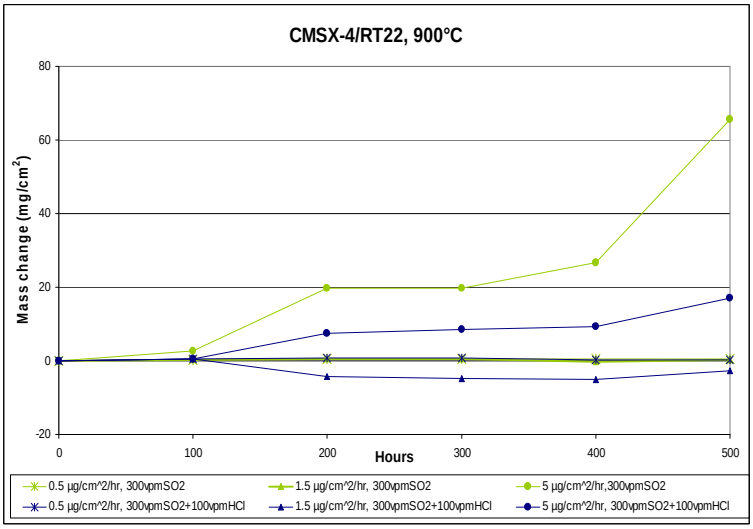

Fig. 88 Comparison of atmosphere compositions, at 900°C on CMSX-4/RT22.

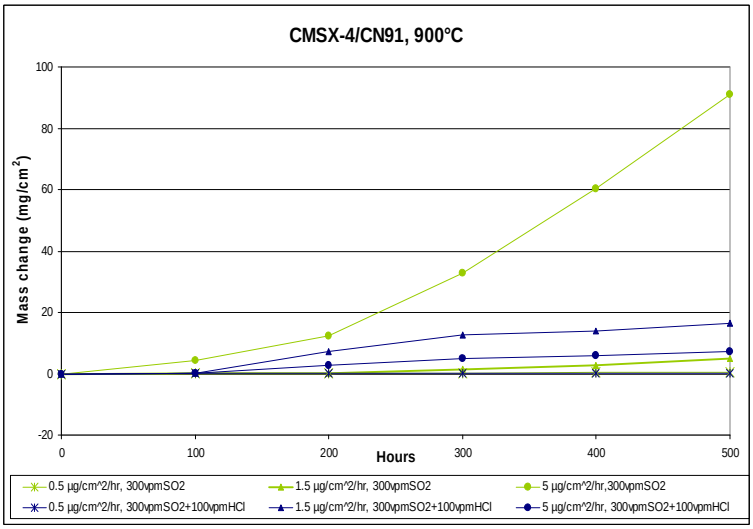

Fig. 89Comparison of atmosphere compositions, at 900°C on CMSX-4/"CN91".

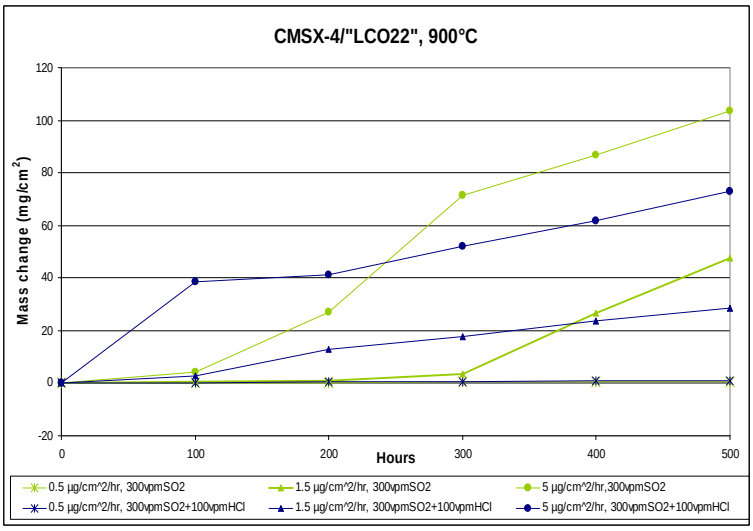

Fig. 90 Comparison of atmosphere compositions, at 900°C on CMSX-4/"LCO22".

Materials effect at 700°C in 300 vpm SO_2 atmosphere

The plots of figures 91, 92 and 93 compare for each deposit flux the protection provided by the three different coatings during the 500 hours exposure at 700°C.

At the lowest gas flux, the Pt-aluminide coatings performed best, especially RT22 since it doesn't experience the spalling that CN91 did (after 300 hours). At intermediate flux (Fig. 92) RT22 had the lowest mass change, which may denote better protective behaviour; "LCO22" has performed worst; its mass change trend shows both high mass gain and marked spalling. At the highest flux (Fig.93), both Pt-aluminide coatings behaved similarly, progressively gaining mass from the onset of the test. This behaviour was different from that observed for "LCO22". The superalloy experienced more mass gain than spalling over the first 200 hours, than mass lost due to scale spallation.

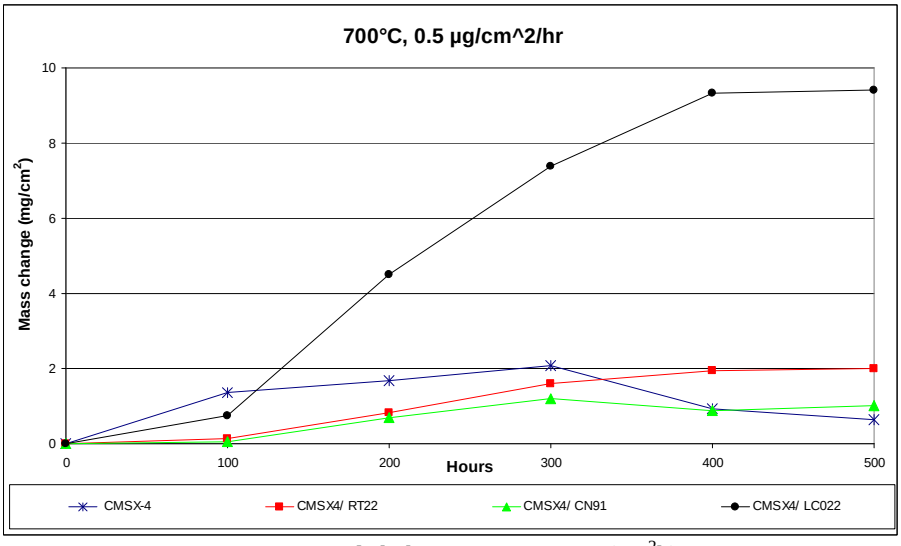

Fig. 91 Comparison among materials behaviours at 0.5 µg/(cm^2h), 700°C, 300 vpm SO_2.

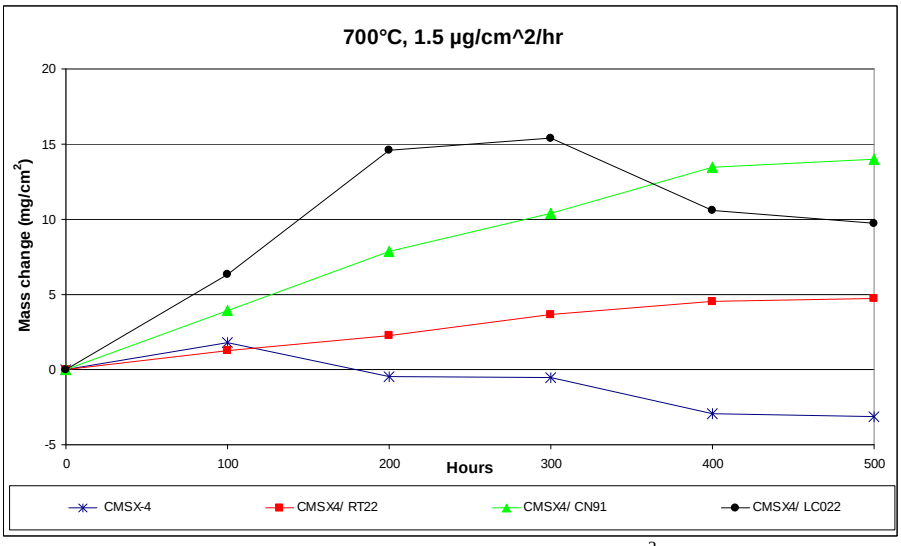

Fig. 92 Comparison among materials behaviours at 1.5 µg/(cm^{2}h), 700°*C*, 300 vpm SO_2.

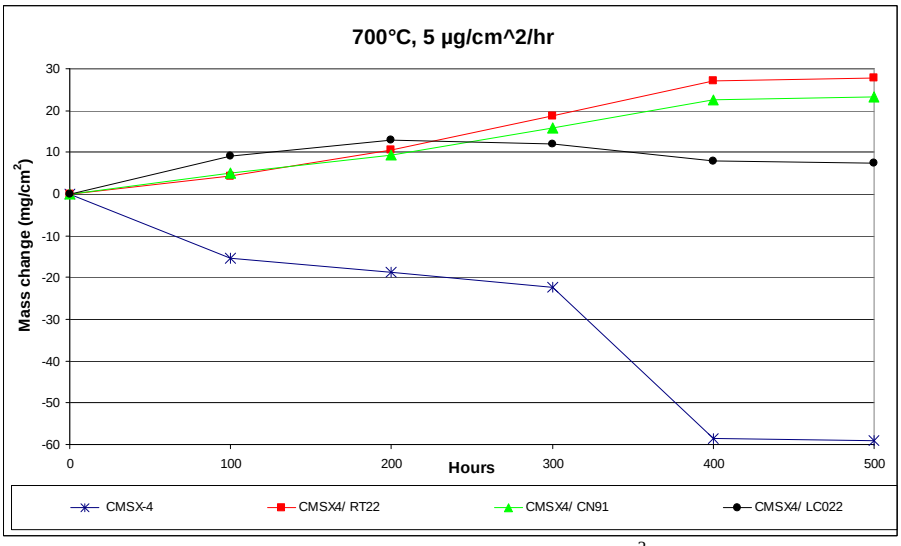

Fig. 93 Comparison among materials behaviours at 5 µg/(cm^{2}h), 700°*C*, 300 vpm SO_2.

Materials effect at 900°C in 300 vpm SO_2 atmosphere

The plots of figures 94, 95 and 96 compare for each deposit flux the protection provided by the three different coatings during the 500 hours exposure at 900°C.

At the lowest flux CN91 has been observed the less mass change, followed by “LCO22”. At intermediate flux RT22 experienced a little bit less mass change over the 500 hours, but the three coatings similarly behaved over the first 300 hours. Also at the highest deposit flux RT22 experienced less mass change, while “LCO22” has been observed with reduced protection after 400 hours.

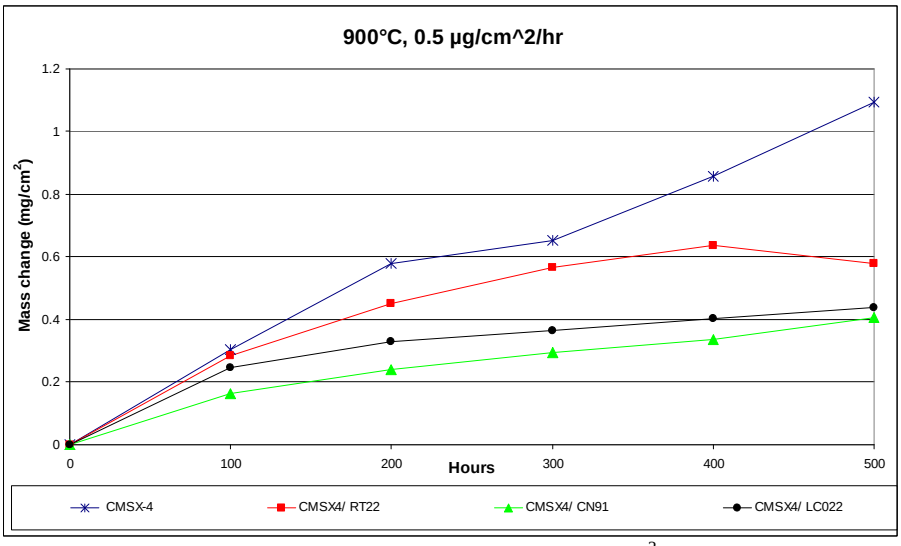

Fig. 94 Comparison among materials behaviours at 0.5 µg/(cm^{2}h), 900°*C*, 300 vpm SO_2.

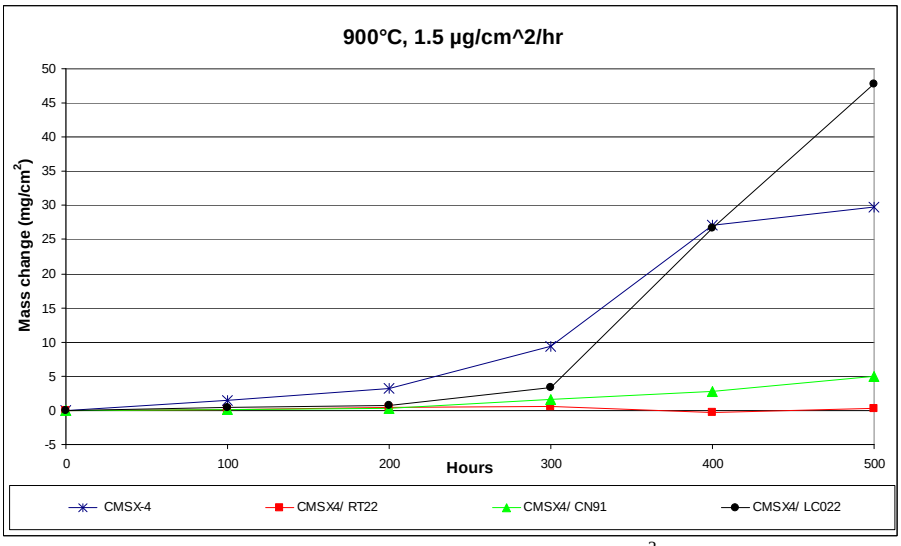

Fig. 95 Comparison among materials behaviours at 1.5 µg/(cm^{2}h), 900°*C*, 300 vpm SO_2.

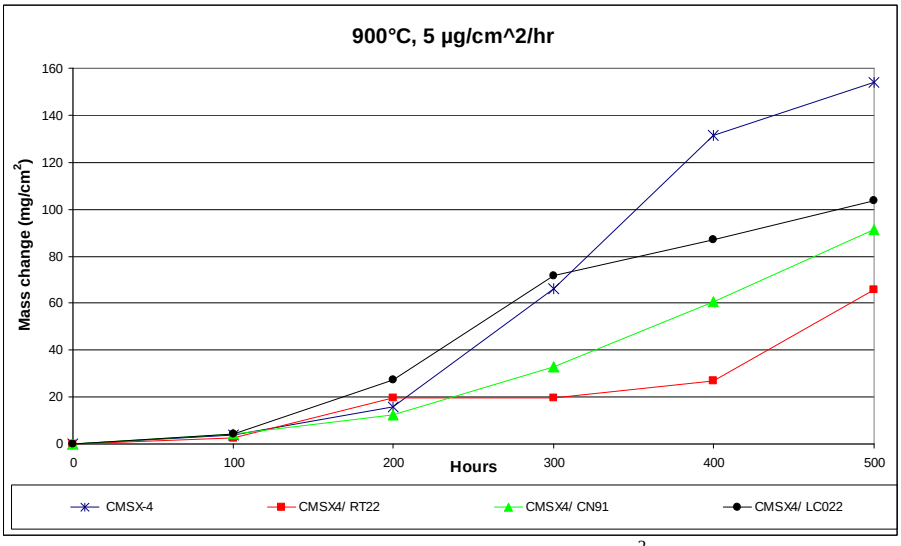

Fig. 96 Comparison among materials behaviours at 5 µg/(cm^{2}h), 900°*C*, 300 vpm SO_2.

Materials effect at 700°C in 300 vpm SO_2 and 100 vpm. HCl atmosphere

The plots of figures 97, 98 and 99 compare for each deposit flux the protection provided by the three different coatings during the 500 hours exposure at 700°C in HCl containing atmosphere.

These three figures show that Pt-aluminide coatings have the lowest mass gain and show no spallation. CN91 coated superalloy has a marginally lower mass gain than RT22/alloy. "LCO22" had the highest mass gain at the lowest and intermediate deposit flux and the highest spallation at the highest deposit flux. Spallation is also observed after 300 or 400 hours at these lower fluxes.

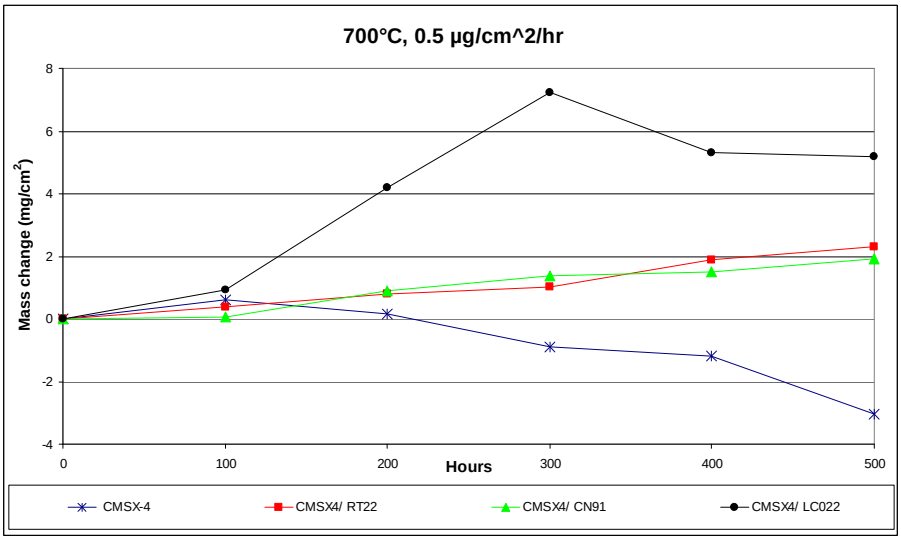

Fig. 97 Comparison among materials behaviours at 0.5 µg/(cm^2h), 700°*C*, 300 vpm SO_2 + 100vpm HCl.

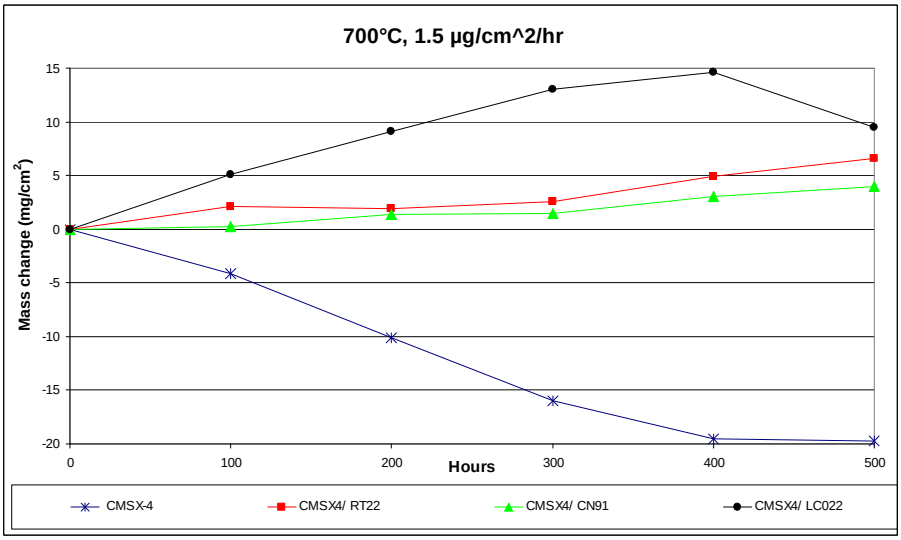

Fig. 98 Comparison among materials behaviours at 1.5 µg/(cm^2h), 700°*C*, 300 vpm SO_2 + 100vpm HCl.

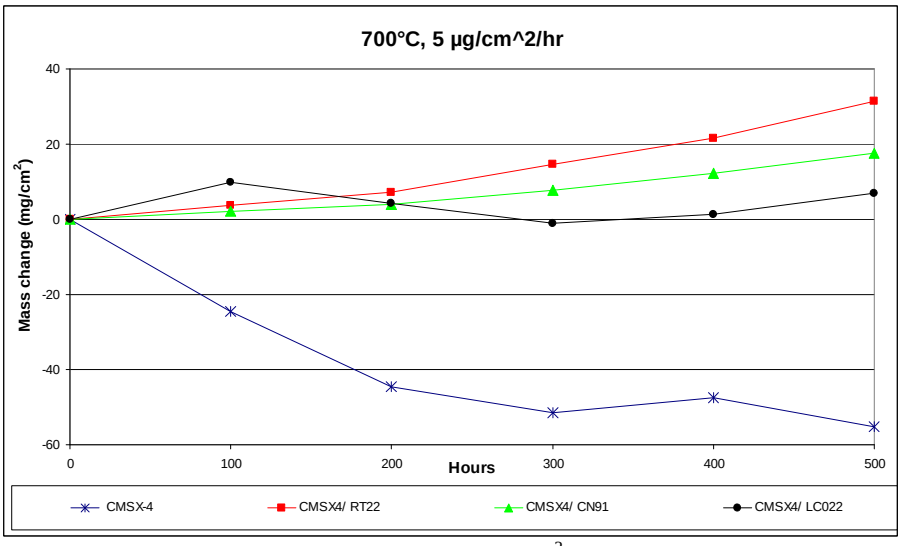

Fig. 99 Comparison among materials behaviours at 5 µg/(cm^{2}h), 700°*C*, 300 vpm SO_2 + 100vpm HCl.

Materials effect at 900°C in 300 vpm SO_2 and 100 vpm HCl atmosphere

The plots of figure 100, 101 and 102 compare for each deposit flux the protection provided by the three different coatings during the 500 hours exposure at 900°C in the HCl containing atmosphere.

At the lowest and intermediate gas flux CN91 and "LCO22" curves show nearly a parabolic increase of their mass, with less mass gain for the Pt-aluminide coating. Of the coatings RT22 experienced the highest mass change and spalling at the lowest flux and the heaviest spallation at the highest flux. At the highest deposit flux the Pt-aluminide coatings behaved similarly and they had much less mass gain than that shown by "LCO22" whose mass gain was greater than that observed for the uncoated alloy.

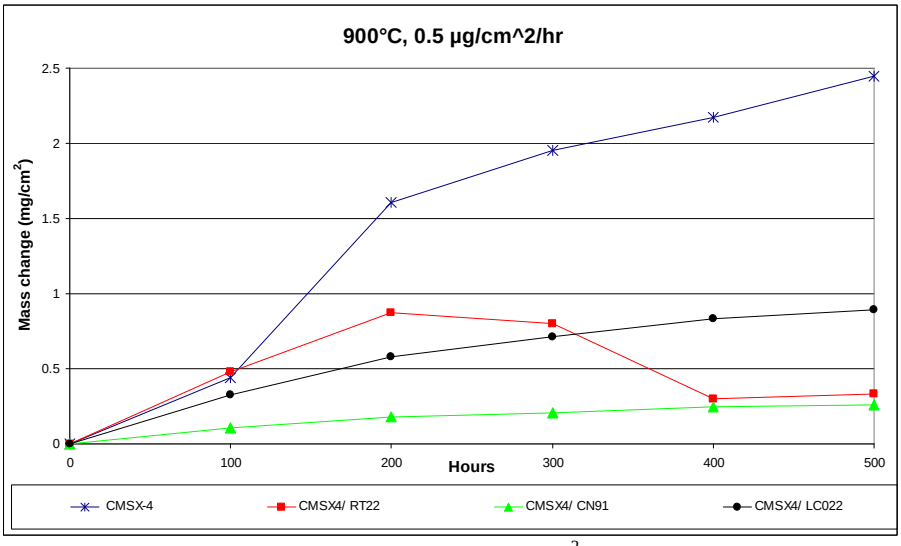

Fig. 100 Comparison among materials behaviours at 0.5 µg/(cm^{2}h), 900°*C*, 300 vpm SO_2 + 100vpm HCl.

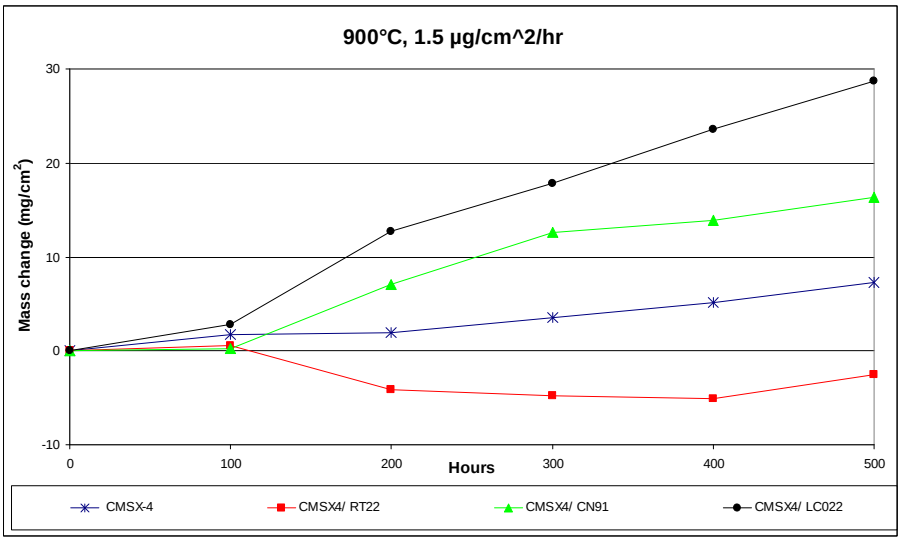

Fig. 101 Comparison among materials behaviours at 1.5 µg/(cm^{2}h), 900°*C*, 300 vpm SO_2 + 100vpm HCl.

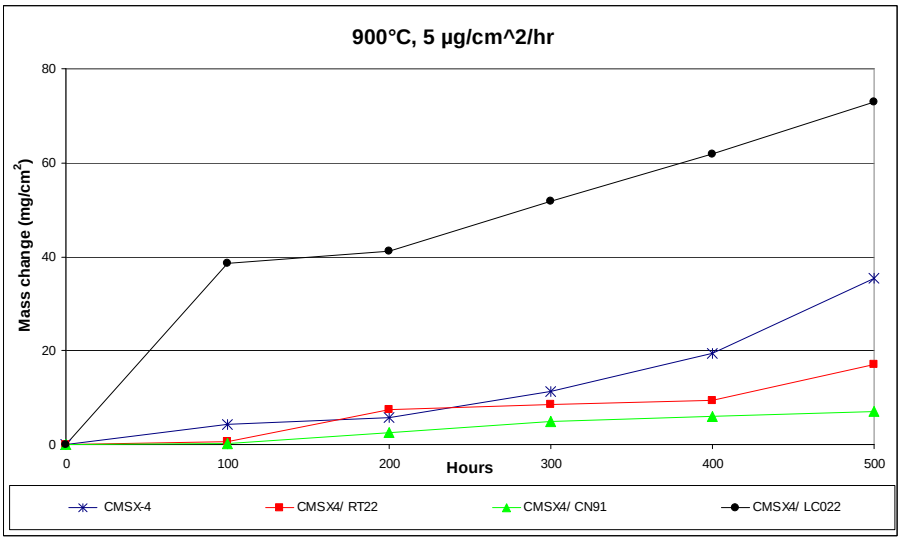

Fig. 102 Comparison among materials behaviours at 5 µg/(cm^{2}h), 900°*C*, 300 vpm SO_2 + 100vpm HCl.

3.2.2 Electron microscopy results

Corrosion morphology

The following pictures obtained by electron microscopy, illustrate the change in corrosion morphology with temperature, gas composition, deposit flux and materials composition.

700ºC, 300vpm SO_2

The result of the ESEM analysis, performed on samples exposed at 700°C and to 300 vpm SO_2 rich atmosphere, is summarised in figure 103, where in each row , moving toward the right, the 3 pictures illustrate the effect of increasing the salt deposit flux for the same material systems.

All four materials systems were shown to have higher damage increasing with the amount of salt deposited, defined either by more spallation or deeper pits.

Pictures of uncoated superalloy CMSX-4 show increasing spallation of the corrosion products layer with increasing deposit flux. The morphology of attack is characterized by a broad front of attack.

RT22 and CN91 coated samples show the typical Type II hot corrosion morphology, that is pitting in localized areas (§ 1.5.4); these pits become deeper with increasing aggressiveness of the environment (salt deposit flux).

For CN91, at the lower deposit flux, only few pits have been recorded, of which some are so deep as to extend beyond the IZ, while for RT22 coated samples a uniform distribution of pits with less depth around the circumference was apparent. There is more uniform corrosion damage to both CN91 and RT22 coated samples with a deposit flux of 1.5 µg/(cm^2h), with CN91more damaged, since the pits extend beyond the IZ, underlying that the front of attack has already entered the substrate, for this coating.

Pictures related to the “LCO22 “ coated specimens illustrate broad front attack, but also show that the coating has been completely depleted of ß-phase, even under the condition of lowest deposit flux. This was related to the original reduced thickness of the coating deposited on the specimen’s surface, which was about 20-30 µm.

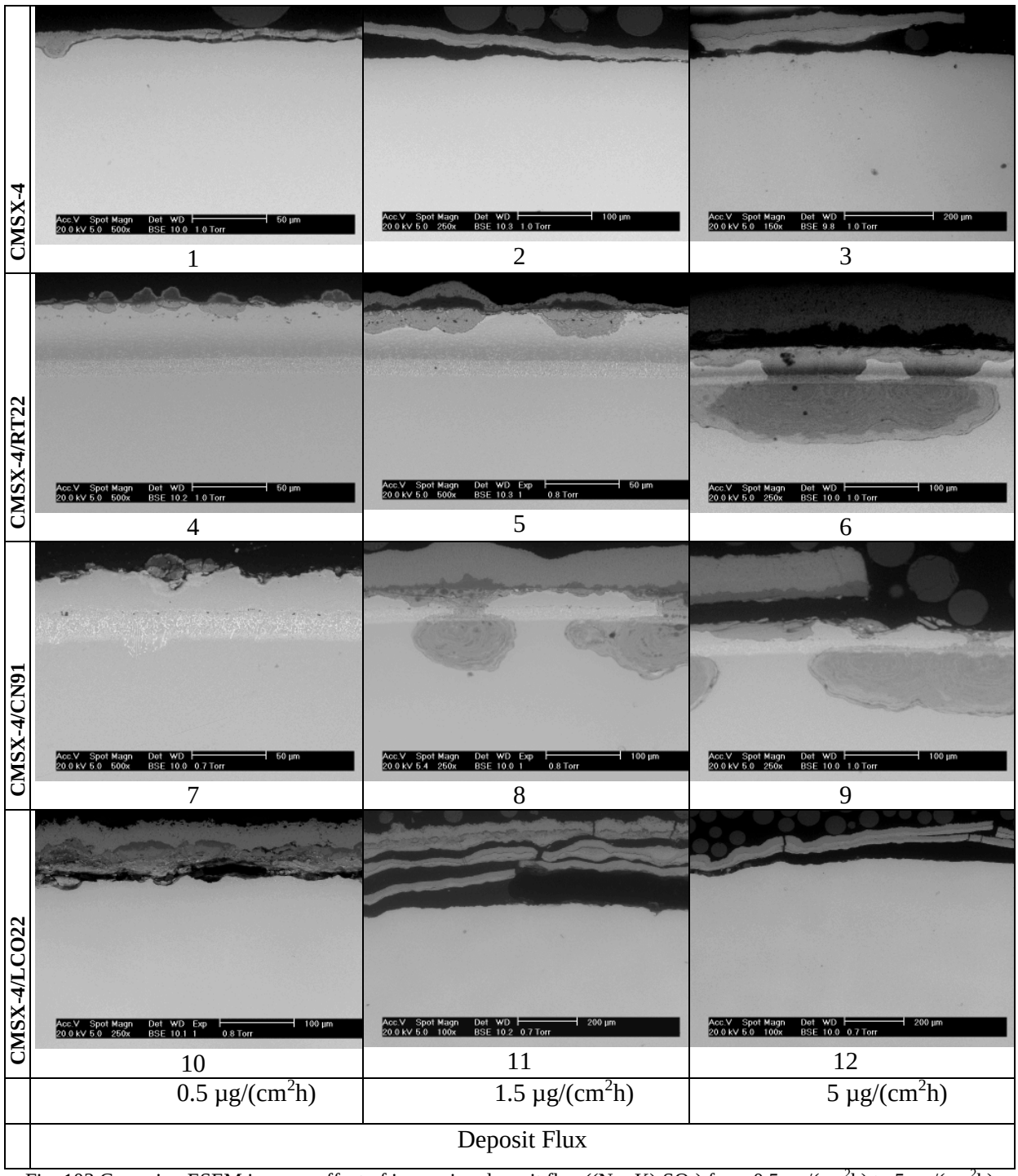

Fig. 103 Corrosion ESEM images: effect of increasing deposit flux ($(Na\text{-}K)_2SO_4$) from 0.5 µg/(cm^2h) to 5 µg/(cm^2h) at 700°C, 300vpm SO_2 rich atmosphere**,** on CMSX-4 superalloy and three coated systems (RT22, CN91 and "LCO22" on CMSX-4).

900ºC, 300vpm SO_2

The result of the ESEM analysis, performed on the samples exposed to 900°C and 300 vpm SO_2 rich atmosphere, is summarised in figure 104, where in each row, moving toward the right, the 3 pictures illustrate the effect of increasing the salt deposit flux for the same material systems.

For all four materials systems, an increase in the deposit flux has resulted in higher damage which has a broad front mode of attack involving internal sulphidation, followed by internal oxidation. Where the damage is deeper, penetration along the grain boundaries may be observed, for example in pictures 13, 14, 15, 18, 19.

Considering the uncoated alloy the increased damage increases with the increase in salt deposition. This may be seen from the picture magnification or better from mass change data and image analysis results.

Considering RT22 and CN91 coated samples the material consumption increases with increase in the deposit flux. At the highest flux the coating appears being completely depleted; in the other two deposit flux conditions tested the depth of the penetration of the damage does not reach the interdiffusion zone.

Referring to CMSX-4/LCO22, the coating is still present after 500 hours of expousure to 0.5 µg/(cm^2h), while it has been destroyed during the exposure at higher deposit fluxes. As already mentioned, the thickness of the as-coated samples were too thin, to provide the desired protection.

CMSX-4	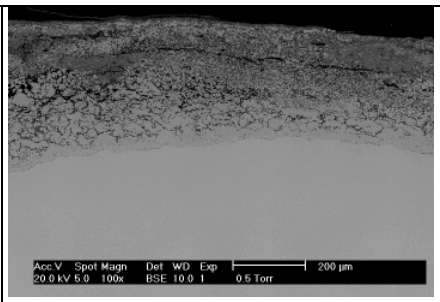	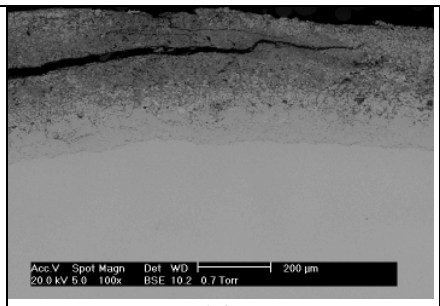	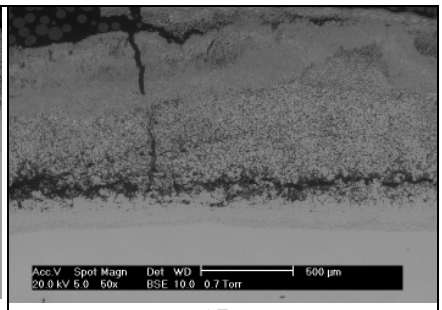
	13	14	15
CMSX-4/RT22	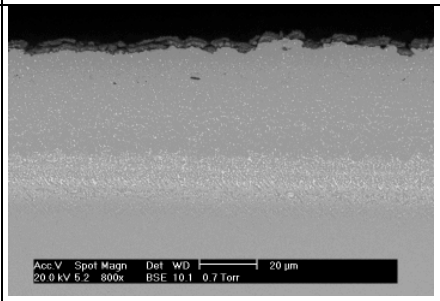	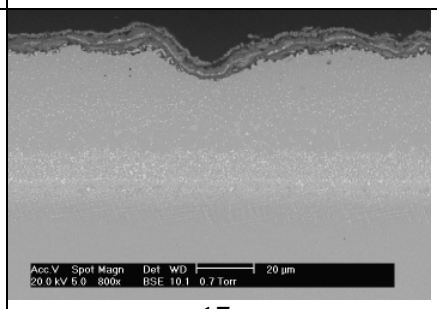	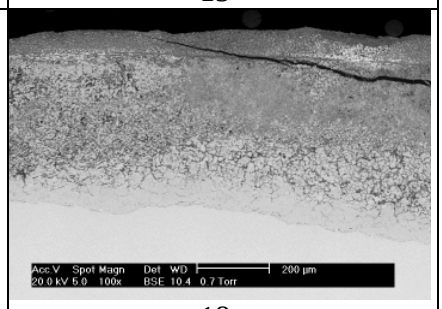
	16	17	18
CMSX-4/CN91	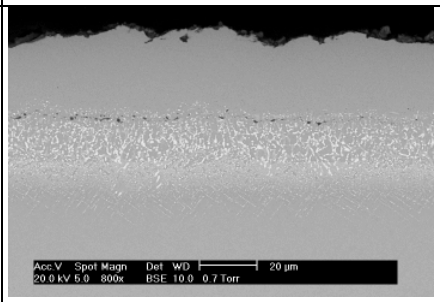	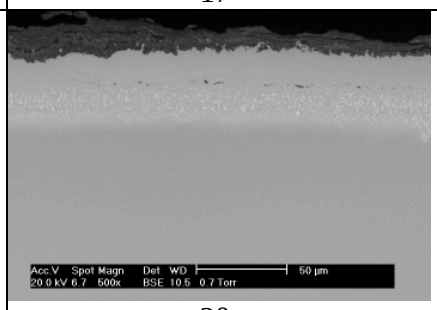	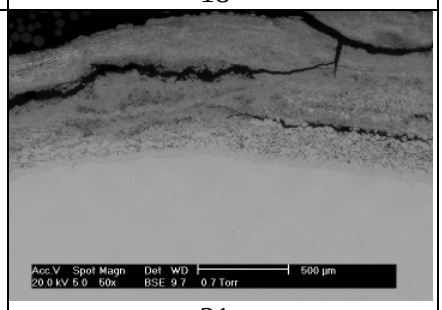
	19	20	21
CMSX-4/LCO22	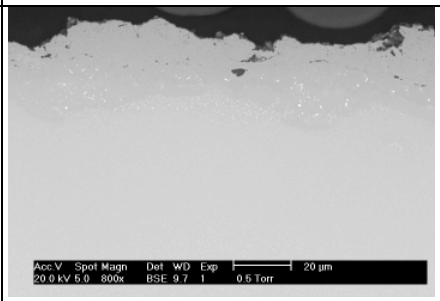	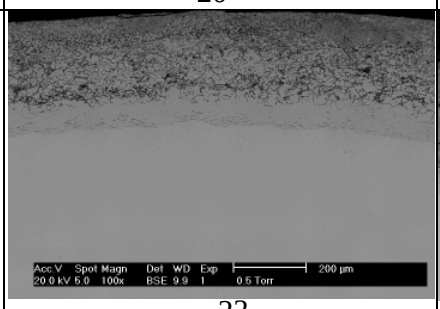	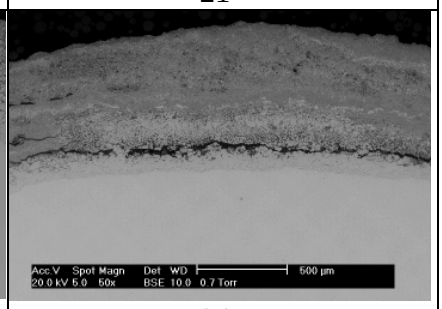
	22	23	24
	0.5 µg/(cm^{2}h)	1.5 µg/(cm^{2}h)	5 µg/(cm^{2}h)
	Deposit Flux		

Fig. 104 Corrosion ESEM images: effect of increasing deposit flux ((Na -K)$_2$SO$_4$) from 0.5 µg/(cm^{2}h) to 5 µg/(cm^{2}h) at 900°C, 300vpm SO$_2$ rich atmosphere**,** on CMSX-4 superalloy and three coated systems (RT22, CN91 and "LCO22" on CMSX-4).

700ºC, 300vpm SO_2 + 100vpm HCl

The result of the ESEM analysis, performed on the samples exposed at 700°C and 300 vpm SO_2 +100vpm HCl rich atmosphere, is summarised in figure 105,where the salt deposit effect on the same material is illustrated across the rows.

The uncoated superalloy has been subjected to periodic spallation of the scale, which led at any time to the underlying material being exposed to the corrosive environment and thus to its consumption.

The Pt-aluminide coatings, as observed in absence of HCl, have developed a localised damage, with pits that extend into the substrate at the highest deposit flux. CN91 looks to have performed better, since at intermediate deposit flux the coating didn't develop pits as deep as the substrate (observed in few cases for RT22) and also at the highest deposit flux the substrate was less attacked.

The pictures of CMSX-4/"LCO22" system (pictures 34, 35, 36) denote a corrosion morphology closer to the localised one, consisting of isolated pits, as a consequence of the exposure to the lowest deposit flux. In the other deposit flux conditions the attack front is broad as observed for the uncoated superalloy, possibly due to the coating's depletion.

900ºC, 300vpm SO_2 + 100vpm HCl

The result of the ESEM analysis, performed on the samples exposed to 900°C and 300 vpm SO_2 +100vpm HCl rich atmosphere, is summarised in figure 106, where the salt deposit effect on the same material is illustrated across the rows.

The pictures demonstrate that the corrosive mechanisms have developed uniformly across the surface, both for the bare superalloy and for the Pt-aluminide coatings. The "LCO22" coated system shows a more undulated surface, however it presents a typical Type I hot corrosion morphology too.

Probably the thin overlay coated led Pt-aluminides coatings to be more protective. Between these Pt-aluminides for 5 µg/(cm^2h) of deposit flux RT22 shows internal damage (Fig.42), which wasn't observed for CN91 (Fig. 45) under similar exposure condition. The uncoated superalloy had classic Type I corrosion morphology with internal sulphide and oxide damage at any deposit flux condition.

The better protection offered by the Pt-aluminide coatings, in the presence of HCl, at the highest value of deposit flux is clearly recognizable as less depth of the damage (pictures 42 and 45 vs pictures 21 and 24). In fact, it does not enrich the IZ.

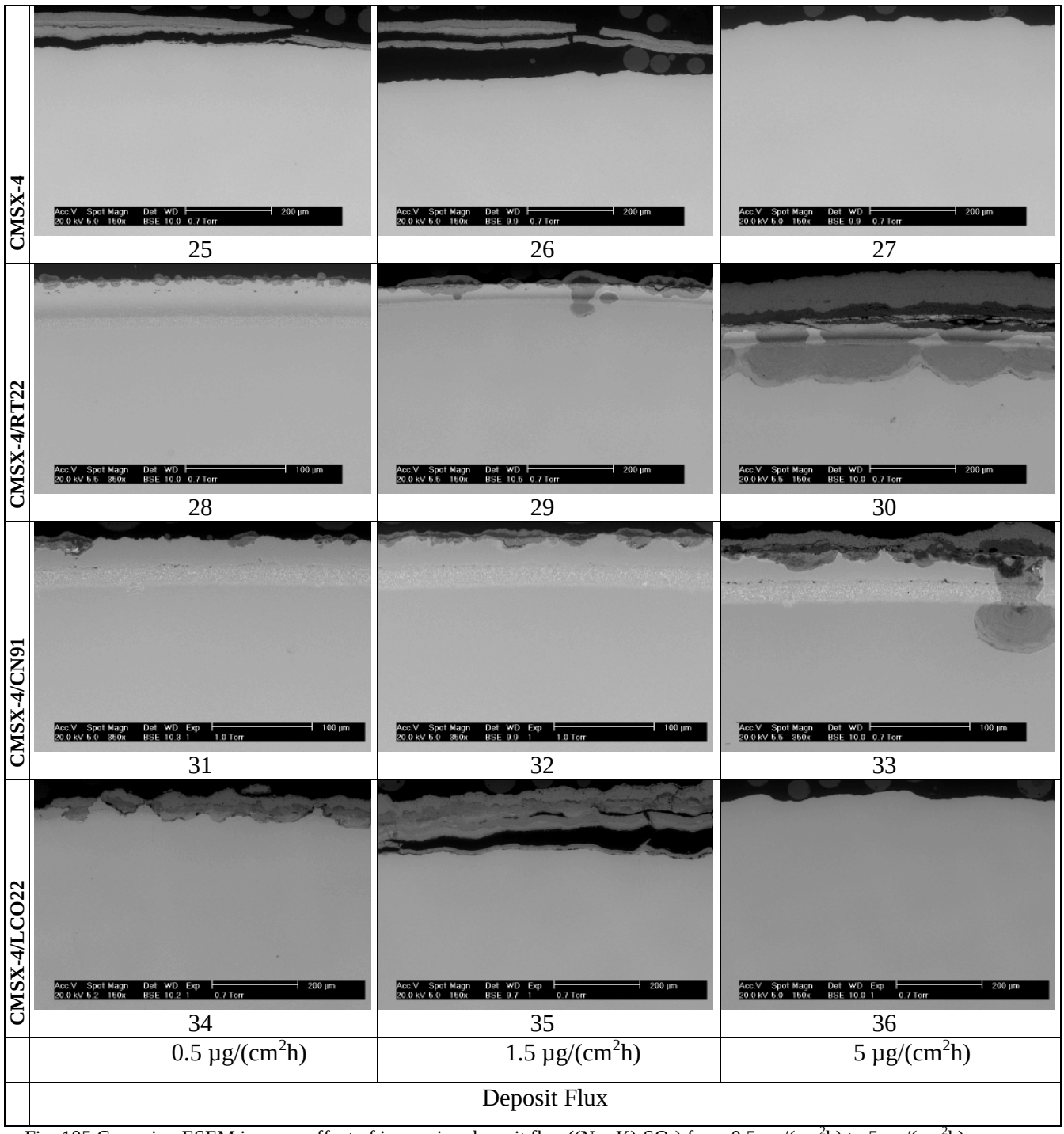

Fig. 105 Corrosion ESEM images: effect of increasing deposit flux ($(Na\text{-}K)_2SO_4$) from 0.5 µg/(cm^2h) to 5 µg/(cm^2h) at 700°C, 300vpm SO_2 +100vpm HCl rich atmosphere**,** on CMSX-4 superalloy and three coated systems (RT22, CN91 and "LCO22" on CMSX-4).

CMSX-4	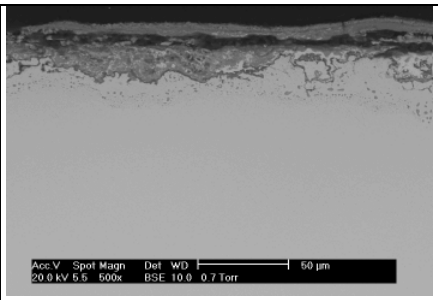	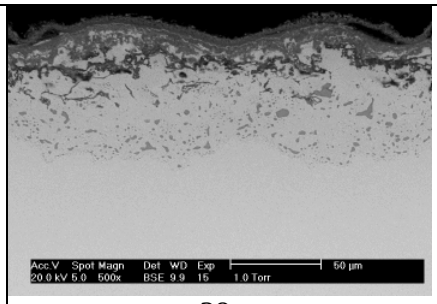	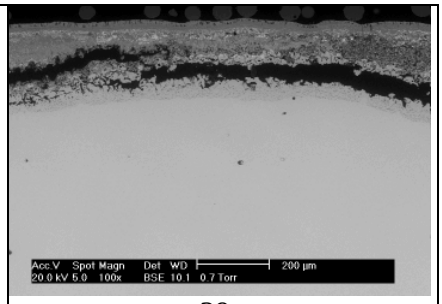
	37	38	39
CMSX-4/RT22	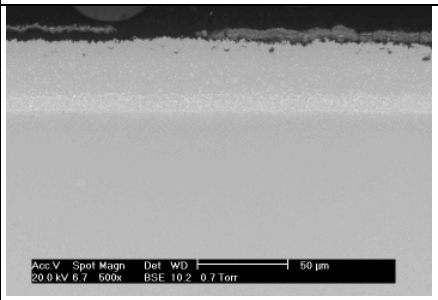	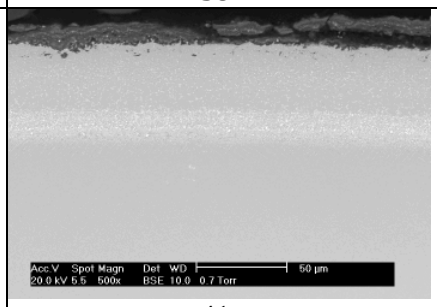	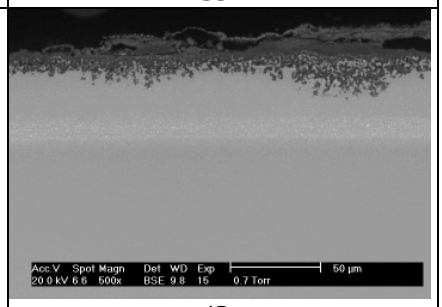
	40	41	42
CMSX-4/CN91	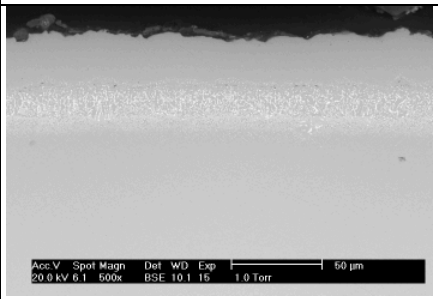	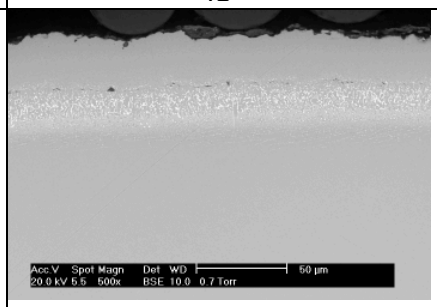	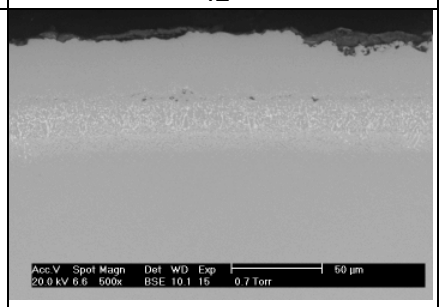
	43	44	45
CMSX-4/LCO22	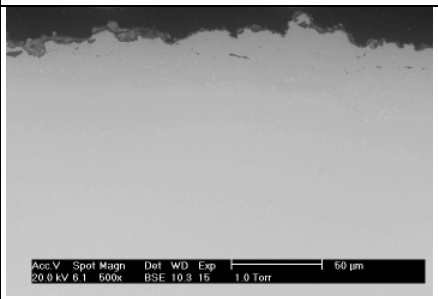	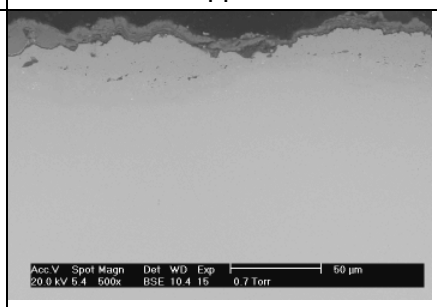	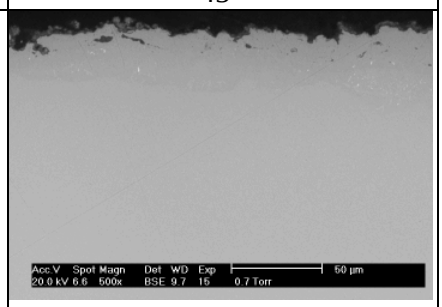
	46	47	48
	0.5 µg/(cm^{2}h)	1.5 µg/(cm^{2}h)	5 µg/(cm^{2}h)
	Deposit Flux		

Fig.106 Corrosion ESEM images: effect of increasing deposit flux ((Na -K)$_2$SO$_4$) from 0.5 µg/(cm^{2}h) to 5 µg/(cm^{2}h) at 900°C, 300vpm SO_2 +100vpm HCl rich atmosphere, on CMSX-4 superalloy and three coated systems (RT22, CN91 and "LCO22" on CMSX-4)

Chemistry of the corrosion processes

EDX analysis has been carried out on corroded samples for a qualitative description of the chemical composition of the corrosion products and their location.

In this section some examples of the map obtained are presented.

CMSX4/CN91, test conditions: 700°C, 1.5 µg/(cm^2 h) deposit flux

Figure 107, the result of backscattered image/mapping analysis of the material systems CMSX-4/CN91, shows:

- external presence of CoO and NiO,
- Al_2O_3 along with Cr_2O_3 in the pits,
- sulphur at the bottom of the pits, thus at the corrosion front.

CMSX4/"LCO22", test conditions: 900°C, 1.5 µg/(cm^2 h) deposit flux

Figure 108, the result of backscattered image/mapping analysis of the material systems CMSX4/"LCO22", shows a scale/deposit layer with the following structure:

- external layer of mainly Al_2O_3 and Cr_2O_3 along with NiO
- Al_2O_3
- sulphides

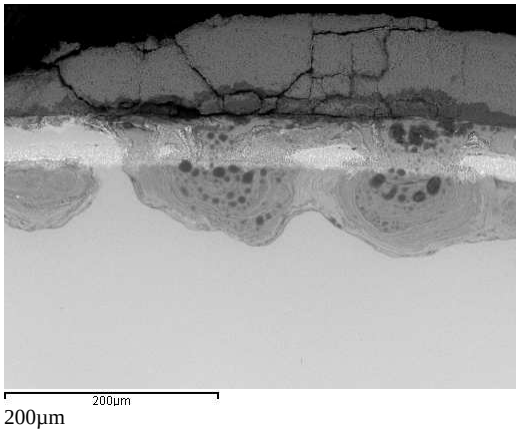

200µm

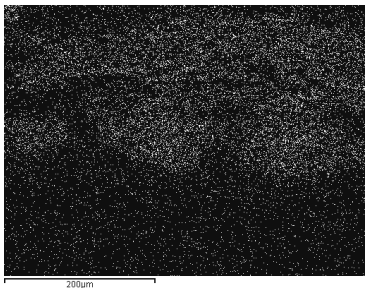

Oxygen

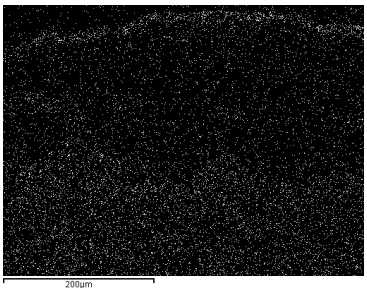

Cobalt

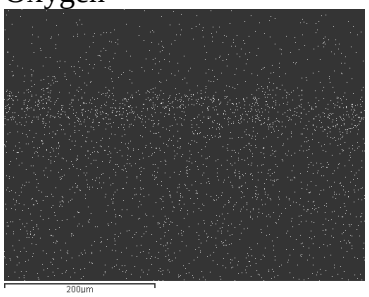

Platinum

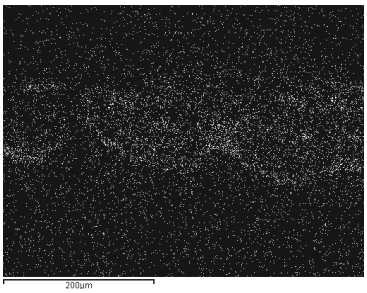

Sulphur

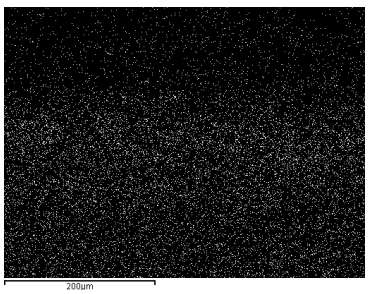

Chromium

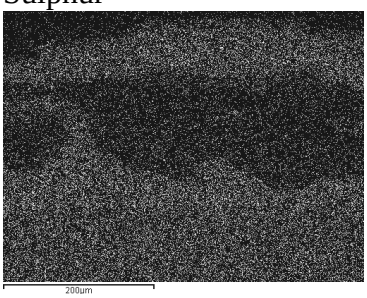

Nickel

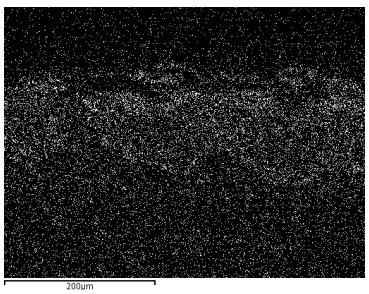

Aluminium

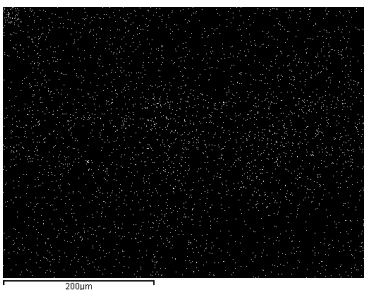

Sodium

Fig.107 Backscattered image/mapping of CMSX4/CN9. Test conditions: 700°C, 1.5 µg/(cm^2 h) deposit flux.

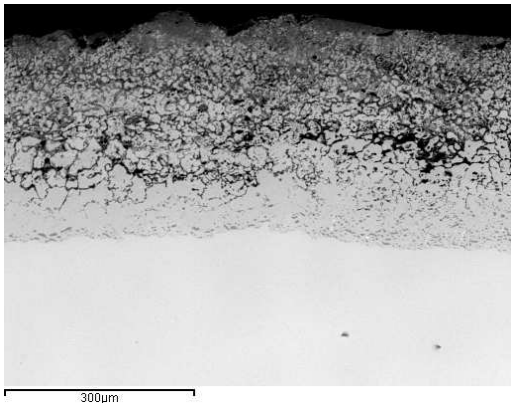

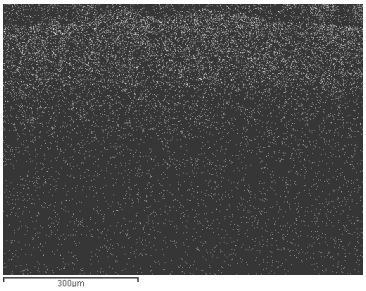

Oxygen

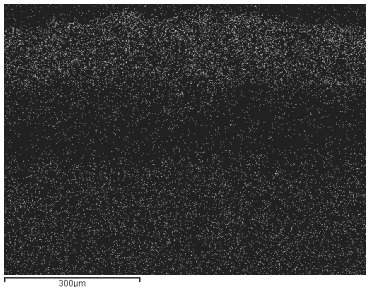

Chromium

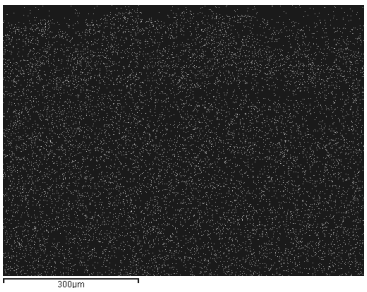

Cobalt

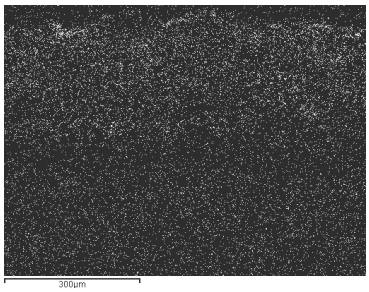

Aluminium

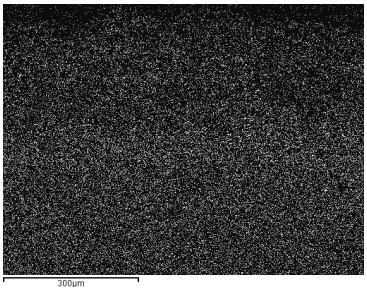

Nickel

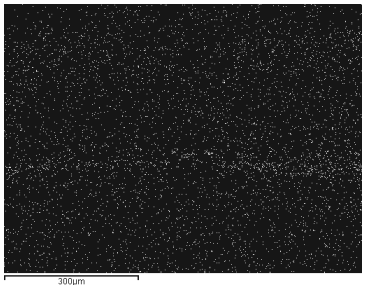

Sulphur

Fig.108 Backscattered image/mapping of CMSX4/"LCO22". Test conditions: 900°C, 1.5 µg/(cm^2 h) deposit flux.

3.2.3 Metal loss measurements

In section 2.2.5 the image analysis has been described as a tool to measure the material loss of specimens after exposure. The analysis transforms values of coordinates into values of metal loss and sound metal loss; this last represents the portion of coating/alloy still existing, but undamaged (visible for example in pictures 18, 21 in Fig.104, and 38, 42 in Fig.106).

The values of metal loss or good metal loss (metal loss plus internal damage), where present, have been plotted as a function of their probability of the depth of attack not being exceeded (Fig. 109-124). The y axis reports in general "metal loss" since, for the same material system, internal damage may occur just for one deposit fluxes.

The plots show, in most of the cases, that the material loss increases with increasing deposit deposition flux.

Probability plots for the test carried out at 700°C and 300vpm $S0_2$.

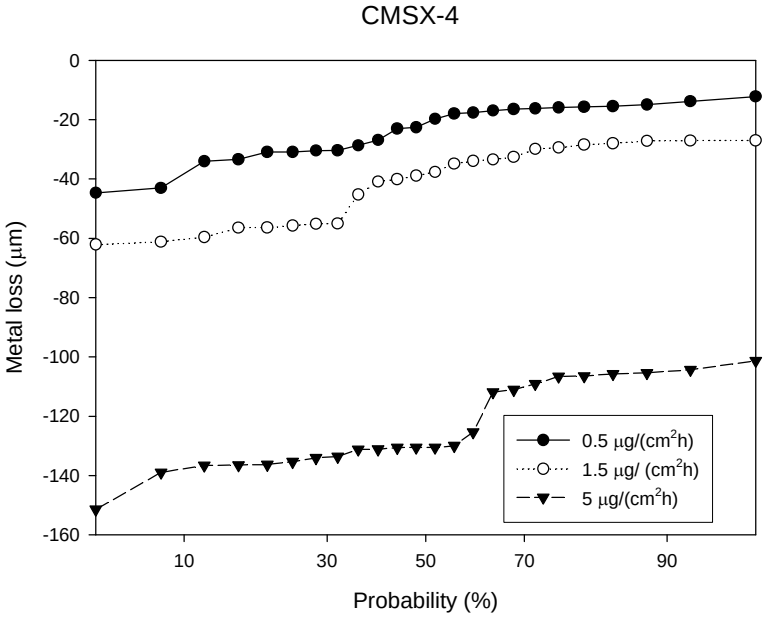

Fig. 109 Probability plot showing the effect of increasing deposit flux ($(Na\text{-}K)_2SO_4$) from 0.5 µg/(cm^2h) to 5 µg/(cm^2h) at 700°C, 300vpm SO_2, on CMSX-4.

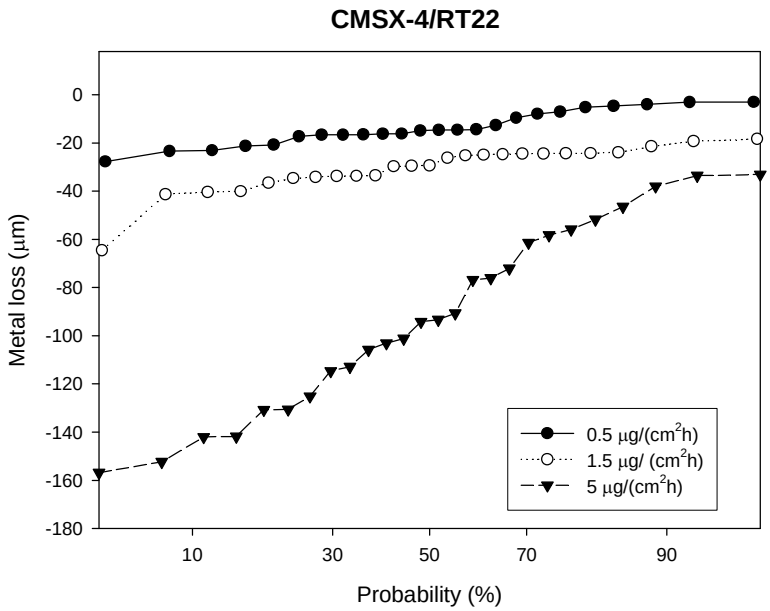

Fig. 110 Probability plot showing the effect of increasing deposit flux ((Na -K)$_2$SO$_4$) from 0.5 µg/(cm^{2}h) to 5 µg/(cm^{2}h) at 700°C, 300vpm SO_2, on CMSX-4/RT22.

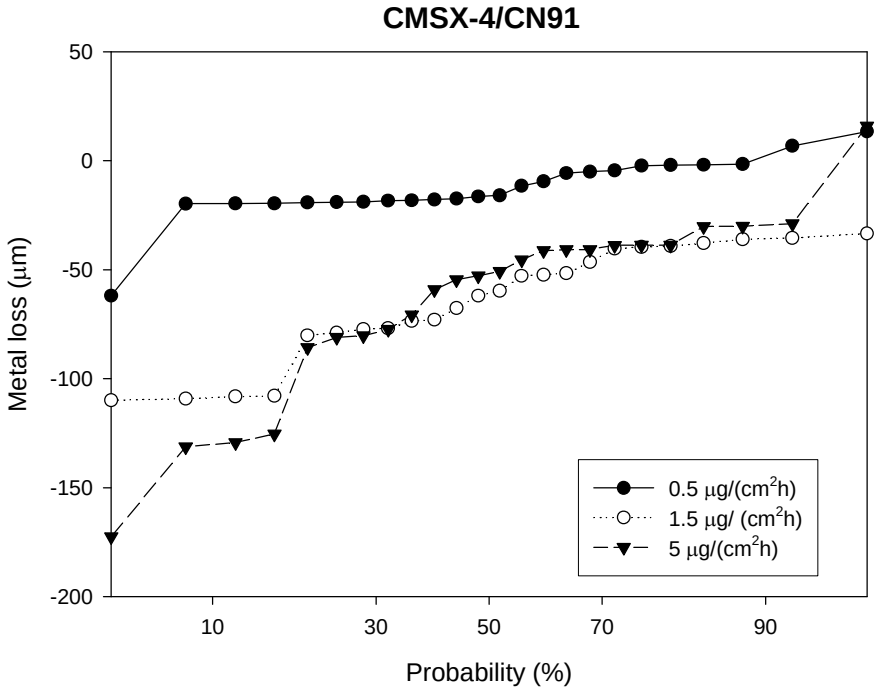

Fig. 111 Probability plot showing the effect of increasing deposit flux ((Na -K)$_2$SO$_4$) from 0.5 µg/(cm^{2}h) to 5 µg/(cm^{2}h) at 700°C, 300vpm SO_2, on CMSX-4/CN91.

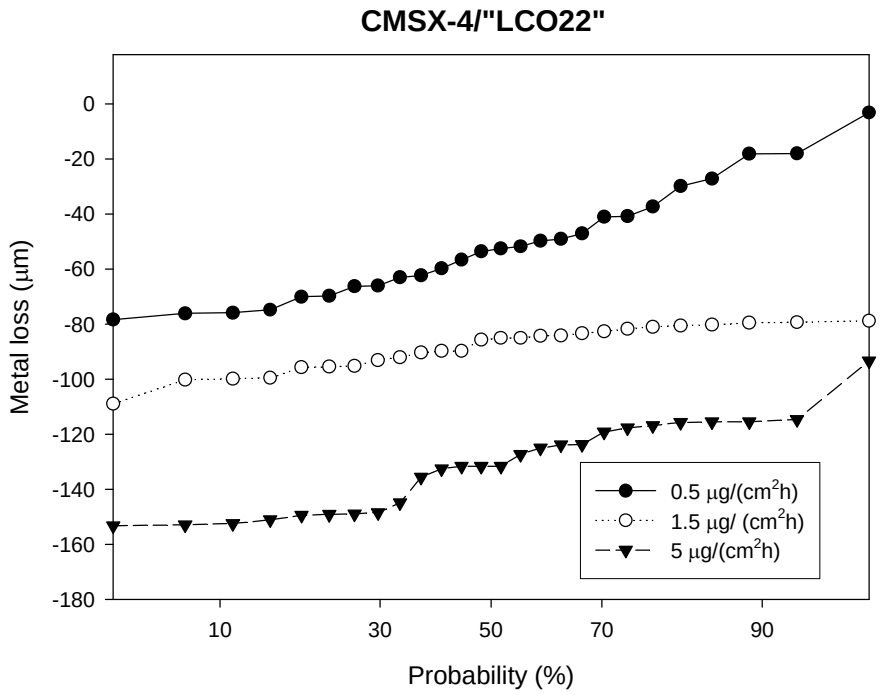

Fig. 112 Probability plot showing the effect of increasing deposit flux ((Na -K)$_2$SO$_4$) from 0.5 µg/(cm^{2}h) to 5 µg/(cm^{2}h) at 700°C, 300vpm SO$_2$, on CMSX-4/"LCO22".

Probability plots for the test carried out at 900°C and 300vpm S0$_2$

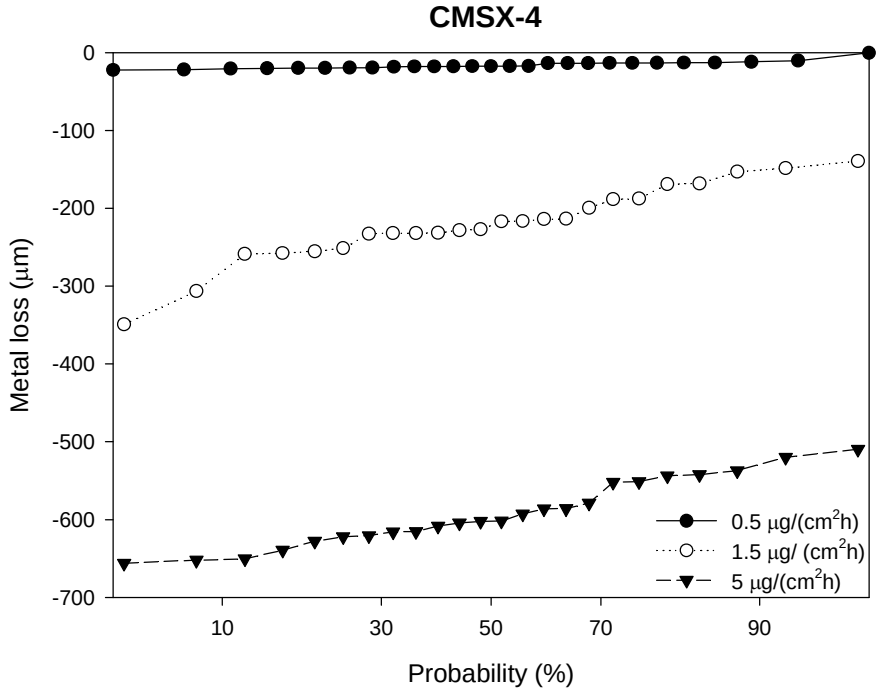

Fig. 113 Probability plot showing the effect of increasing deposit flux ((Na -K)$_2$SO$_4$) from 0.5 µg/(cm^{2}h) to 5 µg/(cm^{2}h) at 900°C, 300vpm SO$_2$, on CMSX-4.

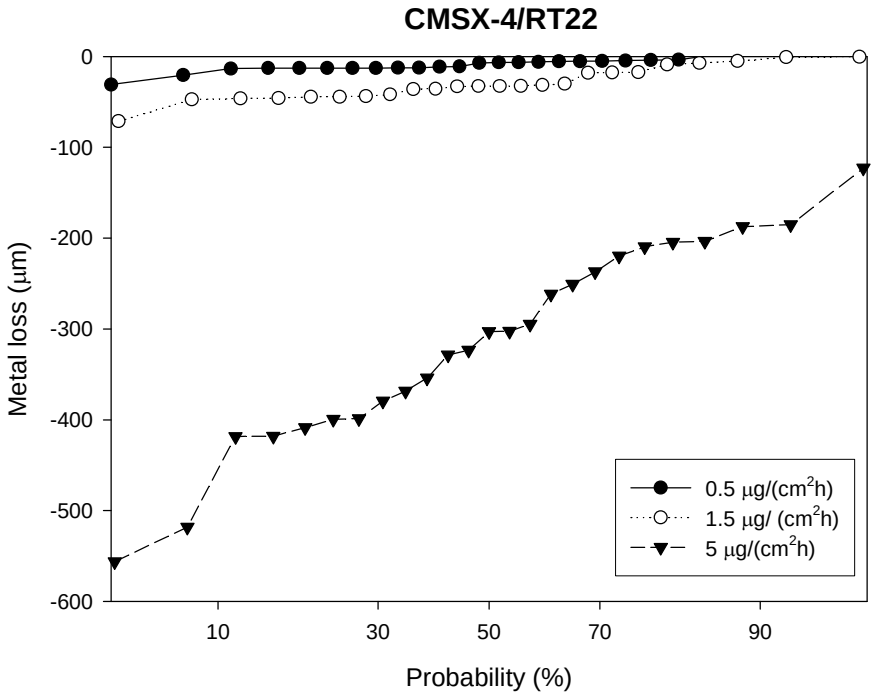

Fig. 114 Probability plot showing the effect of increasing deposit flux ($(Na\text{-}K)_2SO_4$) from 0.5 µg/(cm^2h) to 5 µg/(cm^2h) at 900°C, 300vpm SO_2, on CMSX-4/RT22.

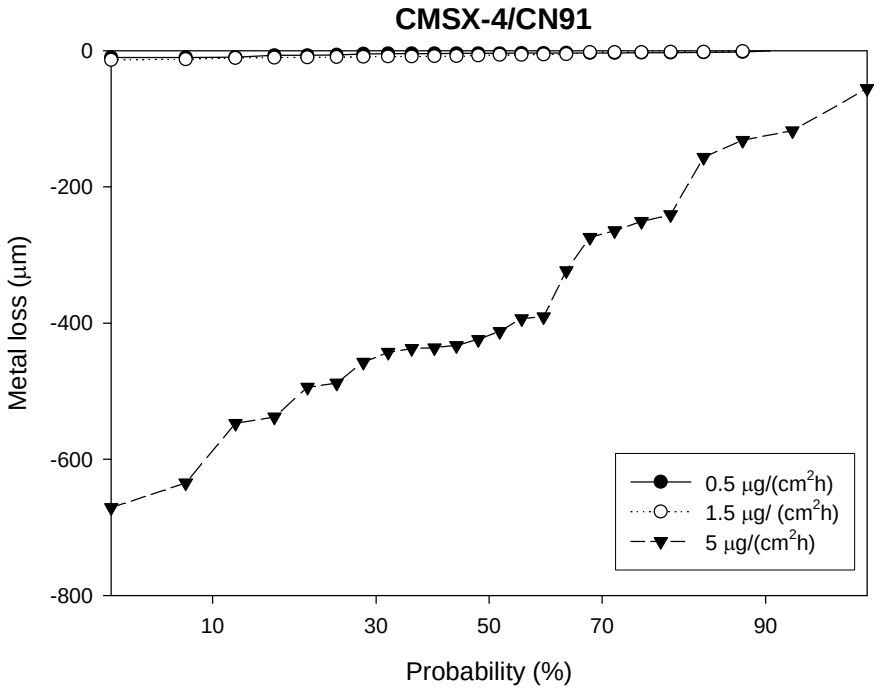

Fig. 115 Probability plot showing the effect of increasing deposit flux ($(Na\text{-}K)_2SO_4$) from 0.5 µg/(cm^2h) to 5 µg/(cm^2h) at 900°C, 300vpm SO_2, on CMSX-4/CN91.

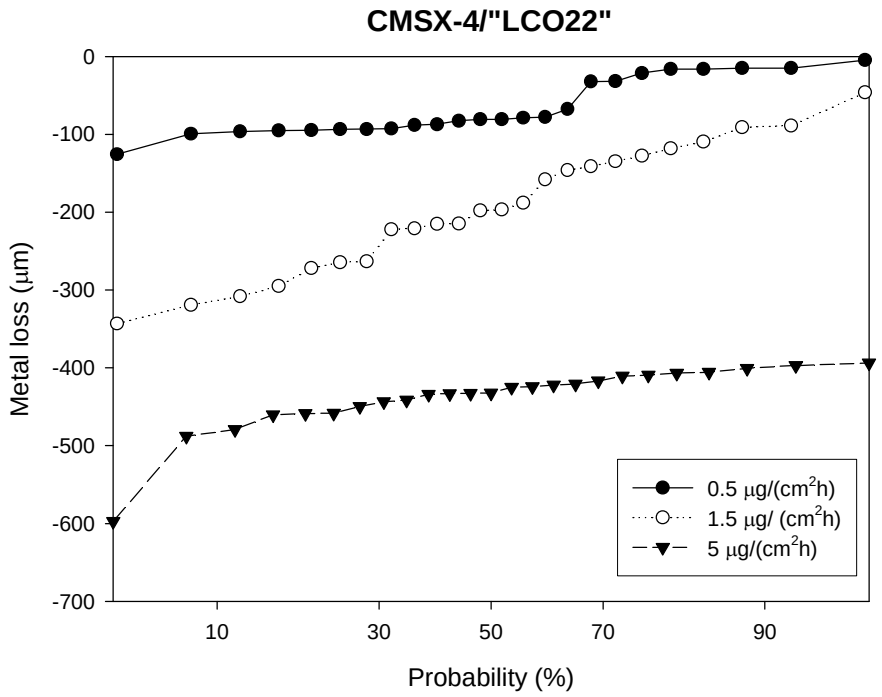

Fig. 116 Probability plot showing the effect of increasing deposit flux ($(Na\ -K)_2SO_4$) from 0.5 µg/(cm^2h) to 5 µg/(cm^2h) at 900°C, 300vpm SO_2, on CMSX-4/"LCO22".

Probability plots for the test carried out at 700°C and 300vpm $S0_2$ + 100vpm HCL

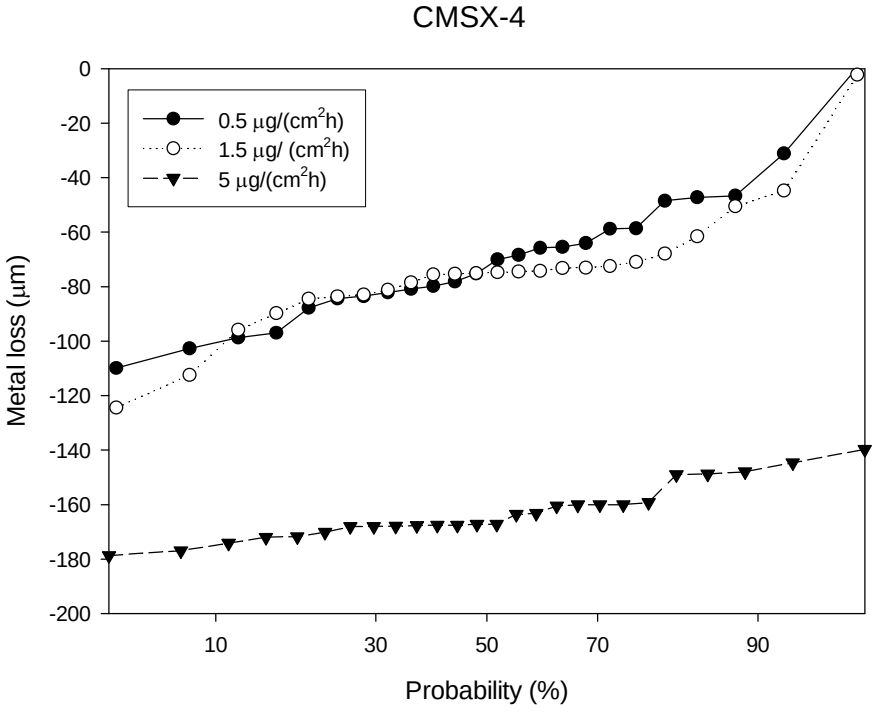

Fig. 117 Probability plot showing the effect of increasing deposit flux ($(Na\ -K)_2SO_4$) from 0.5 µg/(cm^2h) to 5 µg/(cm^2h) at 700°C, 300vpm SO_2+100vpm HCl, on CMSX-4.

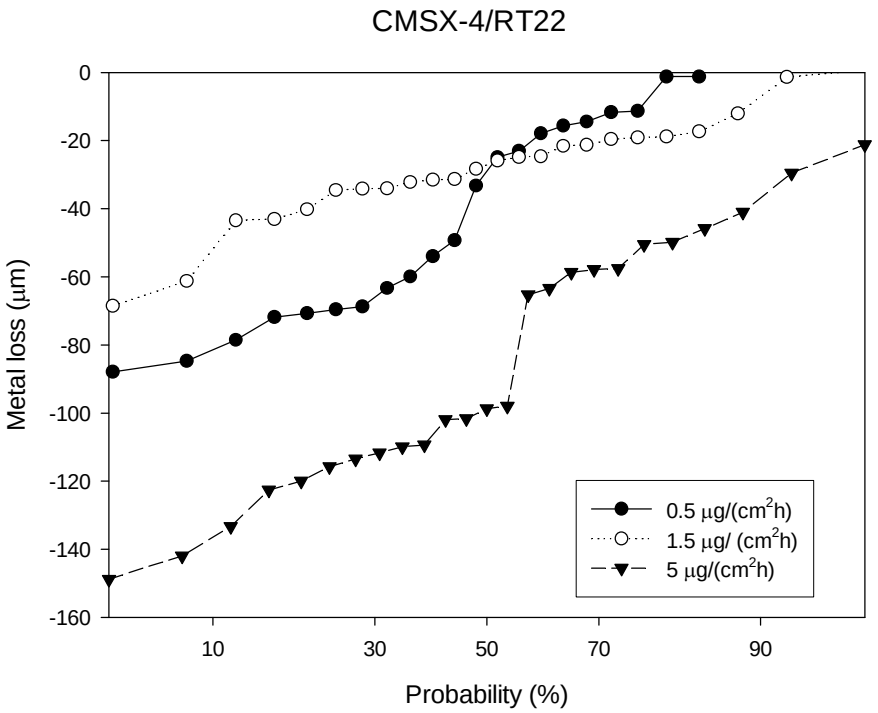

Fig. 118 Probability plot showing the effect of increasing deposit flux ($(Na\text{-}K)_2SO_4$) from 0.5 µg/(cm^2h) to 5 µg/(cm^2h) at 700°C, 300vpm SO_2+100vpm HCl**,** on CMSX-4/RT22.

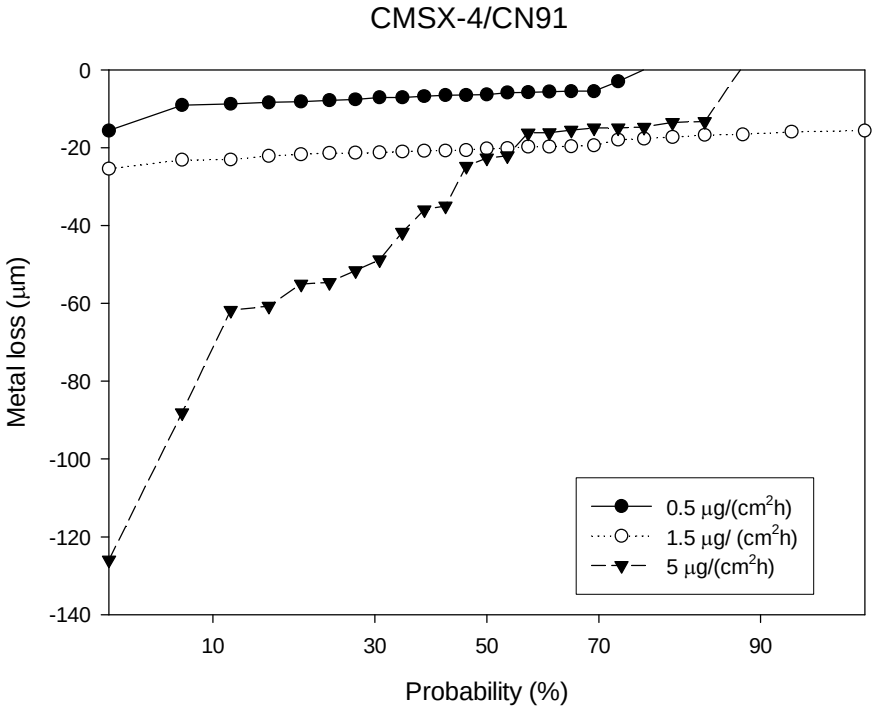

Fig. 119 Probability plot showing the effect of increasing deposit flux ($(Na\text{-}K)_2SO_4$) from 0.5 µg/(cm^2h) to 5 µg/(cm^2h) at 700°C, 300vpm SO_2+100vpm HCl**,** on CMSX-4/CN91.

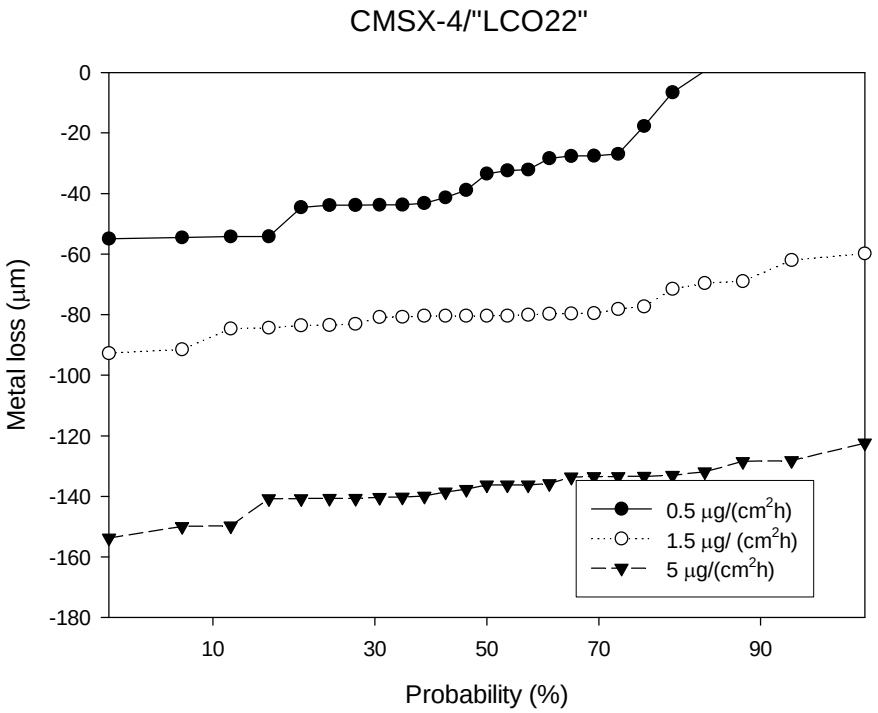

Fig. 120 Probability plot showing the effect of increasing deposit flux ($(Na\text{-}K)_2SO_4$) from 0.5 µg/(cm^2h) to 5 µg/(cm^2h) at 700°C, 300vpm SO_2+100vpm HCl**,** on CMSX-4/"LCO22".

Probability plots for the test carried out at 900°C and 300vpm $S0_2$+100vpm HCl

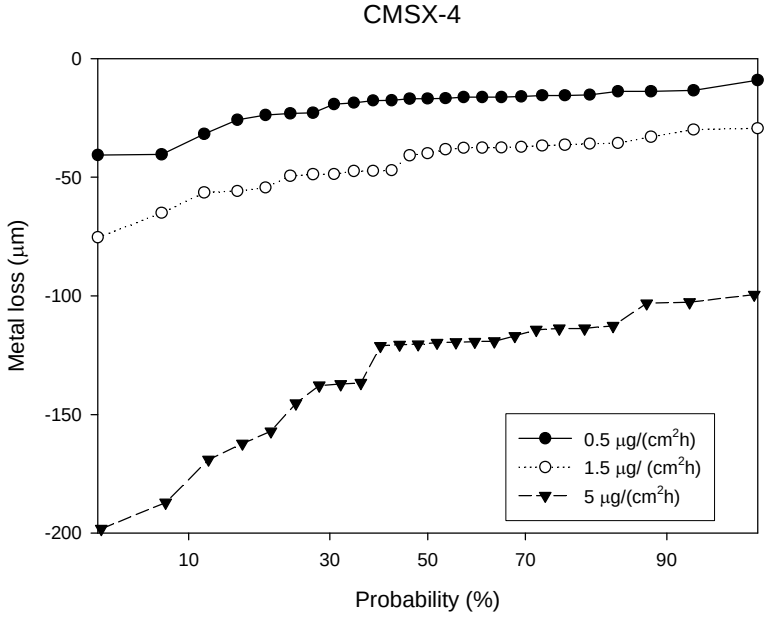

Fig. 121 Probability plot showing the effect of increasing deposit flux ($(Na\text{-}K)_2SO_4$) from 0.5 µg/(cm^2h) to 5 µg/(cm^2h) at 900°C, 300vpm SO_2+100vpm HCl**,** on CMSX-4.

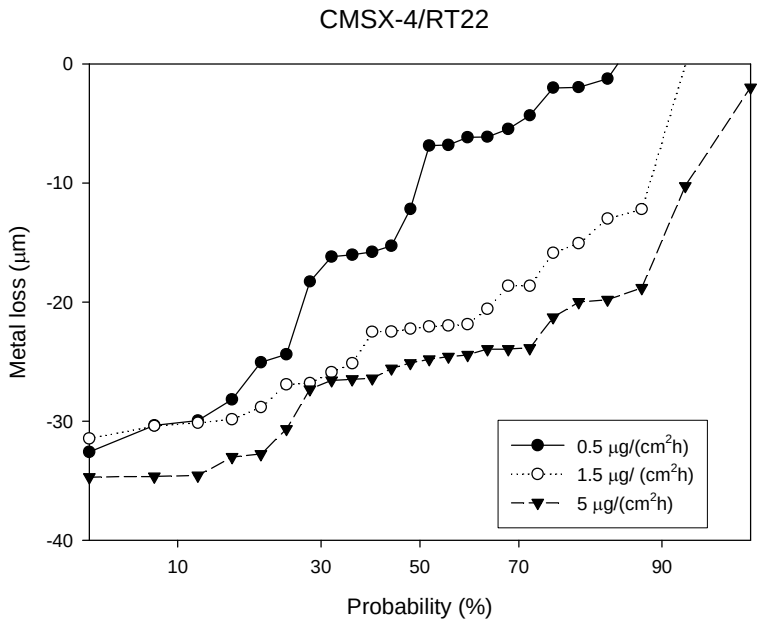

Fig. 122 Probability plot showing the effect of increasing deposit flux ($(Na\text{-}K)_2SO_4$) from 0.5 μg/(cm^2h) to 5 μg/(cm^2h) at 900°C, 300vpm SO_2+100vpm HCl**,** on CMSX-4/RT22.

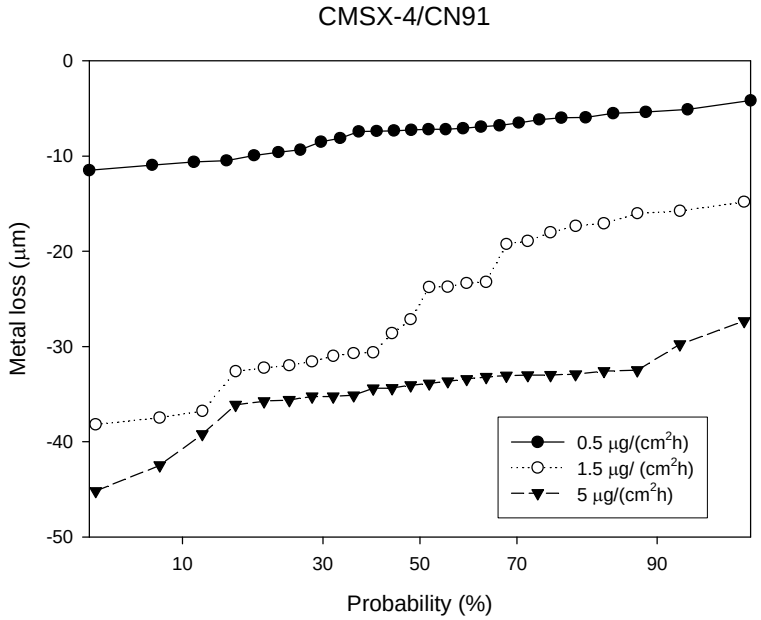

Fig. 123 Probability plot showing the effect of increasing deposit flux ($(Na\text{-}K)_2SO_4$) from 0.5 μg/(cm^2h) to 5 μg/(cm^2h) at 900°C, 300vpm SO_2+100vpm HCl**,** on CMSX-4/CN91.

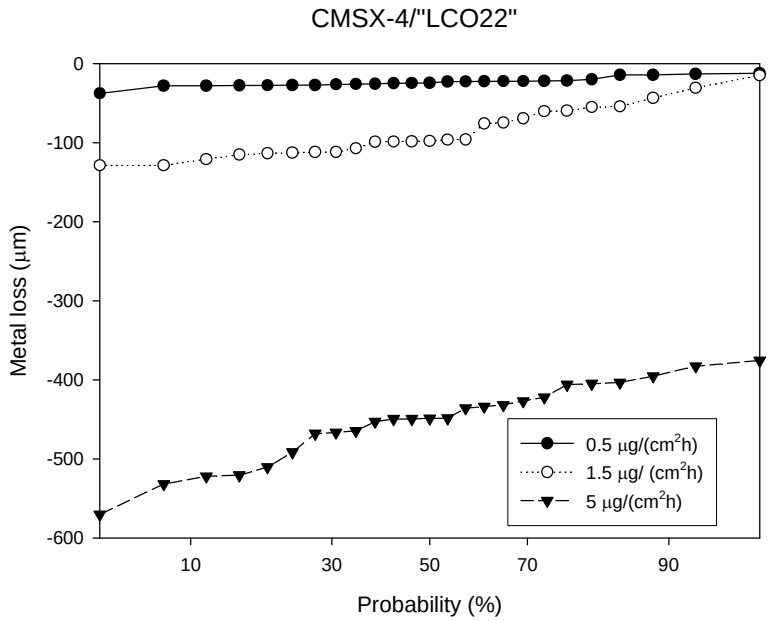

Fig. 124 Probability plot showing the effect of increasing deposit flux ($(Na\text{-}K)_2SO_4$) from 0.5 µg/(cm^2h) to 5 µg/(cm^2h) at 900°C, 300vpm SO_2+100vpm HCl**,** on CMSX-4/"LCO22".

3.2.4 Modelling

The activity called “Modelling” has consisted in the comparison of the values of metal loss observed under different exposure condition with the data generated during the previous study carried out [30]. Consequently, since this stap has required to consider and compare data with information not produced directly with this study, this activity has been described in the following chapter (§ 4.2).

4. Discussion

The need to study alloy/coatings systems behaviour in oxidative and corrosive environments has come from the necessity of defining the reliability of materials that make up power plants turbine blades during their service. Nowadays, a rise in the operating temperature is one key factor for higher power plant efficiency and thus lower CO_2 emission, but, on the other side, it leads to faster materials degradation. Consequently it is necessary to characterise and predict the materials environmental degradation to avoid expensive and unpredictable failure in service.

The study has concerned one alloy and three of the coatings now employed for making up turbine blades: nickel-base superalloy CMSX-4, Pt-aluminide coatings RT22 and CN91 and overlay coating "LCO22". Cylindrical samples of these materials systems have been subjected to isothermal oxidation at the five different temperatures 850, 900, 950, 1000, 1050 °C, for exposure time ranging between 1000 to10,000 hours (with 1000 hour cycles). Samples of the same shape have been tested in corrosive environment at 700 and 900°C, using the "deposit recoat technique", simulating three different values of salt $(K\text{-}Na)_2SO_4$) deposit flux (0.5/1.5/5 µg/(cm^2 h)) and a gas compositions composed either of air + 300vpm SO_2 or Air + 300vpm SO_2 +100vpm $HCl+H_2O$.

4.1 Oxidation

4.1.1 Kinetics of oxidation

The isothermal oxidation tests carried out have allowed to verify the effect of the temperature and exposure time on the protective behaviour of the three different coatings (RT22, CN91 and "LCO22"), in particular on the oxidation kinetics, the characteristics of the oxide scale, and the onset of spalling.

The study of the oxidation kinetics has proceeded from the mass change data plot to the drawing of squared mass change plots (and presented in appendix). Brumm et al. [14] demonstrated that the oxidation of NiAl at low temperature, 700-850°C, follows a parabolic law and thus the square mass change data vs time plot result in a straight line, whose slope identifies the parabolic rate constant of alumina. Figures 125-127 below show the kinetics

described by experimental data relative to the three coated systems tested at 850°C in reality moves a bit away from the ideal parabolic trend. Moreover, a certain variability in the oxidation rate amongst the samples can be observed, especially for CMSX-4/CN91 and CMSX-4/"LCO22", which in turn increases the uncertainty on the value of the rate constant measured (section 4.1.4).

In the following plots each line represents the trend of the square mass change experienced by one samples.

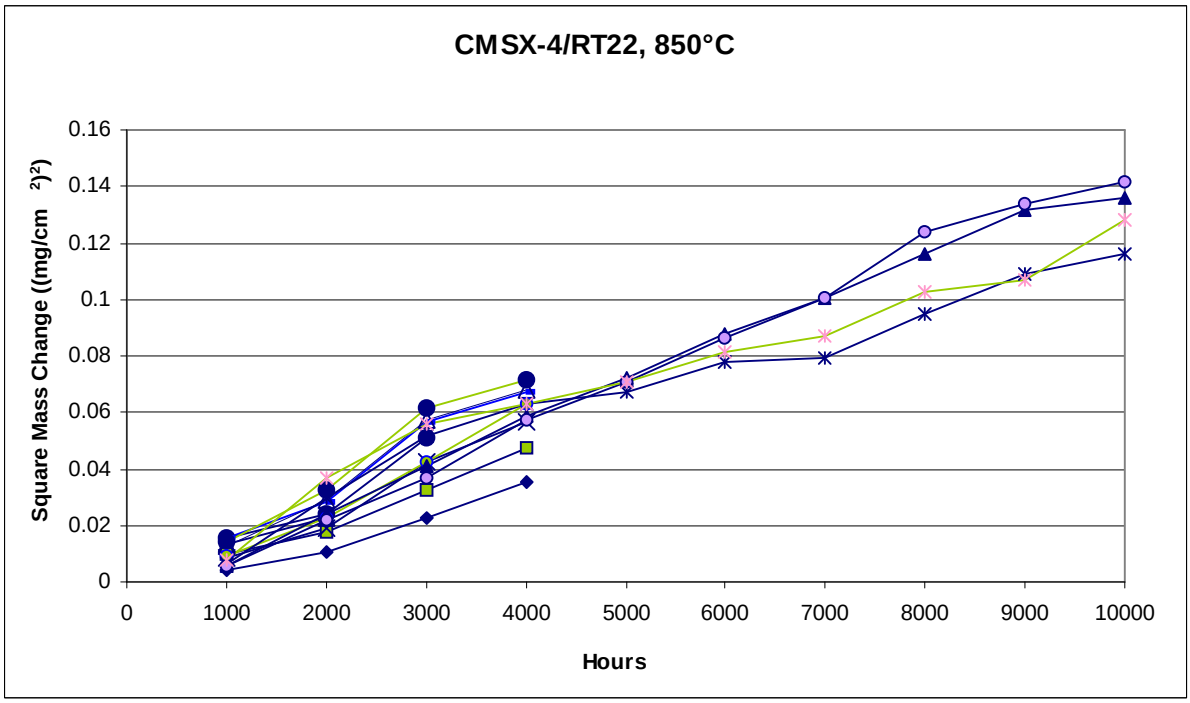

Fig. 125 Square mass change plot for CMSX-4/RT22 system tested at 850°C.

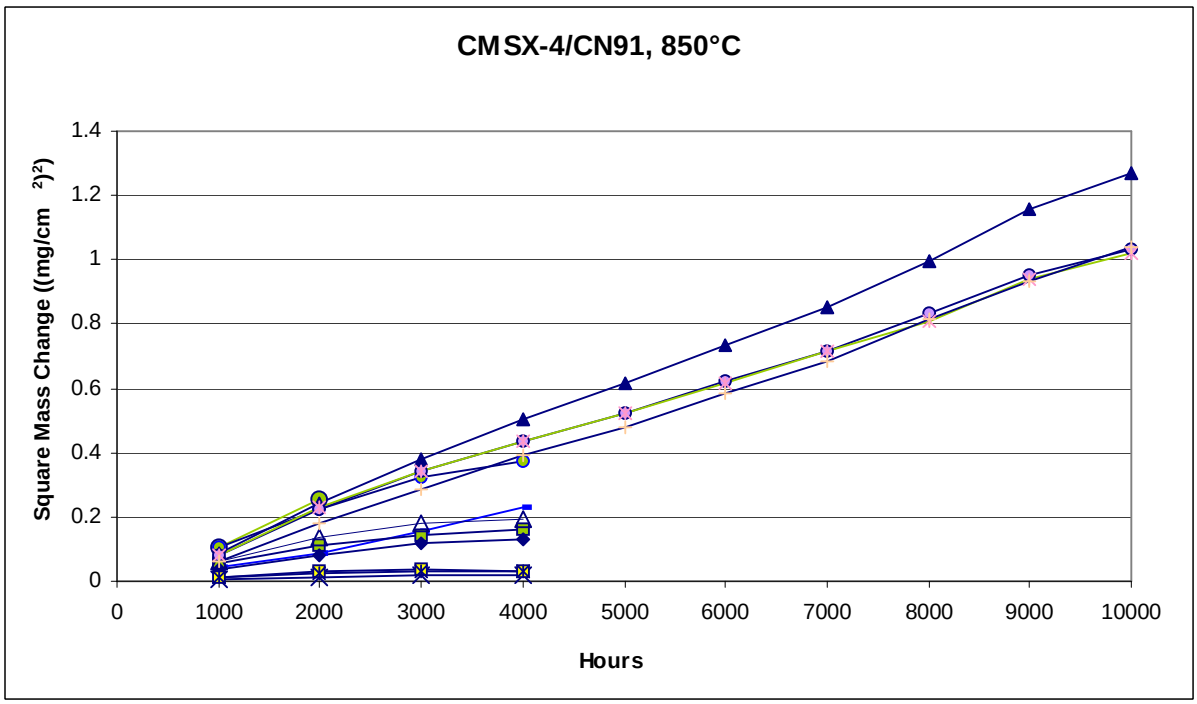

Fig. 126 Square mass change plot for CMSX-4/CN91 system tested at 850°C.

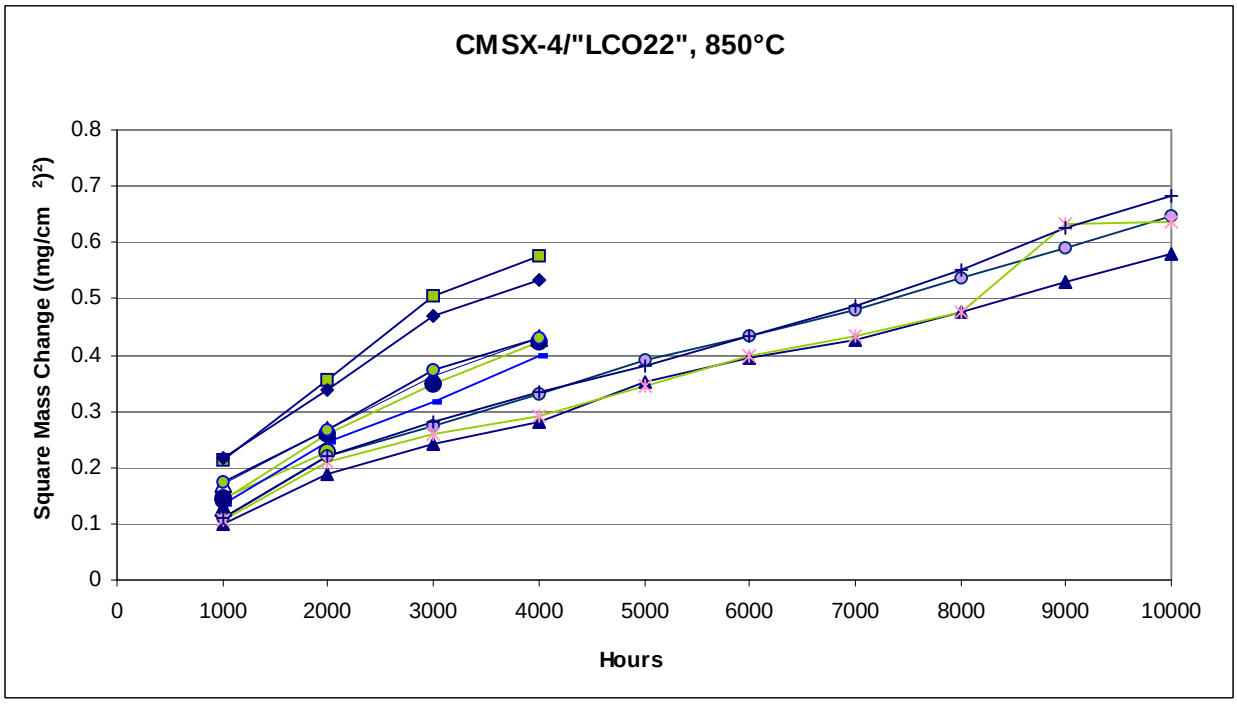

Fig. 127 Square mass change plot for CMSX-4/"LCO22" system tested at 850°C.

At 900°C the square mass change plot is further from a straight line, which is, looking at the following figures, 128-130, more a broken line; the curve is steeper for the first 1000/2000 hours of exposure and afterward the value of parabolic rate constant decreases. At 900°C in few cases for each coated system we can still observe almost a straight line.

As already explained in section 1.4.3 the metastable structures of alumina (γ, δ, θ) transformed into α- Al_2O_3 during the exposure at high temperature and this transformation

occurs after a period of time variable in function of the temperature. α- Al_2O_3 is a slower growing oxide than the metastable alumina and the change in the curve slope, shown in the already mentioned figures 127-129, is considered the result of the transformation of θ-Al_2O_3 into α-Al_2O_3. However, this study hasn't gone through the analysis of the alumina oxide types formed for different exposure times and temperatures. This detailed study, in fact, has been being carried out by the University of Bristol (partner in the SUPERGEN Consortium) by the means of photoluminescence and whose results will be published in the future months.

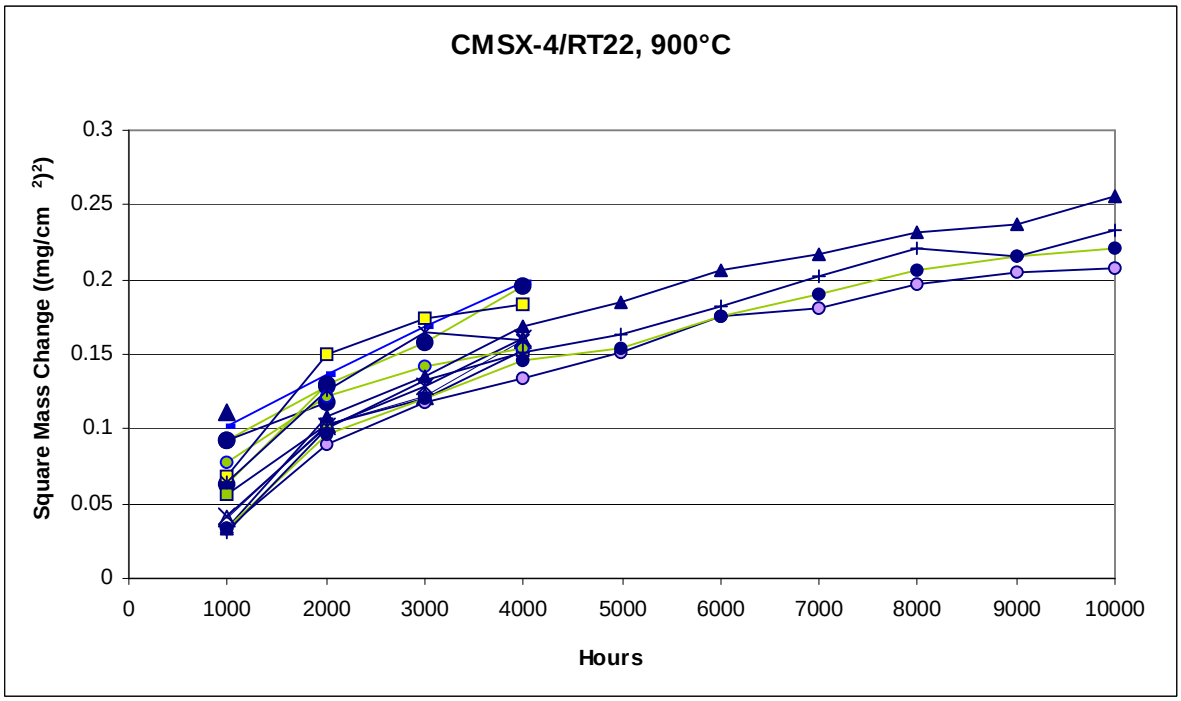

Fig. 128 Square mass change plot for CMSX-4/RT22 system tested at 900°C.

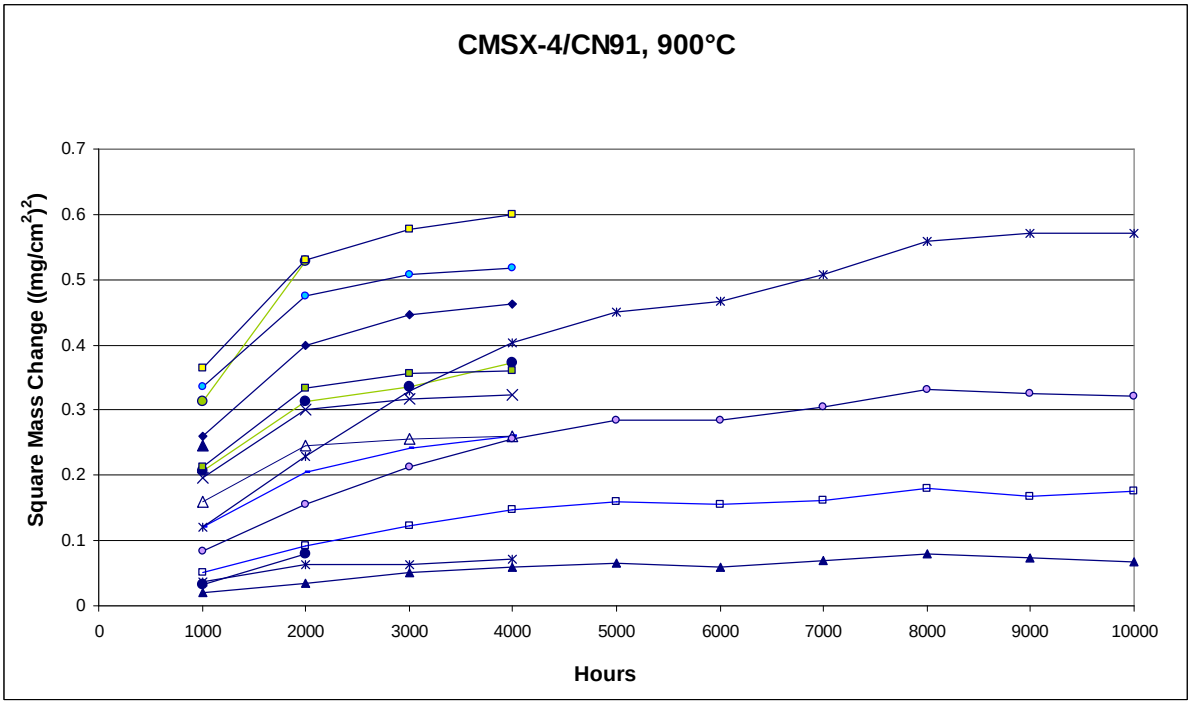

Fig. 129 Square mass change plot for CMSX-4/CN91 system tested at 900°C.

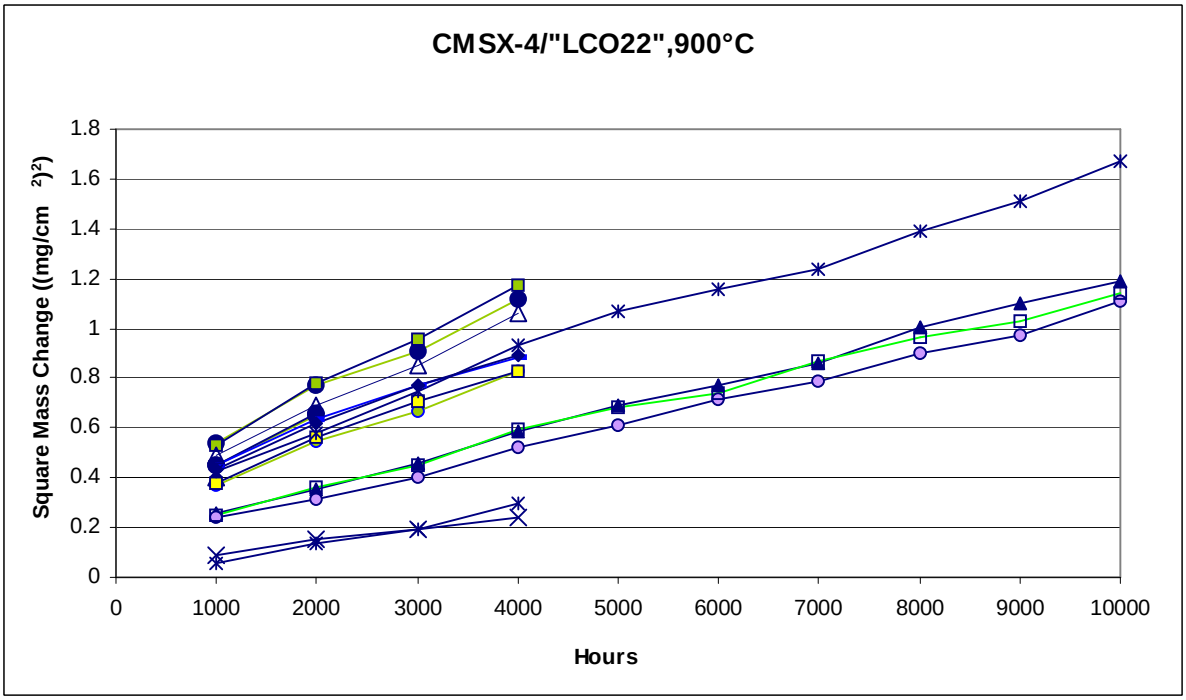

Fig. 130 Square mass change plot for CMSX-4//"LCO22" system tested at 900°C.

According to the observation of Brumm et al. [14], the oxidation at 950-1100°C proceeds according to a non-parabolic rate law and the slope is higher at the beginning of the oxidation and steeper at higher temperature [50]. This has been observed with our oxidation tests carried out at 950, 1000 and 1050°C, as shown by the following figures, 131-139.

Brumm et al. [14], moreover, noticed that the higher the temperature the more rapid is the decrease of the rate. In our case this last element can't be verified, since the exposure time (1000-10,000 hours) is much longer than that of the author's test (500 hours) and the spalling affected heavily the kinetics.

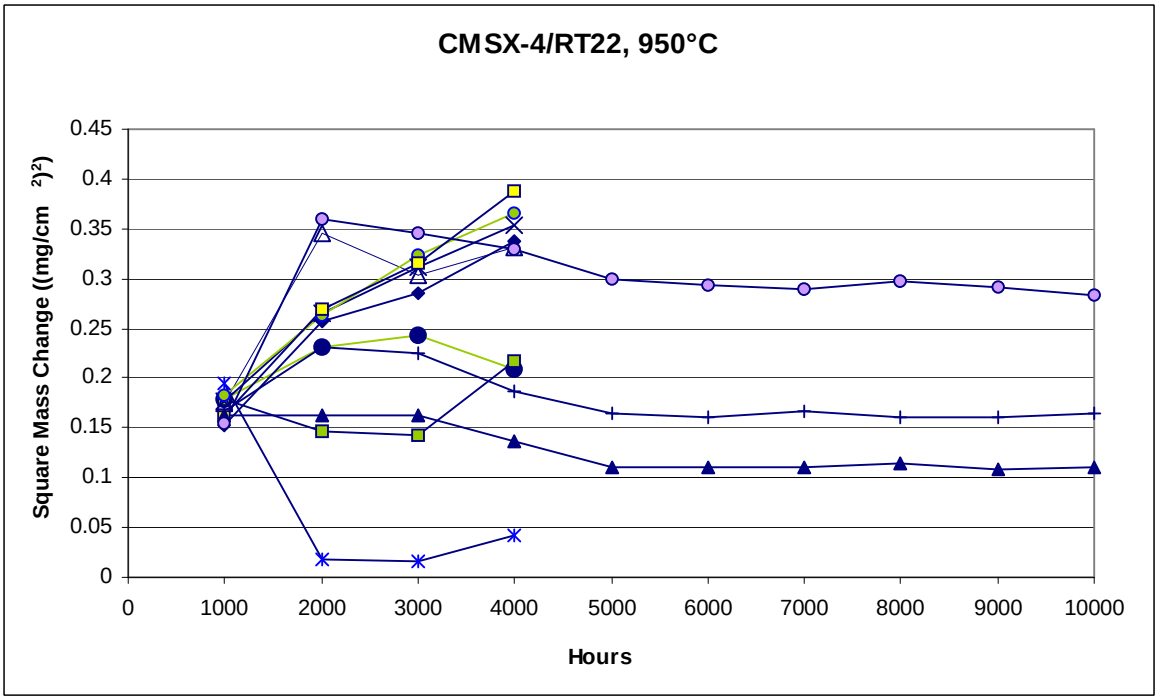

Fig. 131 Square mass change plot for CMSX-4/RT22 system tested at 950°C.

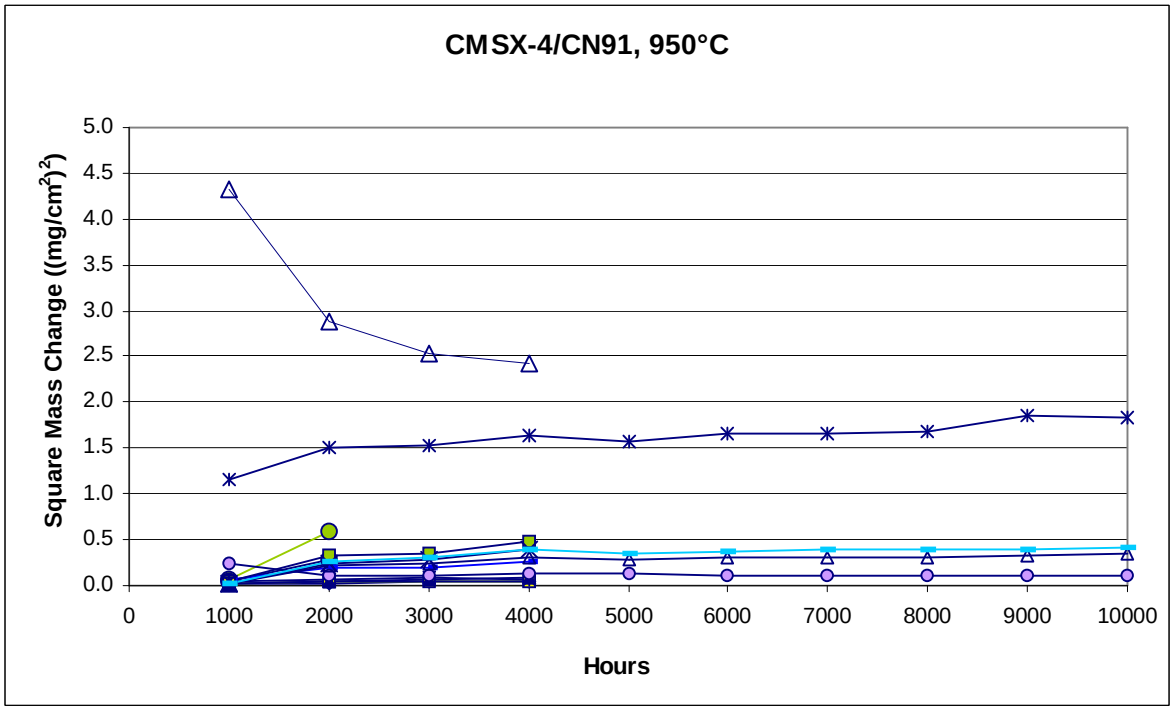

Fig. 132 Square mass change plot for CMSX-4/CN91 system tested at 950°C.

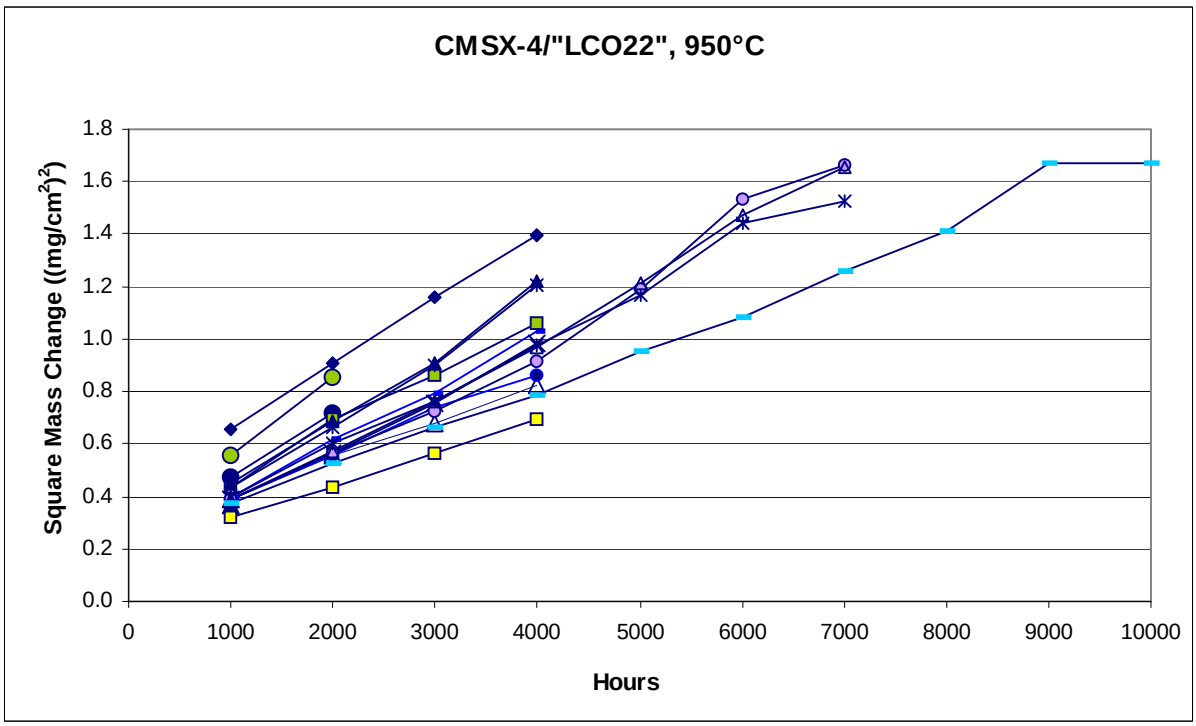

Fig. 133 Square mass change plot for CMSX-4/"LCO22" system tested at 950°C.

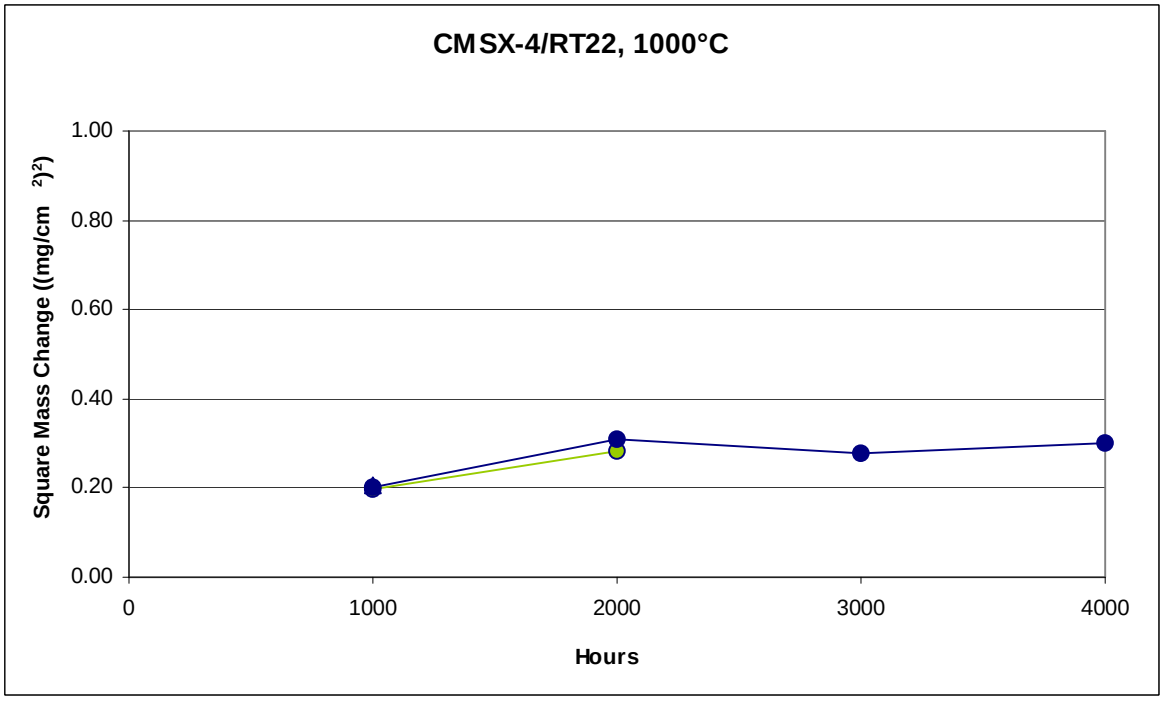

Fig. 134 Square mass change plot for CMSX-4/RT22 system tested at 1000°C.

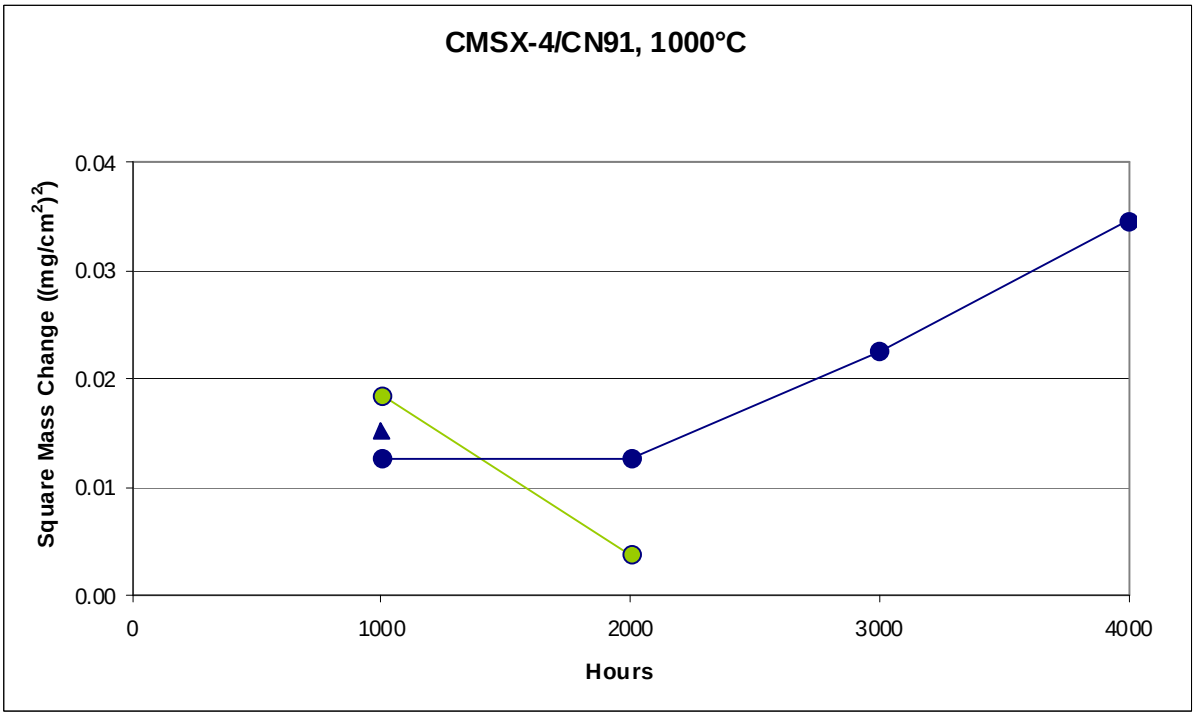

Fig. 135 Square mass change plot for CMSX-4/CN91 system tested at 1000°C.

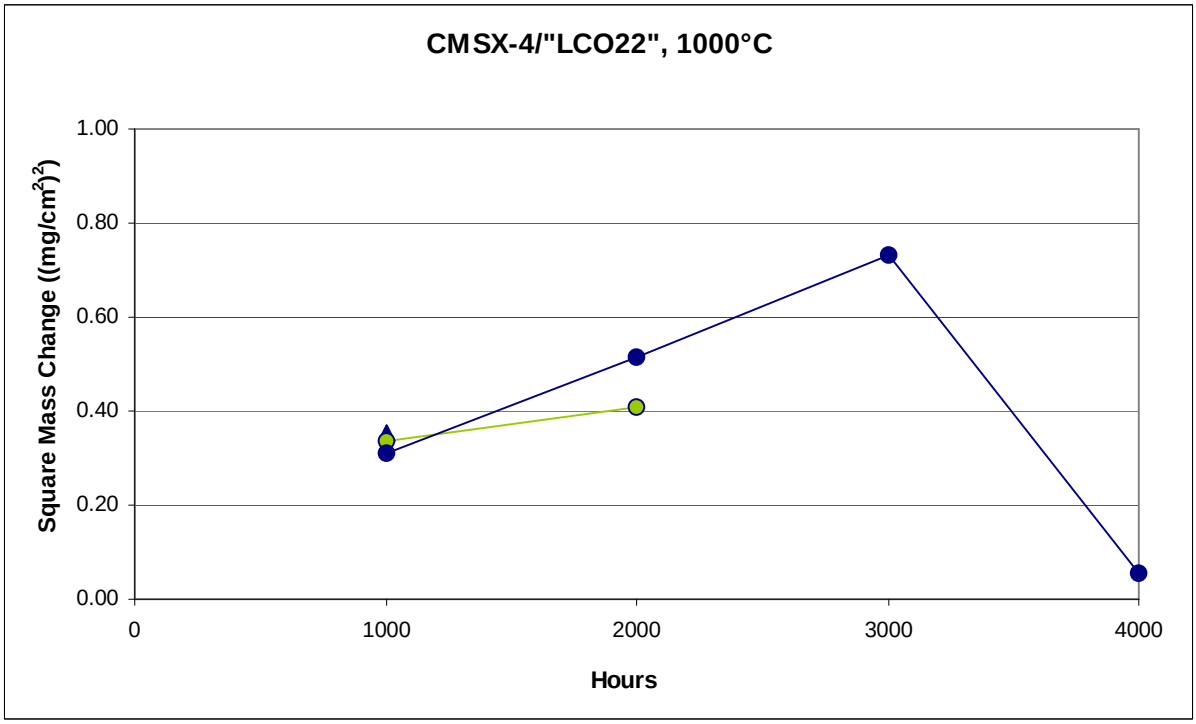

Fig. 136 Square mass change plot for CMSX-4/”LCO22” system tested at 1000°C.

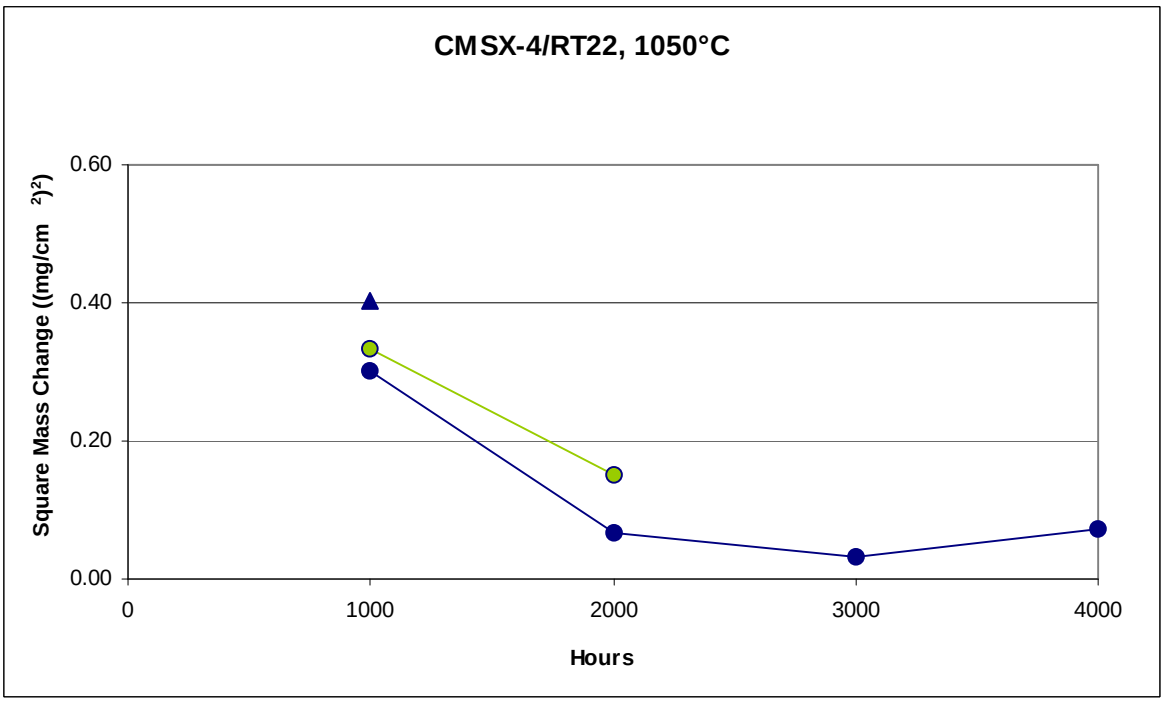

Fig. 137 Square mass change plot for CMSX-4/RT22 system tested at 1050°C.

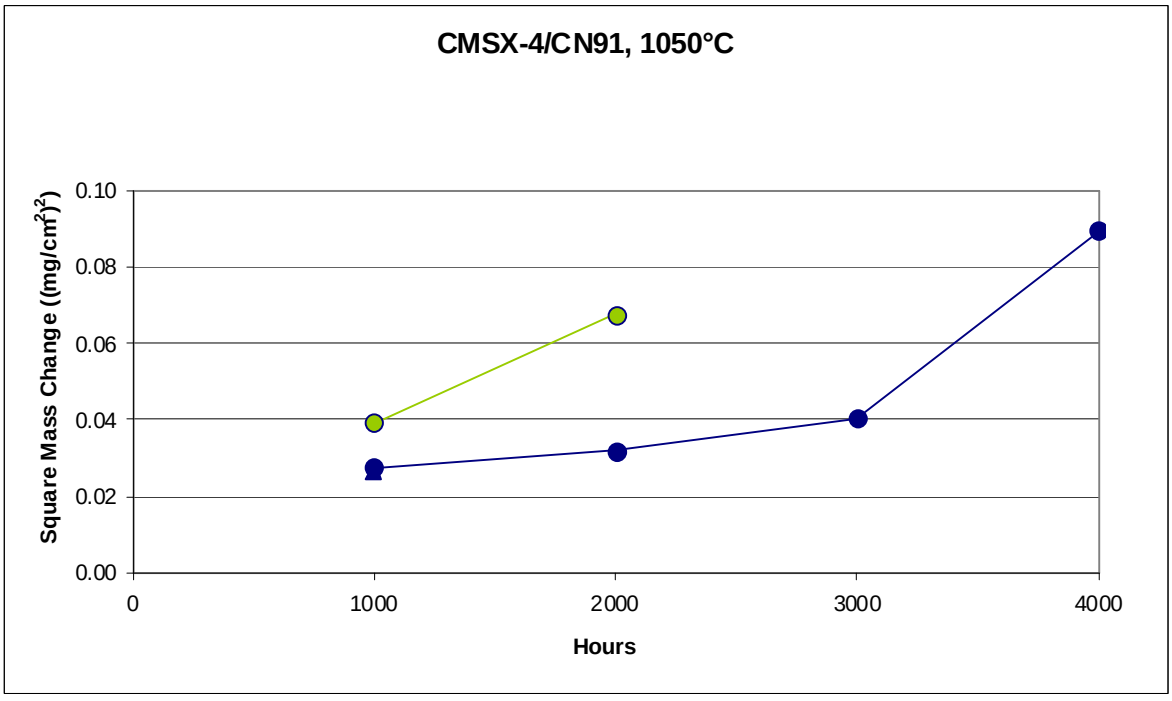

Fig. 138 Square mass change plot for CMSX-4/CN91 system tested at 1050°C.

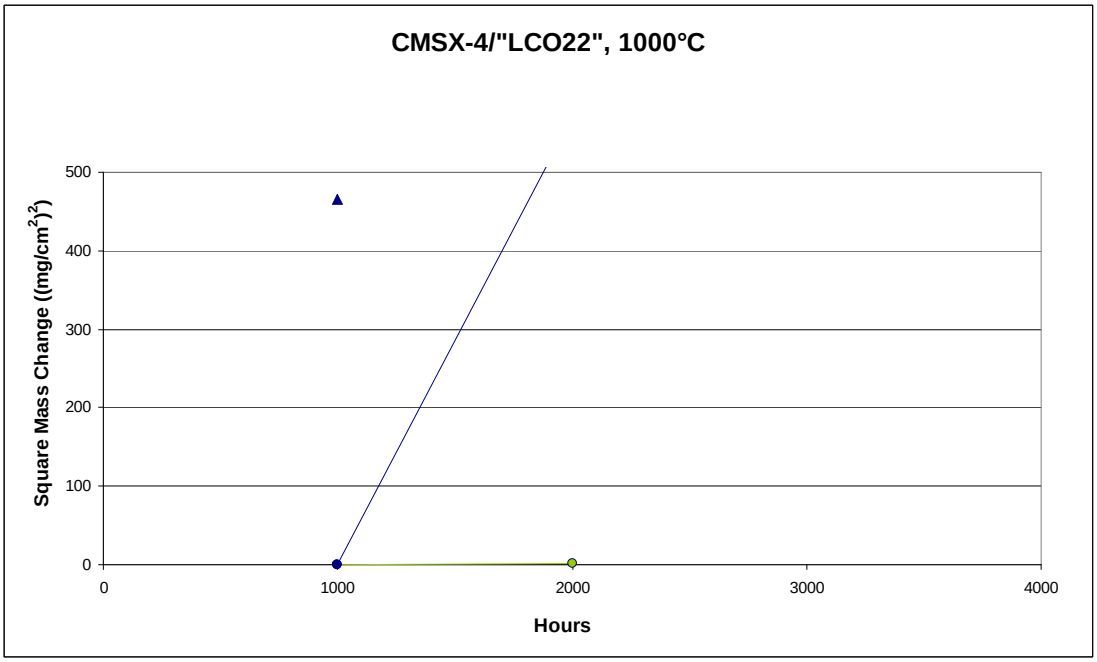

Fig. 139 Square mass change plot for CMSX-4/"LCO22" system tested at 1050°C.

Some authors, for examples Angenete and Stiller [1-7], have studied in detail RT22 and MDC150L coated CMSX-4 behaviours at high temperature (1050°C), both for short exposure time (1 hour) and prolonged exposure (up to 20,000 hours). One of the two Pt-aluminide coatings considered by the authors, RT22, is the same as tested in this study, while MDC150L is an outward grown Pt-aluminide coating and for the similarity with CN91 a comparison between their performances has been considered possible.

The mass change data relative to CMSX-4/RT22, tested at 1050°C, have been plotted in figure 139 and compared to those observed by Angenete et al. [2, 7]. The trend looks different; however the authors have observed mass gain during the first 1000 hours, as we did; both, moreover, have been observed spalling occurring after 1000 and 2000 hours (in our case heavier).

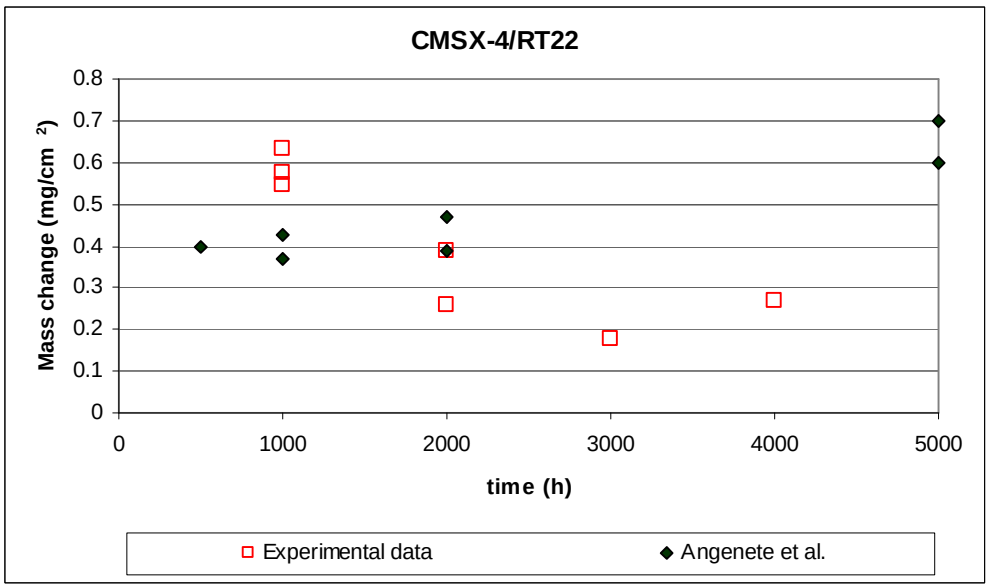

Fig. 140 Comparison between mass change data observed for CMSX-4/RT22, tested at 1050°C, in this study and by Angenete et al. [2, 7].

The authors provide, moreover, average TGO thickness measurements; we have calculated the same values for each temperature and exposure time (table 6 I and II below) from the 24 measurements of the oxide thickness taken as described in section 2.2.4. Comparing the results at 1050°C, we haven't observed for RT22 the increase in TGO thickness as Angenete et al. did and our scale results thicker (2.5 µm vs 5.9 µm after 1000 hours, 4.65 µm after 4000 hours and 4 µm after 5000 hours for the authors). Moreover, after 4000 hours RT22 sample has been observed completely spalled, this can be correlated to a bad quality of the coatings or different exposure condition. The difference in TGO average thickness may be due to the use of two different procedures of measuring: Angenete et al. [7] calculated the average from the mass gain data and the measured area fraction of spalled oxide, while in this thesis *ImageJ* software was used to collect measurements of scale thicknesses from ESEM pictures (§2.24).

Table 6 Average of the TGO (Thermal grown oxide) measurements in microns (μm) for the Pt-aluminide coated systems tested.

CMSX-4/CN91		Exposure time (h)			
		1000	2000	4000	10000
Temperature (°C)	850	2.67	2.80	3.21	5.42
	900	5.30	6.43	4.99	2.11
	950	0.46	3.88	5.70	3.40
	1000	0.40	1.91	1.91	-
	1050	5.91	1.19	2.59	-

I

CMSX-4/RT22		Exposure time (h)			
		1000	2000	4000	10000
Temperature (°C)	850	0.65	0.87	1.00	1.12
	900	2.19	1.95	2.80	2.03
	950	3.79	4.86	3.23	3.20
	1000	3.95	3.76	3.25	-
	1050	5.91	4.65	0.00	-

II

The mass change results, reported in the literature's reference [7] for the outward grown coating MDC150L, illustrate, as we have observed for CN91, mainly mass gain over spalling during 4000 hours of exposure, figure 141. However, as we can observe in the figure, few data are available for the comparison. Moreover, also in this case, we haven't obtained increasing TGO average thickness measurements with time and generally our scale results were thicker.

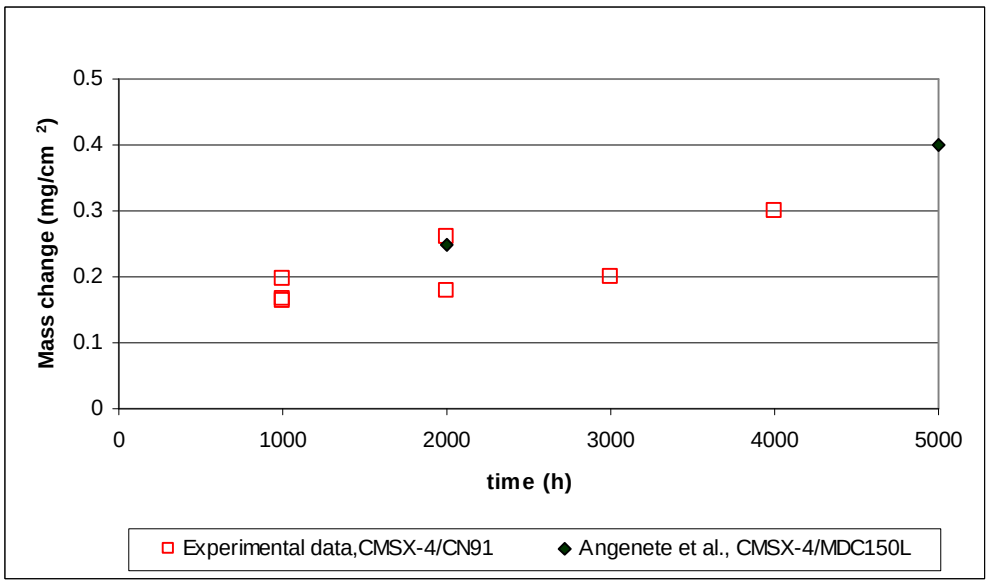

Fig. 141 Comparison between mass change data observed for CMSX-4/CN91, tested at 1050°C, in this study and by Angenete et al. [7].

The coating's ability to protect the substrate depends, amongst other factors, on coating thickness and quality of the deposition process. Considering the overlay coating "LCO22", as shown in picture 26d, the coating deposited on the sample is thinner than expected (about 20-30 µm vs 125 µm), not homogeneously thick and large voids in correspondence of the "grit" line are present. These features have affected the coating performance, as at high temperature (1000-1050°C) it has been depleted, while at lower temperature only a thin layer or part of the coating still exists.

Hence, in order to consider the overlay protective behaviour, it is necessary to consider just the results obtained at lower temperatures (850-900°C and 950°C for short exposure time), because at higher temperatures the oxidation and interdiffusion into the substrate degradated the coating too much.

Mass change plots (Fig.42-44) confirm the idea that oxidation proceeds initially through a transient stage, with high oxidation rate, and afterward through a steady-state having lower oxidation rate [14, 64]; moreover, as observed by Seo et al. [88, 89] who tested CoNiCrAlY (with the same weight composition of "LCO22") on IN718 for 1000 hours at 1000°C, "LCO22" exhibits uniform weight gain after the first stage.

The same authors measured the oxide scale being from 6.2 to 7.5 µm thick; looking at table 7 below, for the same exposure time (1000 hours), the scale is reasonably thinner at 850 and 900°C (respectively 3.28 and 4.42 µm); at 900°C the scale thickness is 5.68 µm and 5.45 µm respectively after 2000 and 4000 hours. In a previous work Seo et al. [88] observed that the square value of the thickness of the oxide scale (grown on CoNiCrAlY

exposed at 1000°C) was proportional to the square root of the exposure time. Figure 142 shows the plot of square of the TGO thickness versus square root of the exposure time obtained from the data gathered with the current study. The result is different to that observed by Seo D. [88], but it's necessary to highlight that the author exposed its sample up to 1000 hours.

Table 7. Average of the TGO (Thermal grown oxide) measurements in microns for the Pt-aluminide coated systems tested.

CMSX-4/ "LCO22"		Exposure time (h)			
		1000	2000	4000	10000
Temperature (°C)	850	3.28	2.72	1.00	2.52
	900	4.42	5.68	5.45	4.56
	950	4.19	5.81	3.81	4.65
	1000	6.04	7.02	6.05	-
	1050	9.67	9.29	6.64	-

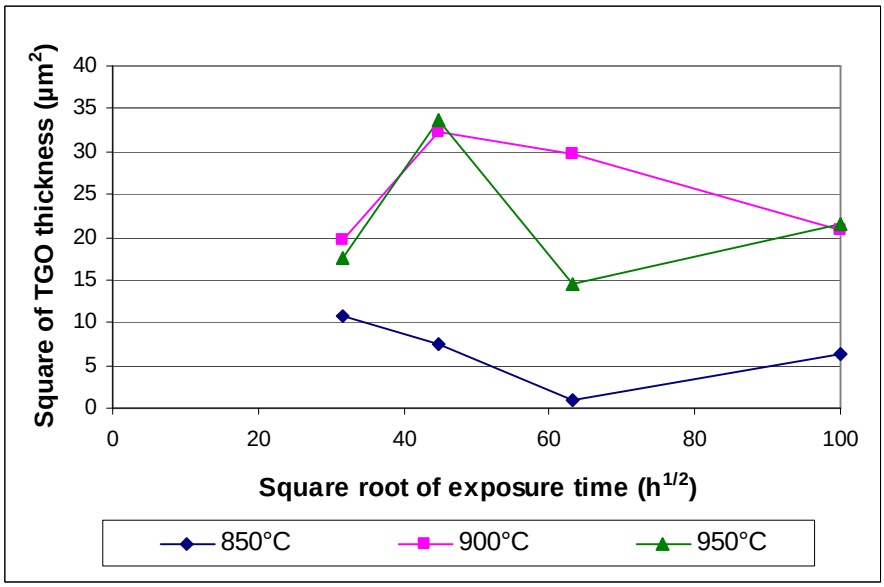

Fig. 142 CMSX-4/"LCO22": Square of the value of TGO thickness vs square root of the exposure time plot.

Spalling

To characterise the phenomenon of spallation both mass change plots and data of oxide thickness must be considered. In this last case in the process of scale thickness measurement, in the absence of oxide, the scale thickness has been attributed value of zero and then calculated the amount (in percentage) of the surface completely exposed has been calculated (and reported in table 8, I-III). Mass change plots, instead, provide different information about spalling, because the weight loss may be due to detachment of part of the oxide, just from the top of the scale; however, in case of higher mass gain than loss, a mass change plot can't show that spallation occurred. That's the case, for example, of RT22 coated system tested up to 4000 hours at 850°C, whose mass change plot show increase mass change, while table 8II indicates that the oxide spalled surface is 4.1, 12.5 and 8.3% after respectively 1000, 2000 and 4000 hours. It's likely that the reduced thickness of the oxide in some cases has resulted in its presence not being observed. The same observation can be made for CN91 coated sample up to 3000 hours of exposure at 850°C.

Table 8. Percentage of oxide spalled.

CMSX-4/CN91		Exposure time (h)			
		1000	2000	4000	10000
Temperature (°C)	850	12.5	12.5	37.5	20.8
	900	4.2	12.5	33.3	58.3
	950	4.1	0.0	4.1	4.1
	1000	8.3	8.3	0.0	-
	1050	33.3	50.0	45.8	-

I

CMSX-4/RT22		Exposure time (h)			
		1000	2000	4000	10000
Temperature (°C)	850	4.1	12.5	8.3	4.1
	900	0.0	0.0	0.0	4.1
	950	0.0	4.1	8.3	8.3
	1000	0.0	4.1	20.8	-
	1050	8.3	37.5	100	-

II

CMSX-4/"LCO22"		Exposure time (h)			
		1000	2000	4000	10000
Temperature (°C)	850	0.0	12.5	8.3	0.0
	900	4.4	0.0	0.0	0.0
	950	0.0	4.2	4.2	0.0
	1000	0.0	8.3	4.2	-
	1050	33.3	33.3	41.7	-

III

A clear relationship between median of oxide thickness and exposure time hasn’t been observed (figures 139-140) but, generally, it can be said that for the lower temperatures (850-900°C) the TGO average increases with temperature for the same exposure time for both the Pt-aluminide coatings. Considering the value of surface spalled, it can be said that for RT22 more spallation has been detected at the highest temperature 1050°C for 2000 and 4000 hours and at 1000°C for 4000 hours (Table 8II); CN91 has experienced the highest spalling either at 1050°C (for each time) and at 850-900°C with 4,000 and 10,000 hours of

exposure. It's, moreover, not possible to find just from the values presented in table 8 a correlation between percentages of surface spalled and average oxide thickness.
However, as explained ahead in section 4.1.4, there have been a number of studies devoted to modelling the growth and the spalling of the oxide scale [e.g. 62, 77, 98, 99, 100].

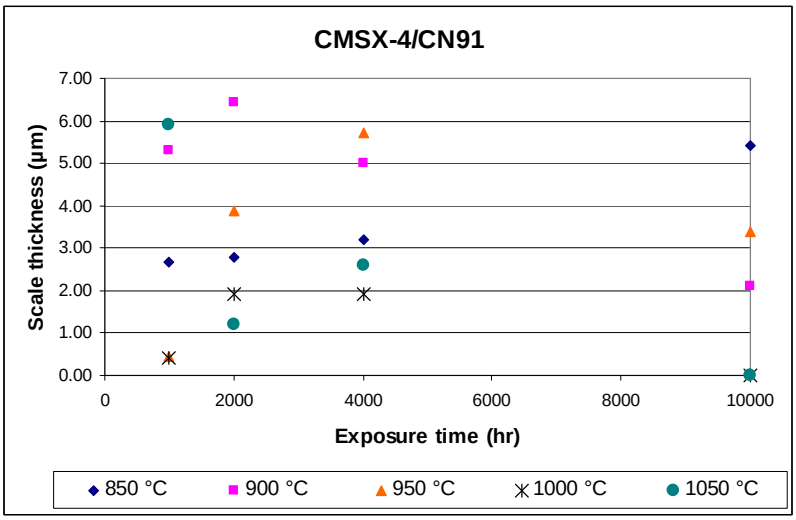

Fig. 143 Mean of the scale thickness measurements (without "0" values) on CMSX-4/CN91.

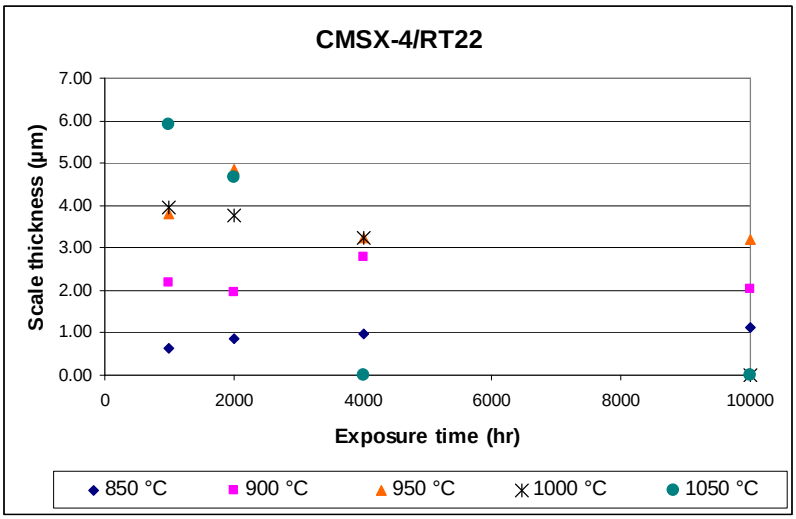

Fig. 144 Mean of the scale thickness measurements (without "0" values) on CMSX-4/RT22.

Spallation of the Pt-aluminide coatings RT22 (inward) and MDC150L (outward) has been studied by Angenete et al. [5] at 1050°C. In accordance to this thesis, RT22 has started to spall after 1000 hours of exposure; Angenete et al. [5], moreover, observed the scale detachment becoming catastrophic after 10,000 of exposure, while the present author has observed a complete free surface after 4000 hours. Concerning the outward grown coating, it has been observed, by Angenete [5], that the coating spalled moderately after 5000 hours, but it would be necessary to know how the measurements have been carried out. In our case mass change plots show increase mass change over the period of exposure, but in the same

time table I reports high percentage of surface exposed and the oxide thickness isn't so thick for motivating the mass gain.

A difficulty in correlating mass change to average of oxide thickness may come from the damage caused to the sample during the preparation (such as cutting and mounting) that can have led to de-cohesion or spallation and the specific activity of measurements (for example the TGO may be so thin to being confused for its absence, or the choice of the point to be measured could be influenced by the appearance of the scale).

Angenete et al. [7] suggest that RT22, tested at 1050°C, spalled mainly as a result of void formation at the coating/scale interface. According to the authors the higher scale loss by outward coating consumption of Al for scale replenishment leads to Ni inward diffusion; in turn this causes a net flow of vacancies which condense at the metal/oxide interface causing void formation. Void formation is the cause of scale detachment on the outward grown coating MDC150L just after 10,000 hours of exposure, while during the previous period spalling is attributed to weakening of the metal-oxide bonds, possibly due to segregation at the interface of impurities (e.g. S impurities).

As mentioned in section 1.4.4 spalling is correlated not just to void formation and metastable-stable alumina transformation, but to NiAl phases' transforming and surface roughening as well. The integrated study of these aspects could better explain the results obtained with this study. Concerning the phase transformation, it is slow at low temperature (850-900°C) and so the stresses arisen have low intensity resulting in less spalling; that can motivate the nearly parabolic trend in mass change we have observed at 850-900°C (Fig.32, 33, 37 and 38). At 950°C the transformation occurs frequently and faster, in fact spallation has been observed to be important (Fig. 34 and 39). At high temperature, since the metastable alumina is expected to grow just during the first hour of exposure the θ-α Al_2O_3 transformation can't be ascribed as the main reason of stress for the scale.

Finally the scale detachment is also a function of the material composition. We have mentioned in section 1.2.2 about the role of the reactive elements in improving scale adherence and reducing oxidation rate by slowing down Al transport mainly. Since, moreover, RT22, being an inward grown coating, incorporated more alloying elements than CN91, this may have increased spallation leading to the general higher percentage of free surface observed (Table 8).

4.1.2 Morphology of oxidation

Other aspects that have been considered in the analysis of the aged samples are the change in microstructure and the onset of spalling.

As already reported by Angenete et al [3], for tests carried out at 1050°C, the IZ (of RT22 coated CMSX-4) grows a little bit inward during the exposure, but after long heat treatment (2000 hours) it does not increase further. In this study thicker IZs have been observed after 2000 hours of exposure at lower temperature, 900 and 950°C, while change in the IZ thickness with time at 850°C was not evident.

Picture c (Fig.26) shows an OZ of RT22 coated sample rich in precipitates; these, as shown by the series of pictures of figure 51, are still present after 10,000 of exposure at 850-900°C, while after 2000 hours of exposure at 950-1000°C and earlier, for the highest temperatures, they have disappeared leaving just few bigger precipitates.

Both Zhang [123] and Angenete [2] say the precipitates form as a result of Al diffusion, which leads to the entrapment of W, Re, Mo and Ta and low solubility of these refractory elements in β-NiAl grains. Moreover, they observed that some of these precipitates increase in size, while others (μ phase) disappeared after 2000 hours of exposure at temperature ≥ 950°C and it is due to the higher solubility of W and Re in the β-NiAl phase since Al concentration has decreased, by 2000 hours at 950°C and above.

Finally, these authors have observed increasing precipitates coarsening beneath the IZ. Similar observations can be made in the present study assuming that the acicular shape particles, seen (Fig.53, micrographs 33-36) when characterising the samples tested at 1050°C, at each exposure time, and at 1000°C after 4000 hours are refractory metal rich particles.

For the second Pt-aluminide coating, CN91, ESEM pictures show increased IZ thickness at temperature higher than 950°C, as observed by Angenete [5], even if just at 1050°C on MDC150LC coated samples. The same authors also observed that CN91 has a precipitates-free OZ, both as-coated and heat treated and that the precipitates coarsening beneath the IZ increases with time at 1050 °C. ESEM pictures of CN91 (Fig. 52) in this study do notshow any acicular precipitate formation at a temperature lower than 1050°C and, at this temperature, not before 1000 hours of exposure.

Scale chemical composition

From the ESEM analysis the scale, grown on RT22, has been observed to consist mainly of two layers: an outer layer of mixed oxide (of Al, Cr, Ni, Ti, Ta) and an inner layer predominantly formed of alpha alumina (Fig.145a). For the scales protecting the surface or remaining after spalling, this is visible at any temperature and exposure time, with an increase in the inner alumina scale thickness with the exposure time.

As described by Birks [53] and reported in section 1.4 the mix oxides and spinels layer is the result of the transient stage of oxidation, during which thermodynamics encourages the formation of several alloying/coating metals oxidation; afterward the lowering of the p_{O_2} at the metal/oxide interface leads to the growth of the dominant underlying alumina scale, which than grows by inward oxygen diffusion. The ESEM analysis has, moreover, shown that the mixed oxide can extend within the two alumina layers (for example at 900-1000 and 1050°C, Fig. 53). Brumm MW and Grabke HJ [14] have proposed that for Ni-Al alloys once $NiAl_2O_4$ forms it allows outward diffusion of cations and the formation of theta alumina at the oxide/gas interface. Afterward, this θ-Al_2O_3, transforms to α- Al_2O_3 (inward transformation) bringing about this mix oxides layer, covered with alpha alumina.

Alternatively, Angenete [7] proposes that during oxidation micro-cracks are likely to form due to growth stresses and convolution, permitting oxygen access to the metal interface and thus the oxidation of virtually all the elements of the coating.

The scale observed on CN91 and represented in figure 145b is, unlike that grown on RT22, homogeneous in colour, but composed of two layers as well: the inner constitutes of α-Al_2O_3 and the outer of mixed transient oxide.

Angenete et al. [6, 7], who compared the scale composition after prolonged oxidation (up to 20000 hours) at 1050°C of CMSX-4/RT22 and CMSX-4/MDC150L (outward Pt-aluminide diffusion coating) systems, have already highlighted the difference existing between the scale grown on the inward and outward coatings. The former is characterised of two layers the inner composed mainly of corundum (having columnar grains) and the second of TiO_2 and Ta_2O_5 along with spinels ($NiAl_2O_4$, $CoAl_2O_4$, $CoCr_2O_4$), characterized by equiaxed grains. That structure is schematised in figure 145c. On the other side the scale formed on the outward diffusion coating is almost exclusively formed of large-grain and columnar corundum with just occasionally TiO_2 grains, hence the homogeneous colour.

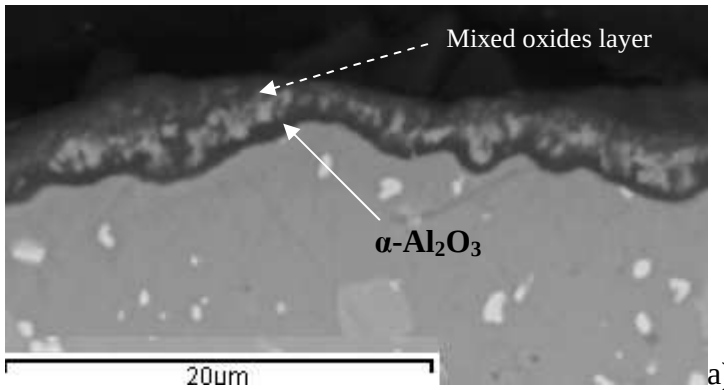

a)

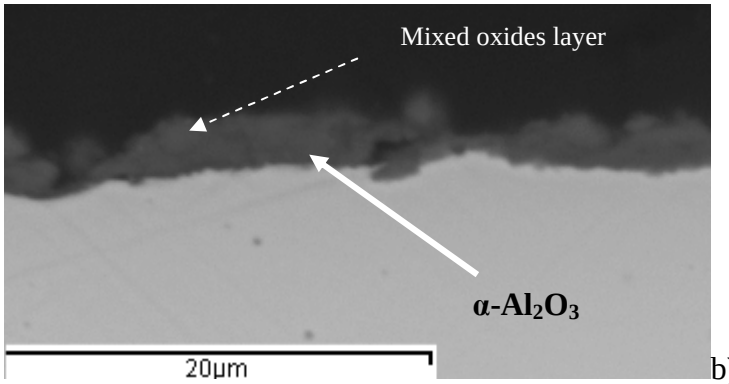

b)

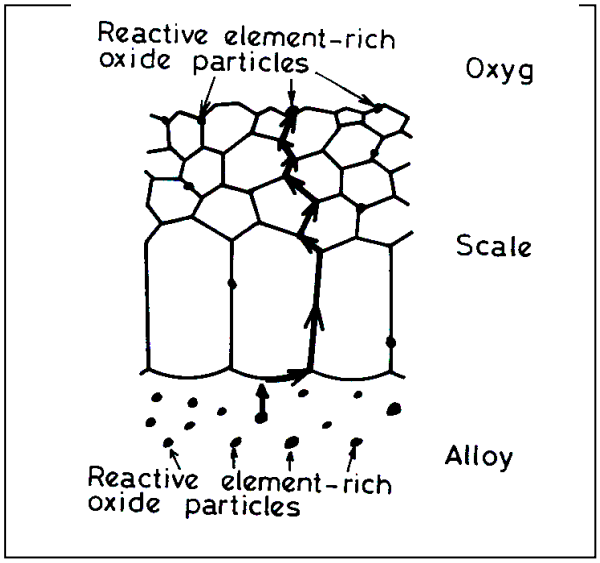

c)

Fig. 145 Comparison between oxide scale formed on RT22 (a) and CN91 (b) coated CMSX-4, after 4000 hours at 900°C, from this work. Figure 145c presents a schematic diagram of a scale formed during high temperature oxidation and of reactive elements diffusion from the substrate [104].

The overlay coating/alloy system also shows the formation of a double layered scale with mixed oxide on the top and α- Al_2O_3 at the coating interface. One image of this oxide scale is reported in figure 146a and is compared to a previous observation (Fig. 146b)[87].

Tang et al. [110] showed that the oxide scale grown on CoNiCrAlY, isothermally oxidised at 1000°C, consisted primarily of spinel type oxides after 1 hour; for longer time, besides the spinel-type oxides, α- Al_2O_3 and Cr_2O_3 (above alumina) were also identified.

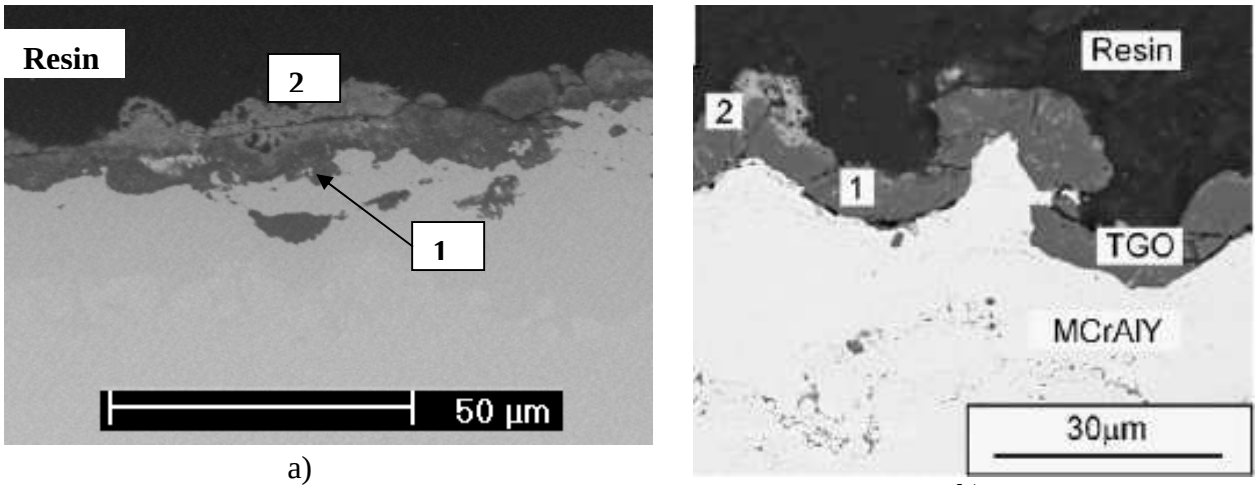

Fig. 146 Scale composition formed on CMSX-4/"LCO22" tested at 900°C for 4000 hours (a) and observed by Seo et al. [87] on INCL718/ CoNiAlCrY at 1050°C after 1000 hours (b):1=alumina, 2=mixed oxides.

4.1.3 Comparison of materials performances

Mass change plots, ESEM analysis and oxide thickness measurements point out the differences in the protective behaviour of the two Pt-aluminides coating.

At the low temperatures, 850 and 900°C, the RT22 coated system has formed always a thinner scale than that of CN91, less of this thinner oxide spalled on each exposure cycle and the mass change plot revealed more homogeneity in the oxidation behaviour amongst the samples. Consequentely, RT22 coatings looked to be best performing between the two Pt-aluminide coatings. At 950°C the reproducibility of CMSX-4/CN91 is again poor. At this temperature the scale grown on CMSX-4/CN91 is thinner than that grown on CMSX-4/RT22 up to 2000 hours of exposure; more spallation has been observed for the outward grown coating after 1000 hours while for 2000 hours of exposure the result is reversed. For longer exposure time on CMSX-4/RT22 experienced more spallation and the average of the oxide thickness is less than that of CMSX-4/CN91. The results obtained at 950°C do not allow to say that one coating provided better protection than the other one. At the highest temperature (1000-1050°C) the coatings RT22 experienced higher mass change and formed thicker scale than CN91 coatings (with the exception of 4000 hours of exposure at 1050°C). More spallation has resulted at these temperatures for the outward grown Pt-aluminide coating for exposure time up to 2000 hours, that is why, probably the oxide scales have been observed thinner for CMSX-4/ CN91. These results suggest that CN91 coatings may be more protective at the highest temperature for long exposure times.

ESEM micrographs produced for each temperature/time for Pt-aluminide coated systems (Fig. 50-51) underline the difference in the evolution of the coatings microstructure. The CMSX-4/CN91 system, resulted in higher metallurgical stability, in fact it formed less and smaller precipitates beneath the IZ at temperature higher than 950°C.

According to what is described in section 1.6, the different behaviour of the two Pt-aluminide coatings is a consequence of the specific growth mechanisms that each of them has during aluminisation. In fact, the different growth direction (inward for RT22 and outward for CN91) causes the differences in the coating compositions and their surface topographies.

As-coated CN91 has smoother surface (due to outward growth of the coating during aluminizing) and once exposed it has formed a large grain scale, as observed by several authors [6, 116], for the outward growing coating MDC150L). The as-coated RT22 has a more heterogeneous topography, rough and porous and this according to Angenete et al. [2] increases the effective area at the gas interface which causes higher mass change for this inward formed coating than for the outward formed coating. However, due to the inward

growth of α- Al_2O_3 the kinetics are expected to decrease after prolonged oxidation. This is observed by the authors, and in our study, at 1050°C, not for lower temperatures.
Svensson et al. [109], following 1 hour oxidation test at 1050°C, observed the formation of metastable alumina phases in the scale grown on the outward diffusion coating (MDC150L), but not the stable slower growing α- Al_2O_3 which instead has been detected in the scale of the inward grown coating (RT22). This result has been attributed to the higher Al and Pt content in RT22 at the oxide/metal interface that promotes α- Al_2O_3 formation.
At 950°C the characteristics of oxidation fall between that observed for the lowest and the highest temperature, the processes are complex; however, it looks from the mass change plots, ESEM pictures and average of the oxide scale thickness measurements that the two Pt-aluminide coatings performed quite similarly.

Mass change plots for the temperatures 850 and 900°C (Fig. 47-48) illustrate how the oxidation kinetics of the NiCoCrAlY overlay coating are similar, despite the poor reproducibility of both the coated systems, to that of the low-activity Pt-aluminide coatings. The same observation has been previously made by Evans et al [33] for temperature as high as 1100°C. The oxidation of the substrate, experienced by the samples at 950, 1000 and 1050°C after the thin coating's destruction, doesn't allow the comparison between overlay and outward grown coating behaviours'.
According to Evans et al [33], since for the Pt-aluminide coatings/alloy interdiffusion occurs more readily than in overlay coating/alloy system (because of less interfacial restraint), the former is more susceptible to aluminium loss. Figure 147 shows the aluminium concentration profile in the as-coated condition and after 4000 hours of exposure at 900°C of the three coated systems (CMSX-4/RT22, CMSX-4/CN91 and CMSX-4/ "LCO22"). Evans et al [33] highlight that, even though the aluminium content of diffusion coating is around twice that of overlay coating, the total available Al reservoir is larger in the latter, because the coating is thicker. Thus, as already presented by Grünling et al. [43] in the schematic representation of the relative corrosion and oxidation resistance of coatings at high temperature (§1.6.2, Fig. 20), CoNiCrAlY are expected to performed better in oxidative environment than Pt-aluminide coatings.
Concerning the lower temperature (850-900°C) the better protection of "LCO22" may be confirmed by less spallation (Table 8 III) occurred for long exposure time (10,000 hours), while for shorter time (1,000-4,000 hours) the resulting percentage of free surface doesn't differ between RT22 and "LCO22" coated specimens. However it's important to highlight that whether alumina reforms after spollation is important and a better study of the oxide

spallation may be carried out testing samples in independent crucibles in order to gather the material spalled.

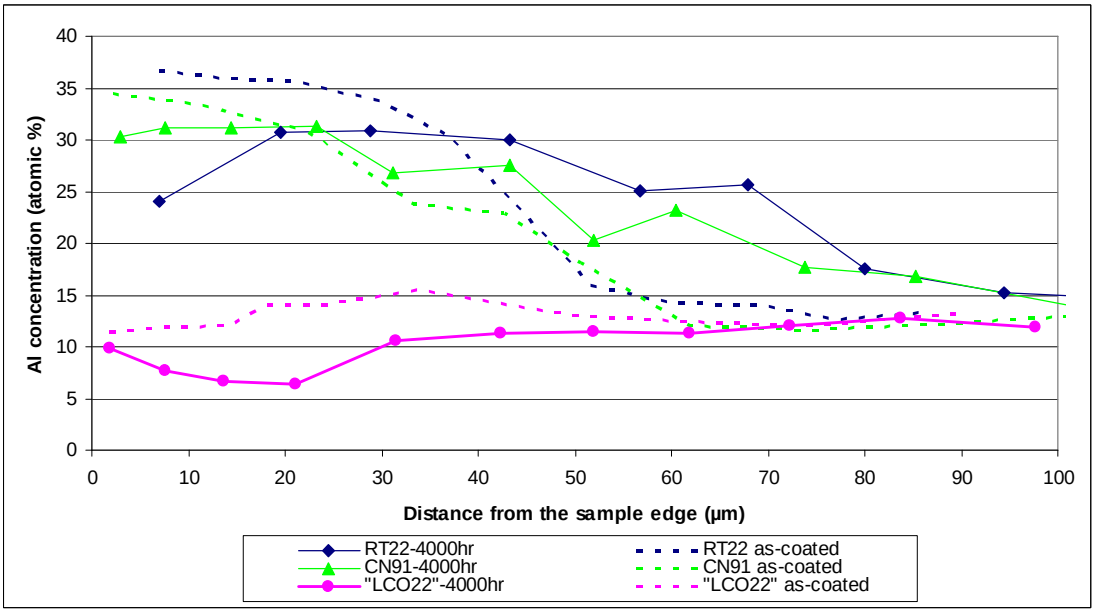

Fig. 147 Comparison amongst aluminium concentration profiles in the as-coated condition and after 4000 hours of exposure at 900°C of the three coated systems (CMSX-4/RT22, CMSX-4/CN91 and CMSX-4/ "LCO22").

The microstructure of the as-coated CoNiCrAlY coatings consists of a mixture of β-NiAl, γ' (Ni_3Al) and γ phase [33, 67] and, according to that explained in section 1.6.3, during oxidation (and corrosion) β-phase decomposes into the less Al rich phase γ' and then γ.
Within the following micrographs, figure 148a, shows the structure of the as-coated CMSX-4/"LCO22" system; from that it is particularly evident that the coating, sprayed on the superalloy, presents, even before the ageing, a state of β phase depletion. Consequently, it is not surprising that the micrographs, correlated to the tests carried out at 850 and 900 ºC (respectively Fig. 148 b, c and d), do not allow to observe the presence of the β phase.

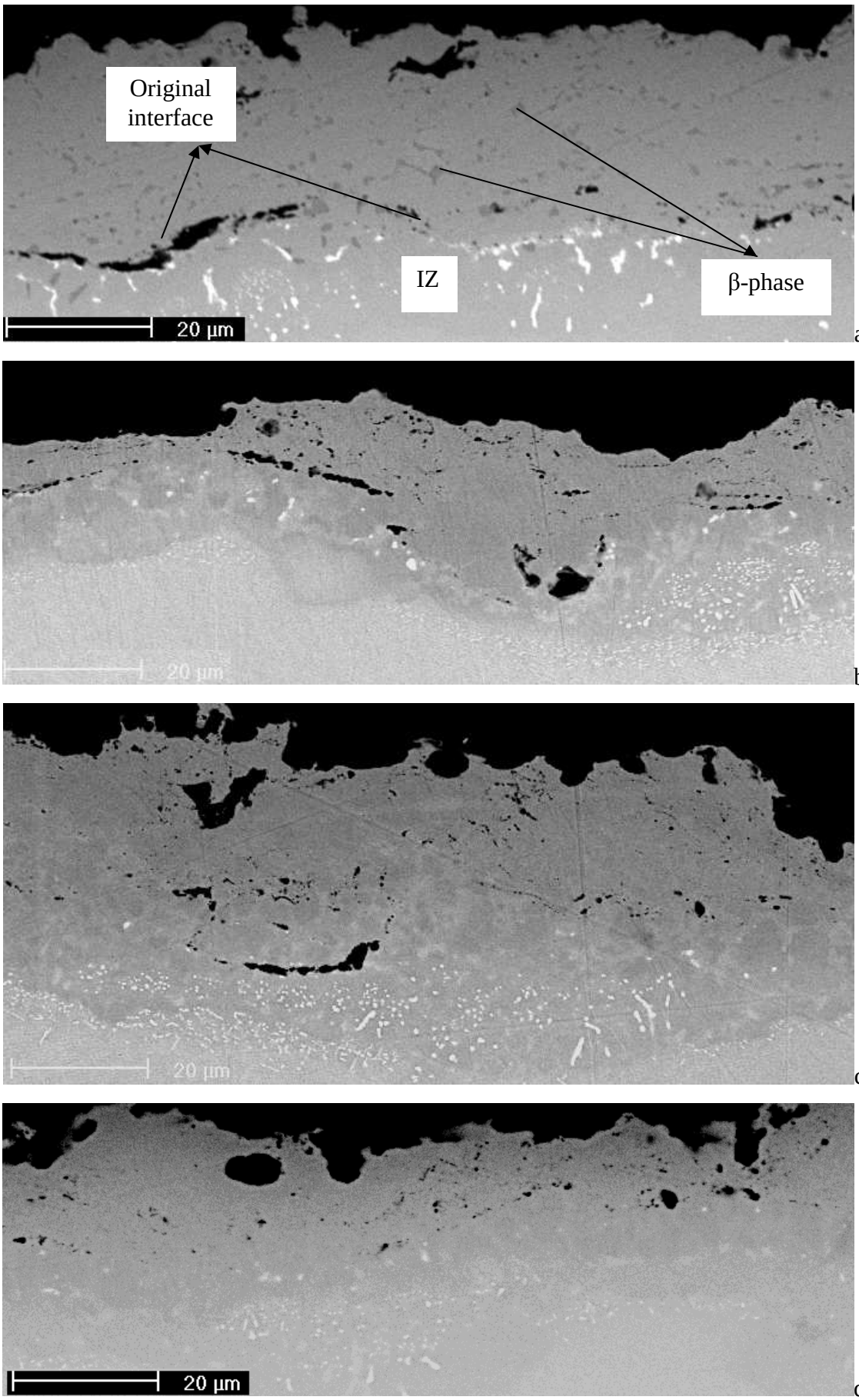

Fig. 148 Microstructures of CMSX-4/"LCO22" : a) as-coated, b)after 1000 hours at 850ºC, c) after 2000 hours at 850 ºC, d) after 1000 hours at 900 ºC.

Moreover, figure 149 illustrates the Al concentration profile (from ~5 to 70 µm) of the overlay coated samples tested for 1000 hours at 850 and 900°C. The concentration, which do not differs in the two cases, ranges between 4 and 6 weight %.

Previously, Raffaitin et al. [81] have tested for 900 hours at 1000°C a NiCoCrAlYTa coated MC2 system, with a coating thickness of 30 µm. After the exposure the aluminium concentration was between 3-5 weight % (considering up 70 µm from the coating surface). According to the authors, after the 900 hours exposure, the coating, due to β-phase decomposition, consisted in γ single-phase, with aluminium concentration of 3wt%. This comparison permits us to conclude again that the CMSX-4/"LCO22" system has experienced the complete β transformation into γ during the exposure and that was due to the thin coating deposited and the bad deposition carried out.

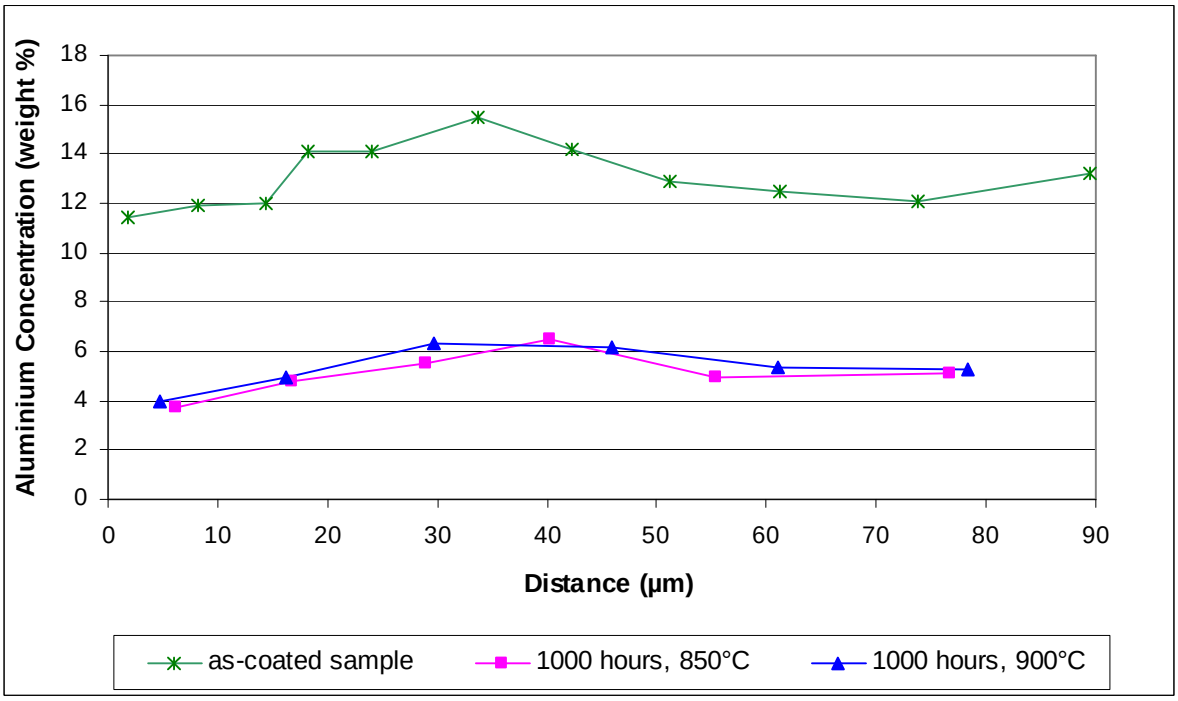

Fig. 149 Aluminium concentration profile of the CMSX-4/"LCO22" samples tested for 1000 hours at 850 and 900°C.

4.1. 4 Oxidation modelling

As already explained in section 1.4.2, which deals with the kinetics of oxidation, Wagner's Theory describe mathematically the oxidation rate of a metal/alloy at high temperature through the equation of a parabola, which means that diffusion of metal and/or oxygen ions through the oxide lattice is rate determining. However, its already known that in reality the oxidation process can not so easily described, since there are different factors that change

during the exposure (for example oxide type forming and scale break down) causing its move away from the parabolic trend. This is clearly visible in the mass change plots reported in section 3.1.1: a nearly parabolic rate is generally observed at the lower temperature 850-900°C, while at higher temperature the continuous scale breakdown caused a complex oxidation rate/mass change trend.

However, in approaching the materials' behaviour modelling, it has first been assumed that the oxidation could be described in a parabolic way, according to the equation:

$$\Delta w^2 = k_p t + C \quad (20)$$

Δw=mass change (mg)

kp= rate constant for alumina ($mg^2/(cm^4\ h)$)

t= time (h)

C=integration constant

Equation 20 has been applied to any value of mass change of the replicated samples tested at 850, 900 and 950°C; hence the rate constant calculated averaging the slope's values obtained. Looking at the squared mass change plots of figures VII and VIII (appendix), respectively CMSX-4/RT22 and CMSX-4/CN91, the curves trend reflects as at 950°C spallation becomes very important in affecting the rate constant and a few specimens have been observed behaving in a nearly parabolic trend. Only the square mass change data correlated to the latter have been employed for the rate constant calculation and the new plots are presented in figure I and II (appendix). In table 9 and figure 150 the rate constant values, calculated for the tests carried out at the temperatures of 850, 900 and 950°C, are presented. Moreover, since the evolution of the oxidation process described in the squared mass change vs time plots doesn't provide in any case a line crossing the origin of the axis (i.e. C never=0), the rate constants have also been calculated for the value 0 of the parameter C (equation 20). These values are also provided in figure 149.

Moreover, figure 151 illustrates the consistency of the rate constant values, calculated with this study, by a comparison with those values observed by Grabke [40] and Hindam [55]. The former provides the rate constant separately for α- Al_2O_3 and θ- Al_2O_3, determined by oxidation of Ni/Fe aluminide alloys; the latter, instead, who tested binary and ternary aluminium containing alloys, provides a range of values for alumina calculated without considering, as we did initially, the formation of different alumina phases. Finally figure 151 provides the value of the constant rate calculated by Seo et al. [88] for CoNiCrAlY exposed at 1000°C.

If, from one side, the parabolic rate constant values calculated result following the trend of previous study, the plot of the logarithm of the square mass change in function of the

logarithm of the time, carried out for the three coated systems and presented in appendix (Fig. III-XI) shows especially for the temperature 900 and 950 °C, the non-parabolic trend.

Table 9 Values of the rate constant, Kp, calculated from the experimental data. Values of Kp minimum (Kmin) and K maximum (Kmax) and values of the constant rate considering C equal to 0.

	Temperature (°C)	10^{-4}/K	Kp ($mg^2/(cm^4\ h)$)	Kp min ($mg^2/(cm^4\ h)$)	Kp max ($mg^2/(cm^4\ h)$)	Kp (with C=0) ($mg^2/(cm^4\ h)$)
CMSX-4/RT22	850	8.90	1.45E-05	8.92E-06	1.90E-05	1.40E-05
	900	8.53	4.40E-05	2.02E-05	1.11E-04	4.91E-05
	950	8.18	8.63E-05	8.09E-05	9.27E-05	1.02E-04
CMSX-4/CN91	850	8.90	7.42E-05	9.33E-06	1.71E-04	7.45E-05
	900	8.53	1.05E-04	6.58E-06	2.64E-04	1.19E-04
	950	8.18	1.60E-05	9.96E-06	2.54E-05	1.81E-05
CMSX-4/ "LCO22"	850	8.90	9.76E-05	5.43E-05	1.44E-04	1.06E-04
	900	8.53	2.04E-04	7.34E-05	3.28E-04	2.35E-04
	950	8.18	2.61E-04	1.61E-04	4.26E-04	2.86E-04

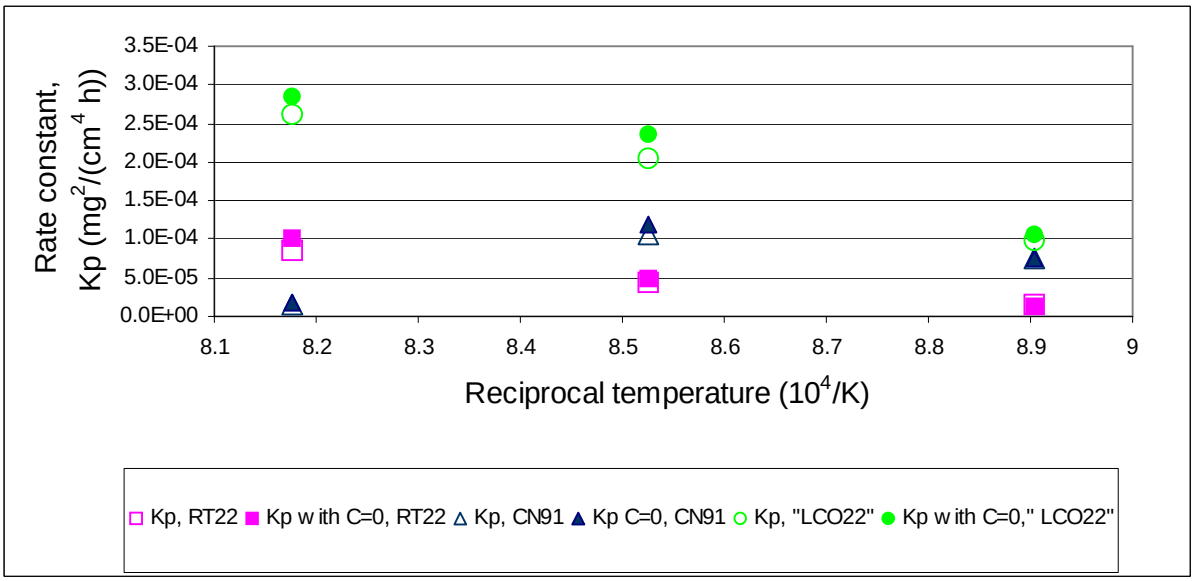

Fig. 150 Arrhenius plot for the parabolic rate constant values calculated from the experimental data for the three coated systems (CMSX-4/RT22, CMSX-4/CN91, CMSX-4/"LCO22") tested at 850, 900 and 950°C.

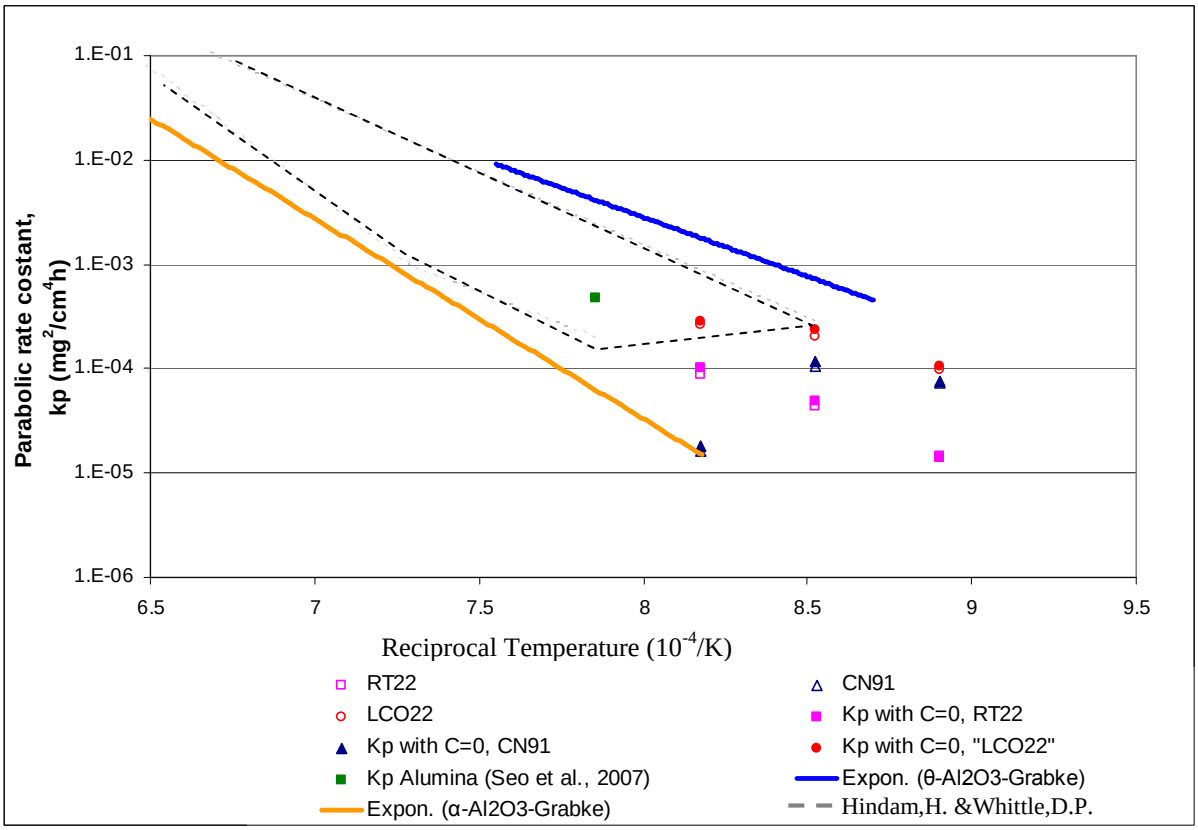

Fig. 151 Comparison between rate constant values calculated from the experimental data and those provided by Grabke H.J. et al. [40] and Hindam H. et al. [55].

The starting point for modelling the oxidation behaviour of the Pt-aluminide coated system has been to consider it following the ideally parabolic trend, but proceeding through two stages: the transient stage, which has higher rate and coincides with the formation of θ- Al_2O_3 (along with other oxides than alumina), and it's described by equation 21, followed by the steady state of oxidation, characterised by α- Al_2O_3 formation and described by equation 22. Thus the entire process deriving from the coming of one stage after the other can be described by equation 23.

$$\left(\frac{\Delta w_\theta}{A}\right)^2 = \left(k_{p\theta} * t\right) + C \qquad \text{if } t<t_c \qquad (21)$$

$$\left(\frac{\Delta w_\alpha}{A}\right)^2 = \left(\frac{w_{\theta c}}{A}\right)^2 + k_{p\alpha}\left(t - t_c\right) \qquad \text{if } t>t_c \qquad (22)$$

$$k_p = k_0 * \exp(-E/RT) \qquad (23)$$

Where

Δw=mass change (mg)

A=material surface (cm^2)

kp_θ= rate constant for θ- Al_2O_3($mg^2/(cm^4\ h)$

kp_α= rate constant for α- Al_2O_3 ($mg^2/(cm^4\ h)$)

k_0 =standard rate constant ($mg^2/(cm^4\ h)$

w_c=critical weight (mg/cm^2)

t=time

t_c=critical time

E=activation energy (J)

R=gas constant (J/(K mol))

T=température (K)

C=integration constant

The following mass change plots, figures 152-153, show the comparison between experimental data and prediction, carried out using the model previously described. As we can observe for the low temperatures, 850 and 900°C, the model can reproduce the mass change of RT22 coated system, while at high temperature the fit isn't good anymore. That is motivated by the fact that at the lowest temperatures spalling occurred, but the mass gain is always greater than the material loss, thus the model, which describes just alumina growth and not its detachment, can well predict the observed mass change. For temperatures higher than 950°C, the scale loss becomes very important and higher than the mass gain, consequently the simulation fails in the mass change prediction.

The model to really predict the material behaviour must include the phenomenon of spallation.

Alternatively, the alumina growth model previously presented, might be employed for mass change prediction at temperature higher than 950°C, if spalled oxide had been collected, and thus its weight added to the sample weight. This procedure could not been applied because each crucible, placed in the furnace contained four samples, and the oxide loss could not be separated.

In the following plots each lines represents the mass change experienced by one samples.

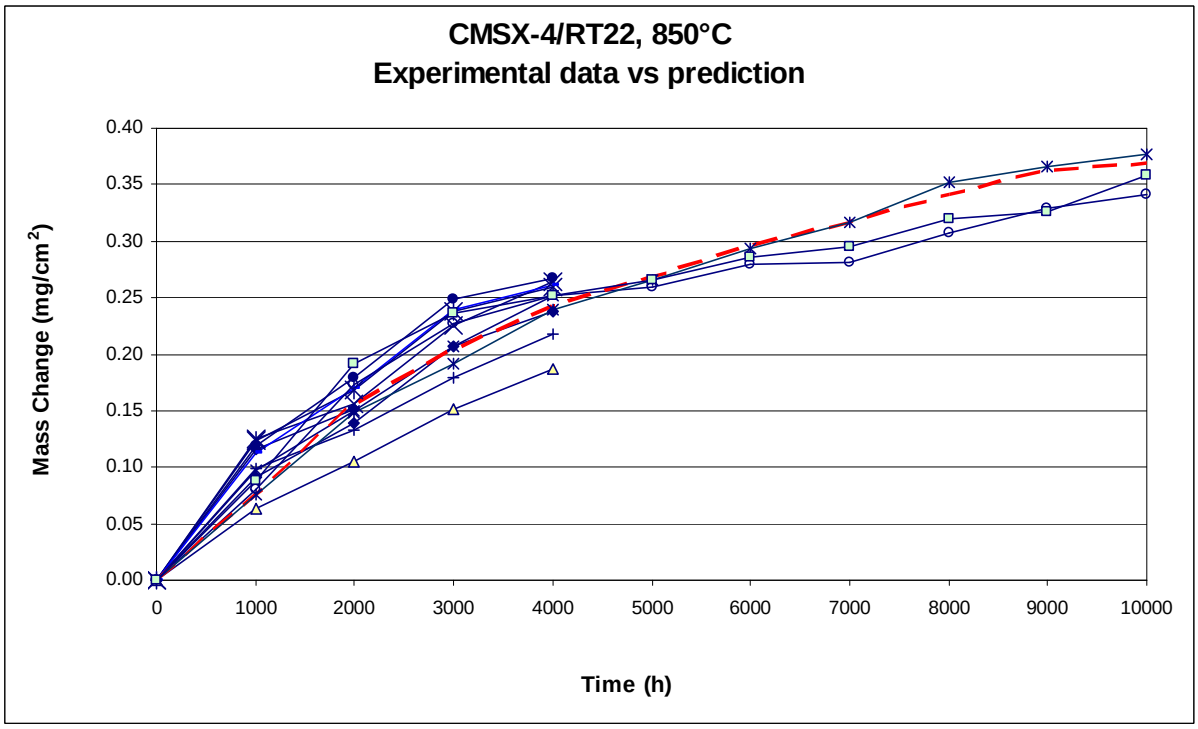

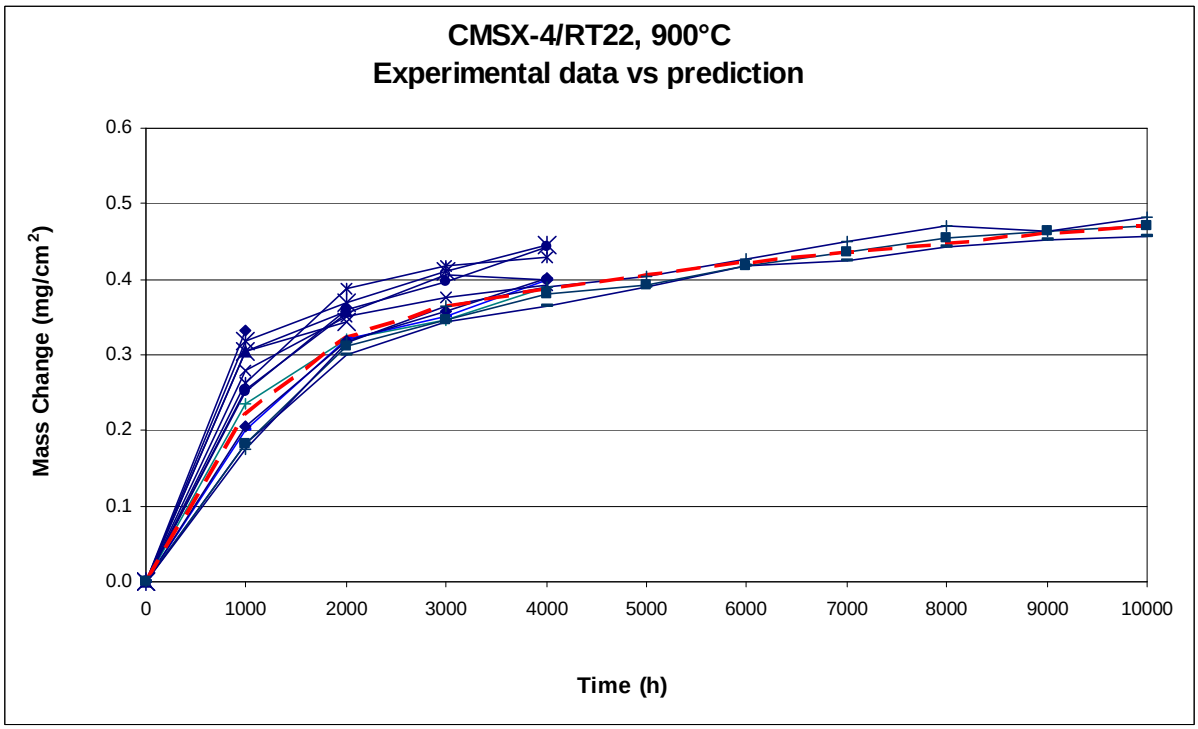

Fig. 152 Comparison between mass change experimental data (- - - -) and mass change prediction (- - - -) at a) 850 and b) 900°C.

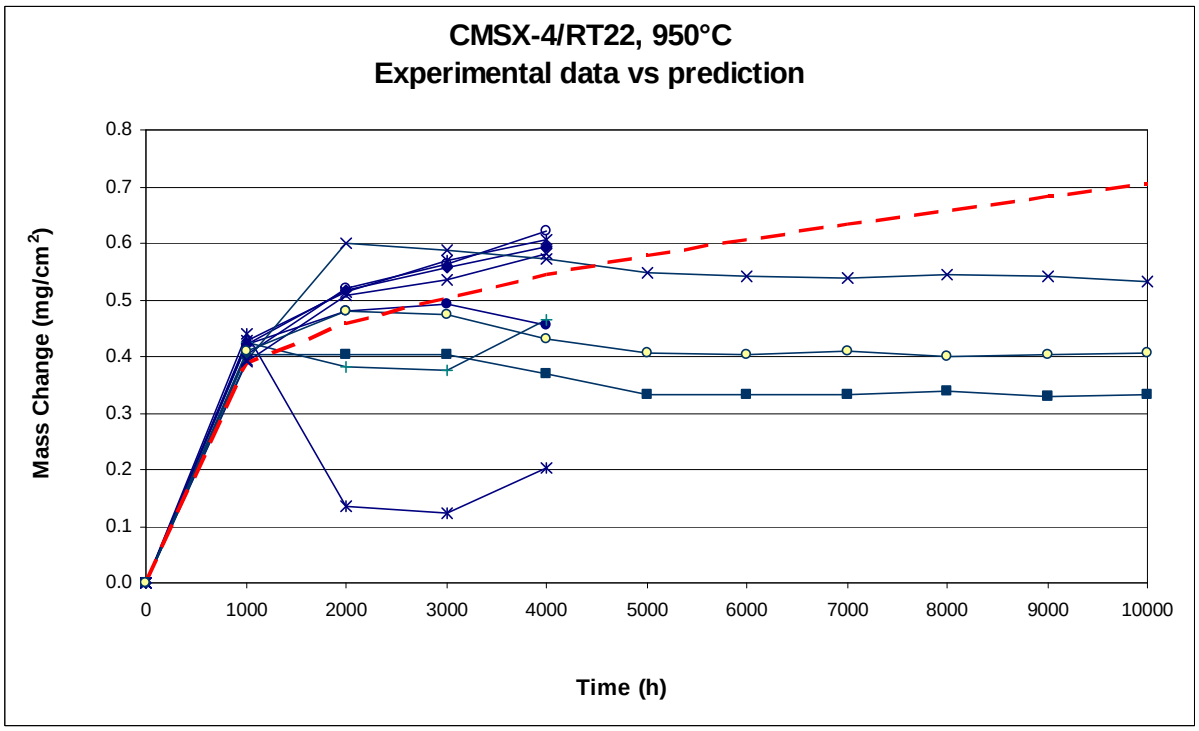

Fig. 153 Comparison between mass change experimental data (- - - -) and mass change prediction (- - - -) at 950°C.

Finally, figure 154 shows a comparison among the value of a rate constant for average alumina-growth calculated from the experimental data and the values of rate constant of theta and alpha alumina used in the model for mass change prediction at 850, 900 and 950°C. The comparison shows for the lower temperature an overlap between the calculated value and that selected for theta-alumina in the model, which confirms the growth of mainly θ- Al_2O_3. For 900°C we can see that the calculated value moves a bit away from the rate constant of theta alumina used in the model, but theta alumina is still confirmed as the main type of alumina. At 950°C the calculated value falls in between the value of theta and alpha alumina, which confirms that alpha alumina growth is much more important than at lower temperature. At 950°C spalling occurred after 2,000 hours which would cause the reformation of theta alumina and other oxides.

The model requires future development study for a better definition of the values of the rates constant, the inclusion of the spalling and the extension of the model to other coated systems.

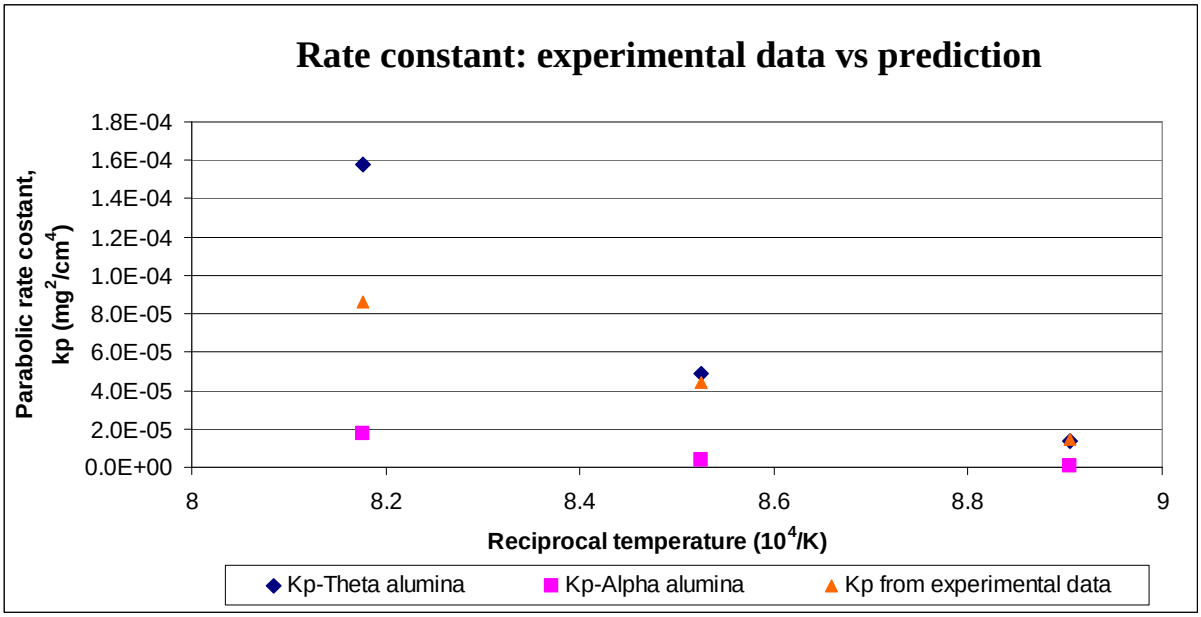

Fig. 154 Comparison between the rate constant calculated from the experimental data and that used in the model.

Previously, presenting the model for alumina growth, it has been said that for temperatures higher than 950°C, that model, not considering spalling, fails in the mass change prediction. For a future improvement of the model, it has been considered useful compared the experimental results to a second model for alumina growth and spalling, NASA COSP model, following described.

The prior models concerning oxide spalling were those proposed by Barrett et al. [9] (COREST) and Smialek [98]. COREST consists of a parabolic description of the oxide growth and a linear curve for the oxide loss. Smialek developed an interfacial model for NiAl, which is based on parabolic alumina growth and on a constant-area fraction of spallaltion at each cycle. Smialek J.L, following studies [99, 100] of oxide growth and spalling associated with cyclic oxidation, has developed a mathematical model for several materials (and thus several oxides, e.g. SiO_2, AlO_3, $NiAl_2O_4$, Cu_2O and NiO) and exposure temperatures (from 500 to 1250°C).

Moreover, from the original model, proposed by Smialek in 1978, a cyclic oxidation model has been presented by Poquillon and Monceau [77]. It has been applied to several Ni-base superalloys, which form α-Al_2O_3 scale during oxidation above 1100°C.

Unlike Smialek's model, which is based on an interfacial discrete spalling model, a second model, developed by Lowell et al. [62], focuses on uniform spallation of an outer layer of the adherent scale. Smialek and Lowell's models, along with those of other researchers, are

included in COSP, which is a general package of models to predict cyclic oxidation. COSP is a publicly available computer program.

Since the availability of COSP for Windows 2.1, the current study has employed it to simulate the possible oxidation behaviour of a Pt-aluminide coated CMSX-4 system. The mass change prediction, carried out by computer calculations, requires to define: oxidation rate, cycle duration, number of cycles, type of oxidation, scale stoichiometric constant, scale phase and spall case.

The results of the simulation carried out at 950 and 1050°C are plotted in the following figure (Fig. 155 a and b), where Kp ($mg^2/(cm^4\ h)$) and Q represent respectively the α-Al_2O_3 rate constant and the spall constant (according to Smialek model [101]), the only two parameters that have been changed for obtaining several simulations. The oxidation type has been chosen “parabolic”, the spall case “uniform thickness” and the stoichiometric constant equal to 2.1243.

In the first case, 950°C, the curve with Kp equal to 8.6E-5 $mg^2/(cm^4h)$ represents the value calculated by the experimental data obtained with this study; the other values, as those attributed to Q, have been selected for a better fit of the mass change data available (Fig. 155a).

The percentage of the oxide spalled, or Q value, selected for the three simulations at 950°C, is 3.6, 4 and 4.5. According to the plot of figure 63 and table 8II the experimental data, regarding CMSX-4/RT22, provide a percentage of spalled oxide of 4.1 (after 2000 hours) and 8.3 (after 4,000 and 10,000 hours). No spallation has been observed after 1000 hours. Consequently, the Q values used in the model underestimate the spalling occurring for long exposure times. This underestimation increases for the highest temperature, 1050°C; in fact, the experimental results are 8.3, 37.5 and 100% of spalled oxide respectively after 1000, 2,000 and 4,000 hours, while the Q values employed in the model for the two simulations are 8 and 9.5.

Thus, we can conclude that for both the temperatures the model fails in the prediction of the material behaviour because it assumes that the loss of the scale is a constant and because it underestimates the oxide loss. However, all the features of the model must be still considered.

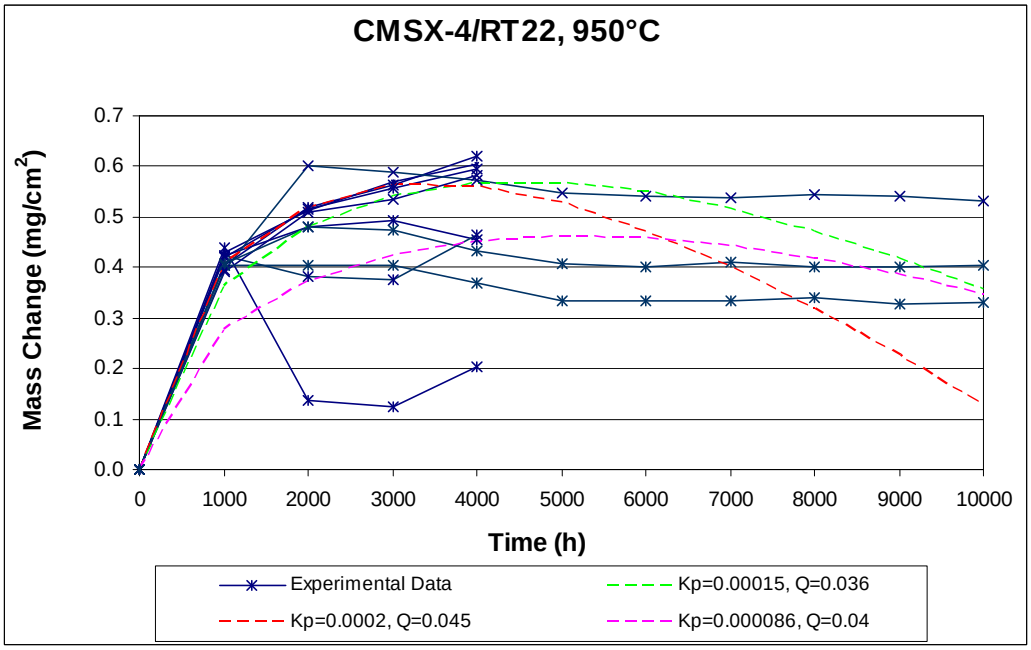

a)

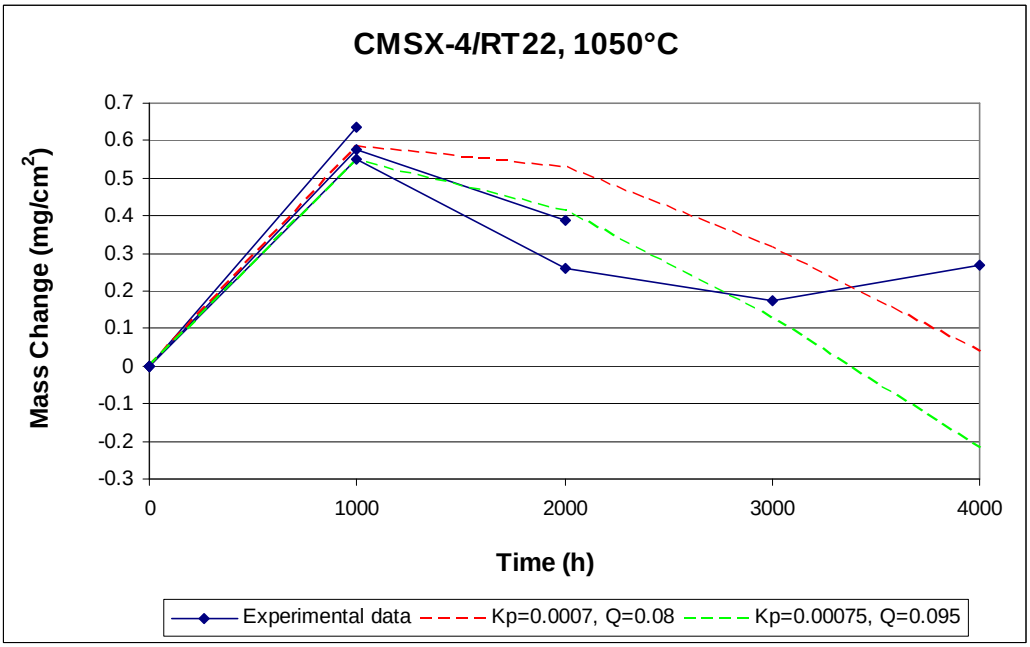

b)

Fig. 155 Simulation of alumina growth and spalling by NASA COSP for Windows 2.1 and comparison with the mass change experimental data gathered at 950°C (a) and 1050°C (b).

4.2 Hot corrosion

The second part of this work has dealt with the study of the hot corrosion behaviour of the uncoated CMSX-4 superalloy and its Pt-aluminide coated systems CMSX-4/RT22, CMSX-4/CN91. It represents the continuation of a series of tests carried out previously (by Encinas-Oropesa [30]), with new observations, which extended the range of exposure condition investigated, and allows the refinement of proposed models for the relationship between materials damage distribution and exposure variables (such as temperature, gas composition and deposit flux). Details of the test carried out are given in section 2.2.2.

4.2.1Temperature effect

The effect of the temperature is that of determining the type of corrosion mechanism; Type I or Type II hot corrosion for ~ 900° and ~ 700°C respectively. These types of hot corrosion can be propagated by basic fluxing, acidic fluxing and sulphidation mechanisms, described in section 1.5, depending on temperature and environmental conditions.

The ESEM analysis carried out on the samples of uncoated superalloy tested at 700°C, for which some pictures are shown in figure 103 (pictures 1-3) highlights that CMSX-4 superalloy has been subjected to Type II hot corrosion (§1.5.2). The level of SO_2 in the gaseous environment would indicate that gas-induced acidic fluxing would be a likely propagation route, through the formation of an equilibrium SO_3/SO_2 ratio in the gas and deposit. The initiation stage has involved reaction with oxides on the alloy/ coatings surface with $(Na/K)_2SO_4$ deposited and the formation of a molten sulphate or partially molten salt solution containing aluminium, nickel, cobalt (chromium oxide should be more resistant according to Donachie [27]). Afterwards the propagation, whose effects we can see in the ESEM images, proceed through dissolving metals into the molten salts and then reprecipitating as non-protective oxide in the outer regions of the deposit/scale mix [53].
The Type II hot corrosion morphology of the uncoated superalloy shows mainly a broad front of attack, figure 103 (micrographs1-3). According to previous author's observations, presented in section 1.5.4, often hot corrosion gives rise to pitting morphology at low temperature (~ 700°C), but a broad front of attack can't be excluded too, and usually is observed for extended exposure times.

The typical Type II hot corrosion morphology has been observed for Pt-aluminide coatings, Fig. 103, pictures 5-9. While the incubation stage has been observed all over the surface, afterward only a few areas moved on from this into the propagation stage whereby pits are formed through a continuous dissolution of metal ions by an electrochemical mechanism. Considering for example the ESEM picture/maps of figure 107, relative to the Pt-aluminide coated system CMSX-4-CN91, one may see represented the characteristic morphology/composition of corrosion products under Type II corrosion as observed by many authors, for example, Luthra [63] and Meier [65]: these pits contain Cr_2O_3, mixed spinels of Co, Cr and Al and sulphates which denote the penetration of molten salt, as well as sulphur ahead at the corrosion front.

The ESEM backscattered images regarding CMSX4/"LCO22" (Fig. 108) demonstrate that the coating deposited on the alloy was very thin; in fact, with the exception of the condition at the lowest deposit flux, where signs of the original coating may be seen, in the remaining two conditions it has been destroyed. Consequently the ESEM pictures of figure 103 visualize mainly the corrosion of the substrate.

ESEM pictures in figure 104 for samples corroded at 900°C show the typical Type I hot corrosion morphology, with a broad front of attack and degradation penetrating through internal sulphidation, sometimes aligned along the metal grain boundaries, which have been observed by several authors [30, 69, 81] and schematised by Khajavi et al. [57] in as presented in figure 156a.

Moreover, as observed by Ecinas-Oropesa [30], the mechanisms of both CMSX-4 and Pt-aluminide coated superalloy degradation have been sulphidation, which is common for nickel-base superalloys when aluminium is present at levels between 1-6% wt [40].

The sulphur is released by salt reduction and it diffuses inward reacting with the alloying elements (Cr, Ti, Ni). As described in section 1.5.3, with the proceeding attack, sulphides are converted to metal oxides; sulphur is released and diffuses further into the metal to form new sulphides.

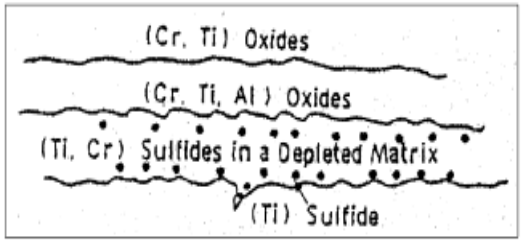

a)

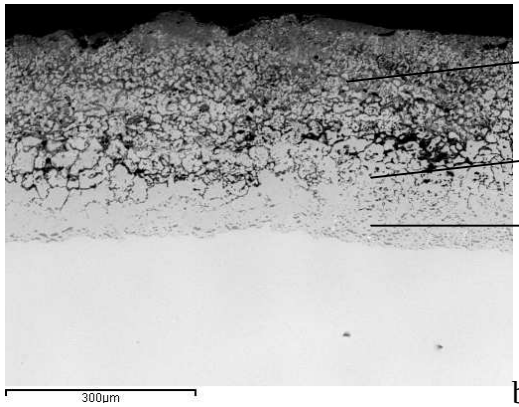

b)

Fig. 156 Schematic representation of Type I hot corrosion scale by Khajavi et al. [57] and the corrosion morphology observed for CMSX-4 (b), tested at 900°C with 1.5 µg/(cm^2 h) deposit flux.

The corrosion morphology observed for the Pt-aluminides coatings tested at 900°C with low/intermediate deposit flux, can be considered a result of the transient corrosion present when both Type I and Type II mechanisms occur, likely due to the changes in the thermodynamics conditions during the exposure. As shown in the following figures, 157 the coated/alloy system may exhibit both localised and broad forms of attack.

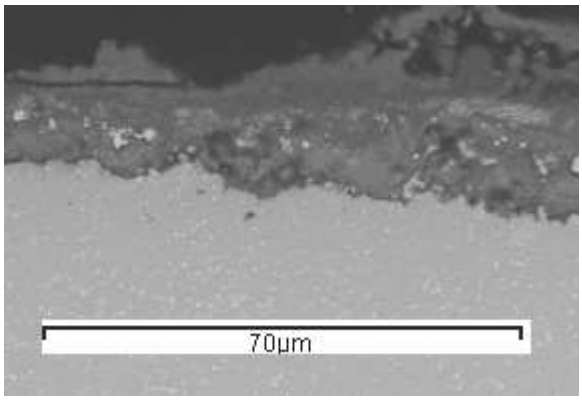

a)

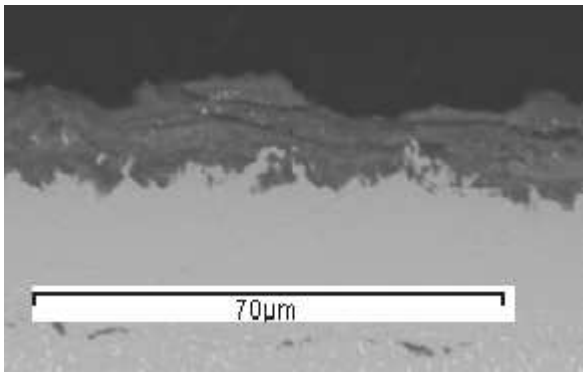

b)

Fig. 157 Type I hot corrosion morphology observed for CMSX-4 coated with RT22(a) and CN91 (b), tested at 900°C with 1.5 µg/(cm^2 h) deposit flux.

As has been observed previously [30] the rate of Type I hot corrosion at 900°C is faster than Type II hot corrosion at 700°C for CMSX-4 (with all other exposure conditions being the same). The comparison between the median metal loss values, for two temperatures tested, are shown in the following figure (Fig. 158). Considering the values of metal loss (median) observed for the highest deposit flux, the corrosion rate of the uncoated superalloy has been 1.2 and 0.26 µm/h respectively at 900 and 700°C.

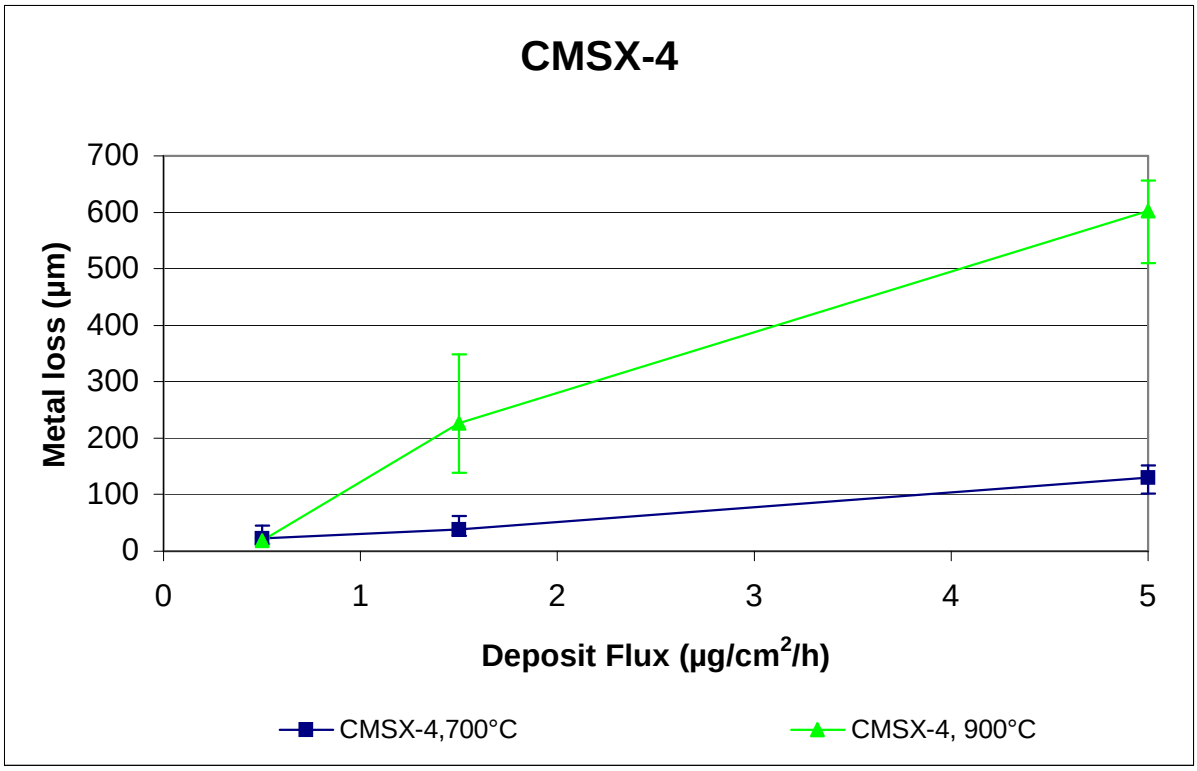

Fig. 158 Median metal loss, corresponding to the 50% probability of not being exceeded, vs deposit flux plot, for CMSX-4 tested in 300 vpm SO_2: comparison between 700 and 900°C test conditions.

Considering CMSX-4/RT22 alloy and CMSX-4/CN91 alloy, figure 159 (a and b): at the lowest flux 0.5 µg/(cm^2h)) the data from tests at both temperatures are similar (within the scatter). But at the highest flux the data from tests at 900°C show the larger metal loss (to the extent that all the coatings are destroyed). At 1.5 µg/(cm^2h), CN91 offered better protection at 900°C whereas "LCO22" offered better protection at 700°C (RT22 results were within scatter at this deposit flux).

It was reported in section 1.6.1 that Pt-aluminide coatings should be expected to perform better in Type I corrosive environments because of the decrease in the pSO_3/pSO_2 ratio, but this behaviour isn't observed in this research. Moreover, Ecinas-Oropesa [30], when

testing 1.5 and 5 µg/(cm^{2}h) of deposit flux in a 50 vpm SO_2 rich atmosphere, also observed less material loss (4% probability) at 900°C for 1.5 µg/(cm^{2}h) deposit flux, while higher losses were observed for the 5 µg/(cm^{2}h) deposit flux.

The values of metal loss (median) observed for the highest deposit flux suggest that RT22 is penetrated respectively in 285 hours at 900°C, a corrosion rate of 0.15 µm/h, and in about 311 hours at 700°C, a corrosion rate of 0.14 µm/h. The initial coating thickness was about 45 µm (without considering the IZ in the measurement). While for CN91, whose initial thickness was about 30 µm, the coating would be penetrated in about 171 hours at 900°C, a corrosion rate of 0.17 µm/h, and in 416 hours at 700°C, a corrosion rate of 0.07 µm/h.

Finally, the last plot (figure 159c), compares the performances of the overlay coating, "LCO22", at 700 and 900°C: here the higher the temperature the higher the metal loss.

The result obtained for the "LCO22" overlay coated system may have been caused by the low thickness of the coating (30 µm), which would result in a materials degradation close to that observed for the uncoated superalloy, which can be seen by comparing figure 159c with figure 158. The uncoated alloy under Type I hot corrosion lost 600 µm (median loss) after 500 hours at 900°C, whereas the "LCO22" coated alloy lost only 430 µm (median loss). This would imply the coating was consumed after 170 hours. Thus a 30 µm "LCO22" overlay must have resisted Type I attack for 166 hours, i.e. a corrosion rate of 0.18 µm/h on average.

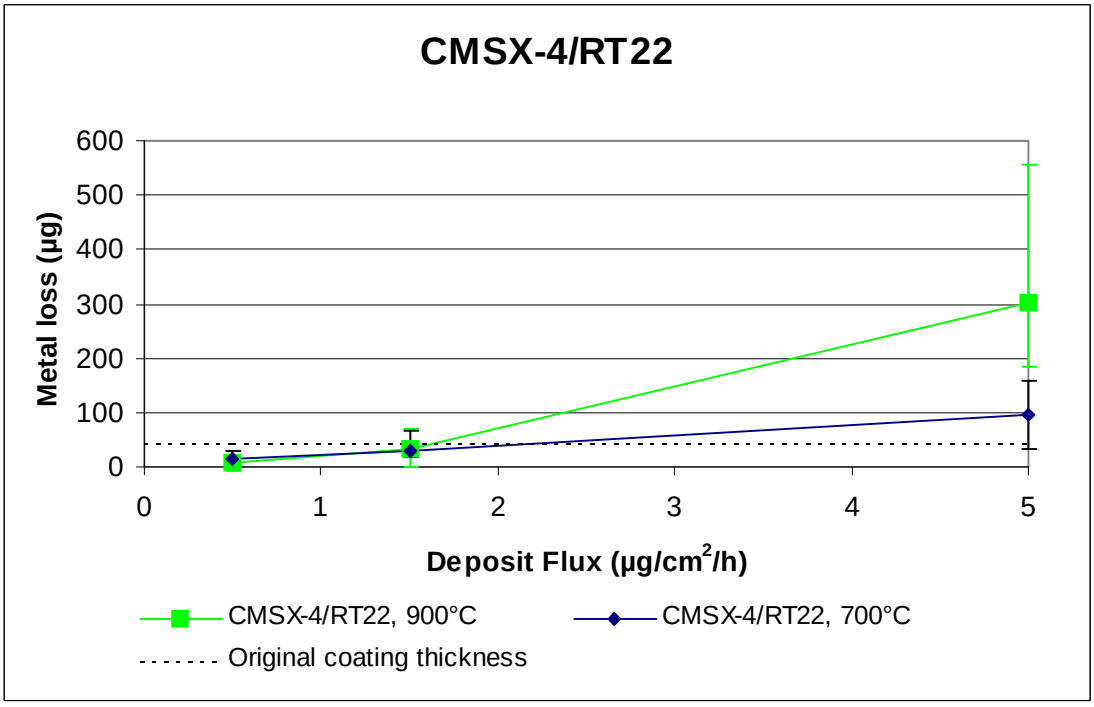

a)

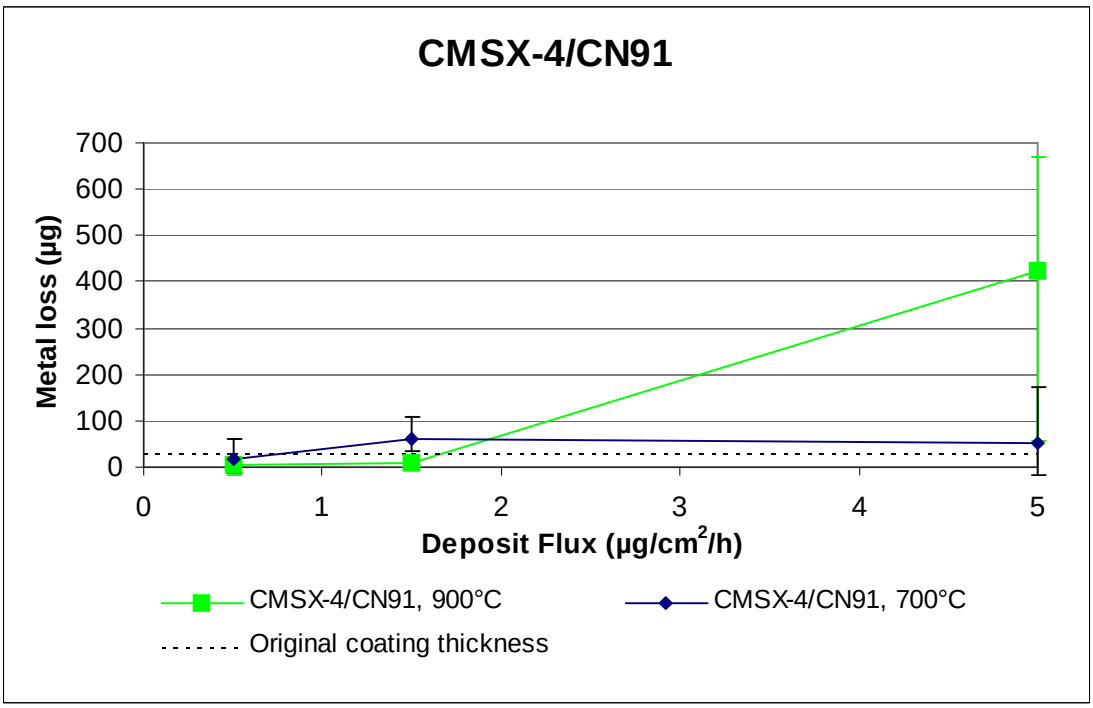

b)

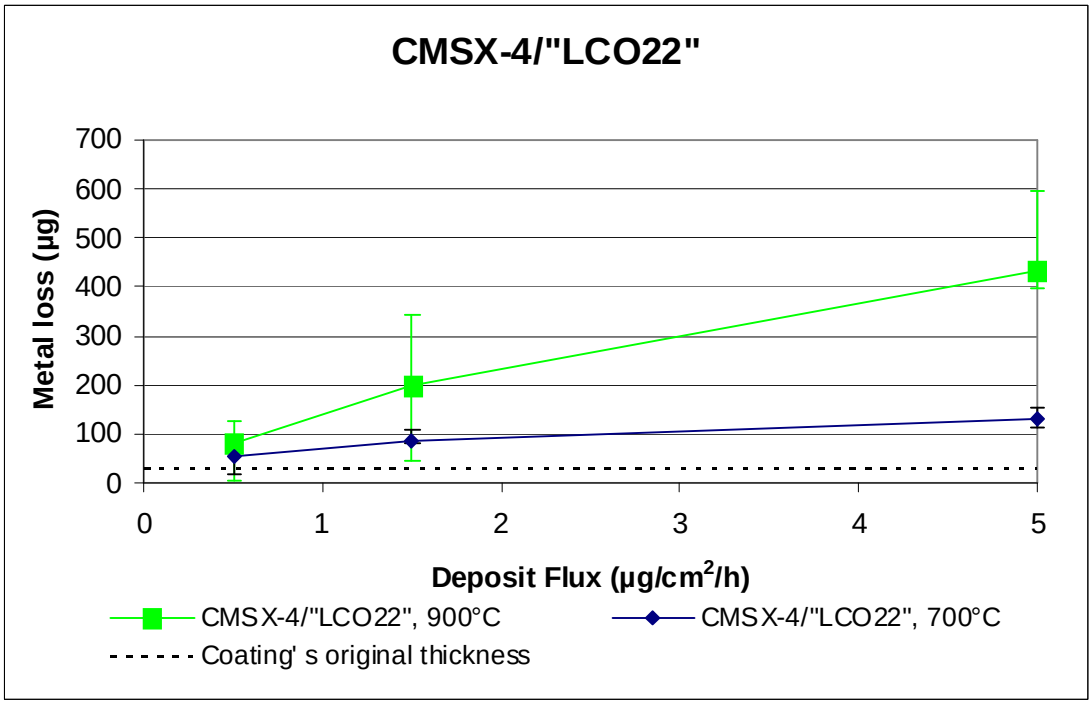

c)

Fig. 159 Metal loss, corresponding to the 50% probability of not being exceeded, vs deposit flux plot, for CMSX-4/RT22 (a), CMSX-4/CN91(b) and CMSX-4/"LCO222"(c) tested in 300 vpm SO_2: comparison between 700 and 900°C.

4.2.2 Deposit flux effect

The plots presented previously in figures 158 and 159 and those following (Fig. 160), which show the metal loss as a function of the deposit flux observed with atmosphere containing HCl, summarise the results of the metrology presented in section 3.2.3, by the selection of metal loss values corresponding to the 50% of probability (median). Moreover, the range of damage observed has been represented by the bar whose minimum and maximum value provided the metal loss respectively with 4 and 96% of probability.

Both at 700°C and 900°C the results show the expected increase in metal loss with increasing deposit flux, which has been previously been reported by several authors (for example Luthra K.L. and Shores D.A. [45]).

Only the curve for CN91 coated specimen (Fig. 159), tested at 700°C, shows a value of metal loss (median) higher for intermediate flux than for the highest deposit flux. The sample tested in this last condition has been observed having greater variability in the depth of the pits.

At 700°C, as summarised in table 10, increasing three times and ten times the deposit flux the damage increases of 1.7 times and 5.8 times for the bare superalloy and 2 and 3.2 for CMSX-4/RT22, damage increases respectively 3.8 times and 3.2 times for CMSX-4/CN91.

At 900°C, as again summarised in table 10, the material loss is kept down increasing three times the deposit flux (12.8 times for CMSX-4, 4.6 times for CMSX-4/RT22 and 1.8 times for CMSX-4/CN91), while the increase in metal loss with 10 times higher deposit flux has been observed very important (34 times for CMSX-4, 42.6 times for CMSX-4/RT22 and 103 times for CMSX-4/CN91).

Table 10 Ratio of metal loss observed with 1.5/5 and 0.5 µg/cm^2/h at 700 and 900°C.

Temperature	CMSX-4	
700°C	1.7	5.8
900°C	12.8	34
	CMSX-4/RT22	
700°C	2	3.2
900°C	4.6	42.6
	CMSX-4/CN91	
700°C	3.8	3.2
900°C	1.8	103
	Metal loss with 1.5 (µg/cm^2/h)/ Metal loss with 0.5 (µg/cm^2/h)	Metal loss with 5 (µg/cm^2/h)/ Metal loss with 0.5(µg/cm^2/h)

The following plots, figure 160, compare the results of metal loss observed for the current corrosion tests with those carried out during a previous one [8, 30], during the which deposit flux of 1.5, 5 and 15 µg/(cm^2h) were tested in air-50/500 vpm SO_2 atmospheres.

Considering the uncoated superalloy CMSX-4, at 700°C (Fig. 160a), the latest metal loss data gathered (for 300vpm SO_2) are consistent with those of the previous study and it can be observed that for deposit flux lower than 5 µg/(cm^2h) the metal loss- deposit flux relation is quite linear, while considering the entire range of deposit flux value, as proposed by Encinas-Oropesa [30], the relation can be approximately sigmoidal. A possible reason for this is that as more deposit is applied the rate of corrosion increases more slowly (i.e. the effect becomes increasingly saturated).

The comparison among the metal loss data observed at 900°C, figure 160b, demonstrate that the trend of increasing metal loss with increasing deposit flux is respected by each of the three series but the material lost in the current work at 300 vpm SO_2 is greater than with the SO_2 concentrations of 50 vpm and 500 vpm, from previous work (the data at 50 vpm and 500 vpm were both similar). The reason(s) for this is unclear.

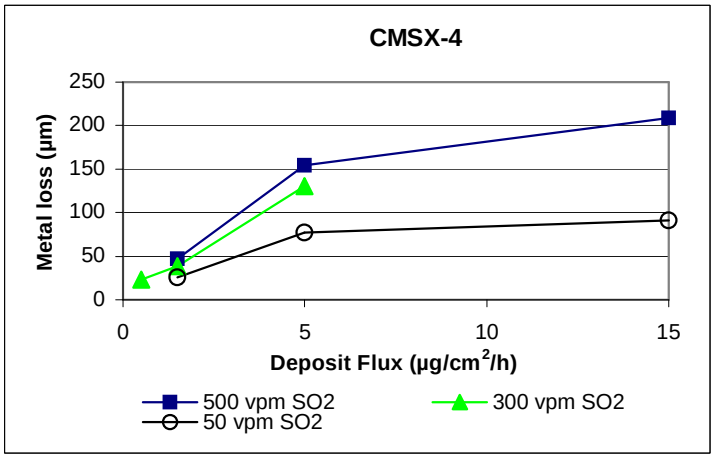

a)

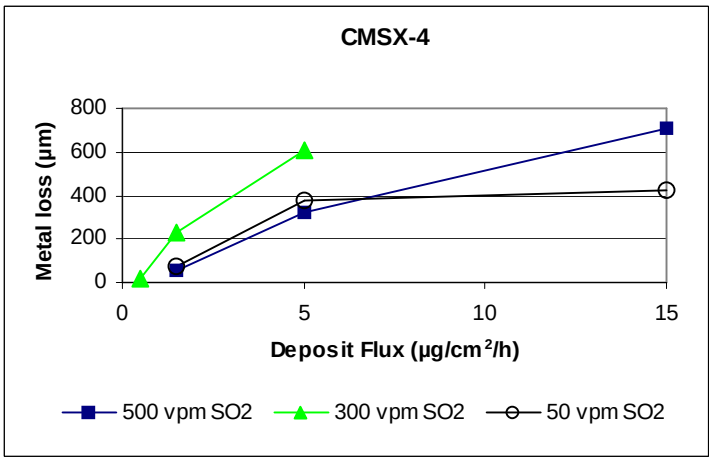

b)

Fig. 160 Metal loss vs deposit flux plot: comparison with data of previous research [30] for CMSX-4 tested at 700 (a) and 900°C (b).

Considering the CMSX-4/RT22 system tested by Encinas-Oropesa [30] as well, but just for the SO_2 concentration of 50 vpm, the following plot, figure 161a) related to the temperature of 700 °C, illustrates a near liner relation between metal loss and deposit flux for the higher concentration of SO_2; but appears more parabolic at lower sulphur dioxide concentration. The plot for 900°C, figure 161b, again illustrates a nearly linear trend between the corrosion damage and the deposit flux variable. However this is confused by the change in corrosion propagation through the coating and to a different rate even into the substrate for the highest flux (5 µg/(cm^2h)) when tested in the 300vpm SO_2 combination of exposure conditions. More data would be very helpful in defining the correlation better.

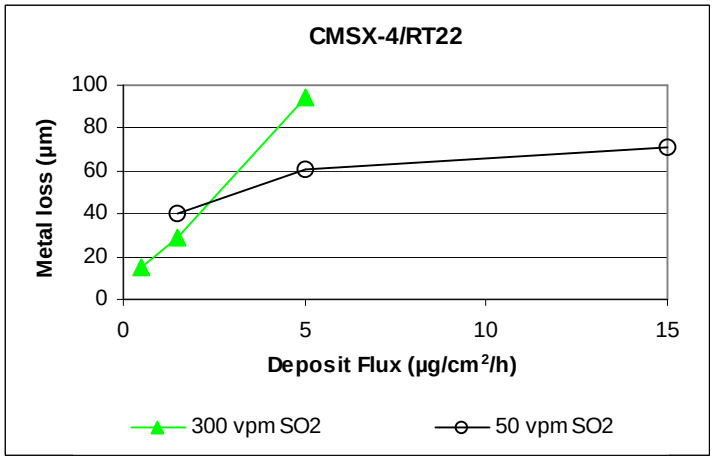

a)

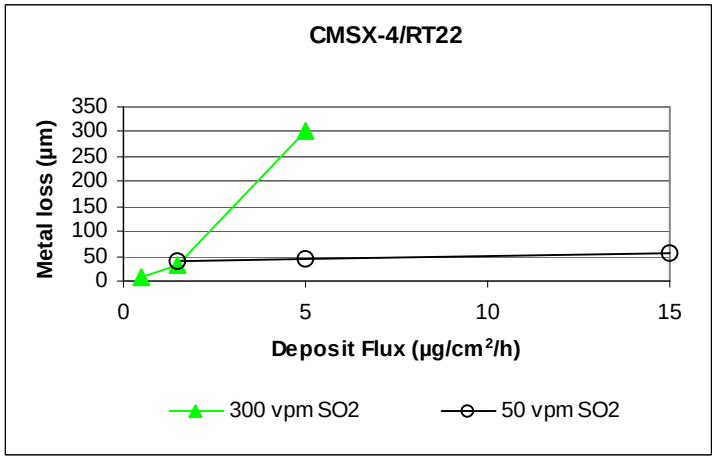

b)

Fig. 161 Metal loss vs deposit flux plot: comparison with data of previous research [30] for CMSX-4/RT22 tested at 700 (a) and 900°C (b).

4.2.3 Gas composition effect

➢ Effect of changing SO_2 concentration

The effect of SO_2 concentration has been analysed comparing the results of material loss observed during this study with 300vpm of sulphur dioxide and those observed previously by Encinas-Oropesa [30], who tested CMSX-4 and CMSX-4/RT22 in 50/500 vpm SO_2 with 1.5/5/15 µg/(cm^2h) flux of potassium/sodium sulphate deposit.

At 700°C, as suggested by figure 162, the metal loss increases linearly (by six and ten times) with increase in SO_2 concentration, for a deposit flux of 1.5/5 µg/(cm^2h). Moreover, looking at table 11, the metal loss increment is quite similar for the same deposit flux, thus the sulphur dioxide concentration effect appears not to be influenced by the deposit flux, for fluxes between 1.5 and 5 µg/(cm^2h).

At 900°C, figure 163, metal loss rises and falls with increasing levels of SO_2. This may indicate that the corrosion damage is independent of the gas phase SO_2 levels for this material/temperature combination, within measurement error, or there is a peak in corrosion rate at 300 vpm SO_2.

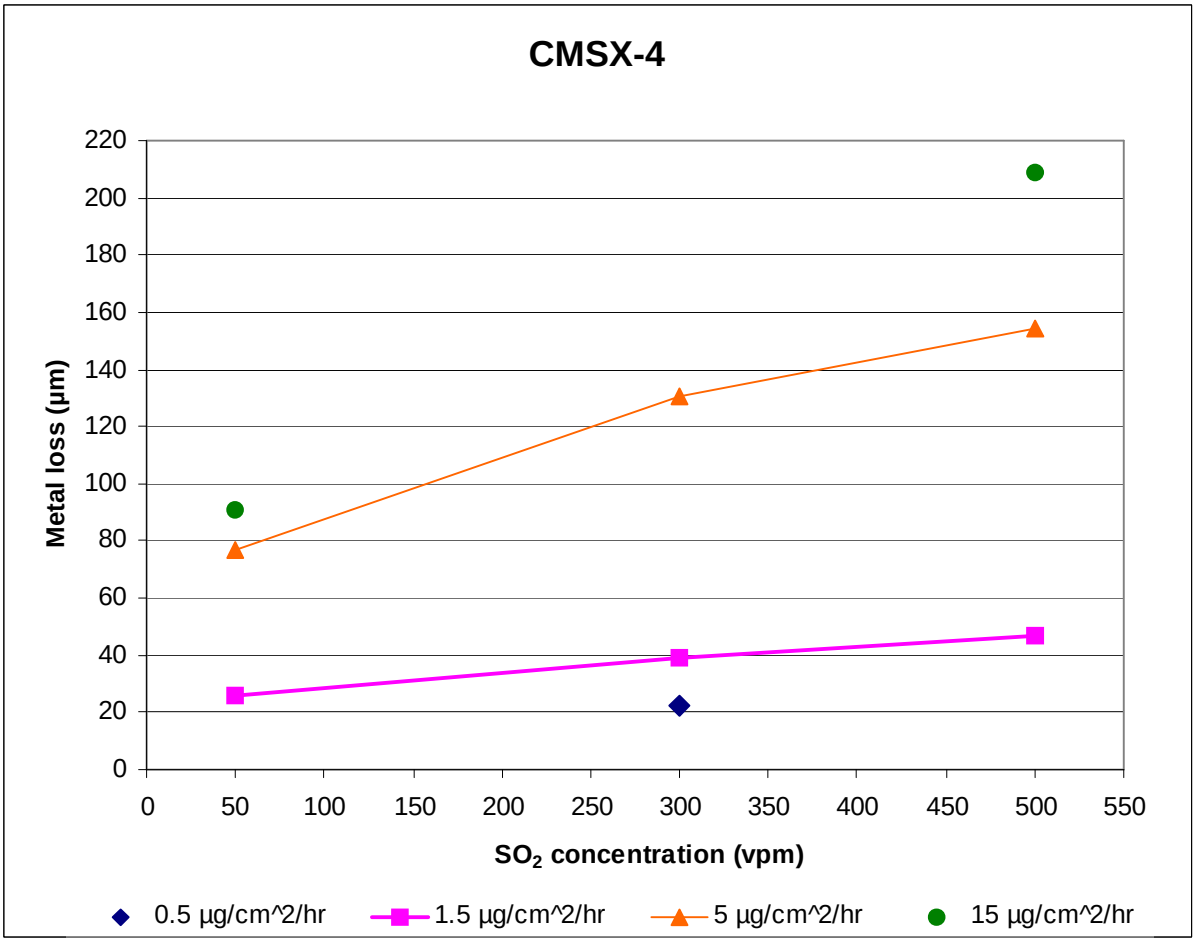

Fig. 162 Effect of SO_2 on CMSX-4 at 700°C

Table 11 Metal loss with 300/500vpm and 50vpmSO_2 ratio observed at 700°Cfor CMSX-4.

Deposit flux	CMSX-4	
1.5 µg/cm^2/h	1,5	1,8
5 µg/cm^2/h	1,7	2,0
	Metal loss with 300vpmSO_2/ Metal loss with 50vpmSO_2	Metal loss with 500vpmSO_2/ Metal loss with 50vpmSO_2

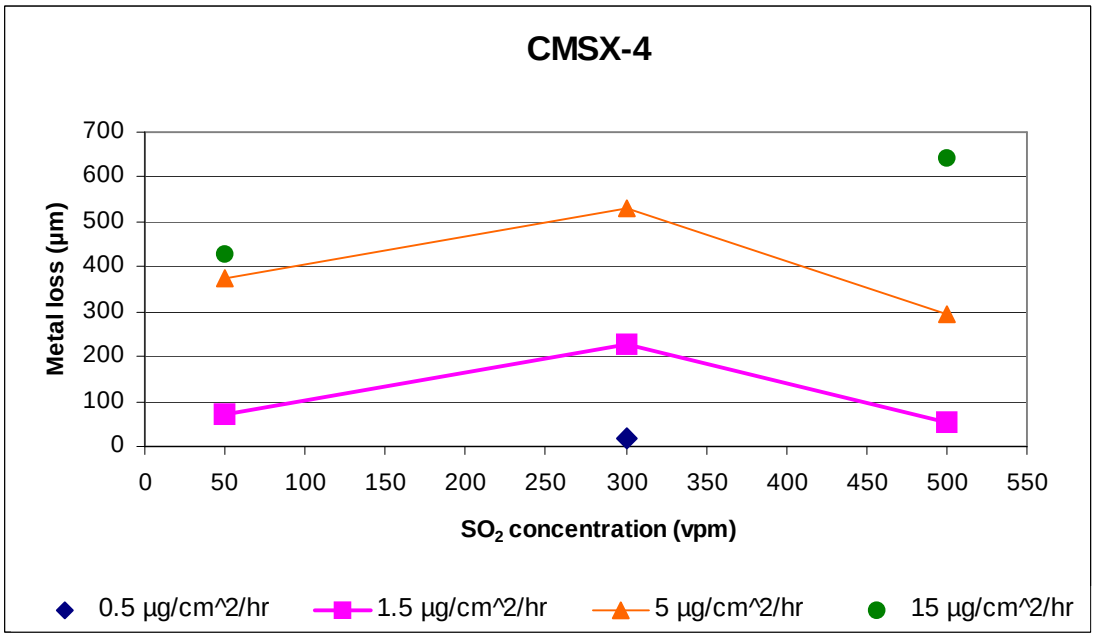

Fig. 163 Effect of SO_2 on CMSX-4 at 900°C

Concerning the Pt-aluminide coated CMSX-4 system tested at both 700 and 900°C the limited data set and the presence of two different Pt-aluminide coatings don't allow defining the correlation between sulphur dioxide concentration and metal loss. However, it can be seen from figure 164-165 that for CMSX-4/RT22 a higher concentration of SO_2 leads to less damage with a lower deposit flux (1.5 µg/cm^2/h), whilst the result is reversed with higher deposit flux (5µg/cm^2/h). In figures 164 and 165 only the data corresponding to CMSX-4/CN91 are named; the other data points correspond to CMSX-4/RT22.

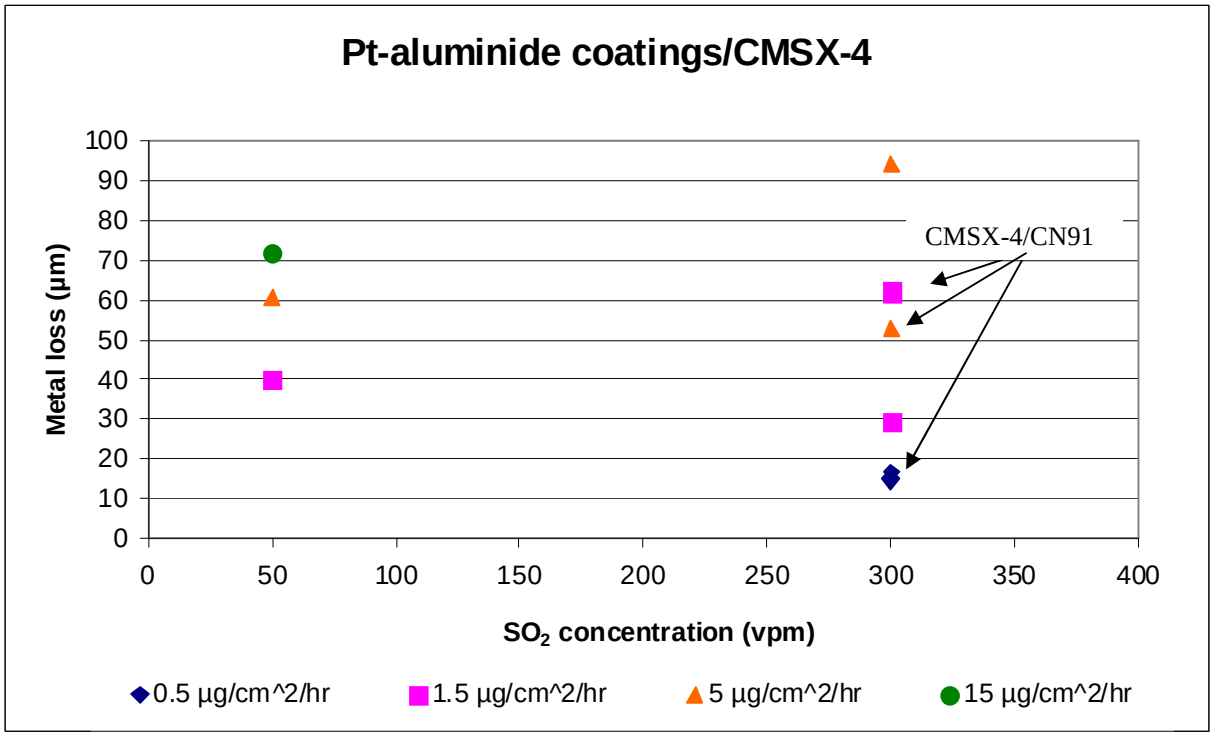

Fig. 164 Effect of SO_2 on Pt-aluminide coated CMSX-4 at 700°C

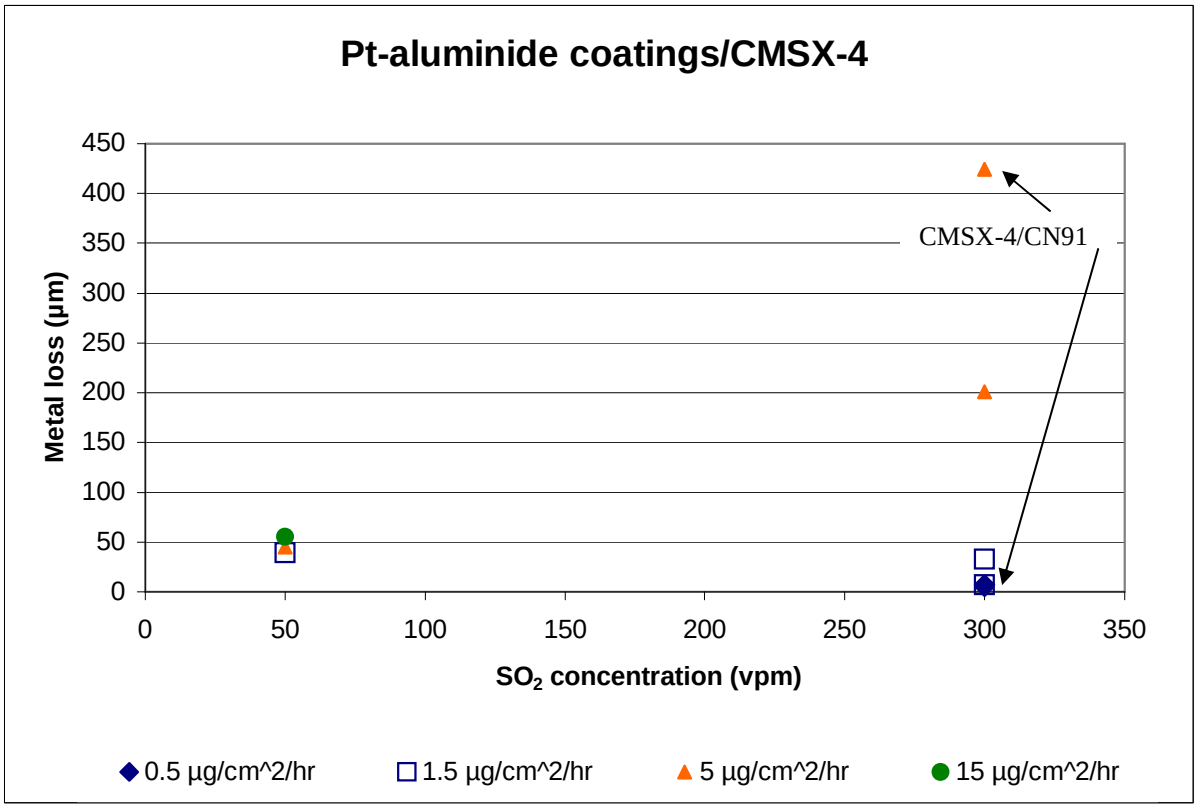

Fig. 165 Effect of SO_2 on Pt-aluminide coated CMSX-4 at 900°C

➢ Effect of HCl adding

Summarizing the mass change and metal radius change data, gathered testing the bare alloy CMSX-4 and its Pt-aluminide/overlay coated systems in 100 vpm of HCl added to 300 vpm of SO_2 rich atmosphere, the following were observed:

- at 700°C

- HCl increased the bare alloy kinetics of degradation (Table 12, Fig. XII in appendix)

- HCl had different effect on the two Pt-aluminide coatings: increased the kinetics of degradation of CMSX-4/RT22 (apart from the intermediate flux where it had neutral effect), decreased the same as for CMSX-4/CN91 system (Table 12, Fig. XII-XIV in appendix). These results can be visibly appreciated comparing the micrographs 5-10 (Fig. 103) to 28-33 (Fig. 105), especially looking at the pit depth and frequency.

- HCl has reduced the CMSX-4/"LCO22" degradation at the lowest deposit flux. For higher deposit flux the presence of HCl hasn't changed the performance of CMSX-4/"LCO22" (Table 12, Fig. XV in appendix)

- at 900°C

- HCl decreased the bare alloy kinetics of degradation, which can be appreciated by comparing the scale of the pictures 13-15 vs 37-39 (Fig. 104 and 106).

- HCl decreased the kinetics of degradation of Pt-aluminide coated specimens, with the exception of CMSX-4/CN91 tested at an intermediate deposit flux. In this case, the 5µg/(cm^2h), result can be visibly appreciated by comparing picture 21 (Fig. 104) to 45 (Fig. 106): the damage at 300vpm SO_2 has proceeded so rapidly that the coating and the interdiffusion zone aren't present and visible anymore, whilst they are still visible after exposure at 300vpm SO_2+100vpm HCl.

Table 12 Value of metal loss (µg) corresponding at 50% of probability of not being exceeded for CMSX-4 and the coated systems CMSX-4/RT22, CMSX-4/CN91, at 700/900°C, 300vpm SO_2/HCl300vpm SO_2+100vpm HCl.

Temperature	Gas composition	CMSX4			RT22			CN91			"LCO22"		
700°C	300vpm SO_2	23	39	131	15	29	94	16	62	53	54	86	132
	300vpm SO_2+100vpm HCl	70	75	168	33	28	102	7	21	23	33	80	136
900°C	300vpm SO_2	18	227	602	7	33	303	4	7	424	81	198	432
	300vpm SO_2+100vpm HCl	17	40	120	12	22	25	7	27	34	24	98	449
		0.5	1.5	5	0.5	1.5	5	0.5	1.5	5	0.5	1.5	5
		Deposition flux (µg/cm^2/h)											

According to several authors (e.g. Eliaz et al. [28], Khajavi et al. [57]) the HCl presence may decrease the sodium/potassium sulphate deposit dew point due to sodium chloride formation, which removes the incubation period and causes higher corrosion kinetics. However, the propagation isn't directly effected by the change in the dew point. Moreover, the production of sulphur trioxide, according to equation 24, may sustain a higher gas induced acidic flux reaction at 700°C.

Furthermore, sodium chloride can react with sulphur dioxide and oxygen to form sodium sulphate, thus removing and creating, as shown in equation 25, respectively SO_2 and Cl_2.

$$2HCl + Na_2SO_4 = 2\ NaCl + SO_3 + H_2O \quad (24)$$

$$2\ NaCl + SO_2 + O_2 = Na_2SO_4 + Cl_2 \quad (25)$$

Chlorine besides reacting with the salt, the gas phases and the scale may penetrate the scaleand react directly with the substrate and selectively remove chromium, aluminium and titanium from the alloy. The process appears to involve the formation of gaseous chlorides, which lead to the formation of pores and channels [15, 20, 30]. Platinum has been found to be effective in inhibiting such chloride induced effects [20].

A combination of these aspects leads to the observed negative, positive and neutral effect of HCl.

If the scale/deposit is prone to crack and spall (as for CMSX-4 at 700°C) the HCl is more ready to react directly with the metal rather than having to pass through a scale. At 900°C probably the gas phases prevailed and chlorine is removed from the deposit, so the bare alloy was less damaged. At 900°C concerning Pt-aluminide coatings, at the highest deposit flux, the scale/salt layer that has formed is thicker in the case with an HCl rich atmosphere (micrographs 18-21 and 39-42, respectively Fig. 104 and 106); this may have protected the substrate for higher material loss.

4.2.4 Materials composition effect

Table 12, previously presented, provides the values of metal loss (median) for the CMSX-4 superalloy and the coated systems tested both at 700 and 900°C, with and without an addition of 100vpm HCl to 300vpm SO_2 in the gas stream.

The table demonstrates, by lower value of metal loss, that the Pt-aluminide coatings had protective effect for the substrate, which is more evident at high deposit flux and at high temperature. According to the table CN91coated alloy, tested at 700°C, with 1.5 $\mu g/cm^2/h$ deposit flux is the only exception. The following figures 166 and 167, where the extremes of the bars represent the 4 and 96% of probability, show that CN91 coated superalloy has suffered at both the temperatures and for the highest deposit flux a metal loss (corresponding to the 96% of probability) even a bit higher than the uncoated CMSX-4. That is probably because the coating once penetrated has led to faster substrate degradation. The protection, as explained in section 1.6, has been guaranteed by the formation of a more homogeneous scale, mainly made up of alumina and chromia over the coated surface.

Comparing the performances of RT22 and CN91, the former has been observed being more protective at 700°C in 300vpm $S0_2$ for low/intermediate deposit fluxes, while the latter for the highest deposit flux and for any flux in 300vpm SO_2+100vpm HCl containing atmosphere (Fig. 166-167). Better protection by CN91 is observed at 900°C for intermediate deposit flux in 300vpm SO_2 rich atmosphere and for the highest deposit flux in presence of HCl (Fig. 168-169). This may be a result of CN91 forming a more homogeneous alumina scale.

Often the Pt-aluminide coatings performed differently, as a result of their different microstructures and elemental compositions (as explained in sections 1.6.1 and 4.1). At 700°C with HCl added to the gas stream the overlay coated provided some protection for the CMSX-4 superalloy before it was destroyed because of the higher Cr content causing Cr_2O_3 scale formation. At 900°C in 300vpm SO_2 atmosphere, with intermediate and high value of deposit flux CMSX-4/“LCO22” experienced less metal loss than CMSX-4. The coating would have provided a protective scale at the beginning of the exposure, but this was only temporary due to the very thin coating that results with interdiffusion.

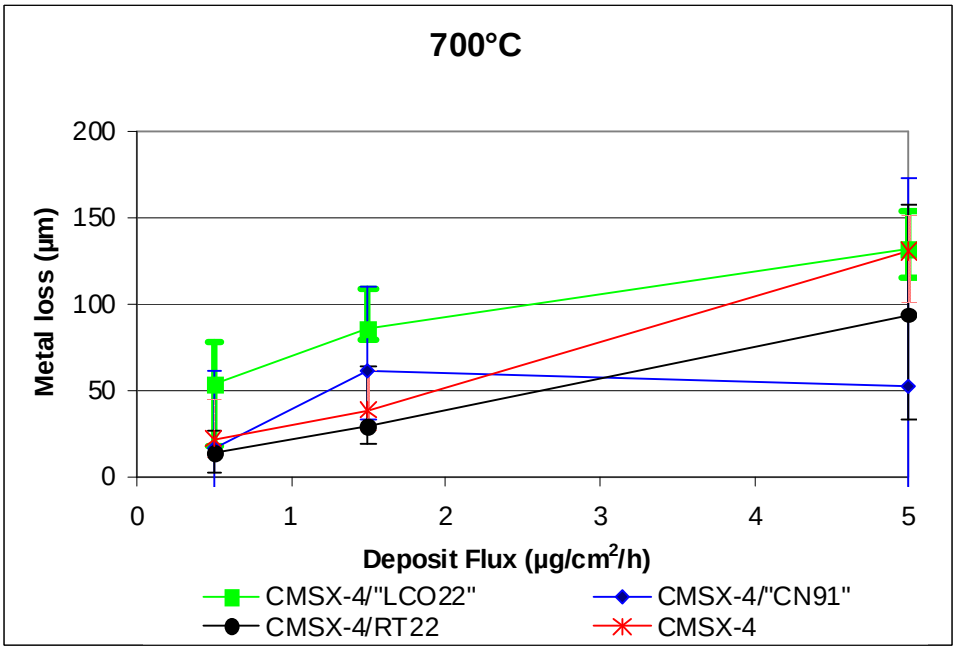

Fig. 166 Comparison among materials performance tested at 700°C in 300 vpm SO_2 rich atmosphere.

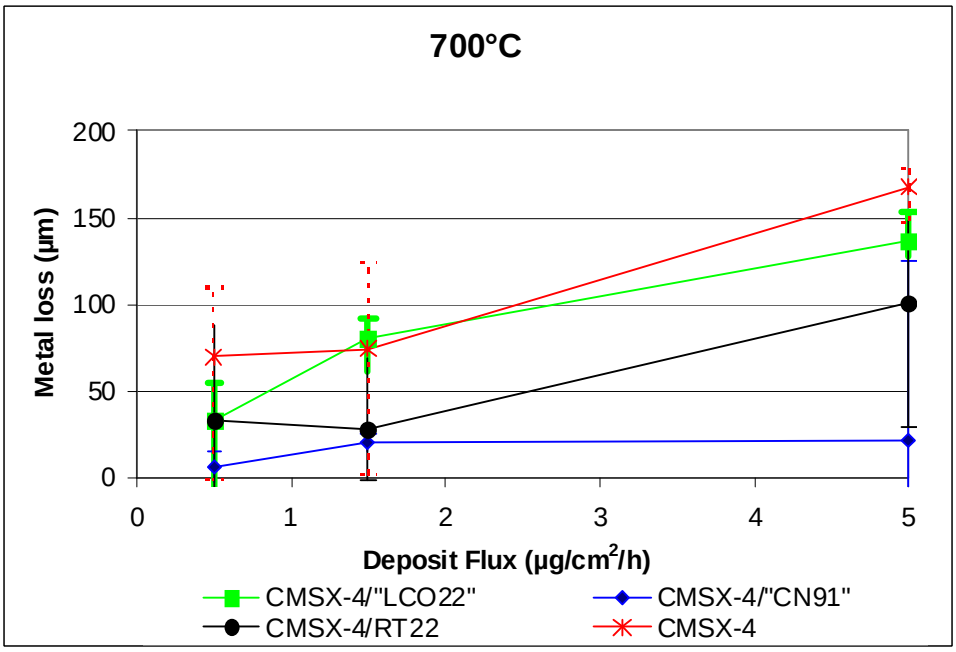

Fig. 167 Comparison among materials performance tested at 700°C in 300 vpm SO_2+100vpmHCl rich atmosphere.

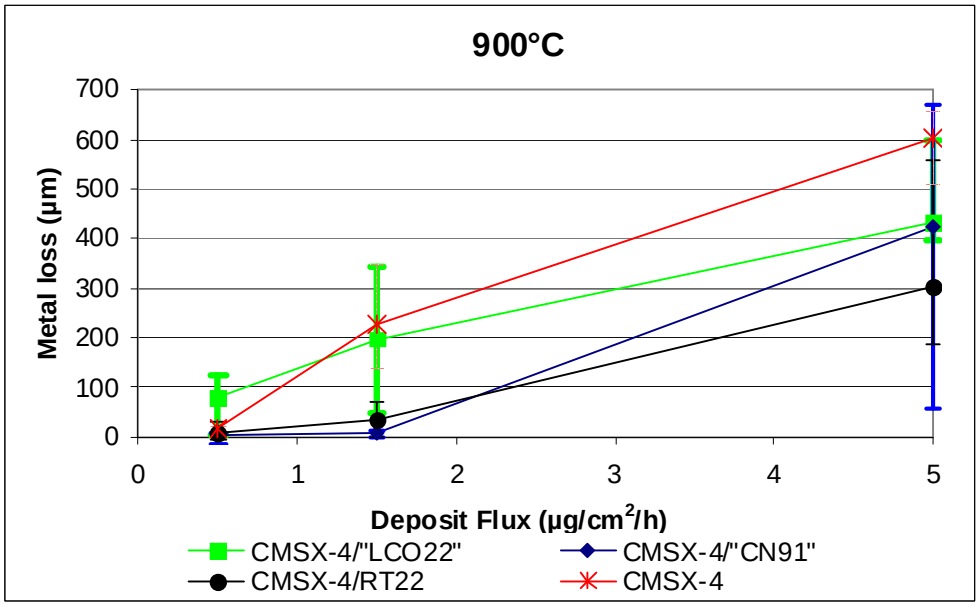

Fig. 168 Comparison among materials performance tested at 900°C in 300 vpm SO_2 rich atmosphere.

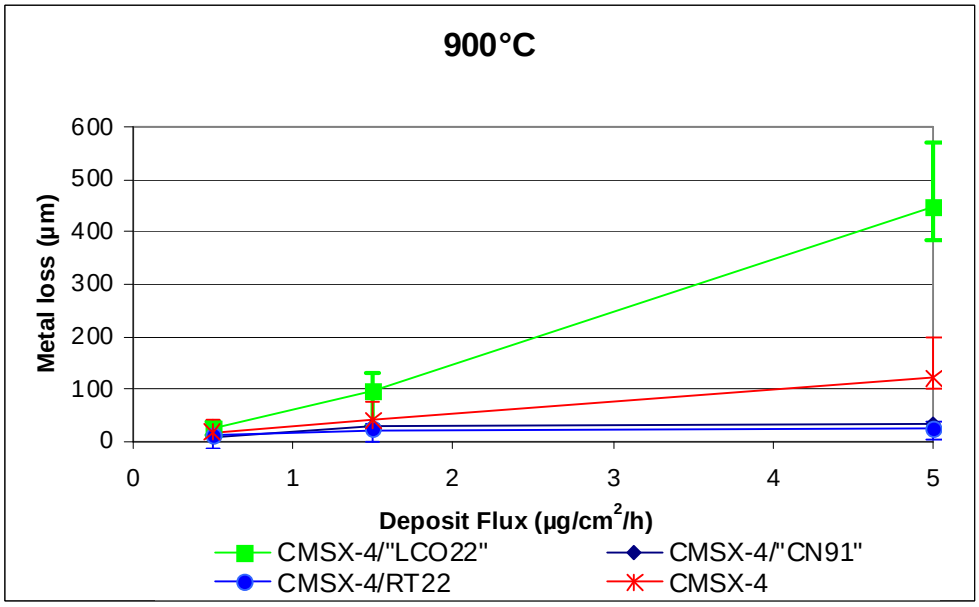

Fig. 169 Comparison among materials performance tested at 900°C in 300 vpm SO_2+100vpmHCl rich atmosphere.

Considering oxidation observations together with corrosion ones in relation to the exposure condition studied, it can be concluded that the main life limiting factor is corrosion. Moreover, in the second case, increase in the deposit flux result more damaging for the turbine materials than the increase in SO_2 concentration.

In section 4.2.1, has been calculated that RT22 is penetrated, using a deposit flux of 5 µg/(cm^2h), in 285 hours at 900°C (temperature during the which greater damage was experienced), a corrosion rate of 0.15 µm/h. Thus, if we think that turbine mending could

occur any three years (26280 hours), maintaining the corrosion rate of 0.15 µm/h, we aspect a metal loss of 3942 µm. This could provide an hint for the original thickness of the coating. CN91 would be penetrated in about 171 hours at 900°C, a corrosion rate of 0.17 µm/h. The same calculation done before tell that in three years a lost of about 4467 µm can occur.

5. Conclusions

5.1 Oxidation

o Isothermal oxidation tests have been carried out at five different temperatures, 850, 900, 950, 1000 and 1050°C, up to 10,000 hours of exposure, in simulated combusted natural gas environments, in order to reproduce the exposure environment of industrial natural gas fired turbines.

o The oxidation kinetics for temperatures higher than 850°C are found to move away from the parabolic law. At 900°C the non-parabolic trend is mainly due to the higher oxidation rate observed for the first 1,000 hours than that observed during the following hours of exposure. The transformation of θ-Al_2O_3 into α-Al_2O_3 has been associated with this behaviour.

For temperatures equal to and higher than 950°C the non-parabolic trend is caused by the onset of the spallation.

The rate constants for θ- and α- Al_2O_3 growth are consistent with the values found in the literature, with values, calculated at 850, 900 and 950°C, expressed in $mg^2/(cm^4\ h)$, respectively of :

- 1.45 E-05, 4.4 E-05 and 8.63 E-05 for CMSX-4-RT22,
- 7.42 E-05, 1.05 E-04 and 1.06 E-05 for CMSX-4/CN91
- 9.76 E-05, 2.04 E-04 and 2.61 E-04 for CMSX-4/"LCO22"

o ESEM analysis has allowed the characterisation, with respect to exposure time, temperature and materials system, at the change in materials morphology and scale composition. The main observations are:

- CMSX-4/ RT22: at 1050°C, the IZ grows a little bit inward during the exposure, but after long heat treatment (2,000 hours) it doesn't increase further. In this study thicker IZ have been observed after 2000 hours of exposure at lower temperature 900 and 950°C, while change in the IZ thickness with time at 850°C was not evident. RT22 as-coated sample is rich in precipitates; these are still present after 10,000 of exposure at 850-900°C, while after 2000 hours of exposure at 950-1000°C and earlier, for the highest temperatures, they have disappeared leaving just a few bigger precipitates. With the aging increasing precipitate coarsening beneath the IZ has been observed. In this study we assume that the acicular shaped particles, seen when characterising the samples tested at 1050°C, at each exposure time, and at 1000°C after 4,000 hours are refractory metal rich particles.

- CMSX-4/CN91: increased IZ thickness at temperature higher than 950°C has been observed. CN91 coated alloy has a precipitates free OZ, both as-coated and heat treated, while precipitates are present beneath the IZ and their coarsening increases with time at 1050 °C. No acicular precipitates have been observed at a temperature lower than 1050°C and, at this temperature, not before 1000 hours of exposure.
- For all the materials systems the oxide scale grown on the material system during the exposure consists mainly of two layers: an outer layer of mixed oxide/spinels (e.g $NiAl_2O_4$, $CoAl_2O_4$, $CoCr_2O_4$) and an inner layer predominantly formed of alpha alumina. Only for CMSX-RT22 TiO_2 and Ta_2O_5 have been observed in the first layer mentioned.

o Measurements of the TGO thickness and of the percentage of spalled surface have been carried out. In order to find a correlation between scale thickness measurements, percentages of oxide spalled, time and temperature a deeper modelling activity must be carried out about alumina growth and its failure.

o At the low temperatures, 850 and 900°C, the RT22 coated system showed to be the best performing coating between the two Pt-aluminide coatings; it has formed always a thinner scale than that of CN91, less of this thinner oxide spalled on each exposure cycle and the mass change plot revealed more homogeneity in the oxidation behaviour amongst the samples. The results obtained at 950°C do not allow to say that one coating provided better protection than the other one. At the highest temperature (1000-1050°C), usually, the coatings RT22 experienced higher mass change and formed thicker scale than CN91 coatings. More spallation has resulted at these temperatures for the outward grown Pt-aluminide coating for exposure time up to 2,000 hours, that is why, probably the oxide scale have been observed thinner for CMSX-4/ CN91. These results suggest that CN91 coatings may be more protective at the highest temperature for long exposure times.

o At 850-900-950°C CMSX-4/"LCO22" behaved similarly to CMSX-4/CN91, but with less variability amongst the samples behaviour than the Pt-aluminide coating. At higher temperature, 1000 and 1050°C, CMSX-4/"LCO22" oxidation kinetics are faster than for the Pt-aluminide coatings, but the original, thin, coating deposited has been observed to be destroyed early in these exposure tests and so oxidation of the substrate had occurred.

o A model has been presented for predicting the oxide growth that considers the transient stage characterized by θ-Al_2O_3 and the steady-state by α-Al_2O_3 growth. Moreover, using NASA COSP model, a model developed for oxide growth and spalling during cyclic oxidation, a comparison between the data of mass change, obtained with this study, and

those coming from a prediction, carried out employing rate constants from this study, has been shown.

- The model doesn't provide a perfect prediction of the materials mass change because it assumes that the loss of the scale is a constant and because it underestimates the oxide loss for long exposure time or for high temperature (1050°C).

All the features of the NASA COSP model are still required to be investigated for improving the materials behaviour prediction.

5.2 Hot corrosion

- The experimental component of this study has allowed reproduction of materials degradation by Type I and Type II hot corrosion and its dependence on salt deposit flux and gas composition.
- Optical microscopy has highlighted the typical broad front attack of Type I hot corrosion, with sulphidation damage preceding internal oxidation, for the uncoated CMSX-4 and for the CMSX-4 /"LCO22" system (that experienced the complete destruction of the coating) exposed at 900°C, both in presence and absence of HCl.
- Corrosion has been observed for the Pt-aluminide coated systems that shows features of both Type I and Type II damage.
- The optical microscopy has, moreover, shown the typical pitted corrosion morphology associated with Type II hot corrosion for the Pt-aluminide coated systems tested at 700°C, both in presence and absence of HCl. Rare pits and mainly broad attack have been observed for CMSX-4 and CMSX-4 /"LCO22".
- Both optical microscopy and pre/post exposure metrology have allowed the determination of the hot corrosion-deposit flux relationship: the corrosion damage increases with increasing salt deposit flux. At 700°C (with 300 vpm SO_2 atmosphere), Pt-aluminide coatings are more effected than the uncoated CMSX-4 by increase of the deposit flux, for low deposit flux, while Pt-aluminide coatings are much less effected by high deposit flux. At 900°C (with 300 vpm SO_2 atmosphere) the materials behaviour is reversed.
- The analysis of the hot corrosion damage dependence on SO_2 concentration suggested that:

- uncoated CMSX-4: at 700°C the metal loss increases linearly by increasing SO_2 concentration (for a deposit flux of 1.5 and 5 µg/(cm^2h)). At 900°C the corrosion damage is independent of the SO_2 levels.
- more data are required to establish the sulphur dioxide-material loss relationship for Pt-aluminide coated CMSX-4 at 900°C.

o Adding HCl to the gas environment reduced Type I hot corrosion damage to CMSX-4, but increased Type II hot corrosion of the uncoated superalloy. HCl also reduced the CMSX-4/"LCO22" degradation at the lowest deposit flux. For higher deposit flux the presence of HCl does not change the performance of CMSX-4/"LCO22".

o HCl had negative and positive effects on the two Pt-aluminide coatings. The two types of Pt-aluminide coatings, inward and outward grown coating, do not behave similarly when exposed to the same corrosive conditions.

o The study has permitted the observation of the protective behaviour of the Pt-aluminide coatings at 700°C (even if they have been completely destroyed with the highest deposit flux). Neither of the two Pt-aluminide coatings performed better than each other for each condition of deposit flux. Thus, the choice of which coatings to apply to the gas turbine blade should be taken considering the salt deposit flux expected. However, from a similar comparison at 900°C, it's clear that the best protection from Type II and Type I hot corrosion can not be obtained with the same coating.

o Compared to CMSX-4 no protection has been derived from using "LCO22" in these tests for Type II and Type I hot corrosion attack. This is likely to be due to the thin coating deposited on CMSX-4, thus the corrosion rates measured are dominated by attack of the substrate alloy.

6. Recommendation

6.1 Oxidation

- To investigate shorter exposure time in order to study separately α and θ-Al_2O_3 kinetics.
- To avoid cycles of oxidation, but keep the exposure till the end of the required period to better simulate isothermal oxidation.
- To carry out the after exposure analysis on repeated samples, in order to widen the data set of oxide thickness/element concentrations and thus the results' reliability.
- To cut the samples after mounting in a way to avoid sample damage and scale detachment.
- To use samples belonging to the same batches, for each study to avoid batch to batch variation and to allow repeatability and reproducibility of the observations.
- To repeat the tests with "LCO22" coated CMSX-4 with thicker coating in order to look at a more realistic material condition and to investigate the importance of the coating thickness on substrate protection.
- To test the samples in separate crucibles in order to collect the material spalled for studying the phenomenon of spallation.
- To investigate the features of NASA COSP spalling model that is available to develop the life time prediction model for the coated material systems tested.

6.2 Hot corrosion

- To test more SO_2 concentrations for better investigating its effect on Pt-aluminide coatings at both 700 and 900°C.
- To test different additions of HCl to the same concentration of sulphur dioxide in order to better investigate its effect in changing the corrosion mechanism at 700 and 900°C.
- To repeat the tests with "LCO22" coated CMSX-4 with thicker coating in order to look at a more realistic material condition and to investigate the importance of the coating thickness in the substrate protection.

7. References

1. Angenete, J. (2002), Aluminide diffusion coatings for Ni based superalloys (2002, PhD thesis), Chalmers University of technology, Goteborg University, Goteborg, Sweden.
2. Angenete, J., Stiller, K., 2001. A comparative study of two inward grown Pt modified Al diffusion coatings on a single crystal Ni base superalloy. Materials Science and Engineering a316, 182-194.
3. Angenete, J., Stiller, K., 2002. Comparison of inward and outward grown Pt modified aluminide diffusion coatings on a Ni base single crystal superalloy. Surface & Coatings Technology 150, 107-118.
4. Angenete, J., Stiller, K., 1999. SEM and TEM studies of PtAl diffusion coatings under isothermal oxidation. Microscopy of oxidation. Proceedings of the Fourth International Conference on the Microscopy of Oxidation. Cambridge, 20-22 September, 1999.
5. Angenete, J., Stiller, K., Balkchinova, E., 2004. Microstructural and microchemical development of simple and Pt-modified aluminide diffusion coatings during long term oxidation at 1050°C. Surface & Coatings Technology 176, 272-283.
6. Angenete, J., Stiller, K., Langer, V., 2003. Oxidation of simple and Pt-modified aluminide diffusion coatings on Ni-base superalloys-I. Oxide scale microstructure. Oxidation of Metals 60, 1/2, 47-82.
7. Angenete, J., Stiller, K., 2003. Oxidation of simple and Pt-modified aluminide diffusion coatings on Ni-base superalloys-II. Oxide scale feilure. Oxidation of Metals 60, 1/2, 83-101.
8. Bacos, M.P., Josso, P. Vialas, N., Poquillon, D., Pieraggi, B., Monceau, D., Nicholls, J.R., Simms, N., Ecinas-Oropesa, A., Ericsson, T., Stekovic, S., 2004. ALLBATROS advanced long life blade turbine coating systems. Applied Thermal Engineering 24, 1745-1753.
9. Barrett, C.A., 1976. NASA Lewis Research Center, Cleveland, NASA-TN-D-8132 E-8432.
10. Baxter, D.J., Gilliland, D., Lanza, F., Toledo, G.P., Bregani, F., 1997. The oxidation and corrosive degradation of vacuum plasma spayed coatings in industrial gas turbine environmental. Materials Science Forum Vols 251-254, 801-808
11. Bhadescia, H.K.D.H..Rafting in Nickel Based Supetalloys. http://www.msm.cam.ac.uk (November 2008)
12. Bhadescia, H.K.D.H.. First, second and third generation of single-crystal Ni-base superalloy. University of Cambridge. http://www.msm.cam.ac.uk
13. Bordenet B. 2004 High temperature corrosion in gas turbine: Thermodynamic modelling and experimental results. PhD Thesis. Von der Fakultät für Maschinenwesen der Rheinisch-

Westfälischen Technischen Hochschule Aachen zur Erlangung des akademischen Grades eines Doktors der Ingenieurwissenschaften genehmigte Dissertation.

14. Brumm, M.W., Grabke, H.J., 1992. The oxidation behaviour of Ni-Al-I. Phase transformations in the alumina scale during oxidation of Ni-Al and Ni-Al-Cr alloys. Corrosion Sciece 33, 1677-1690.
15. Brunetaud, R., Coutsouradis, D., Gibbons, T.B., Lindblom, Y., Meadowcroft, D.B., Stickler, R., 1982. High Temperature Alloys for Gas Turbines 1982. D.Reidel Publishing Company.
16. Bürgel, R., 1986, Coating service experience with industrial gas turbine. Materials Science and Technology, 2, 302-308.
17. Chan, W.Y., Evans, H.E., Ponton, C.B., Nicholls, J.R., Simms, N.J., 1999. The influence of $NiAl_3$ on the high temperature oxidation of a plasma-sprayed overlay coating. Microscopy of oxidation. Proocedings of the Fourth Interntional conference on the Microscopy of Oxidation. Trinity Hall, Cambridge, 20-22 September 1999.
18. Chen, G., Rühle, M., 2005. Transient alumina transformation on a sputtered K38G nanocrystal coating. Surface and Coating technology 191, 263-266.
19. Chen, W. R., Wu, X., Marple, B.R., Patnaik, P.C. 2006. The growth and influence of thermally grown oxide in a thermal barrier coating. Surface & Coatings Technology 201, 1074-1079.
20. Coatings for high temperature applications. CEC High Temperature Materials Information Centre, Petten, The Netherlands.1983. Applied Science Publishers.
21. Cobalt Monograph. Centre d'information du cobalt. Brussels,1960.
22. Coutsouradis, D., Davin, A., Lamberigts, M., 1987. Cobalt-based Superalloys for Applications in Gas Turbines. Materials Science and Engineering, 88, 11-19.
23. Coutsouradis, Felix, Fischmeister, Habraken, Lindblom, Speidel, 1978. High temperature alloys for gas turbine. Applied science Publishers LTD, London.
24. C-Tech Innovation, 2003. Electricity Report.
25. Culp, A.W.Jr, 1991. Principles of energy conversion. McGraw-Hill, Inc.Second Edition.
26. Deodeshmukh, V., Mu, N., Li, B., Gleeson, B., 2006. Hot corrosion and oxidation behaviour of a novel Pt-Hf-modified *y'*-Ni_3Al+*y*-Ni-based coating. Surface & Coating Technology 201, 3836-3840.
27. Donachie, M.J., Donachie, S.J., 2002. Superalloys. A technical Guide. Second Edition. ASM International.
28. Eliaz, N., Shemesh, G., Latanision, R.M.; 2002. Hot corrosion in gas turbine components. Engineering Failure Analysis 9, 31-43.
29. Elliot, P., 1991. A practical guide to high-temperature alloys. Materials & Design 12, 299-307.

30. Encinas-Oropesa, A., 2005. Doctorial Thesis. Study of hot corrosion of single crystal super-alloy and platinum-aluminide coatings. Cranfield University.
31. Energy Information Administration, 2007. International Energy Outlook 2007 Office of Integrated Analysis and Forecasting U.S. Department of Energy Washington, DC 20585.
32. Energy Systems and Sustainability. Power for a Sustainable Future. Boyle, G., Everett, B., Ramage, J., 2003. Oxford.
33. Evans, H.E., Taylor, M.P., 2005. Oxidation of high-temperature coatings. Journal of Aerospace Engineering 220, 1-10.
34. Gesmundo, F., 1997. Mathematical modelling of alloy oxidation. Materials Science Forum Vols 251-254, 3-18.
35. Giurappa, I., 2001. Identification of hot corrosion resistant MCrALY based bond coating for gas turbine engine application. Surface & Coatings Technology 139, 272-283.
36. Gupta, Devendra. Advanced Technological Materials. William Andrew Publishing. Noyes, 2005.
37. Goebel, J.A. Pettit, F.S., Goward, G. W., 1973.Mechanism for the hot corrosion of nickel-base alloys. Metalurgical Transactions 4, 261-278.
38. Goebel, J.A. Pettit, F.S., 1970. Na2SO4-induced accelerated oxidation (hot corrosion) of nickel. Metalurgical Transactions 1, 1943-54.
39. Grabke, H.J., 1997. Oxidation of aluminides. Science Forum Vols 251-254, 149-162.
40. Grabke, H.J., 1999. Oxidation of NiAl and FeAl. Intermetallics 7, 1153-1158.
41. Garriga-Majo, D.P., Shallock, B.A., McPhail, D.S., Chater, R.J., Walker, J.F., 1999. International Journal of Inorganic Materials 1, 325-336.
42. Griffiths, R.T., 1995.Combined Heat and Power. A practical Guide to the Evaluation, development, Implementation and Operation of Cogeneration Schemes. Energy Pubblication.
43. Grünling, H.W., Rechtenbacher, H., Singheiser, L., 1997. Some Practical Aspects of Corrosion and Coatings in Utility Gas Turbines. Materials Science Forum Vols. 251-254, 483-502.
44. IEE Power & Energy Series 43, 2003. Thermal Power Plant. Simulation and Control. Damian Flynn.
45. Luthra, K. L., Shores, D.A., 1980. Mechanism of Na_2SO_4 Induced Corrosion at 600°-900°C. Journal of The Electrochemical Society 127, 2202-2210.
46. Hass, D.D.. “Directed Vapor Deposition of Thermal Barrier Coating”. Ph.D. Thesis, University of Virginia, 2000. www.ipm.virginia.edu/research/PVD/Pubs/thesis6/chapter2.PDF (Mach 2008).

47. Hayashi, S., Ford, S.I., Young, D.J., Sordelet, D.J., Besser, M.F., Gleeson, B., 2005. α-NiPt(Al) and phase equilibria in the Ni-Al-Pt system at 1150°C. Acta Materalia 53, 3319-3328.
48. Healt, G.R., Heimgartner, P., Irons, G., Miller, R., Gustafsson, S., 1997. An assessment of thermal spray coating technologies for high temperature corrosion protection. Materials Science Forum Vols 251-254, 809-816.
49. High temperature alloys for gas turbines and other applications 1986. Proceedings of a Conference held in Liège, Belgium, 6-9 October 1986. Part I. D. Reidel Pubblishing Company.
50. High temperature corrosion. Per Kofstad, 1988. Elsevier Applied Sciences Publishers LTD.
51. High temperature corrosion of engineering alloy. Lai, G.Y., 1990. ASM International.
52. High temperature materials corrosion in coal gasification atmospheres. CEC High temperature Materials Information Centre, Petten (N.H.), The Netherlands. J.F. Norton, 1984.
53. High temperature oxidation of metals. Birks, N., Meier, G. H., Pettit, F. S., 2006. Second Edition. Cambridge.
54. Higuera, V., Belzunce. F.J., Riba, J., 2006. Influence of the thermal-spray procedure on the properties of a CoNiCrAlY coating. Surface & Coatings Technology 200, 5550 – 5556.
55. Hindam, H., Whittle, D.P., 1982. Microstructure, adhesion and growth kinetics of protective scales on metals and alloys. Oxidation of Metals 18, 245-284.
56. Horlock, J.H., 1992.Combined Power Plants. Including Combined cycle Gas Turbine (CCGT) Plants. Pergamon Press.
57. Khajavi, M.R., Shariat, M.H., 2004. Failure of first gas turbine blades. Engineering Failure Analysis 11, 589-597.
58. Lee, W. Y., Stinton, D. P., Berndt, C.C., Erdogan, F., Lee, Y.D., Mutasim, Z., 1996. Concept of Functionally Graded Materials for Advanced Thermal Barrier Coating Application. Journal of American Ceramic Society, 79, 3003-3012.
59. Lelait, L., Alpérine, S., Mévrel, R., 1990. Alumina scale growth at zirconia/MCrAlY interface: a microstructural study. Microscopy of oxidation. Proceedings of the First International Conference held at the University of Cambridge, 26-28 march, 1990. Bennet M. J and Lorimer. G.W..
60. Leyens, C., Pint, B.A., Wright, I.G., 2000. Effect of composition on the oxidation and hot corrosion resistance of NiAl doped with precious metals. Surface and Coating Technology 133-134, 15-22.
61. Life prediction for hot gas path materials in coal-fired gas turbines. Project Summary 259, December 1999. Department of Trade and Industry. Claner Coal Technology Programme.

62. Lowell, C.A., Smialek, J.L., Barrett, C.A.. Proceeding of the International Conference on High Temperature Corrosion, San Diego, 2-6 March1981. NACE,1983, 219-226.
63. Luthra, K. L., Shores, D.A., 1980. Mechanism of Na_2SO_4 Induced Corrosion at 600°-900°C. Journal of The Electrochemical Society 127, 2202-2210.
64. Meier, G.H., Pettit, F.S., 1989. High-Temperature corrosion of aluminia-forming coatings for superalloy. Surface & Coatings Technology 39/40, 1-17.
65. Meier, G.B., Pettit, F.S., 1990. Microscopy of the corrosion of high temperature coatings. Microscopy of Oxidation. Proceedings of the International Conference held at the University of Cambridge, 26-28 March, 1990. Bennett & Lorimer.
66. Mévrel, R., 1989. State of the art on high-temperature corrosion-resistant coatings. Materials Science and Engineering, A120, 13-24.
67. Mobarra, R., Jafari, A.H., Karaminezhaad, M., 2006. Hot corrosion behaviour of MCrAlY coatings on IN738LC. Surface & Coatings Technology 201, 2202-2207.
68. MSc in Advance Materials. Surface Science and Engineering. Nicholls, J. Lectures Note. Cranfield University, 2007.
69. Nakamori, M., Kayano, I., Tsukuda, Y., Takahashi, K., Torigoe, T., 1997. Hot corrosion and its prevention in high temperature heavy oil firing turbines. Materials Science Forum Vols. 251-254, 633-640.
70. Natesan, K., 1993. Applications of coatings in coal-fired energy systems. Surface & Coatings Technology 56, 185-197.
71. Nicholls, J.R., Hancock, P., 1983. The analysis of oxidation and hot corrosion data-a statistical approach. NACE-6.
72. Nicholls, J.R., Simms, N.J., Chan, W.Y., Evans, H.E., 2002. Smart overlay coatings-concept and practice. Surface & Coatings Technology 149, 236-244.
73. Oakey, J.E., Simms, N.J., Allen, D.H., 2002. Environmental degradation issues in gas turbines and their relevance to plant life extantion-R&D initiatives. Enviromental degradation in gas turbine, OMMI 3, Issue 1.
74. Okazaki, M., 2001.High-temperature strength of Ni-base superalloy coatings. Science and Tecnology of Advanced Materials 2, 357-366.
75. Pomeroy, M.J., 2005. Coating for gas turbine materials and long term stability issues. Materials and Design 26, 223-231.
76. Pomeroy, M.J., 2005. Identification of hot corrosion resistant MCrALY based bond coating for gas turbine engine application. Surface & Coatings Technology 139, 272-283.
77. Poquillon, D., Monceau, D., 2003. Application of a Simple Statistical Spalling Model for the Analysis of High Temperature, Cyclic-Oxidation Kinetics Data. Oxidation of Metals, 59,409-431.

78. Pint, B.A., More, K.L., Wright, I.G., Tortorelli, P.F., 1999. Characterization of thermally cycled alumina scales. Microscopy of oxidation. Proceedings of the Fourth Interntional conference on the Microscopy of Oxidation. Trinity Hall, Cambridge, 20-22 September 1999.
79. Pratt & Whitney Aircraft Group, 1979. Hot Corrosion Degradation of Metals. A Unified Theory . Final Scientific Report. Florida (USA).
80. Quadakkers, W.J., Piron-Abellan, J., Shemet, V., Singheiser, L., 2002. Metallic interconnections for solid oxide fuel cell-a review. Life Cycle Issues in Advanced Energy Systems. Proceedings of the 3rd International Workshop on environmental Degradation in Advanced Energy Systems. Woburn, 2002.
81. Raffaitin, A., Crabos, F., Andrieu, E., Monceau, D., 2006. Advanced burner-rig test for oxidation-corrosion of MCrAlY/superalloys systems. Surface & Coatings Technology 201, 3829-3835.
82. Rapp, R.A., 1969 Hot Corrosion. Materials 4, 583.
83. Rapp, R.A., 2002. Hot corrosion of materials: a Fluxing mechanism? Corrosion Science 44, 209-221.
84. Schütze, M., 2000. Corrosion and Environmental Degradation. Vol I. WILEY-VCH.
85. Schütze, M., 1997. Protective Oxide Scale and their Breakdown. D.R. Holmes, Institute of Corrosion.
86. Secretary of State for Trade and Industry by Command of Her Majesty; 2003. Energy White Paper. Crown Copywriter.
87. Seo, D., Ogawa, K., Suzuki, Y., Ichimura, K., Shoji, T., Murta, S., 2008. Comparative study on oxidation behaviour of selected MCrAlY coating by elemental concentration profile analysis. Applied Surface Science (to be published).
88. Seo, D., Ogawa, K., Tanno, M., Shoji, T.,Murata, S., 2007.Influence of heat exposure time on isothermal degradation of plasma sprayed CoNiCrAlY coatings. Surface & Coatings Technology 201, 7952-7960.
89. Shihi, S., Zhang, Y., Li, X., 1989. Sub-melting Point Hot Corrosion of Alloys and Coatings. Material Science and Engineering, A120, 277-282.
90. Shulz, U., Fritscher, K., Rätzer-Scheibe, H-J, Kaysser, W.A., Peters, M., 1997. Thermocycling behaviour of microstructurally modified EB-PVD thermal barrier coatings. Materials Science Forum Vols 251-254, 957-964.
91. Sidhu, T.S., Prakash, S., Agrawal, R.D., 2006. Hot corrosion and performance of nickel-based coatings. Current Science 90, 41-47.
92. Simms, N.J., Nicholls, J.R., Oakey, J.E.. Corrosion and Lifetime Modelling of Components in Coal fired Combined Cycle Power Systems. Lifetime Modelling of High Temperature

Corrosion Processes, 2001. Proceedings of an EFC Workshop 2001, held in Frankfurt am Main, Germany, February 2001. Ed. Schütze, M.; Quadakkers, W.J.; Nicholls, J.R.

93. Simms N.J. and Oakey J.E. (1997). 'Measurement of Corrosion Damage in Coal-fired Combined Cycle Power Systems', in Microscopy of Oxidation 3, Proceedings of the Third International Conference held at Trinity Hall, University of Cambridge 16-18 September 1996, pp. 657-668.
94. Simms, N.J., Oakey, J.E., Nicholls, J.R., 2000. Development and application of a methodology for the measurement of corrosion and erosion damage in laboratory, burner rig and plant environment. Materials at High Temperature 17, 355-362.
95. Simms, N.J., Oakey, J.E., Stephenson, D.J., Smith, P.J., Nicholls, J.R., 1995. Erosion-corrosion modelling of gas turbine materials for coal-fired combined cycle power generation, Wear 186-187, 24-255.
96. Simms, N.J., Saunders, S.R.J., Osgerby, S., Oakey, J.E., 2003. Measurements and compilation of materials degradation data in the COST522 programme. Life Cycle Issues in Advance Energy Systems, 137-151.
97. Simms, N. J., Smith, P.J., Ecinas-Oropesa, A., Ryder, S., Nicholls, J.R., Oakey, J.E. Development of Type II hot corrosion in solid fuel fired gas turbines. Lifetime Modelling of High Temperature Corrosion Processes, 2001. Proceedings of an EFC Workshop 2001, held in Frankfurt am Main, Germany, February 2001. Ed. Schütze, M.; Quadakkers, W.J.; Nicholls, J.R.
98. Smialek, J.L., 1978. Oxide morphology and spalling model for NiAl. Metallurgical Materials Transaction A, 9, 309-320.
99. Smialek, J.L., 2003. A deterministic interfacial cyclic oxidation spalling model. Acta Materialia, 5, 469-483.
100. Smialek, J.L., 2004. Universal characteristics of an interfacial spalling cyclic oxidation model. Acta Materialia, 52, 2111-2121.
101. Smialek, J.L., Nesbitt, J.A., Barrett, C.A., Lowell, C.E.. Cyclic Oxidation Testing and Modelling:a NASA Lewis Prospective. Cyclic Oxidation of High Temperature Materials. EFC 27, 148-168.
102. Smith, F.W. 1981. Structure and properties of engineering alloys. McGraw-Hill Book Company.
103. Stinger, J., 2002. High Temperature Corrosion Issues in Energy-Related Systems. Materials Research 7, 1-9.
104. Stott, F.H., 1997. The oxidation of Alumina-Forming Alloys. Materials Science Forum Vols. 251-254, 19-32.

105. Strawbridge, A., Evans, H.E., Ponton, C.B., 1997. Spallation of Oxide Scales from NiCrAlY Overlay Coatings. Materials Science Forum Vols. 251-254, 365-372.
106. Superalloys II. High temperature materials for aerospace and industrial power.Sims, C. T., Stoloff, N.S., Hagel, W. C.;1987. John Wiley & Sons.
107. SUPERGEN. Sustainable power generation and supply. Powering the future. EPSRC Secretary of State for Trade and Industry by Command of Her Majesty.
108. Sureau, S., Poquillon, D., Monceau, D., 2007. Numerical simulation of cyclic oxidation kinetics with automatic fitting of experimental data. Scripta Materialia, 56, 233-236.
109. Svensson, H., Angenete, J., Stiller, K., 2004. Microstructure of oxide scales on aluminide diffusion coatings after short time oxidation at 1050°C. Surface & Coatings Technology 117-178, 152-157.
110. Tang, F., Ajdelsztajn, L., Kim, G.E., Provenzano, V., Schoenung, J. M., 2004. Effects of surface oxidation during HVOF processing on the primary stage oxidation of a CoNiCrAlY coating. Surface & Coatings Technology 185, 228-233.
111. Taylor, T.A., Bettridge, D.F., 1996. Development of alloyed and dispersion-strengthened MCrAlY coating. Surface & Coatings Technology 86-87, 9-14.
112. Tatlock, G., Newcomb, S., 1999. Microscopy of oxidation. Proocedings of the Fourth International conference on the Microscopy of Oxidation. Trinity Hall, Cambridge, 20-22 September 1999.
113. The Superalloys. Fundamentals and Application. Cambridge University Press. Roger C., Reed. 2006.
114. Tolpygo, V.K., Clarke, D.R., 1999. Microstructural study of the theta-alpha transformation in alumina scales formed on nickel-aluminides. Microscopy of oxidation. Proceedings of the Fourth International Conference on the Microscopy of Oxidation. Cambridge, 20-22 September, 1999.
115. Tolpygo, V.K., 2007. Development of internal cavities in platinum-aluminide coatings during cyclic oxidation. Surface & Coatings Technology (to be published)
116. Tolpygo, V.K., Clarke, D.R., 2000. Surface rumpling of a (Ni, Pt) Al Bond Coat induced by cyclic oxidation. Acta Materialia 48, 3283-3293.
117. Toma D., Brandl, W., Köster, U., 1999. Studies on the transient stage of oxidation of VPS and HVOF sprayed MCrAlY coating. Surface Coatings & Technology 120-121, 8-15.
118. Toscano, J., Vaβen, R., Subanovic, M, Gil, A., Naumenko, D., Singheiser, L., Quadakkers, W. J., 2006. Parameters affecting TGO growth and adherence on MCrAlY-bond coats for TBC's. Surface Coatings & Technology 201, 3906-3910.
119. Vialas, N., Monceau, D., 2006. Effect of Pt and Al content on the long-term, high temperature oxidation behaviour and interdiffusion of a Pt-modified aluminide coating deposited on Ni-base superalloys. Surface and Coating technology 201, 3846-3851.

120. Vialas, N., Monceau, D., 2006 Substrate effect on the high-temperature oxidation behaviour of a Pt-modified aluminide coating. Part I: influence of the initial chemical composition of the coating surface. Oxidation of Metals 66, 155-189.
121. Vialas, N., Monceau, D., 2007. Substrate Effect on the High Temperature Oxidation Behaviour of a Pt-modified Aluminide Coating. Part II: Long-term Cyclic-oxidation Tests at 1050°C. Oxidation of Metals 68, 223-242.
122. Yedong, H., Zhengwei, L., Huibin, Q., Gao, W., 1997. Standard free energy change of formation per unit volume: a new parameter for evaluating nucleation and growth of oxides, sulphides, carbides and nitrides. Materials Research Innovation 1, 157-160.
123. Zhang, Y. H., Knowles, D. M., Whiters, P.J., 1998. Microstructural development in Pt-aluminide coating on CMSX-4 superalloy during TMF. Surface & Coatings Technology 107, 76-83.

8. Appendix

Oxidation

In the following plots each line represents the mass change experienced by one samples. A variable number of samples (two, four or seven) have been tested for each exposure time.

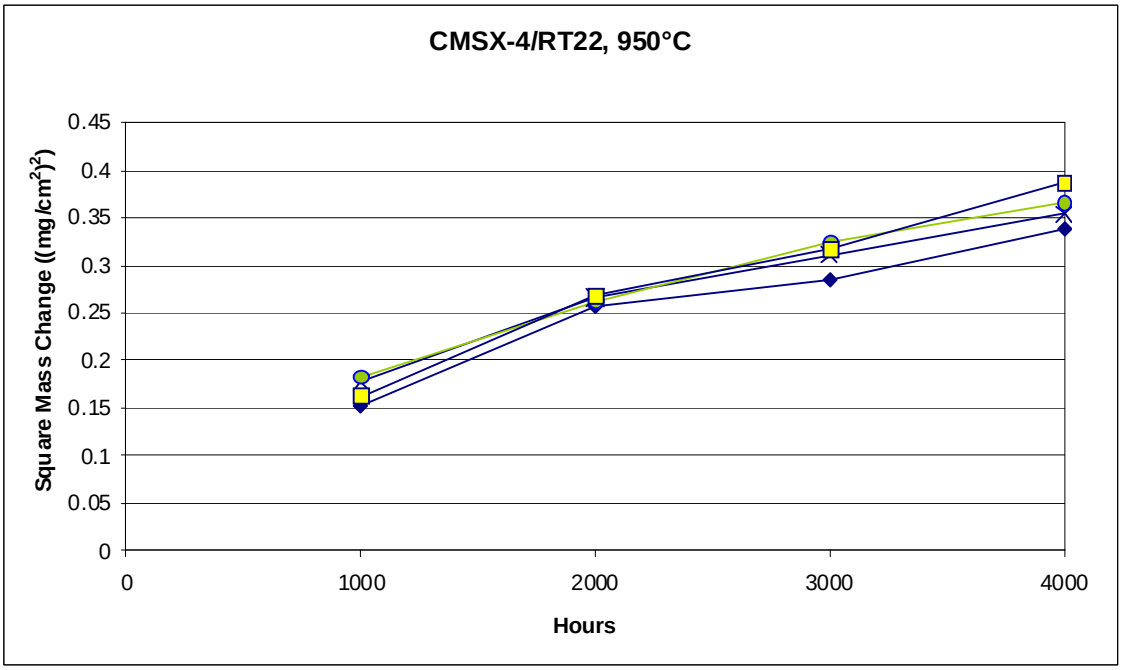

Figure I Square mass change data of CMSX-4/RT22 system tested at 950°C employed for rate constant calculation.

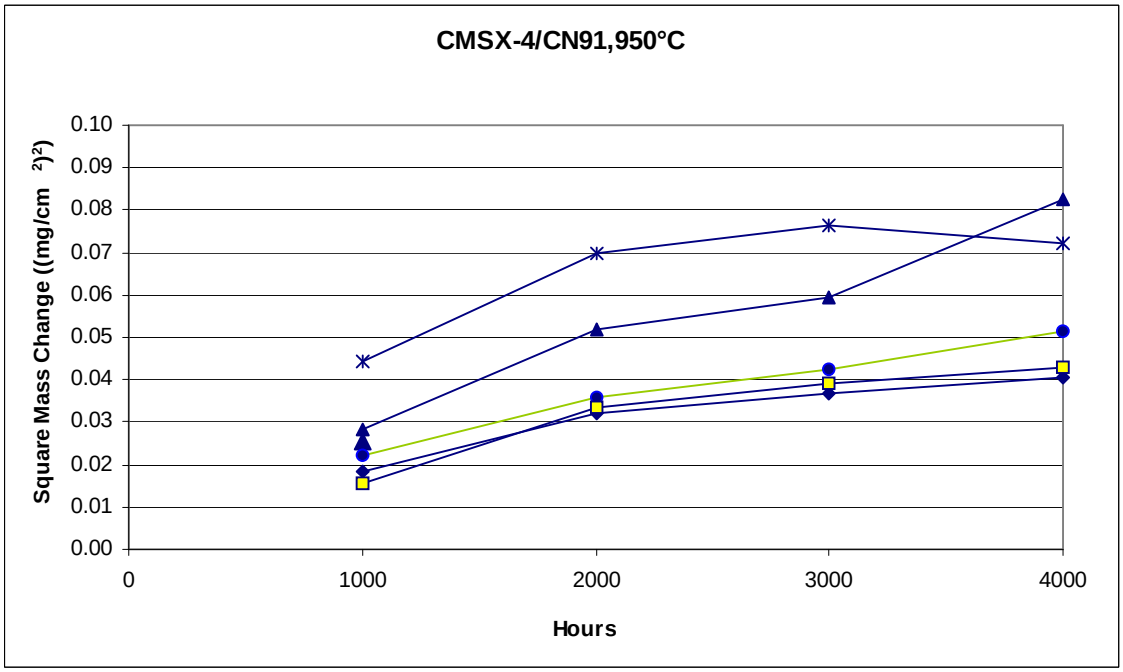

Figure II Square mass change data of CMSX-4/CN91 system tested at 950°C employed for rate constant calculation.

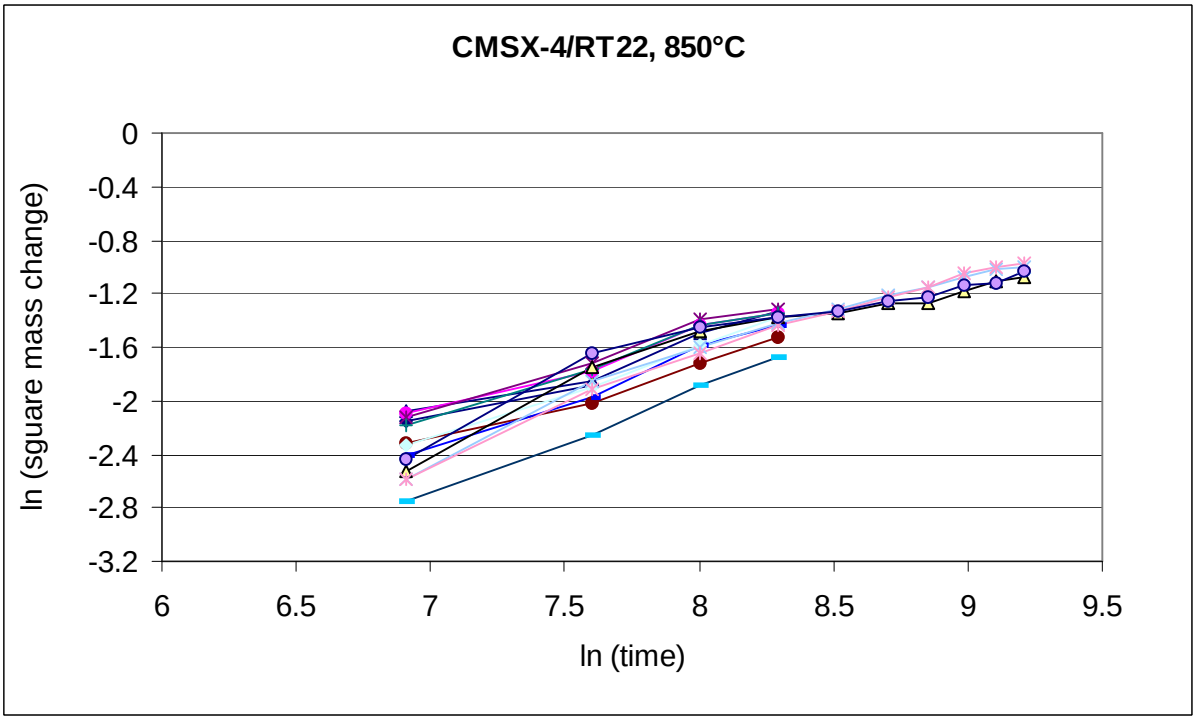

Figure III Logarithm of square mass change vs logarithm of time for CMSX-4/RT22 tested at 850°C

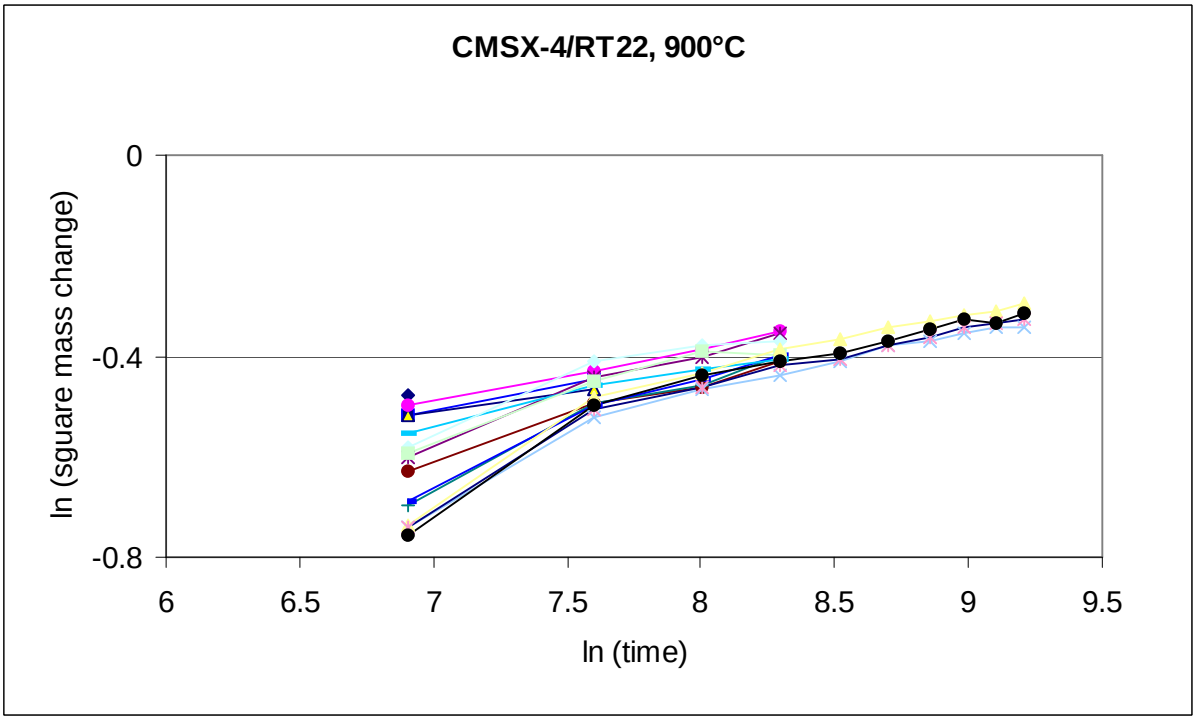

Figure IV Logarithm of square mass change vs logarithm of time for CMSX-4/RT22 tested at 900°C

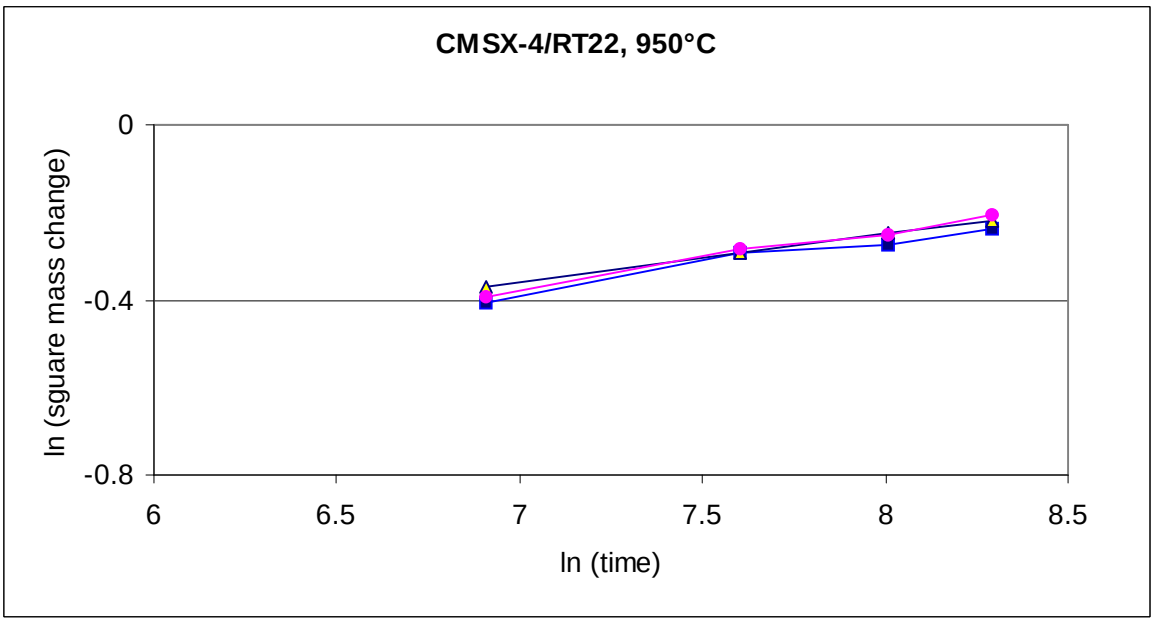

Figure V Logarithm of square mass change vs logarithm of time for CMSX-4/RT22 tested at 950°C

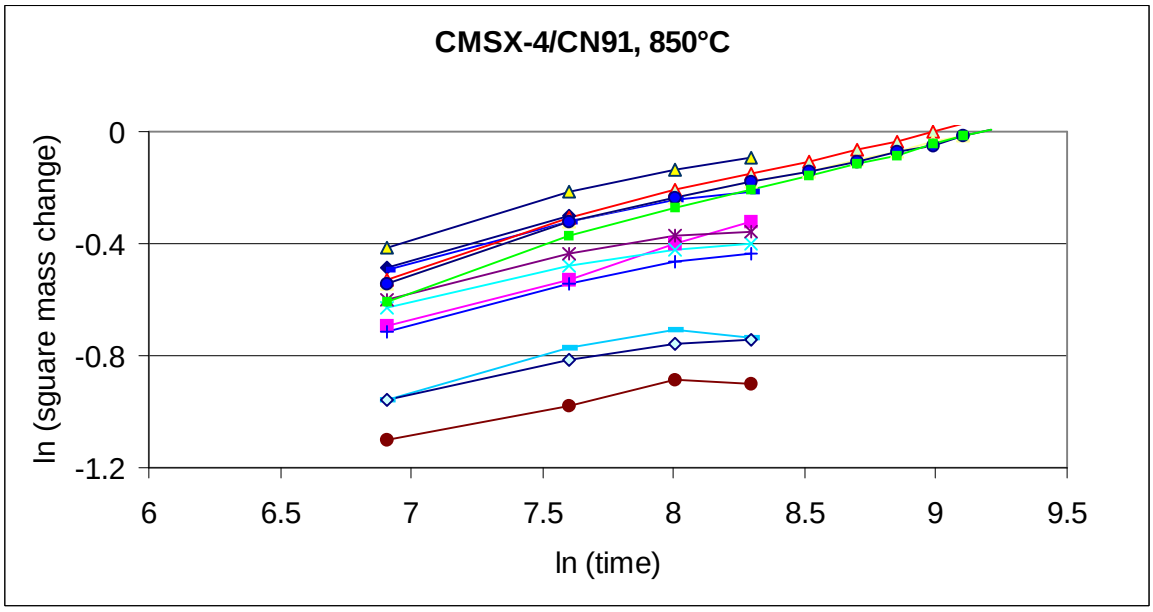

Figure VI Logarithm of square mass change vs logarithm of time for CMSX-4/CN91 tested at 850°C

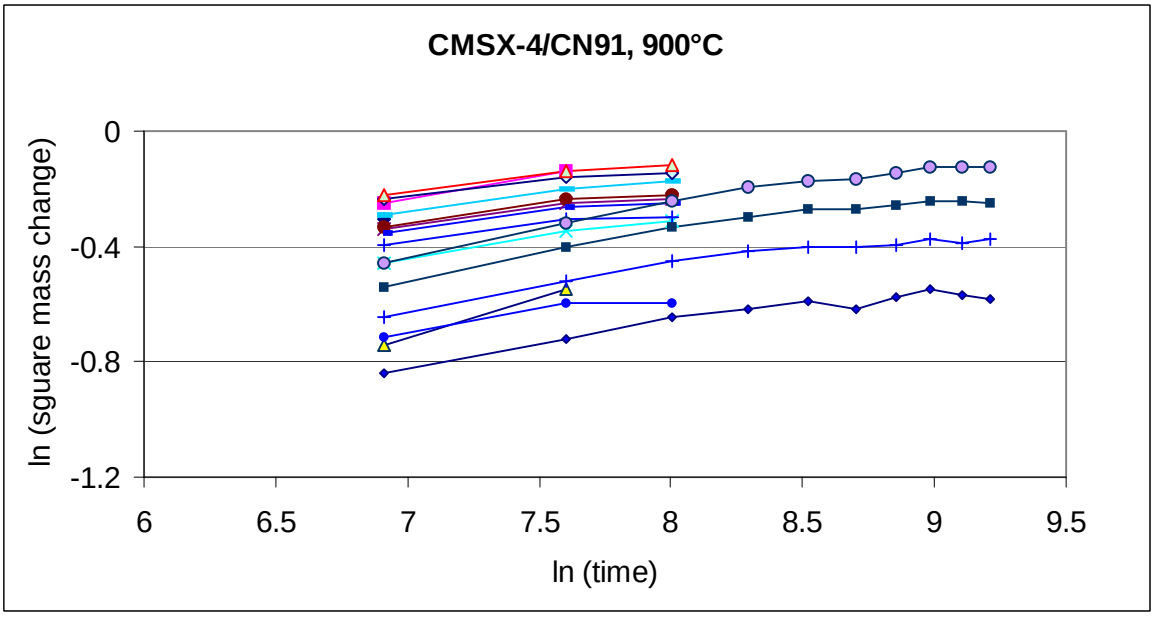

Figure VII Logarithm of square mass change vs logarithm of time for CMSX-4/CN91 tested at 900°C

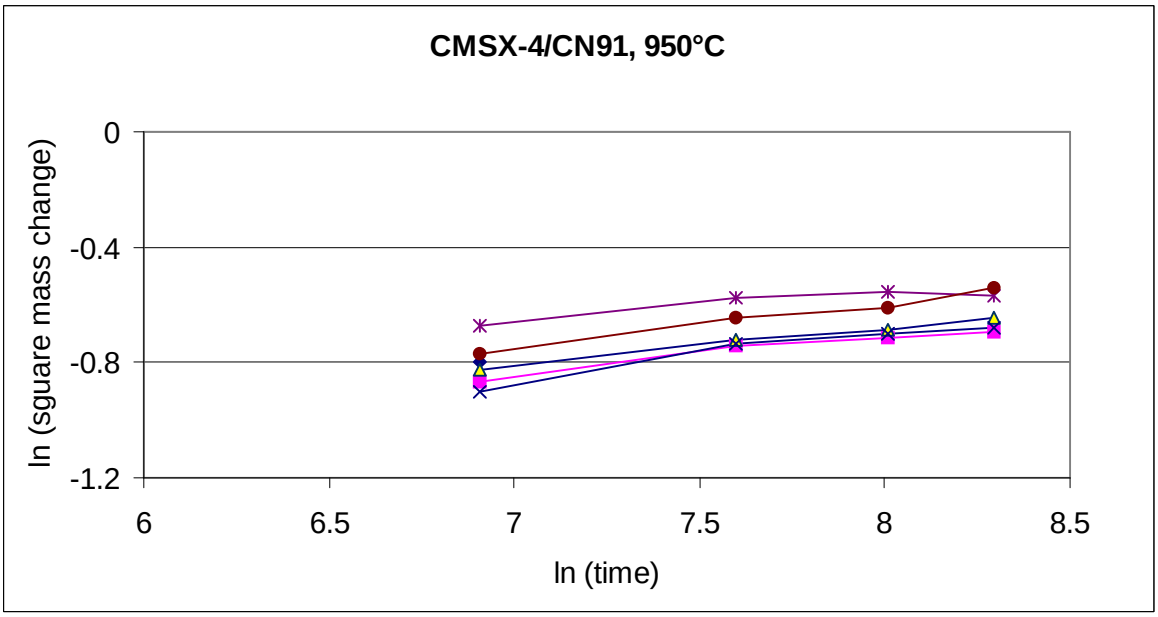

Figure VIII Logarithm of square mass change vs logarithm of time for CMSX-4/CN91 tested at 950°C

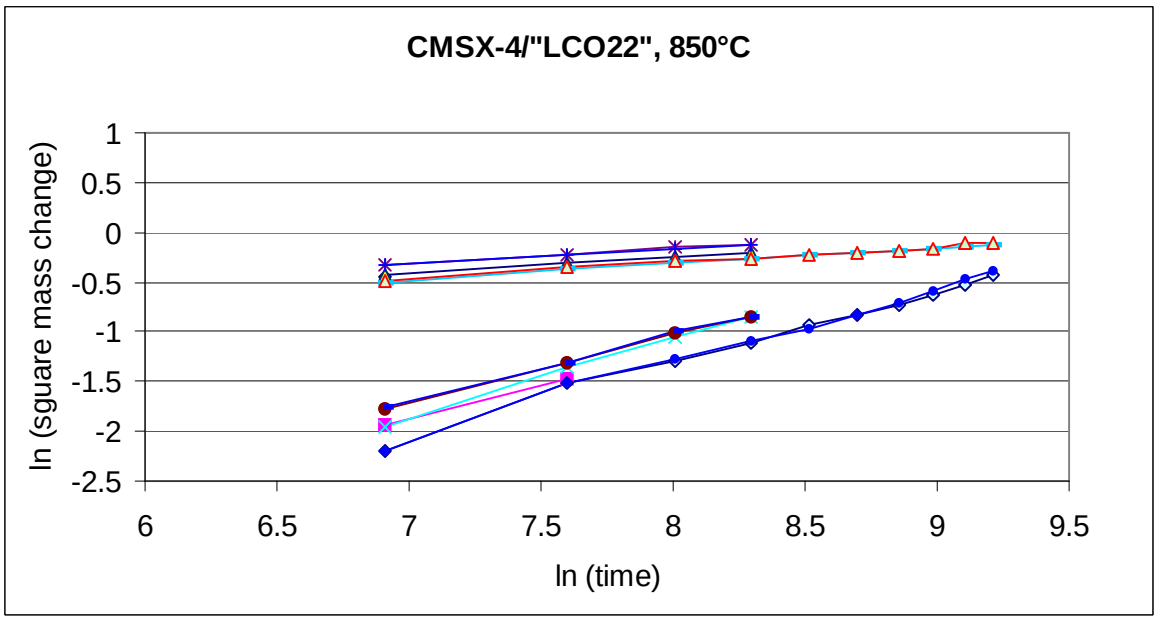

Figure IX Logarithm of square mass change vs logarithm of time for CMSX-4/"LCO22" tested at 850°C

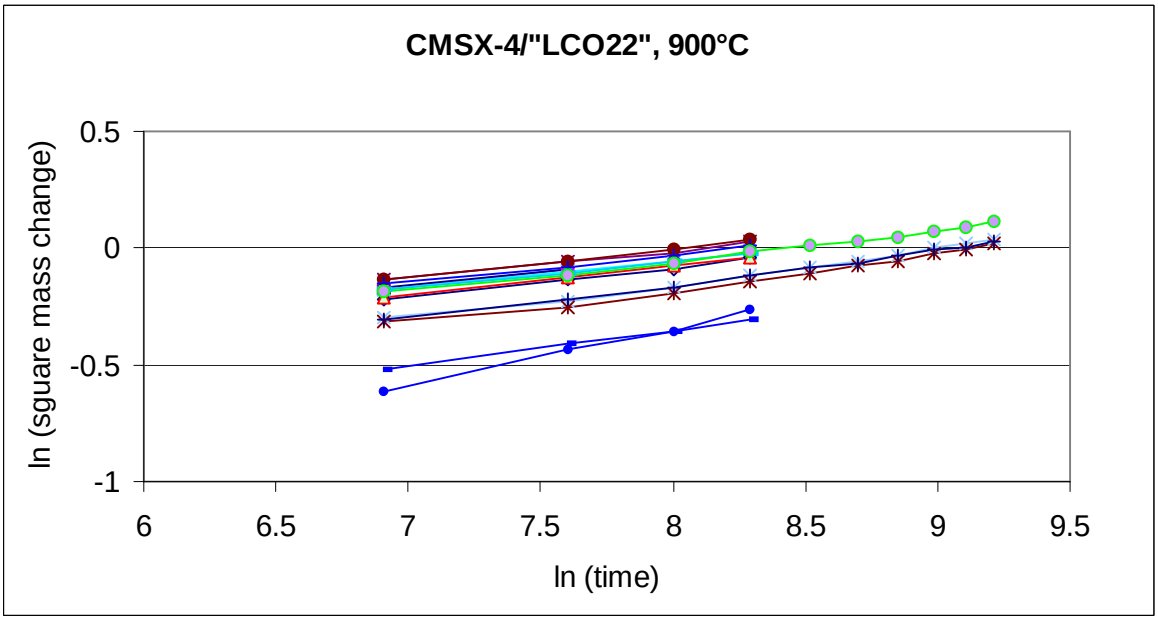

Figure X Logarithm of square mass change vs logarithm of time for CMSX-4/"LCO22" tested at 900°C

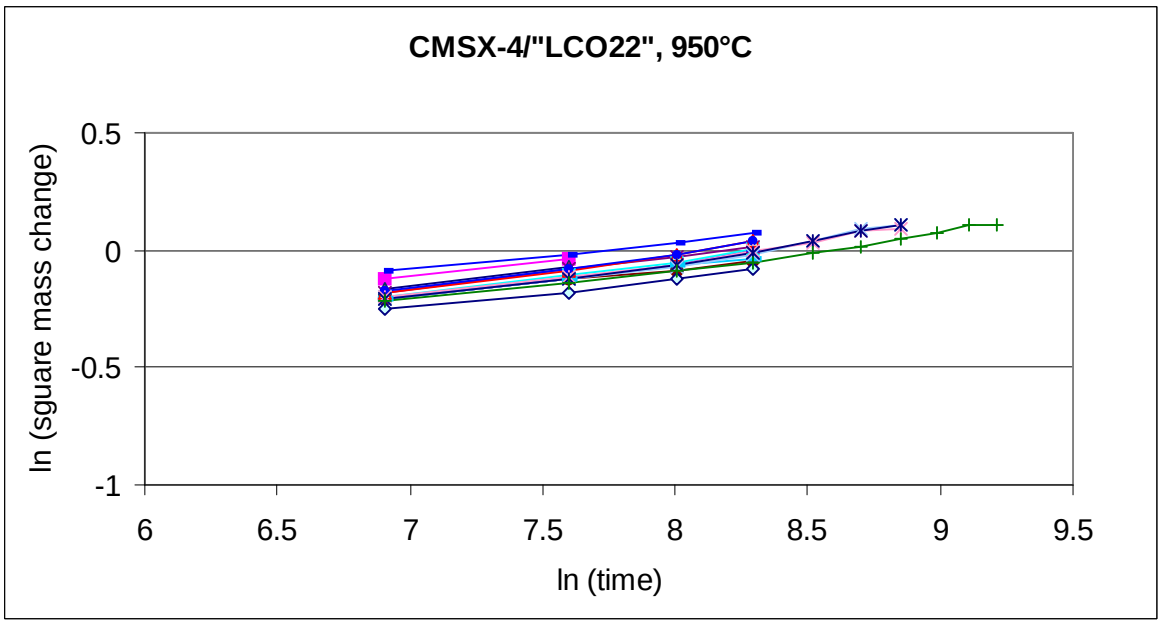

Figure XI Logarithm of square mass change vs logarithm of time for CMSX-4/"LCO22" tested at 950°C

Hot Corrosion

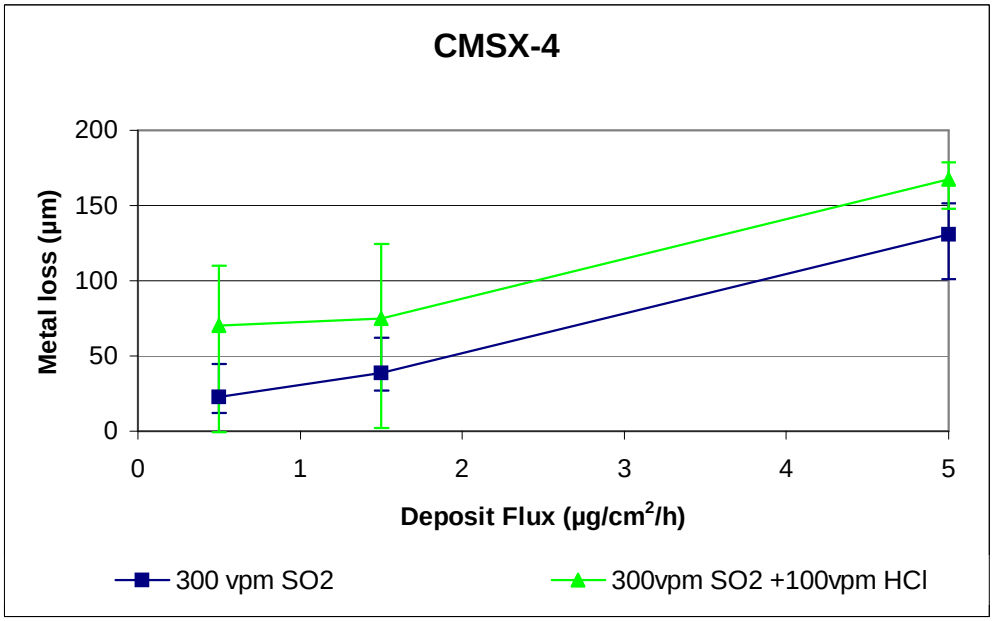

Figure XII. Effect of adding 100vpmHCl to 300 vpmSO_2 on CMSX-4 at 700°C.

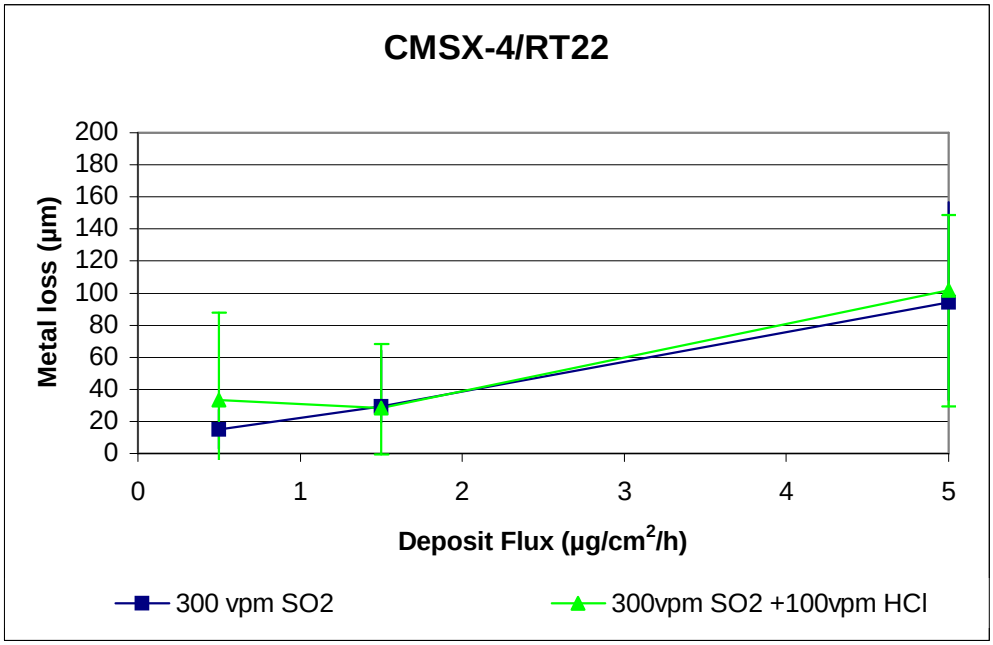

Figure XIII. Effect of adding 100vpmHCl to 300 vpmSO_2 on CMSX-4/RT22 at 700°C.

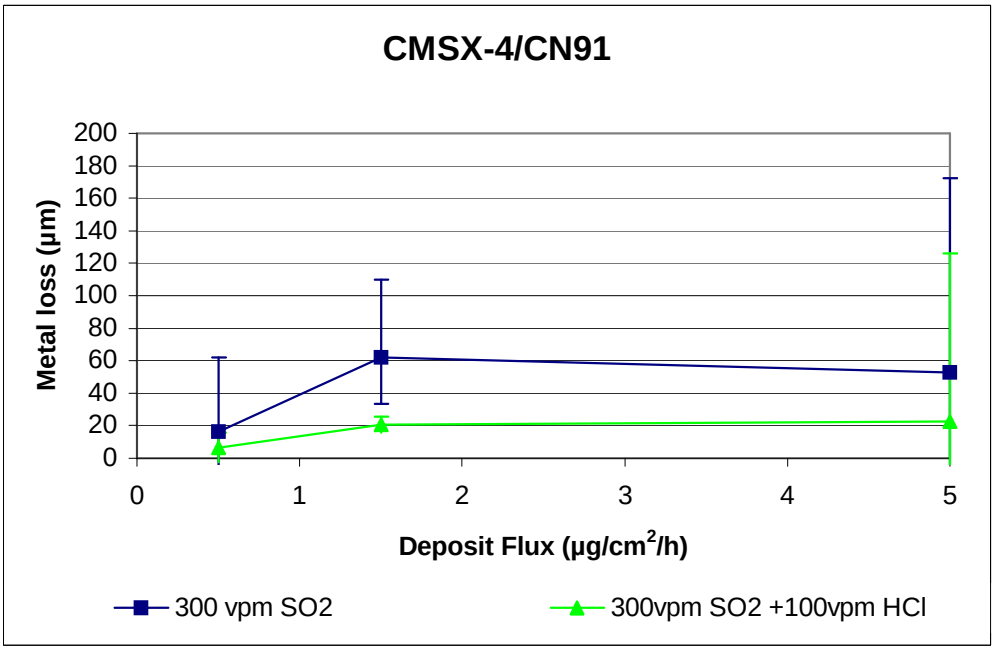

Figure XIV. Effect of adding 100vpmHCl to 300 vpmSO_2 on CMSX-4/RT22 at 700°C.

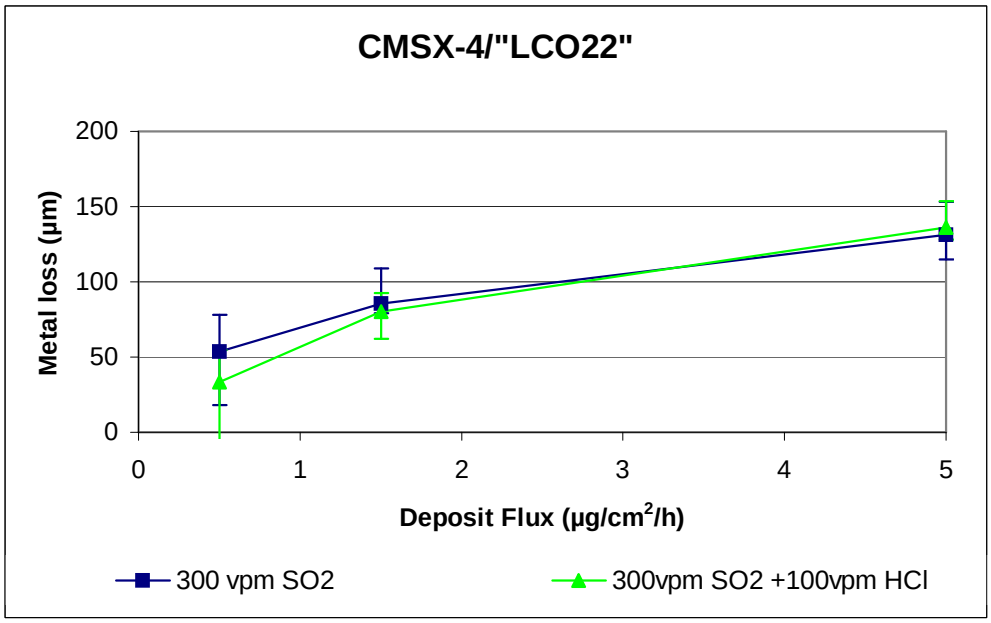

Figure XV. Effect of adding 100vpmHCl to 300 vpmSO_2 on CMSX-4/"LCO22" at 700°C

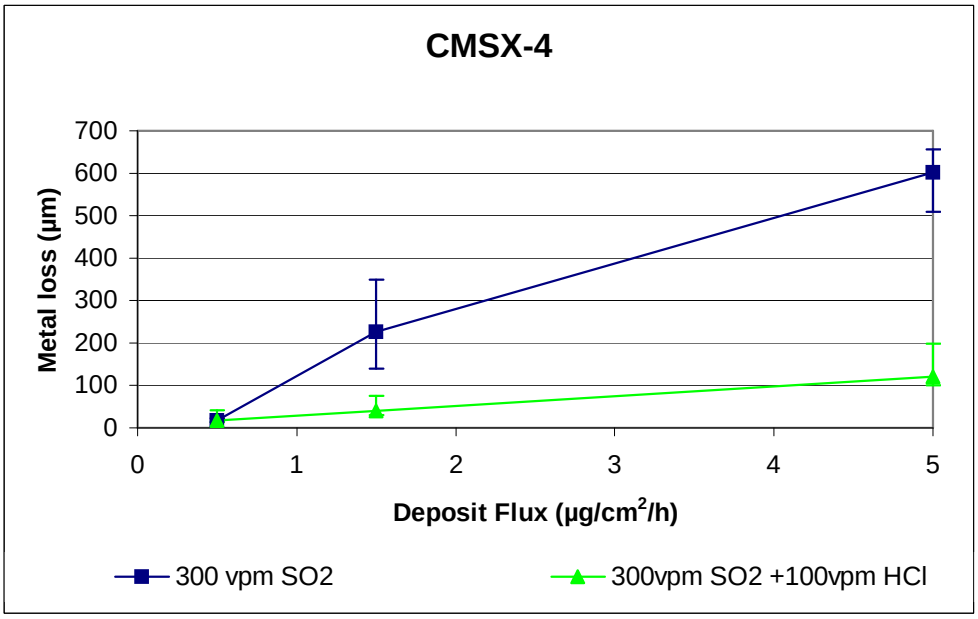

Figure XVI. Effect of adding 100vpmHCl to 300 vpmSO_2 on CMSX-4 at 900°C.

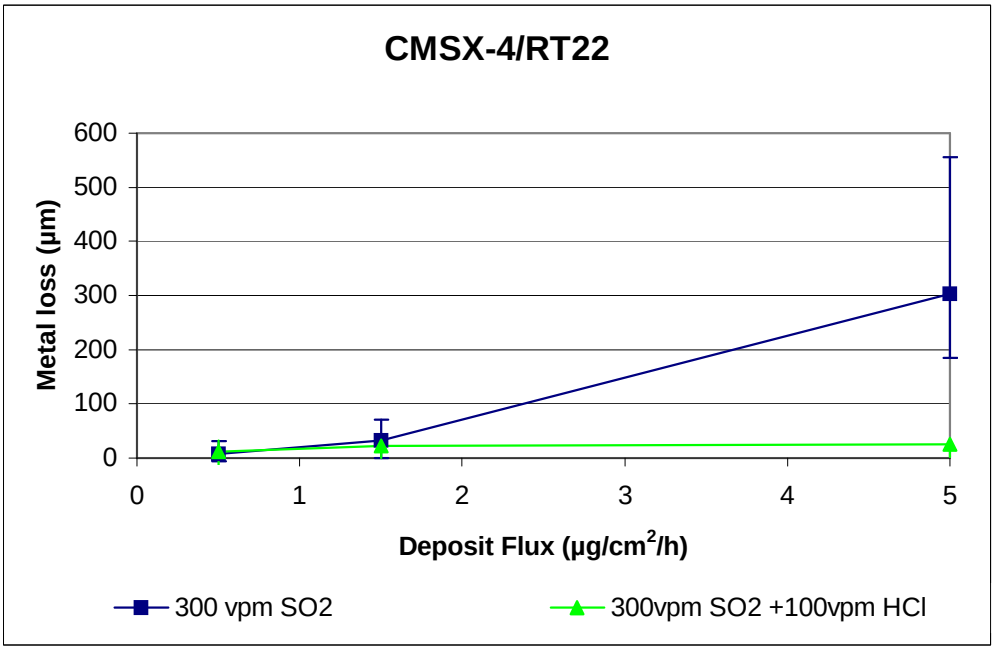

Figure XVII. Effect of adding 100vpmHCl to 300 vpmSO_2 on CMSX-4/RT22 at 900°C.

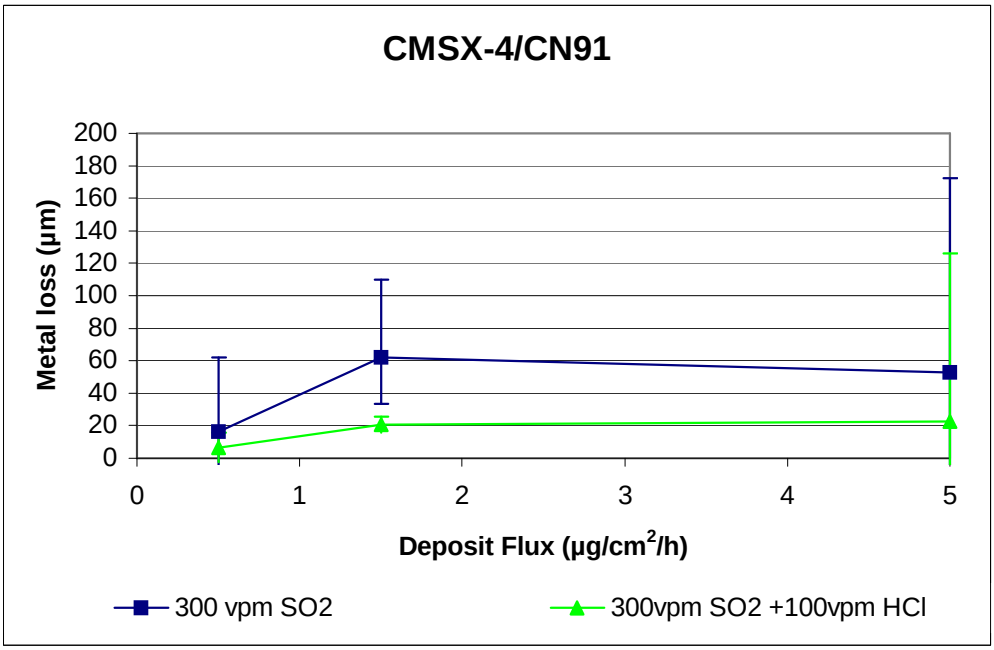

Figure XVIII. Effect of adding 100vpmHCl to 300 vpmSO_2 on CMSX-4/CN91 at 900°C.

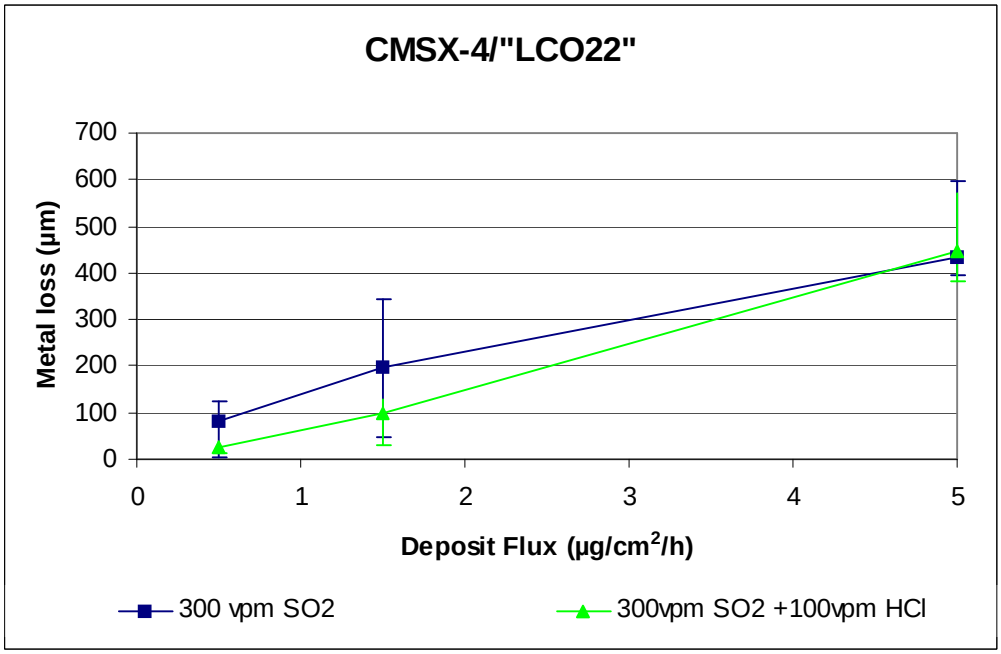

Figure XIX. Effect of adding 100vpmHCl to 300 vpmSO_2 on CMSX-4/"LCO22" at 900°C

		Exposure time (hours)			
		1000	**2000**	**4000**	**10000**
Temperature (°C)	**850**	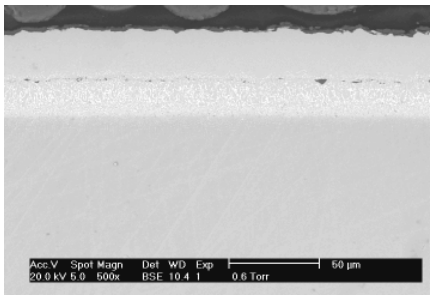 1	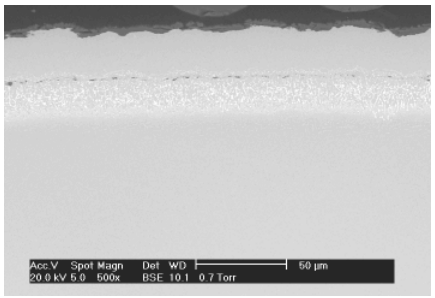 2	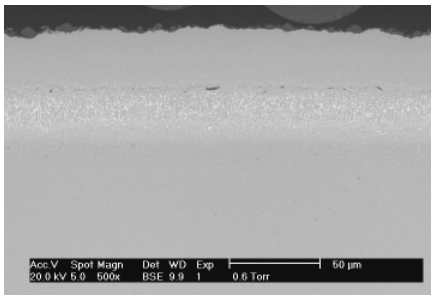 3	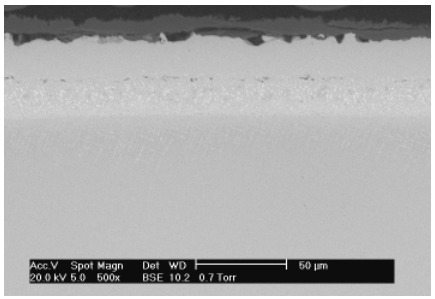 4
	900	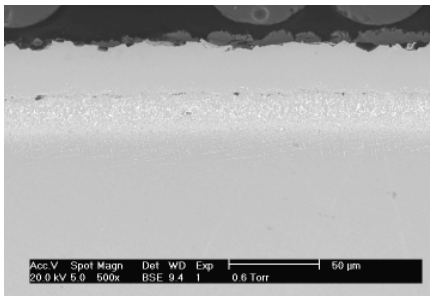 5	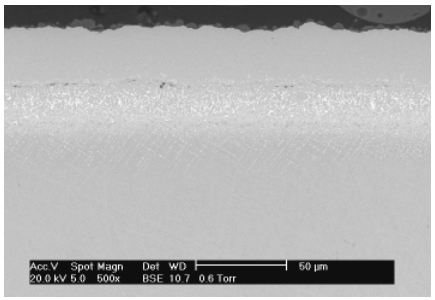 6	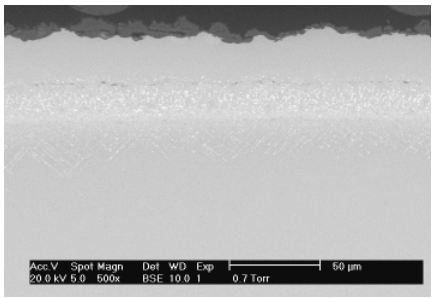 7	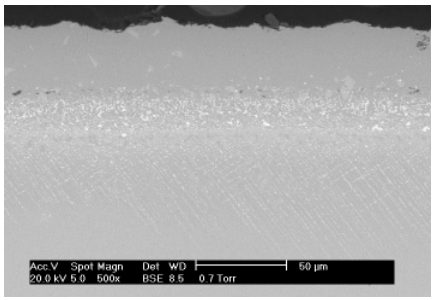 8
	950	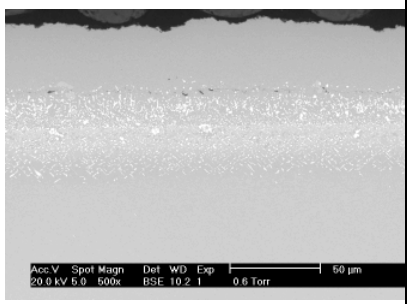 9	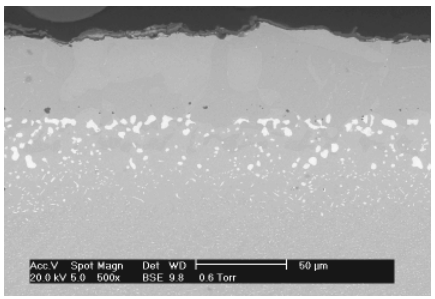 10	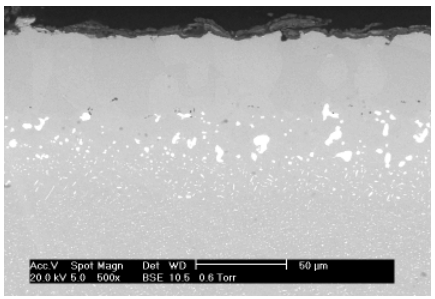 11	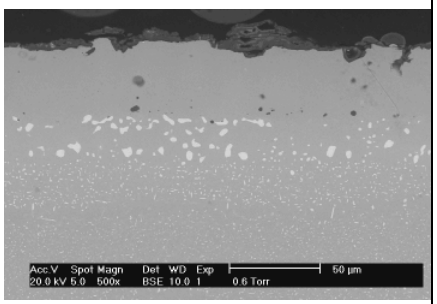 12
	1000				

	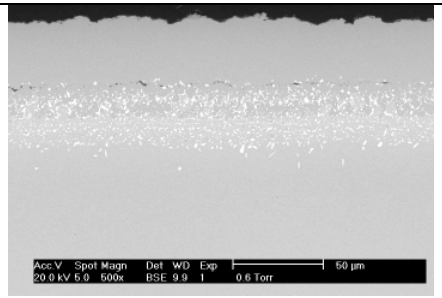 13	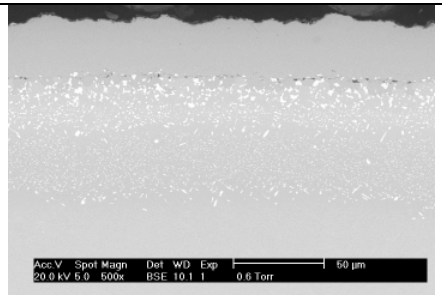 14	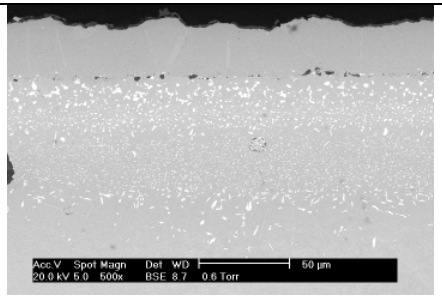 15	–
1050	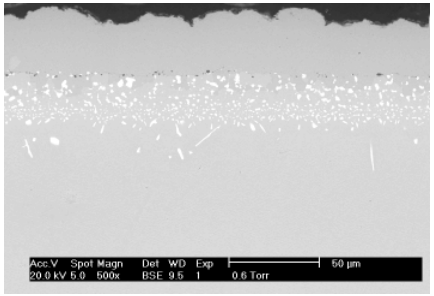 16	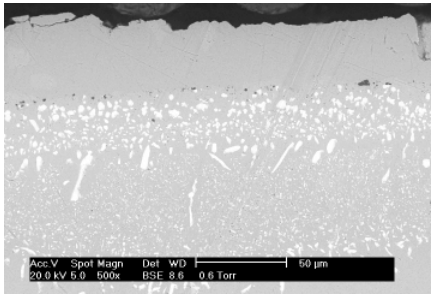 17	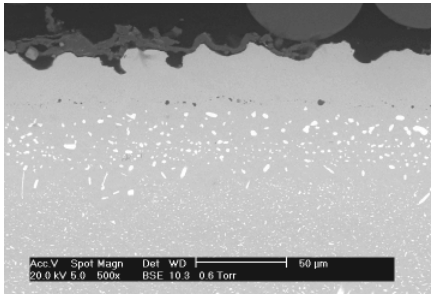 18	–

Fig 52 ESEM pictures of CMSX-4/CN91 systems.

		Exposure time (hours)			
		1000	**2000**	**4000**	**10000**
Temperature (°C)	**850**	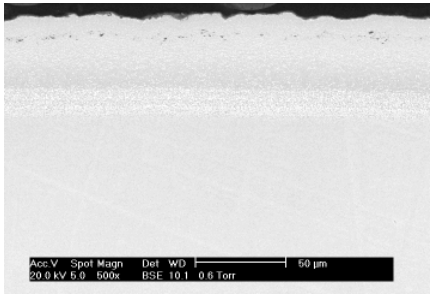 19	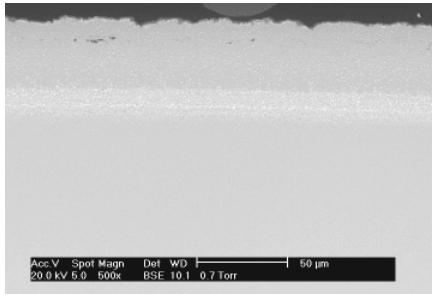 20	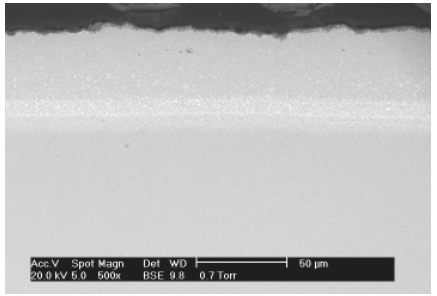 21	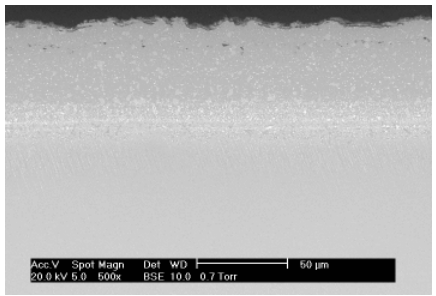 22
	900	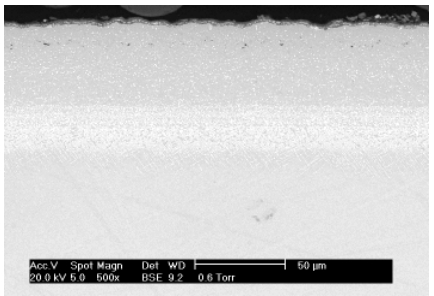 23	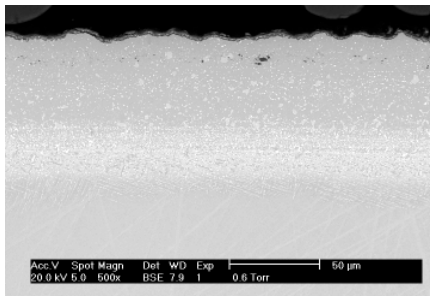 24	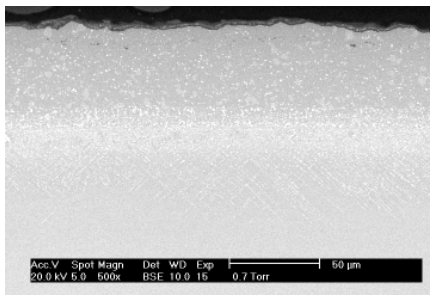 25	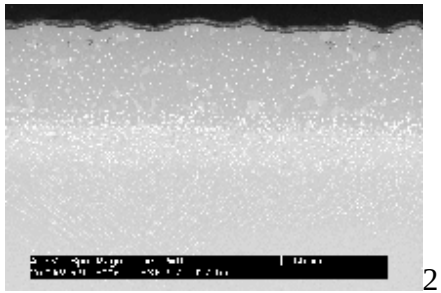 26

Temperature (°C)					
	950	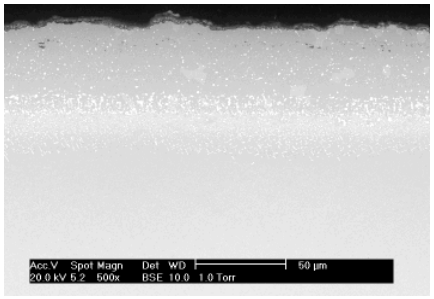 27	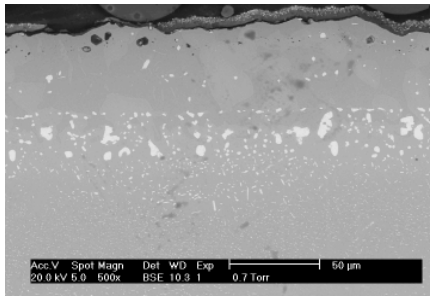 28	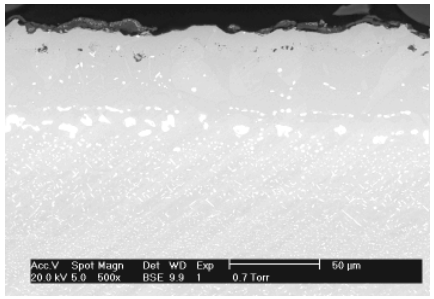 29	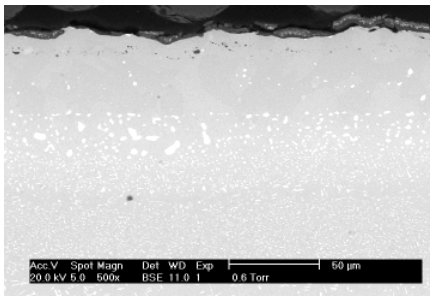 30
	1000	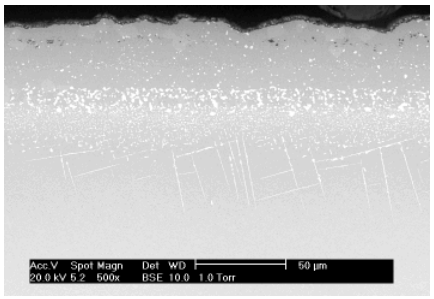 31	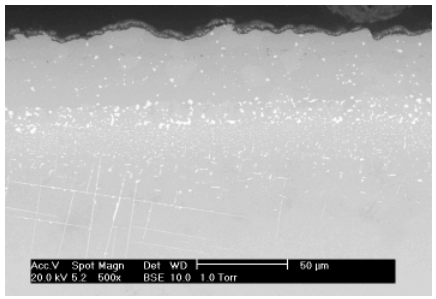 32	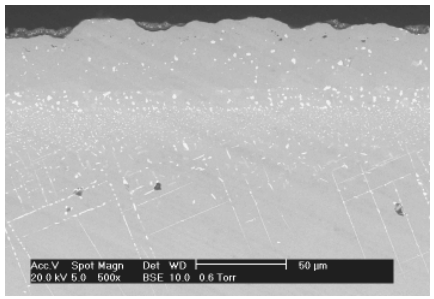 33	–
	1050	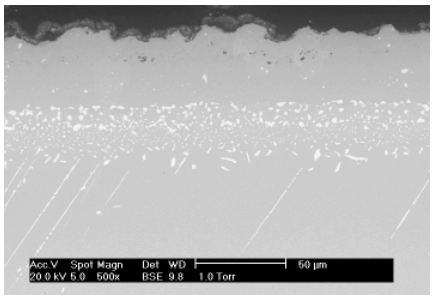 34	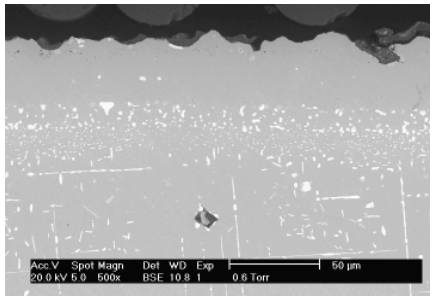 35	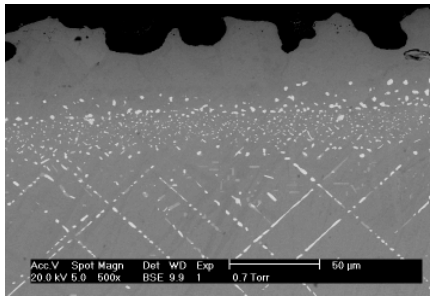 36	–

Fig 53 ESEM pictures of CMSX-4/RT22 systems.

		Exposure time (hours)			
		1000	**2000**	**4000**	**10000**
Temperature (°C)	**850**	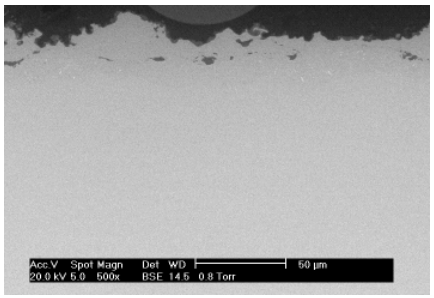	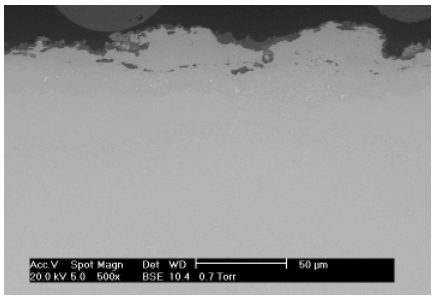	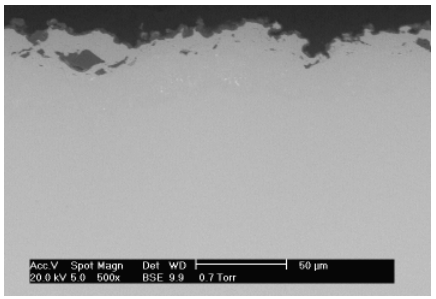	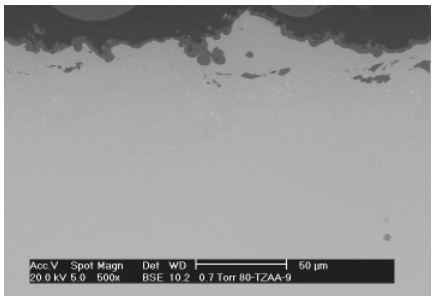
		37	37	38	39
	900	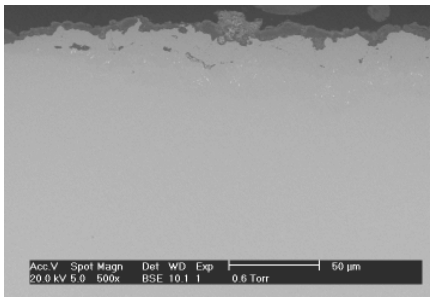	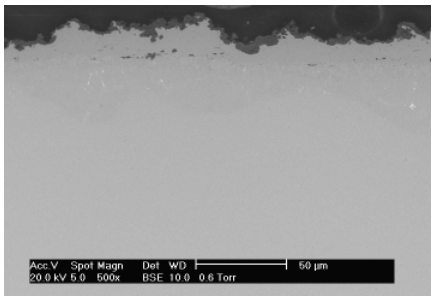	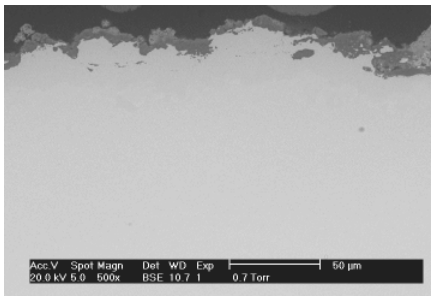	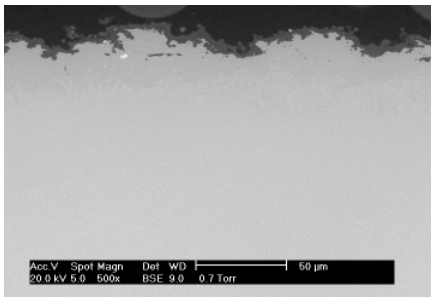
		40	41	42	43
	950	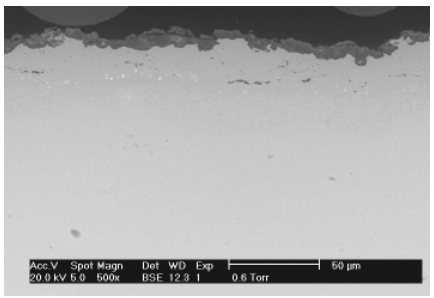	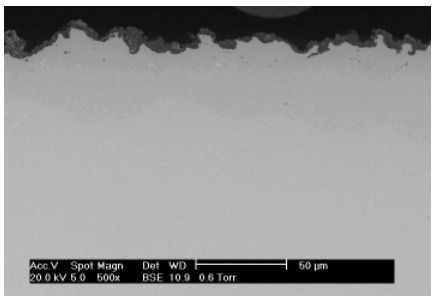	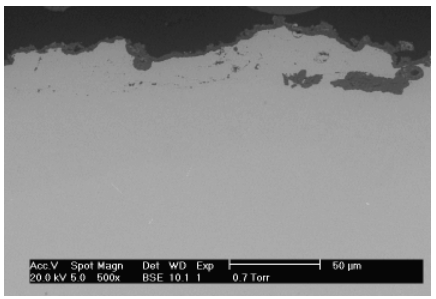	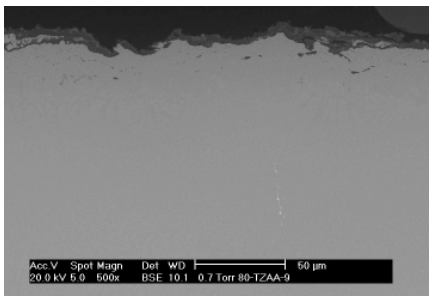
		44	45	46	47
Te	**10 00**				

		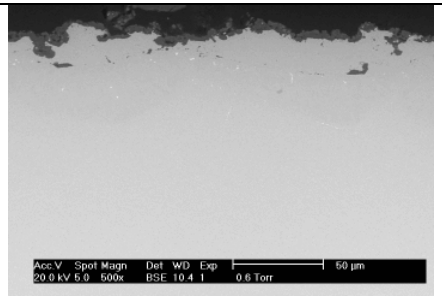 48	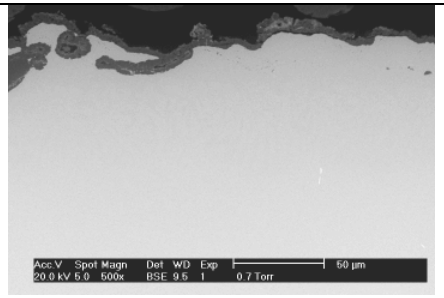 49	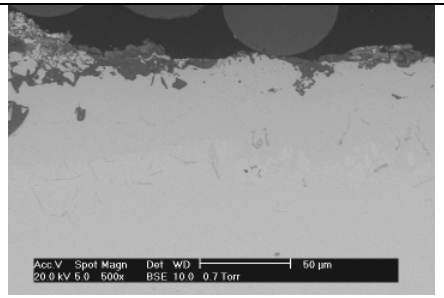 50	–
	1050	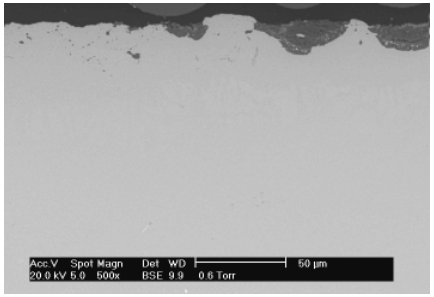 51	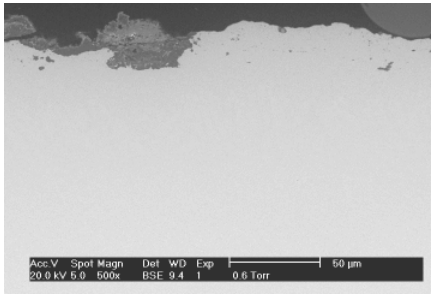 52	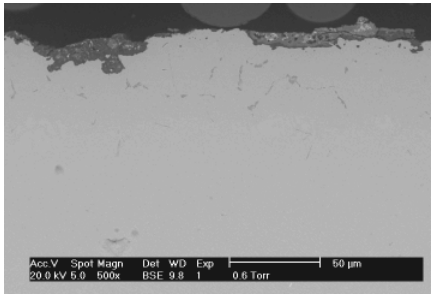 53	–

Fig 54 ESEM pictures of CMSX-4/”LCO22” systems.

EDX analysis performed on RT22

Figure 55 represents an example of the results of the EDX analysis performed on RT22 coated CMSX-4 tested for 2000 hours at 950°C.

The following scale features have been observed:

- outer oxide layer: composed of mixed oxide such as TiO_2 and Ta_2O_5 (the brightest grains), Al_2O_3, Cr_2O_3 likely along with spinels (e.g. $NiAl_2O_4$, $CoAl_2O_4$, $CoCr_2O_4$);
- inner oxide layer: composed of Al_2O_3.